sRecovery Act: Geologic Characterization of the South Georgia Rift Basin for Source Proximal CO_2 Storage

Final Technical Report

For the period: September 16, 2009 through September 30, 2014

South Carolina Research Foundation

Michael Waddell, Principal Investigator
South Carolina Research Foundation
1600 Hampton St.
Suite 414
Columbia, SC 29208

Date of report: Revised February, 10th, 2015

DE-FE0001965

DISCLAIMER

This report was prepared as an account of work sponsored by an agency of the United States Government. Neither the United States Government nor any agency thereof, nor any of their employees, makes any warranty, express or implied, or assumes any legal liability or responsibility for the accuracy, completeness, or usefulness of any information, apparatus, product, or process disclosed, or represents that its use would not infringe privately owned rights.

Reference herein to any specific commercial product, process, or service by trade name, trademark, manufacturer, or otherwise does not necessarily constitute or imply its endorsement, recommendation, or favoring by the United States Government or any agency thereof. The views and opinions of authors expressed herein do not necessarily state or reflect those of the United States Government or any agency thereof.

The South Carolina Research Foundation (SCRF) makes every effort to collect, provide, and maintain accurate and complete information. However, data acquisition and research are ongoing activities of SCRF, and interpretations may be revised as new data are acquired. Therefore, all information made available to the public by SCRF should be viewed in that context. Neither the SCRF nor any employee thereof makes any warranty, expressed or implied, or assumes any legal responsibility for the accuracy, completeness, or usefulness of any information, apparatus, product, or process disclosed in this report. Conclusions drawn or actions taken on the basis of these data and information are the sole responsibility of the user.

Acknowledgements

This material is based upon work supported by the U.S. Department of Energy (DOE) National Energy and Technology Laboratory (NETL) under Grant Number DE-FE0001965. This project is managed by the South Carolina Research Foundation and funded by DOE/NETL and cost sharing partners.

ABSTRACT

This study focuses on evaluating the feasibility and suitability of using the Jurassic/Triassic (J/T_R) sediments of the South Georgia Rift basin (SGR) for CO_2 storage in southern South Carolina and southern Georgia The SGR basin in South Carolina (SC), prior to this project, was one of the least understood rift basin along the east coast of the U.S. In the SC part of the basin there was only one well (Norris Lightsey #1) the penetrated into J/T_R. Because of the scarcity of data, a scaled approach used to evaluate the feasibility of storing CO_2 in the SGR basin.

In the SGR basin, 240 km (~149 mi) of 2-D seismic and 2.6 km^2 3-D (1 mi^2) seismic data was collected, process, and interpreted in SC. In southern Georgia 81.3 km (~50.5 mi) consisting of two 2-D seismic lines were acquired, process, and interpreted. Seismic analysis revealed that the SGR basin in SC has had a very complex structural history resulting the J/T_R section being highly faulted. The seismic data is southern Georgia suggest SGR basin has not gone through a complex structural history as the study area in SC.

The project drilled one characterization borehole (Rizer # 1) in SC. The Rizer #1 was drilled but due to geologic problems, the project team was only able to drill to 1890 meters (6200 feet) instead of the proposed final depth 2744 meters (9002 feet). The drilling goals outlined in the original scope of work were not met. The project was only able to obtain 18 meters (59 feet) of conventional core and 106 rotary sidewall cores. All the conventional core and sidewall cores were in sandstone. We were unable to core any potential igneous caprock. Petrographic analysis of the conventional core and sidewall cores determined that the average porosity of the sedimentary material was 3.4% and the average permeability was 0.065 millidarcy. Compaction and diagenetic studies of the samples determined there would not be any porosity or permeability at depth in SC. In Georgia there appears to be porosity in the J/T_R section based on neutron log porosity values. The only zones in Rizer #1 that appear to be porous were fractured diabase units where saline formation water was flowing into the borehole.

Two geocellular models were created for the SC and GA study area. Flow simulation modeling was performed on the SC data set. The injection simulation used the newly acquired basin data as well as the Petrel 3-D geologic model that included geologic structure. Due to the new basin findings as a result of the newly acquired data, during phase two of the modeling the diabase unit was used as reservoir and the sandstone units were used as caprock.

Conclusion are: 1) the SGR basin is composed of numerous sub-basins, 2) this study only looked at portions of two sub-basins, 3) in SC, 30 million tonnes of CO_2 can be injected into the diabase units if the fracture network is continuous through the units, 4) due to the severity of the faulting there is no way of assuring the injected CO_2 will not migrate upward into the overlying Coastal Plain aquifers, 5) in Georgia there appears to porous zones in the J/T_R sandstones, 6) as in SC there is faulting in the sub-basin and the seismic suggest the faulting extends upward into the Coastal Plain making that area not suitable for CO_2 sequestration, 7) the complex faulting observed at both study areas appear to be associated with transfer fault zones (Heffner 2013), if sub-basins in the Georgia portion of the SGR basin can be located that are far away from the transfer fault zones there is a strong possibility of sequestering CO_2 in these areas, and 9) the SGR basin covers area in three states and this project only studied two small areas so there is enormous potential for CO_2 sequestration in other portions the basin and further research needs to be done to find these areas.

TABLE OF CONTENTS

Figures

Tables

EXECUTIVE SUMMARY

This study focuses on evaluating the feasibility and suitability of using the Jurassic/Triassic (J/T_R) sediments of the South Georgia Rift basin (SGR) for CO_2 storage in southern South Carolina and southern Georgia. The SGR basin in South Carolina (SC) prior to this project was one of the least understood rift basin along the east coast of the U.S. In the SC portion of the basin, there was only one well (Norris Lightsey #1) the penetrated into Jurassic/Triassic. Because of the scarcity of legacy basin data the project was divided into three phases and a scaled approach was used to evaluate the feasibility and efficacy of storing CO_2 in SGR basin.

The project is divided into three phases over four years with "Go/No Go" decisions after Phase I and Phase II. The phases go from coarse (analyzing regional data) to fine ending in selecting a site for and ultimately drilling a characterization borehole. Our three project phases were: I) preliminary geologic storage assessment based on existing data and analyses; II) regional assessment of target CO_2 storage formation(s) characteristics and injectivity assessment; and III) CO_2 containment assessment and risk analysis. Within the three phases are twelve tasks with additional subtasks. The project was designed to answer several fundamental questions pertaining to the efficacy of CO_2 storage in the SGR basin: 1) based on existing data are there porous zones with the potential to store at least 30 million tonnes of CO_2; 2) are the igneous layers competent enough as caprock seals to prevent the injected CO_2 from migrating upward into the Coastal Plain aquifers; 3) are the physical and chemical properties of the possible porous zones conducive for CO_2 injection and long-term storage; and 4) will the injection of CO_2 enhance continuing injectivity or reduce injectivity?

During Phase II, the project collected approximately 240 kilometers (km) [~149 miles (mi)] of new seismic data in South Carolina and 81.3 km (50.5 mi) of new seismic in southern Georgia. During Phase III, a characterization test boring was drilled in SC and named the Rizer #1. The results of the new seismic survey reveal that the SC portion of the SGR basin has had a very complex structural history resulting in highly faulted J/T_R section. In southern Georgia, the SGR basin has not had such a complex structural history.

The Rizer #1 characterization borehole did not reach the proposed total depth due to geologic problems. The project team was only able to drill to 1890 meters (m) (6200 ft) instead of the proposed final depth 2744 m (9002 ft). The drilling goals outline in the original scope of work were not met. The project team was only able to obtain 18 m of conventional core and 106 rotary sidewall cores. All the cores and sidewall cores were in sandstones. We were unable to core any potential caprock.

Petrographic and core analysis studies conducted on the conventional core and the rotary sidewall cores determine the average porosity of the sedimentary material was 3.4% and the average permeability was 0.065 millidarcy (mD) (see Appendix 1 for detail analysis). These dismal porosity and permeability values resulted in conducting a diagenetic and compaction study to determine if porous zones would exist deeper in the section. The results of the study were that the majority of the porosity destruction was from compaction. It was determine that the Triassic section was buried approximately 2.8 km (1.7 mi) deeper than present depth and there appears to be no zones with 10% or greater porosity that exist at depth in the SC portion SGR basin study area.

During drilling, saline water was flowing into the boring along a faulting diabase unit at an estimated flow rate of ~200 gallons per minute. This would suggest that the diabase units are highly fracture and the fractures are interconnected. This led to the hypothesis that the sandstone

horizons in the SC portion of the SGR basin could serve as caprock and the highly fractured diabase layers could serve as CO_2 reservoirs. To test this hypothesis, the injection simulations were modeled using the diabase as reservoir and the sandstone as caprock. The simulations demonstrated that 30 million tonnes of CO_2 could be injected into multiple diabase units. However, due to the intense faulting and fracturing it was determined that with the current knowledge of the geology, we cannot be certain that the injected CO_2 will be contained in the J/T_R section.

The southern Georgia study area was selected because the seismic data could be calibrated to existing well data. GGS-3457, former oil exploration well, has geophysical logs that were used to correlate major horizons with seismic reflectors. The neutron porosity log values indicate that over 120 meters of sandstone have porosity values greater than 10%. At the time of seismic acquisition we did not know the study area was located in a transfer fault zone (Heffner 2013). It appears from the seismic interpretations that some of the faulting may extend upward into the overlying Coastal Plain sediments. As the injection simulation modeling shows, these faults may provide a conduit for upward migration of CO_2 into the Coastal Plain aquifers.

The SGR basin still has potential for storing over 30 million tonnes of CO_2. *It needs to be noted that this project only characterized a very small part of the entire SGR basin.* Based on our study, the SGR is not a single basin but a series of smaller sub-basins. In SC, the 240 km (149 mi) of seismic data suggest that the study area in SC is unsuitable for CO_2 due to extensive faulting and the low porosity and permeability values. In Georgia there appears to be numerous sub-basins that have potential for storing CO_2. Geophysical logs suggest there is porosity in the J/T_R section that would make CO_2 storage possible. Examining legacy seismic data in the Georgia study area it appears some of these sub-basins have not had a complex structural history. These sub-basins are unexplored so there would have to be extensive characterization before considering CO_2 sequestration. When considering a CO_2 injection in SGR basin, the site should be located away from the transform fault zones identified in Heffner 2013 in order to avoid structural problems.

Conclusion are 1) the SGR is composed on numerous sub-basins, 2) this study only look portions of two sub-basins, 3) in SC 30 million tonnes of CO_2 can be injected into the diabase units if the fracture network is continuous through the units, 4) due to the severity of the faulting there is no way of assuring the injected CO_2 will not migrate upward into the overlying Coastal Plain aquifers, 5) in Georgia there appears to porous zones in the Jurassic/Triassic sandstones, 6) as in SC the faulting in the sub-basin we study it appears the faulting extends upward into the Coastal Plain making that area not suitable for CO_2 sequestration, 7) the complex faulting observed at both study areas appear to associated with transfer fault zones (Heffner 2013), if sub-basins in the SGR in Georgia can be located away from these transfer fault zones there is a strong possibility of sequestering CO_2 in the SGR, and 9) The SGR covers area in three states and this project only studied two small areas so there is enormous potential for CO_2 sequestration in the basin.

Introduction

This study evaluated the feasibility of CO_2 storage in the Jurassic/Triassic (J/T_R) strata of the buried South Georgia Rift basin (SGR). All data and analyses associated with this determination to be uploaded into the NATCARB database. The J/T_R sequence, based on preliminary assessment of limited geological and geophysical data, has both the appropriate areal extent and multiple horizons where significant amounts of CO_2 may potentially be stored. The presence of several igneous layers within the sequence was thought to provide adequate seals to prevent upward migration of CO_2 into the Coastal Plain aquifer systems. Several wells have penetrated the rift sediments in the lower Coastal Plain of South Carolina. However, the majority of the well data from those wells are from the upper J/T_R sediments. One wildcat well (i.e., Norris Lightsey #1) located on the northern up-dip margin of the basin was drilled to over 3,000 m below ground surface (bgs). Available data for the Norris Lightsey #1 well indicate that it was logged from land surface to 2,973 m bgs. A thick (~25 m) basalt layer was encountered at approximately 1738 m to 1774 m bgs with six additional basalt layers beneath it. Clastic sediments occupy the intervals between the basalt flows that we believe are capable of storing large amounts of CO_2 with the overlying basalts providing the seals. Further, the target storage depth is well below the 1 km (.62 mi) critical depth to maintain CO_2 as a supercritical fluid (*CO2CRC*, 2008). Given the significant number of CO_2 sources in the southeastern U.S., particularly in southeastern South Carolina (Figure 1), and the promising conditions of the SGR, we believe that through this carefully designed project for geologic characterization of the SGR in southern South Carolina we can demonstrate: 1) that the SGR basin is a significant CO_2 storage site; and 2) that it could be commercially developed.

A highly capable team of researchers and technical professionals were assembled and lead by the Earth Sciences and Resources Institute - University of South Carolina (ESRI-SC). The integrated team members are Department of Earth and Ocean Sciences at the University of South Carolina – Columbia (USC-Columbia) the South Carolina Geological Survey, the Illinois State Geological Survey, Bay Geophysical, Inc., and Weatherford Laboratories. We believe, based on our initial assessment of available information from the refereed literature and from borehole data, that the Mesozoic basins, particularly the J/T_R saline formations in the SGR, may be capable of safely storing very large quantities of CO_2. The Carbon Sequestration Atlas of the United States and Canada (*NETL*, 2008) identifies a Triassic basin in southern South Carolina as a saline formation suitable for CO_2 storage (Figure 1). *Hovorka, et al.* (2006) states that the Mesozoic rift basins along the eastern seaboard are prospective areas for CO_2 storage. They map the entire southeastern quarter of South Carolina in this favorable category. *McBride, et al.* (1989) analyzed regional seismic profiles across the SC Coastal Plain for insight into the structural style and stratigraphy of the buried J/T_R SGR. They concluded that basin-fill below the Cretaceous-Tertiary on-lap may locally reach 6 km (3.7 mi) in thickness. *McBride, et al.* (1989) also identified a thick (i.e., 250 m) basalt flow named the "J" basalt at the base of the Cretaceous-Tertiary Coastal Plain that is larger than 100,000 km^2 (38610 mi^2) in areal extent and comparable to the Columbia Plateau flood basalts. Initially the "J" basalt was thought to be aerial extensive sill-like layer across the SGR but this study determined it was not. Figure 2 shows the partial gamma log and lithology of the Norris Lightsey #1 well. The location of this well, shown in Figure 1 as the blue "star", is near the suspected up-dip margin of the SGR. The geologic sequence shown in Figure 2 for the Norris Lightsey #1 well is below the "J" basalt described above.

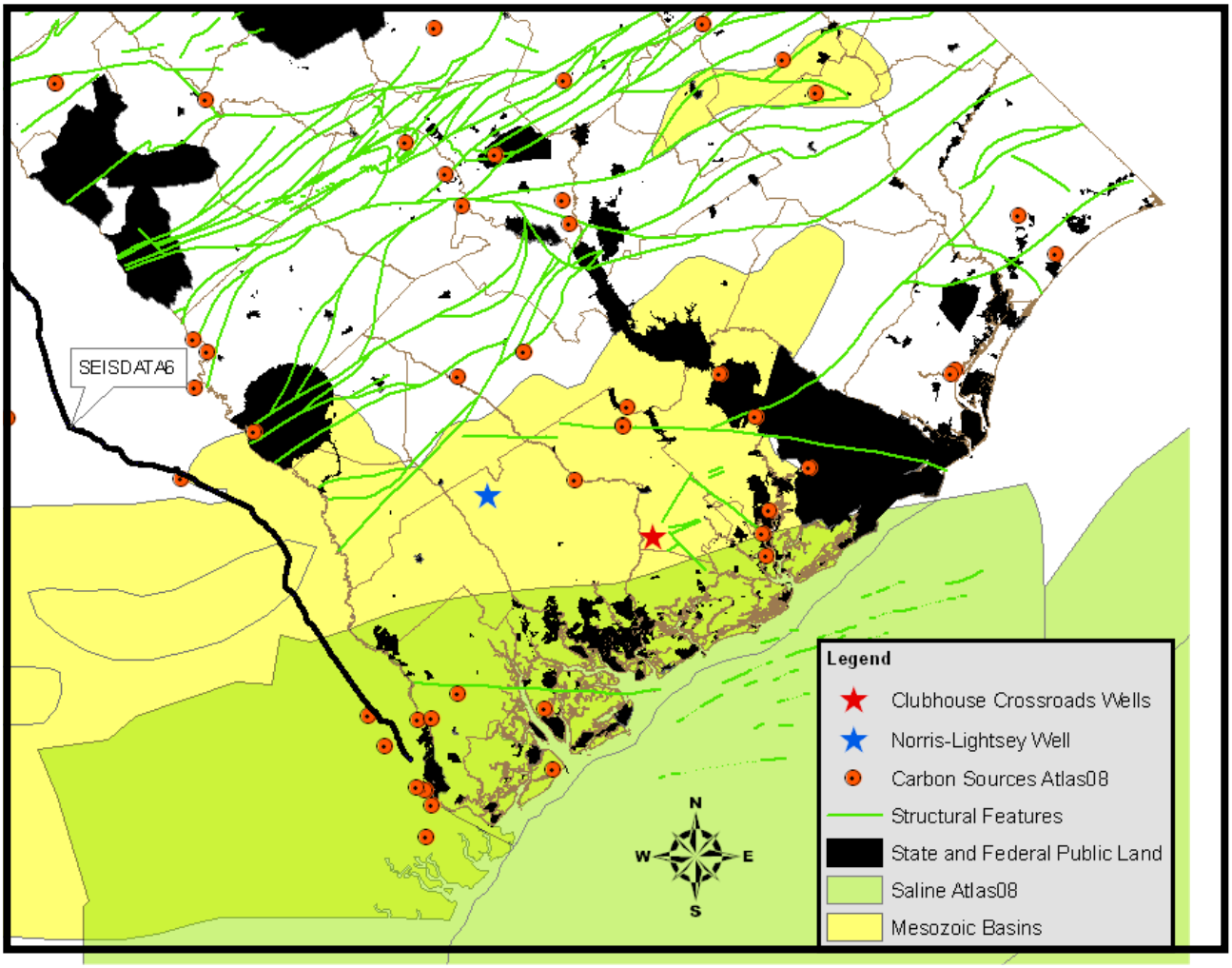

Figure 1. Locations of CO_2 producers in and around the South Georgia Rift Basin (yellow). The green shaded area represents deep saline formations (NatCarb 2008 Atlas).

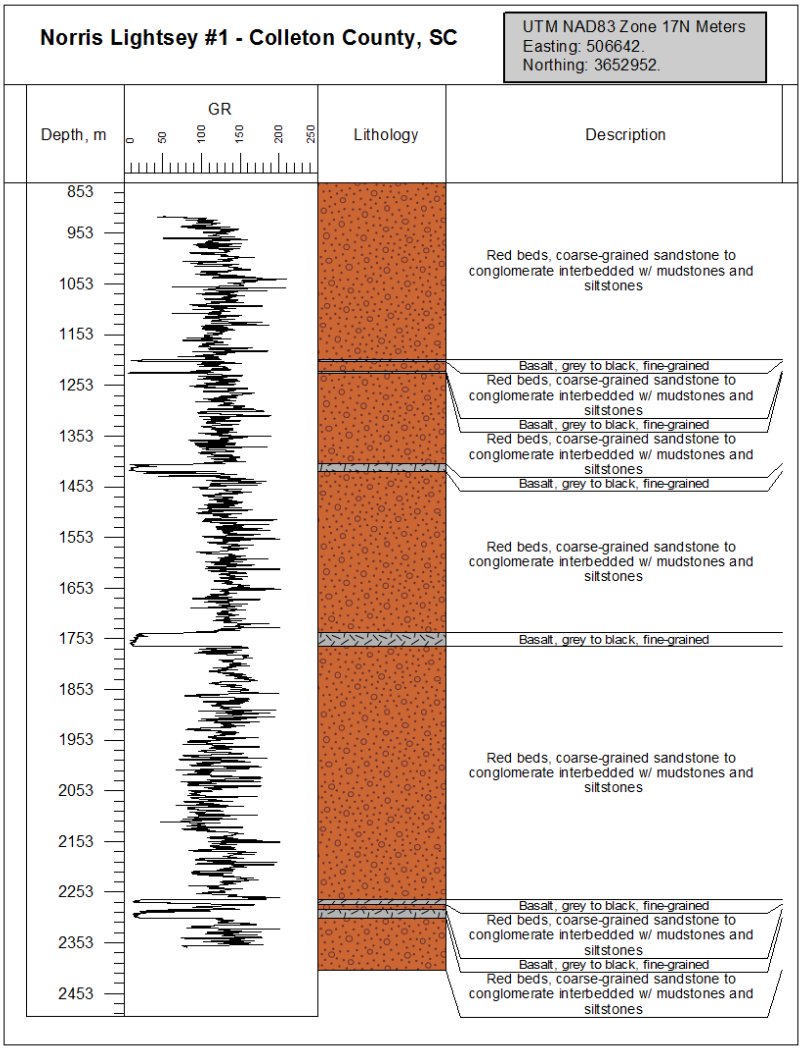

Figure 2. Partial gamma log and lithology of Norris Lightsey #1 well in the SGR basin.

Our initial study plan was to followed a natural progression of spatial scale refinement whereby we consider (1) all available existing data pertaining to the SGR basin and analogous basins; (2) collect new seismic data across three areas that are deemed "promising" from our analysis; (3) select the most promising site to drill a deep characterization borehole from among the three sites; (4) drill the characterization borehole, and (5) perform all relevant petrophysical and geochemical tests within the borehole and on cores taken from the caprock and the formation sediments. Only one 18.5 m conventional core was taken in a sandstone and no cores were ever

obtain for the potential diabase caprock. We never achieved any of our initial goals associated with the drilling program due to drilling problems, however, we did achieve the goals of the related seismic program. The rate of mineralization and rate of dissolution assessment could not be completed also due to the drilling problems and therefore lack of data.

Geologic Setting

The overall regional geologic setting is a critical component to understanding the depositional and diagenetic history of the study interval in Rizer #1 because regional tectonic events were not only instrumental in creating the SGR basin, but were also critical in driving the post-burial processes that altered the SGR basin strata. Although the study area is presently situated on the trailing edge of a passive continental margin, it experienced three regional tectonic stages since the breakup of the Pangea supercontinent and the formation of the North Atlantic Basin (Withjack *et al*., 1998; Figure 3).

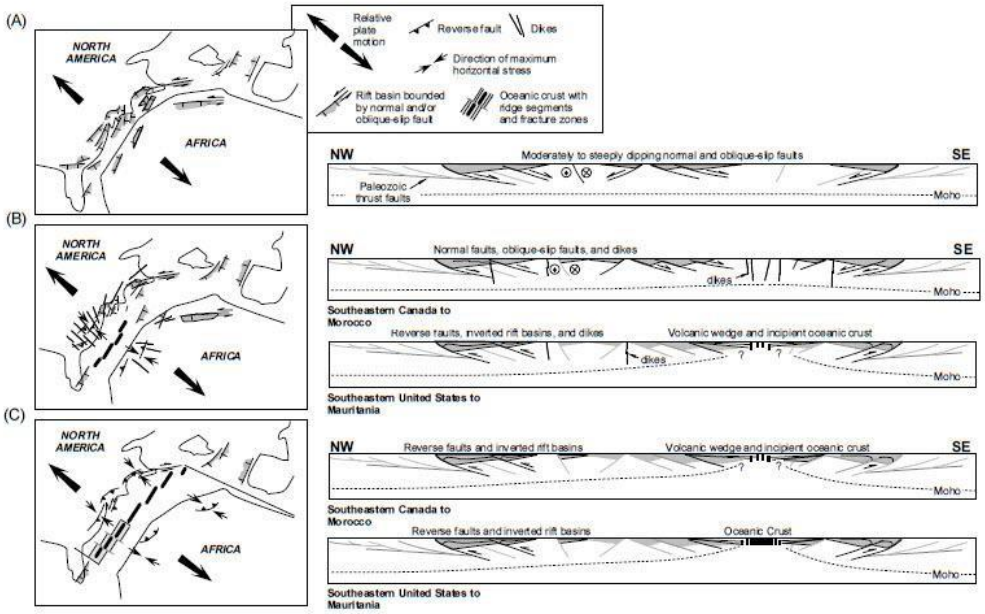

Figure 3. Graphical model by Withjack *et al*. (1998) showing evolution of central eastern North America in map and cross-sectional views. (A) Shows Middle to Late Triassic activity with northeast striking rift basins subsiding and filling with sediment. (B) Shows late Triassic

to Early Jurassic activity which includes basin inversion in the south and is shortly before or after eastern North America (ENA) magmatic activity with northwest-striking dikes. (C) Shows Early Jurassic (post ENA magmatic activity) to Early Cretaceous when rifting ceased. (From Withjack *et al*., 1998).

During early Mesozoic time a massive rift zone formed within the Pangea supercontinent (Olsen, 1997; Withjack *et al*., 2012). The North American portion of this rift zone, which was separated from other portions on the northwestern margins of Africa and Europe with the breakup of Pangea, is one of the world's largest rift systems being 500 km (311 mi) wide by 3000 km (1864 mi) long (Withjack *et al*., 2012).

Rift basins, such as the SGR examined in this study, formed in eastern North America from the Middle Triassic to Early Jurassic (Figure 4 and Figure 5); Manspeizeer and Cousminer 1988; Withjack *et al*., 1998). Strata within southern basins (south of the Culpepper Basin in Virginia), however, are exclusively Late Triassic in age, whereas basins to the north contain strata ranging from Middle Triassic to Early Jurassic in age (Olsen *et al*., 1989; Olsen, 1997). Most rift basins are asymmetric, bounded on one side by a normal fault or faults that strike northeast- southwest (Figure 3) and have displacements that locally exceed 10 km (6.2 mi) (Hutchinson and Klitgord, 1988; Schische, 1992, 1993; Withjack *et al*., 1995). The Upper Triassic synrift basins in the southern and central segments of eastern North America (ENA) are thought to be thicker (5-10 km) (3.1-6.2 mi) than in the northern segment (Figure 4; Withjack *et al*., 2012).

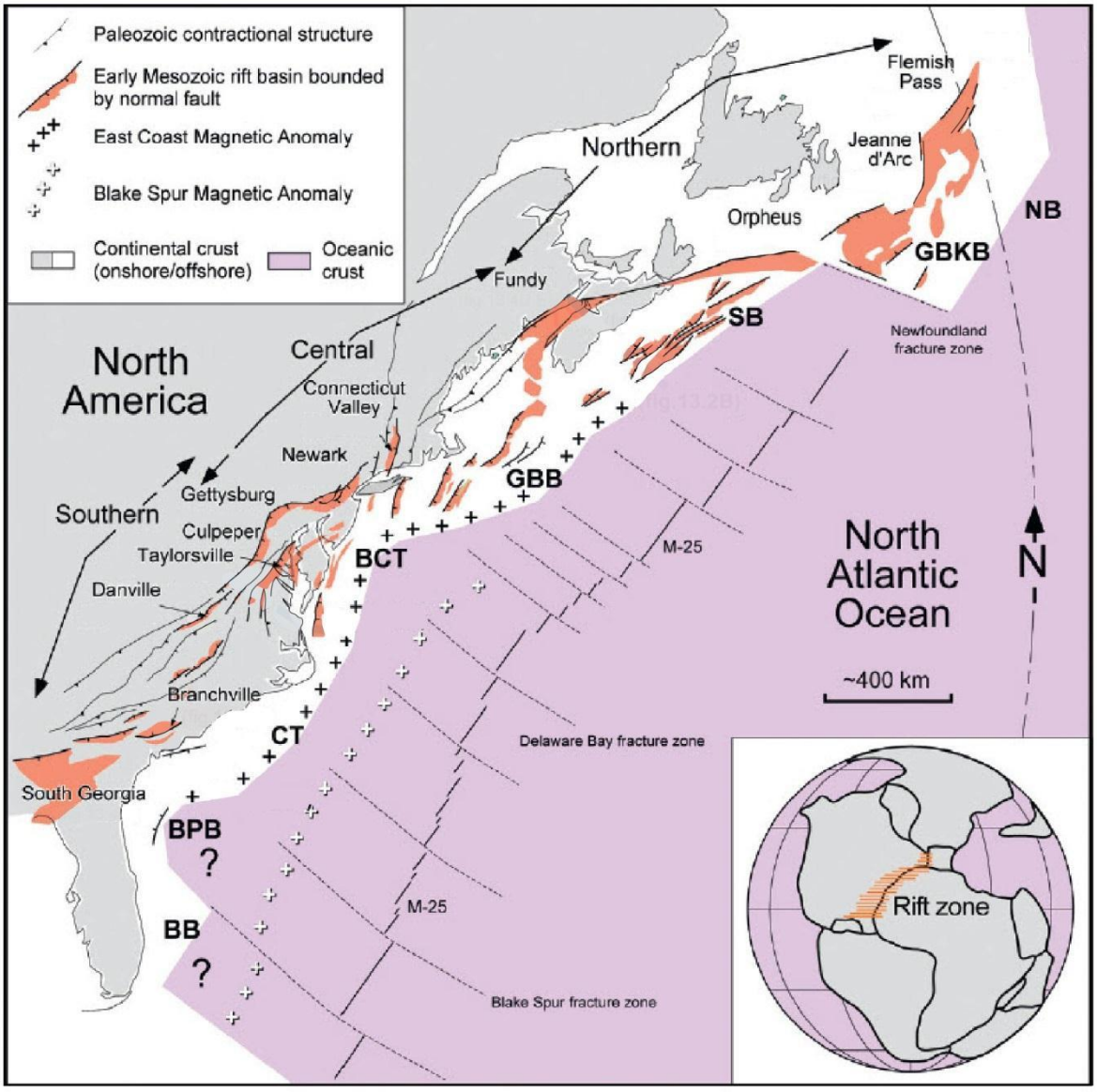

Figure 4. Major Paleozoic contractional structures and early Mesozoic rift basins of eastern North America with key tectonic features of the eastern North Atlantic as synthesized by Withjack *et al*. (2012) from Benson (2003), Foster and Robinson (1993), Klitgord *et al.* (1988), Olsen *et al*. (1989), Rankin (1994) and Welsink *et al*. (1989).The South Georgia Rift Basin (SGRB) is the southernmost basin identified in the system. Mesozoic/Cenozoic postrift basins are: BB, Bahamas basin; BPB, Blake plateau basin; CT, Carolina trough; BCT, Baltimore Canyon trough; GBB, Georges Bank basin; SB, Scotian basin; GBKB, Grand Banks basin; NB, Newfoundland basin. Pangaean supercontinent during the Late Triassic is based on a reconstruction of Olsen (1997) and shows the approximate extent of rift zone between the eastern edge of the North American plate and the northwestern edge of the African plate (Withjack *et al*., 2012). Figure is modified from Withjack *et al*. (2012).

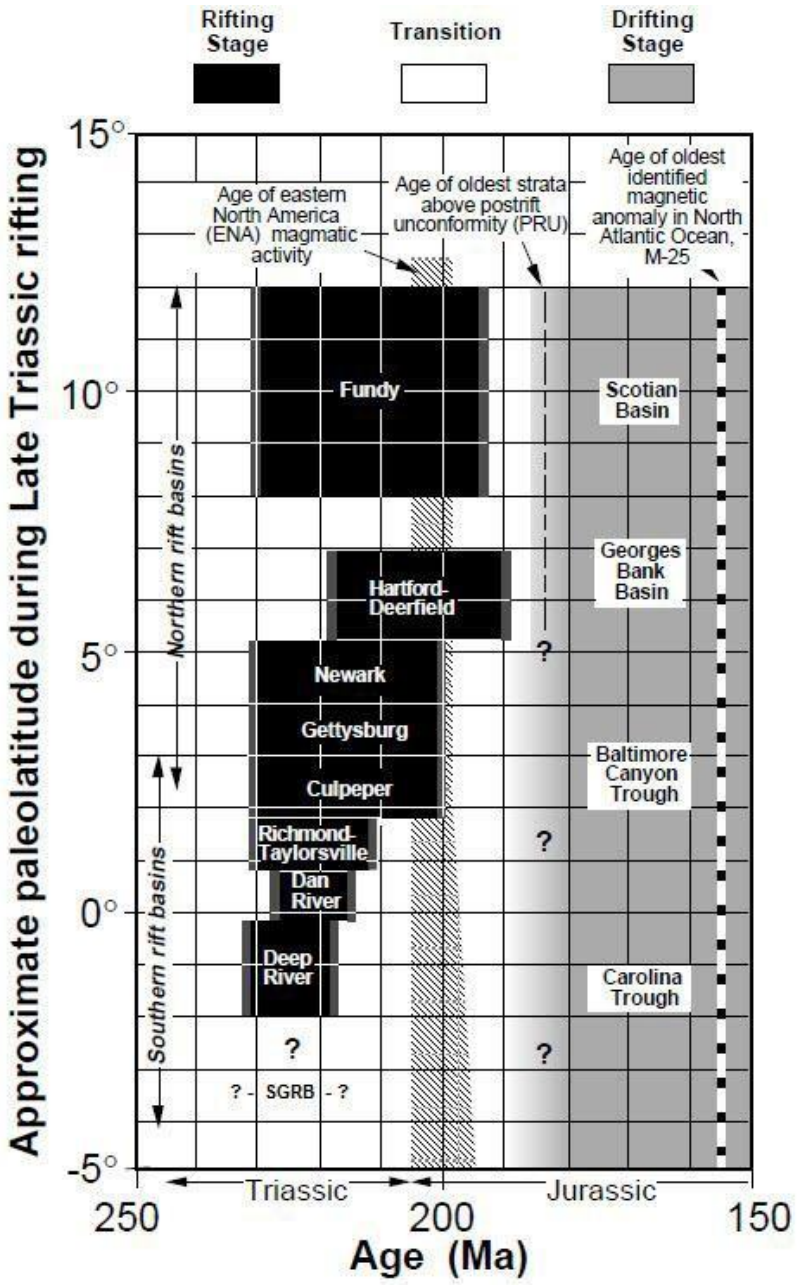

Figure 5. Graphic, which is modified from Withjack *et al.* (1998), shows the spatial and temporal distribution of central eastern North American rift basins starting with the SGRB in the south to the Fundy rift basin in the north. Also depicted are associated synrift basin / trough deposits and associated eastern North America (ENA) magmatic activity.

Based on regional outcrop studies of south and central ENA basins, continental conditions prevailed throughout their Late Triassic depositional histories (McAlpine, 1990; Olsen, 1997; Withjack *et al*., 2012). Paleoclimatic conditions are theorized to have varied from early Late

Triassic (Carnian) to late Late Triassic (Norian) as Pangea and the low latitude southern segment ENA rift basins drifted northward (Withjack *et al.,* 2012). This period is characterized by apparent drying with shallow water cyclical lacustrine strata predominating in the southern and central basins (Withjack *et al*., 2012 after Olsen and Kent, 2000 and Olsen, 1997).

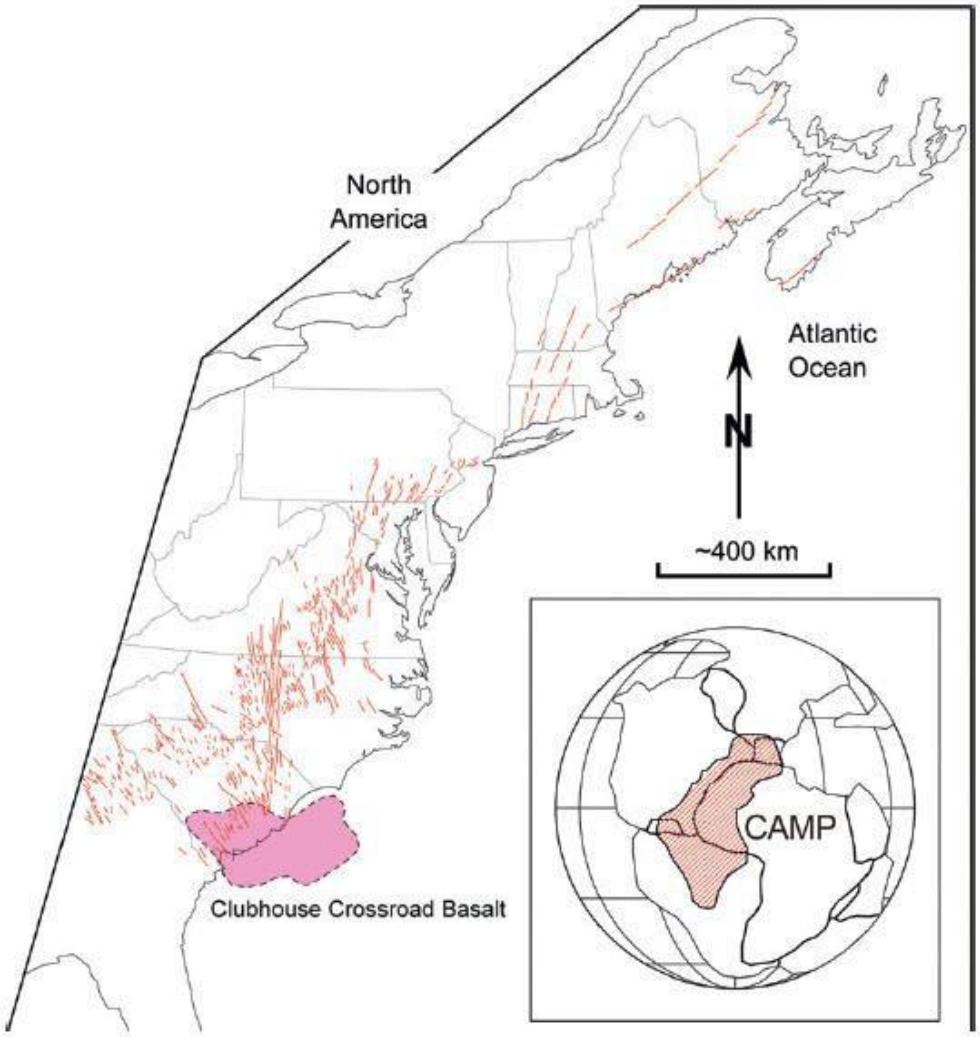

Figure 6. Figure from Withjack *et al*. (2012), showing early Jurassic-age dikes (thin lines) in ENA and the possible extent of the Clubhouse Crossroads Basalt (after Oh *et al*., 1995; McHone, 2000; and McHone *et al*., 2004).

It was believed no sedimentary rocks of Early Jurassic age are present within any onshore rift basin south of the Culpeper Basin. However, in this study there is the possibility of some Jurassic sediments being present in the southern portion of the basin in southern Georgia. (Figure

6; Olsen *et al*. 1989; Olsen, 1997; Withjack *et al*.1998). It is reported that an angular unconformity separates synrift and post rift strata in the subsurface of South Carolina (Behrendt, 1986; Costain and Coruh, 1989; Withjack *et al.,* 1998). The oldest strata, which overlies the onshore South Carolina portion of the SGR basin, is the Upper Cretaceous aged Middendorf Formation (Colquhoun *et al*., 1983). Offshore, however, "a thin package" of sedimentary rocks separates ENA basalts from the underlying postrift unconformity (Dillon et al., 1983; Withjack *et al*., 1998). According to Withjack *et al*. (1998), rifting ceased and erosion took place before eruption of the ENA basalts at approximately 200 Ma. (Findings from this study indicate a minimum of 4400ft [1.35km] of erosion from Rizer #1 portion of the SGR.) During this same period preceding the ENA magmatic event, numerous basement-involved reverse faults formed, including the Cooke fault in South Carolina (Behrendt *et al*., 1981; Hamilton *et al*., 1983; Withjack *et al*., 1998) and numerous reverse faults with associated propagation folds in the Richmond rift basin of southern Virginia (Venkatakrishnan and Lutz, 1988; Withjack *et al*., 1998).

ENA magmatic activity, which during the Early Jurassic included inclusion of diabase dikes and sills and the extrusion of basalt flows (King, 1971; Olsen *et al*., 1989, 1996; McHone, 1996; Withjack *et al*., 1998), is part of one of the world's largest igneous provinces, the Central Atlantic Magmatic Province (CAMP; Figure 6). North of the Culpeper basin, basalt flows are intercalated with synrift strata but are not present within exposed rift basins to the south (Olsen, 1997). (A majority of igneous layers observed within the Rizer #1 study interval are at relatively low-angle, and, consequently, are interpreted as intrusive sills.) Ragland *et al*. (1992)

determined the age for the ENA magmatic activity (flows, dikes, and sills) was 200 ±5 Ma (Figure 5), based on review of all geologic, paleomagnetic, and geochemical data available.

Postrift contractional deformation is recognized as pervasive within the ENA (Withjack *et al*. (2012). Many of these postrift contraction features are inversions or flower structures (such as the fault block penetrated by Rizer #1). The degree of inversion for Taylorsville basin in the southern segment of the ENA and the Fundy basin in the northern segment are both interpreted to be approximately 2 km (6600ft; Figure 7; as is the Rizer #1 portion of the SGR). Since no collision of subduction zones existed near the ENA during Mesozoic time "incipient ridge-push forces and/or an initial continental resistance to plate motion may produce shortening…" (Withjack *et al*., 2012 after Boldreel and Andersen, 1993; Bott, 1992; Dewey, 1988; Schlische *et al*., 2003; Withjack *et al*., 1995, 1998). In the southern segment of the ENA, postrift contractional deformation (Figures 8 and 9) occurred both prior to and after the ENA magmatic event, including approximately 140m (460 ft) of reverse displacement along the Cooke fault in South Carolina preceding the magmatic event (Behrendt *et al*., 1981; Hamilton *et al*., 1983; Withjack *et al*., 1998).

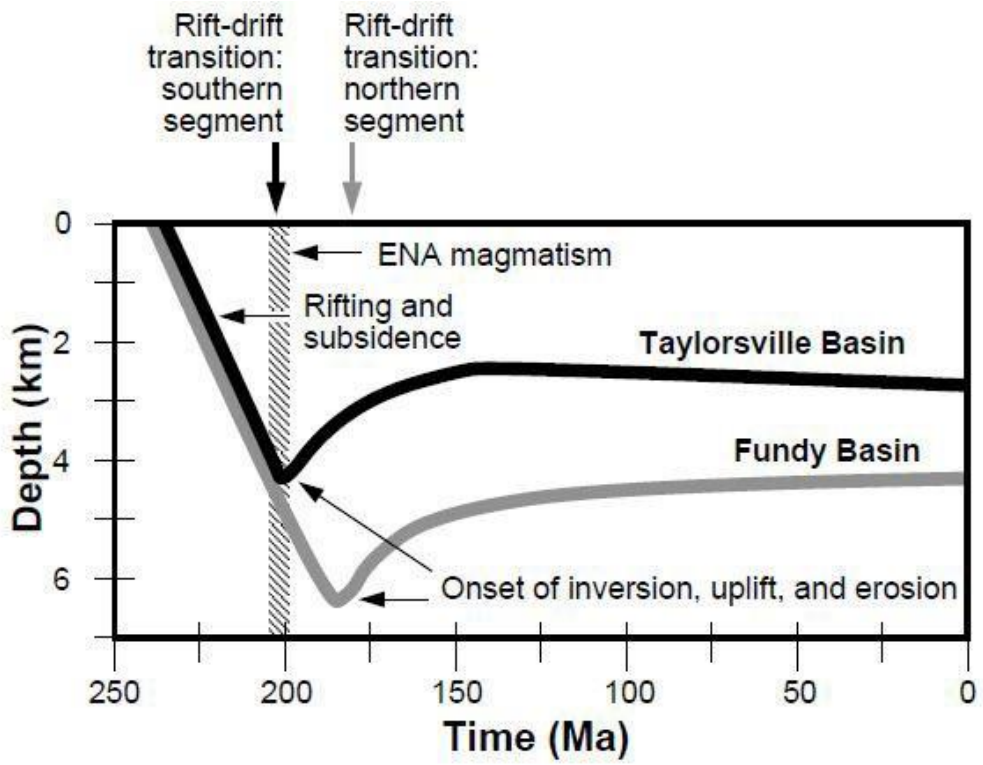

Figure 7. Subsidence histories of the Taylorville and Fundy rift basins (Tseng *et al.*, 1996; Withjack *et al.*, 1998). Figure is from Withjack *et al.* (1998).

As previously mentioned, the CAMP basalt flows, encountered within the Clubhouse Crossroads No. 3 borehole, are unconformably overlain by Upper Cretaceous, Santonian- to Turonian-aged Middendorf Formation. The missing section spans over a 100 Ma period.

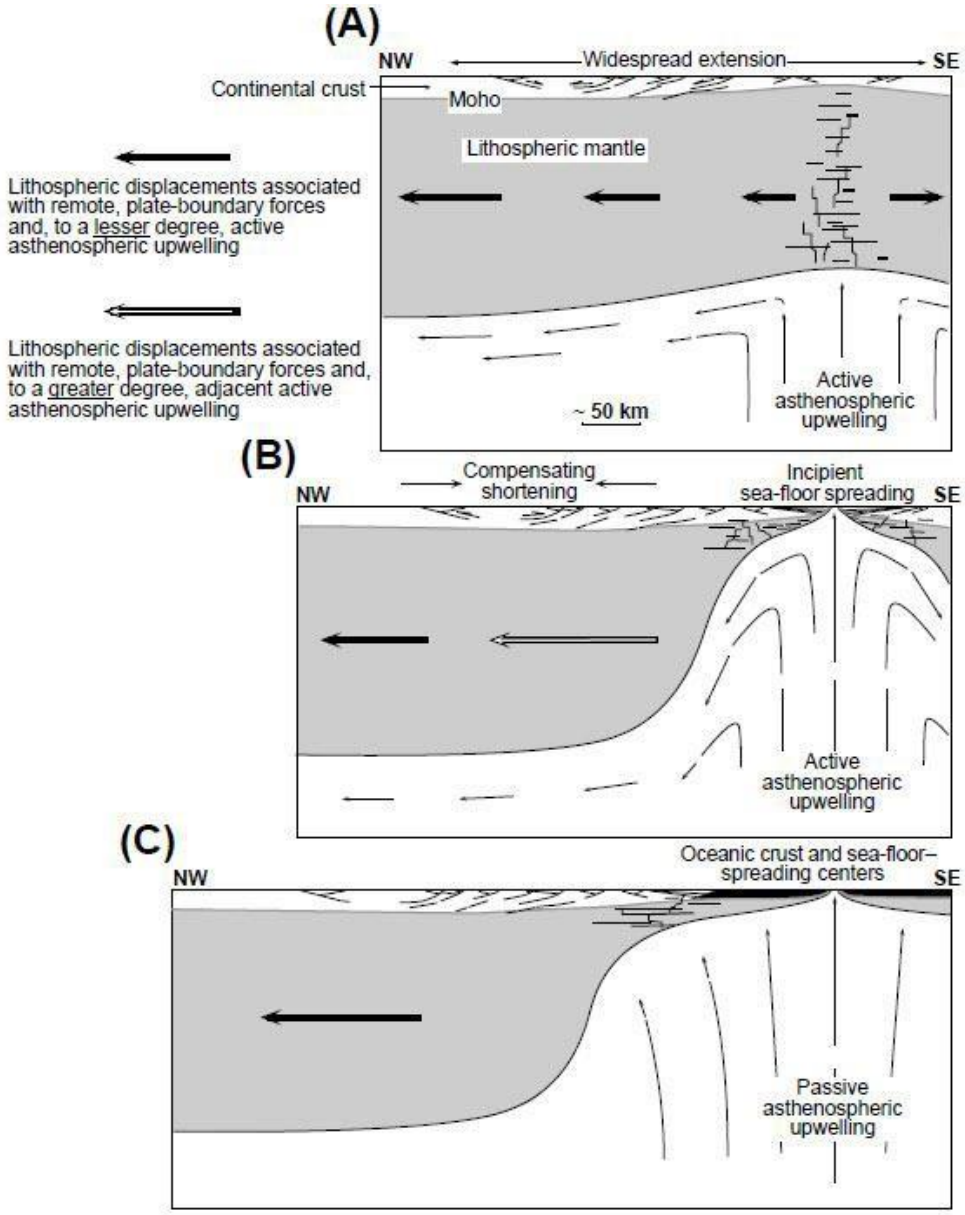

Figure 8. A graphic representation of the three stage rift-drift tectonic model for eastern North America (ENA) from Withjack *et al*. (1998). The first stage of early rifting (A) creates a setting of widespread extension, which produces the rift basins within the ENA. Late rifting (B) is a period when lithospheric displacement near the upwelling exceeds displacement far away, resulting in "compensating shortening" in the intervening zone. The final stage of drifting (C) is a period of uniform lithospheric displacement with most inversion activity ceasing. Figure from Withjack *et al.* (1998).

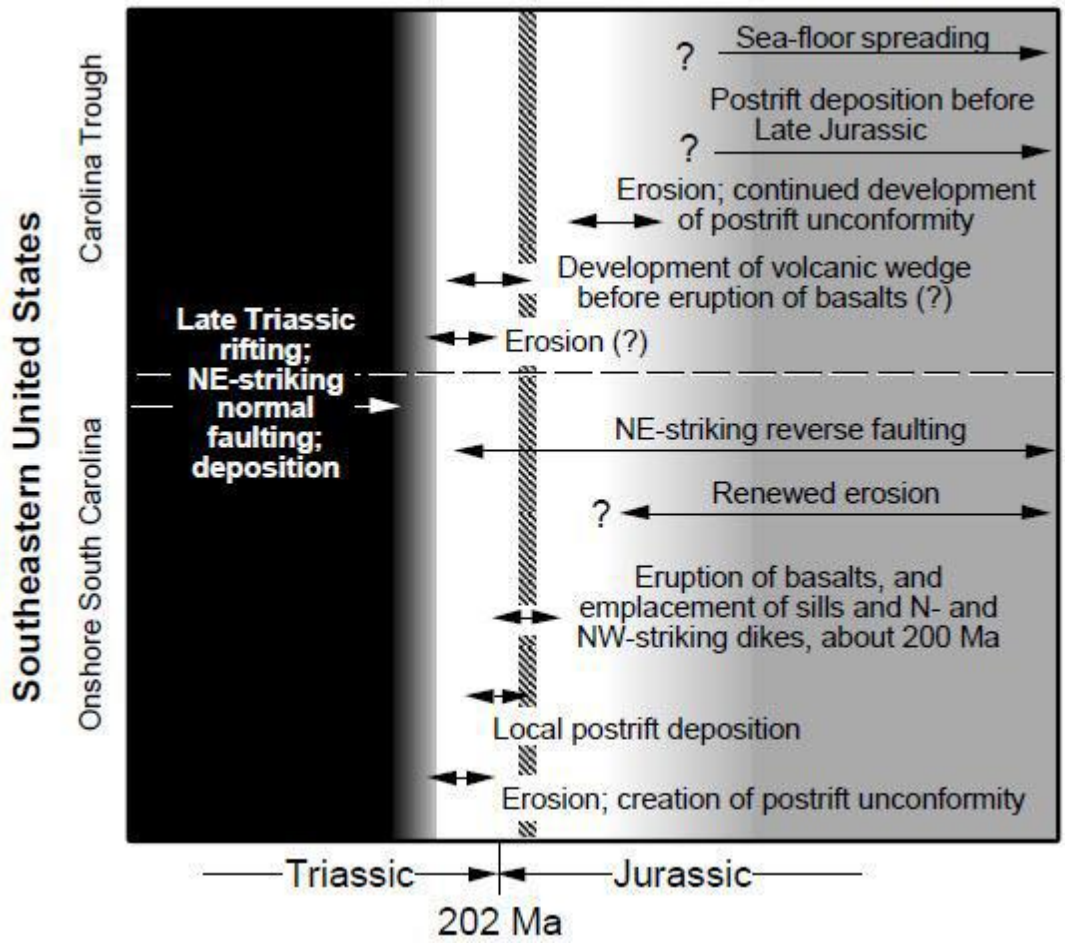

Figure 9. Graphical depiction of sequence of events during rift-drift transition in southeastern United States. Figure is from Withjack *et al*. (1998).

Experimental Methods

Our technical approach was based on the scientific method. The principles and empirical processes of discovery and demonstration that were followed involved (1) the observation of phenomena, (2) the refinement of our hypothesis, (3) experimentation to demonstrate the truth or falseness of our hypothesis, and (4) a conclusion that validates or modifies our hypothesis. We divided our project into three phases with critical "Go/No Go" decisions following the first two stages to avoid the wasteful use of resources should our preliminary investigations clearly show that the SGR basin is not suitable for CO_2 storage. We decided to use a scaled approach to the project dividing the project into three phases. Our three project phases are: I) preliminary geologic storage assessment based on existing data and analyses; II) regional assessment of target CO_2 storage formation(s) characteristics and injectivity assessment; and III) CO_2 containment assessment and risk analysis.

Results and Discussions

Phase I Assimilating existing Geologic and Geophysical Data

The project team identified 27 wells onshore Georgia and South Carolina that are located in the South Georgia Rift Basin. Three wells (i.e., OCSG 3664, 3671 and the GE Cost 1) are located offshore Georgia and maybe part of the SGR (Figure 10). The Georgia well geophysical log data were obtained in a TIFF file format. Selected wells were subsequently digitized by a private vendor into the LAS file format.

The project team also located rock cores from the Dorchester 211 well located in the South Carolina study area. It penetrated approximately ~30 m (100 ft) into mafic igneous rock at the base of the Coastal Plain. Paper copies of the geophysical logs from the Dorchester 211 well were also digitized by a private vender into the LAS file format. Core from this well is located at the SC Geological Survey and was examined in some detail. The mafic igneous rocks in Dorchester 211 were described as basalt flows. Another major development is the project team was able to obtain a complete lithology description for the Norris Lightsey #1 well, as well as some core analysis data (porosity and permeability) for select intervals in the Lightsey well. In Table 1 are the data for each well which is listed as lithologic, core, paleontology, and geophysical. All the well data that have been entered into the Petrel® project. Elevation is either ground level or Kelly Bushing which is located on the drilling floor of a drilling rig. Table 2 list all of the initial legacy data that was loaded into the Petrel® project.

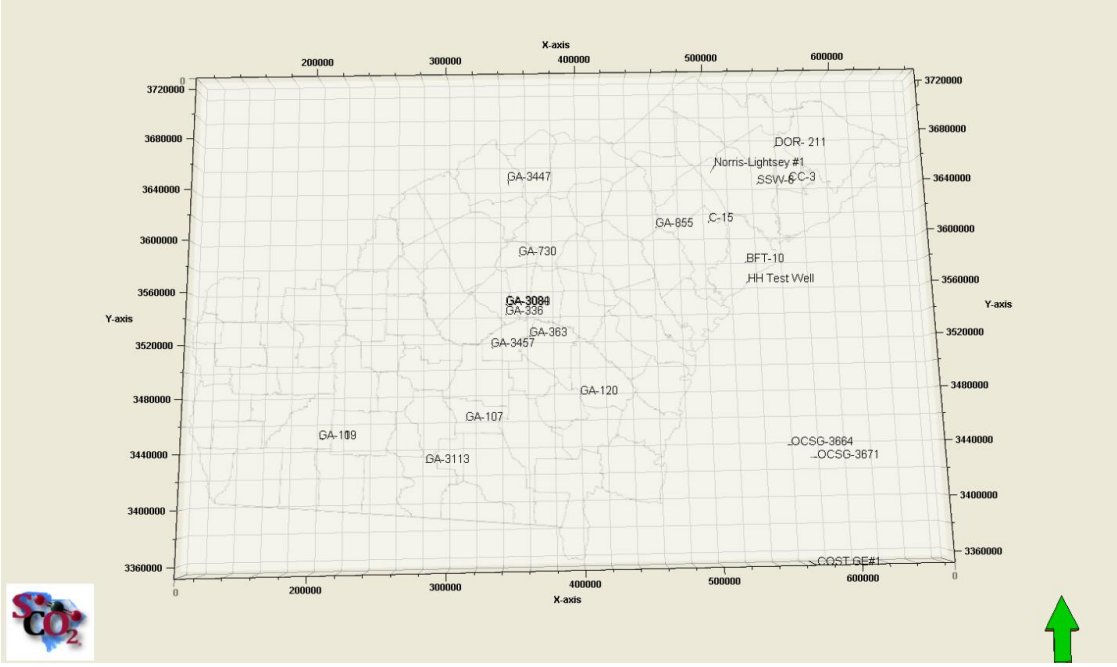

Figure 10. Petrel® imbedded map showing the distribution of digital well data for the project.

Table 1. Data for each well is listed as lithologic, core, paleontology, and geophysical logs.

Well Name	DATUM	STATE	ELEV (ft)	DEPTH (ft)	Easting	Northing	Data
Club House Crossroads 1	NAD83	SC	18 GL	2600	559941.00	3638868.00	Litho
Club House Crossroads 2	NAD83	SC	20 GL	2375	564423.00	3640960.00	Litho
Club House Crossroads 3	NAD83	SC	20 GL	7778	563854.00	3640494.00	Litho/GL
Dorchester 211	NAD83	SC	76 GL	1984	554606.00	3668596.00	Core/GL
Norris Ligthsey 1	NAD83	SC	75 GL	12500	506642.00	3652952.00	Litho/GL
SSW 6	NAD83	SC	18 GL	2400	539105.00	3638240.00	GL
C-15	NAD83	SC	63 GL	2900	500391.00	3608787.00	GL
Beaufort (BFT) #10	NAD83	SC	12 GL	3455	527503.00	3576833.00	Paleo/GL
Hilton Head Test Well	NAD83	SC	10 GL	3799	527886.00	3561469.00	GL
James Gillis No.1 (GA-789)	NAD27	GA	351 GL	3240	355135.57	3584604.75	Paleo/GL
McCoy No.1 (GA-3447)	NAD27	GA	382 GL	9386	347077.85	3643499.04	Litho/GL
B & L Farms No.1 (GA-3105)	NAD27	GA	302 GL	4529	284369.40	3571328.42	Litho/GL
Union Camp Corporation No. 1 (GA-3466)	NAD27	GA	10 GL	8468	441179.53	3455155.93	GL
Union Bag Camp Paper Co. (GA-724)	NAD27	GA	14 GL	4624	439110.37	3445038.88	GL
A.P. Snipes et al. No.1 (GA-3457)	NAD27	GA	287 GL	11470	333642.07	3515105.21	GL
Jelks & Rodgers No.1 (GA-363)	NAD27	GA	26 DF	4254	467108.88	3506025.66	Paleo/GL
J.T. Stalvey No.1 (GA-3113)	NAD27	GA	157 GL	8550	284952.52	3430724.79	GL
Langdale Co. No.1 (GA-3120)	NAD27	GA	171 GL	5052	303389.56	3415889.82	Litho/GL
J.H. Pullen No.1 (GA-109)	NAD27	GA	330 GL	7487	207217.47	3449385.34	Litho/GL
Adams-McCaskill No.1 (GA-120)	NAD27	GA	70 GL	4355	399048.05	3478907.61	Litho/GL
Adams-McCaskill No.1 (GA-119)	NAD27	GA	77 GL	4375	398208.09	3473989.16	GL
Helen Pryor No.1 (GA-855)	NAD27	GA	130 GL	2677	459867.86	3605195.95	Ltho/GL
Ronnie Towns No.1 (GA-3080)	NAD27	GA	157 GL	4075	345330.34	3546648.06	GL
Charles M. Jordan No. 1 (GA-336)	NAD27	GA	185 GL	4002	344512.84	3539483.73	GL
D.B. McRae No.1 (GA-3084)	NAD27	GA	164 GL	3642	344705.51	3546965.58	Ltho/GL
Doster & Ladson No. 1 (GA-107)	NAD27	107	217 GL	4296	314356.67	3460818.43	Core/GL
OCSG 3664	NAD83	Offshore GA	104 KB	6896	553529.00	3438510.00	GL
OCSG 3671	NAD83	Offshore GA	101 KB	11635	572184.00	3428865.00	GL
COST GE 1	NAD83	Offshore GA	99 KB	13254	567358.00	3352233.00	Ltho/GL

Table 2. Listing of data from a variety of seismic lines that have been loaded into the main Petrel® project.

Seismic Line	State	Source	Seismic Line	State	Source
VT-1	SC	Virginia Tech	Seisdata 6	GA	Industry
VT-2	SC	Virginia Tech	COCORP GA-5	GA	Cornell University
VT-3	SC	Virginia Tech	COCORP GA-8	GA	Cornell University
VT-4	SC	Virginia Tech	COCORP GA-10	GA	Cornell University
VT-5	SC	Virginia Tech	COCORP GA-11	GA	Cornell University
SC-1	SC	USGS/Virginia Tech	COCORP GA-12	GA	Cornell University
SC-2	SC	USGS/Virginia Tech	COCORP GA-13	GA	Cornell University
SC-3	SC	USGS/Virginia Tech	COCORP GA-14	GA	Cornell University
SC-4	SC	USGS/Virginia Tech	COCORP GA-15	GA	Cornell University
SC-5	SC	USGS/Virginia Tech	COCORP GA-16	GA	Cornell University
SC-6	SC	USGS/Virginia Tech	COCORP GA-17	GA	Cornell University
SC-7	SC	USGS/Virginia Tech	COCORP GA-18	GA	Cornell University
SC-8	SC	USGS/Virginia Tech	COCORP GA-19	GA	Cornell University
SC-9	SC	USGS/Virginia Tech	COCORP GA-20	GA	Cornell University
SC-10	SC	USGS/Virginia Tech	COCORP GA-21	GA	Cornell University
SR-47	SC	ESRI-SC/SCGS	COCORP FL-1	FL	Cornell University
SR-47	SC	ESRI-SC/EOS/SCGS	COCORP FL-2	FL	Cornell University

Determine Structural Controls on Mesozoic Reservoirs in South Georgia Rift Basin with Existing Surface Seismic Surveys

As stated above all of the VT, SC series, as well as the SR-27 seismic lines were converted from two-way travel time to depth in meters and loaded into Petrel® software package. In order to understand the structural controls on the Mesozoic reservoirs, in addition to the above seismic data, we incorporated all of the available well data from GA and SC to generate a base of the Cretaceous structural map for the Coastal Plain in Petrel® (Figure 11). Using depth converted seismic data and well data, the project team constructed a refined base of the Cretaceous structural map as well as a structural contour map for top of the "J" horizon for the SC study area.

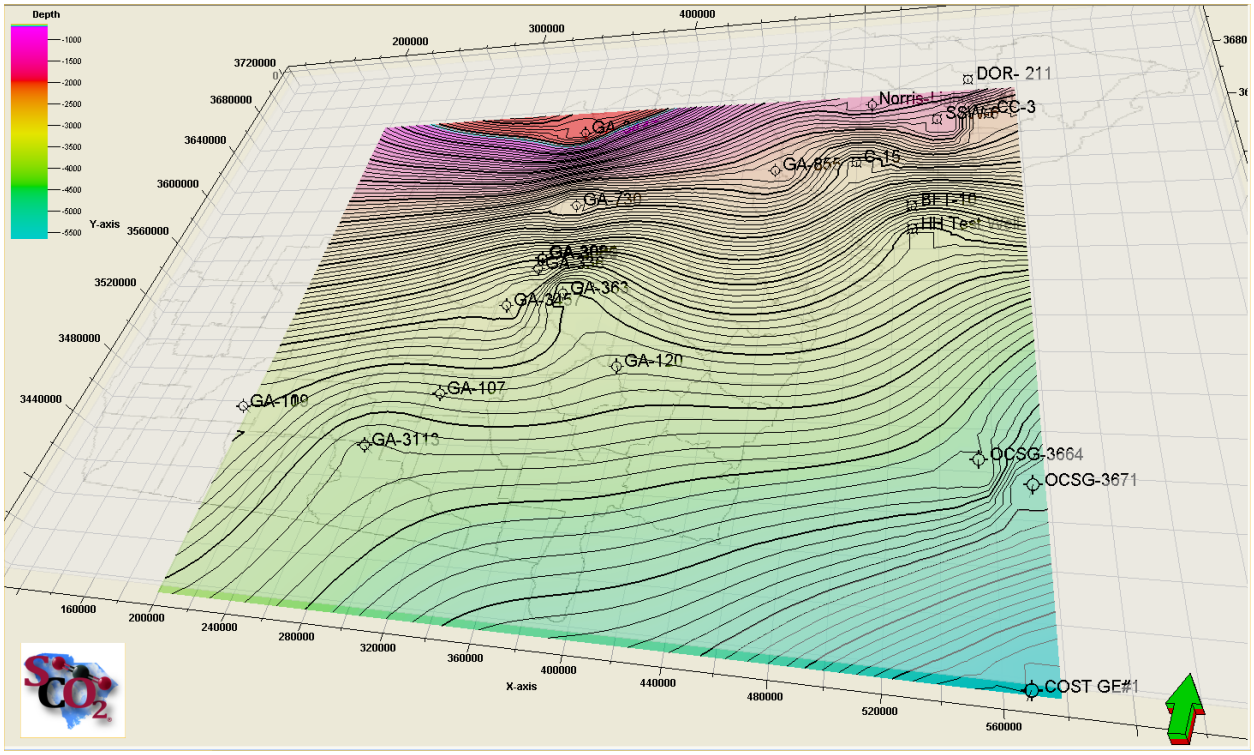

Figure 11. Preliminarily structural map, in depth below sea level, of the base of the Cretaceous. This version does not incorporate all of the wells in GA.

Table 3. Summary of relevant information from nearby Georgia wells for integration with the SEISDATA 6 seismic profile.

Georgia (GA) Wells	Approximate Distance from SEISDATA 6	Total Depth (ft)	Key Observations	Evidence of Triassic Unconformity	Evidence of mafic igneous rock
GA 855	About 3 miles from CDP 11542 – CDP 11565	2,697	Penetrated mostly Coastal plain sediments	No	No
GA 3353	12 miles from CDP 9569 – CDP 9627	3,812	Red beds mixed with basic intrusive at 1,207 ft	Yes at 1,178 ft	Yes, but very, very thin layer at 1,207 ft
GA 3441	25 miles from CDP 8121 – CDP 8312	5,653	Penetrated mostly sedimentary rocks	Yes at 1,099 ft	Yes, but very, very thin layer at 5,600 ft
GA 3447	27 miles from CDP 8298 – CDP 8393	9,406	Metamorphic rock from 8,327 ft to 9,406 ft (Schist and Quartzite)	Yes at 1,106 ft	No
GA 3439	28 miles from CDP 8556 – CDP 8650	2,582	Metamorphic rock (Schist) from 1,099 ft to 2,582 ft	Yes at 1,083 ft	No

Phase II New Seismic Data and Selection of Drill Site

Seismic Data Acquisition

Approximately 240 km (~150 mi) of new seismic data was acquired and seismic acquisition in South Carolina (Figure 12) and 81.3 km (50.5 mi) collected in South Georgia (Figure 13). The South Carolina seismic data was collected in the following counties, Orangeburg, Bamberg, Colleton, Dorchester and Allendale. In southern Georgia, 2-D seismic reflection data was collected to explore a portion of the South Georgia Rift basin (Figure 13). The Georgia seismic data was collected in the following counties, Jeff Davis, Coffee, and Telfair. The 81.3 km (50.5 mi) were divided into two lines approximately 40.5 km (~25 mi) each, with Line 1 intersecting Georgia well GGS-3457. Well GGS-3457 was a deep exploratory well drilled in the 1980's for oil and gas. Line 2 intersects Line 1 at the southern portion of Line 1 to maximize the extent of coverage away from GGS-3457. Well GGS-3457 has a set of usable logs such as gamma, density porosity and neutron porosity that provided promising results in terms of carbon storage. Log analysis suggest over 120 m (394 ft) of sandstones with porosities values greater than 10%. The design of the seismic survey was to extrapolate information away from the well to better define the extent of the SGR basin and map potential reservoir and caprock for CO_2 sequestration.

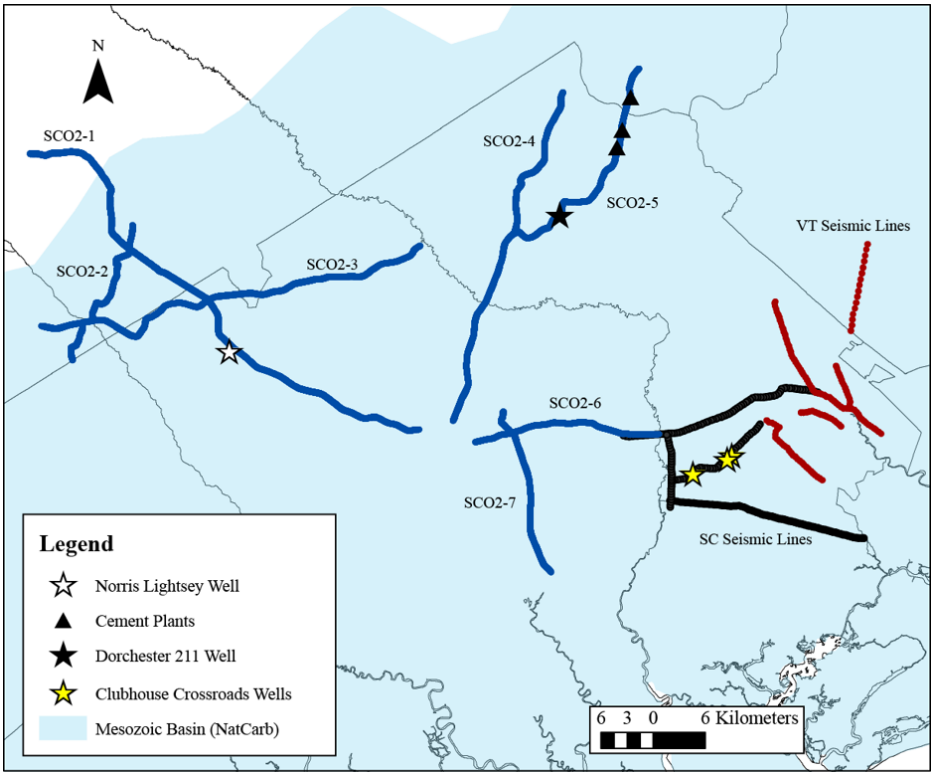

Figure 12. Map showing the existing seismic reflection data in the study area along with the new seismic data lines (blue and red). The "blue" lines have been processed and incorporated into Petrel® for interpretation.

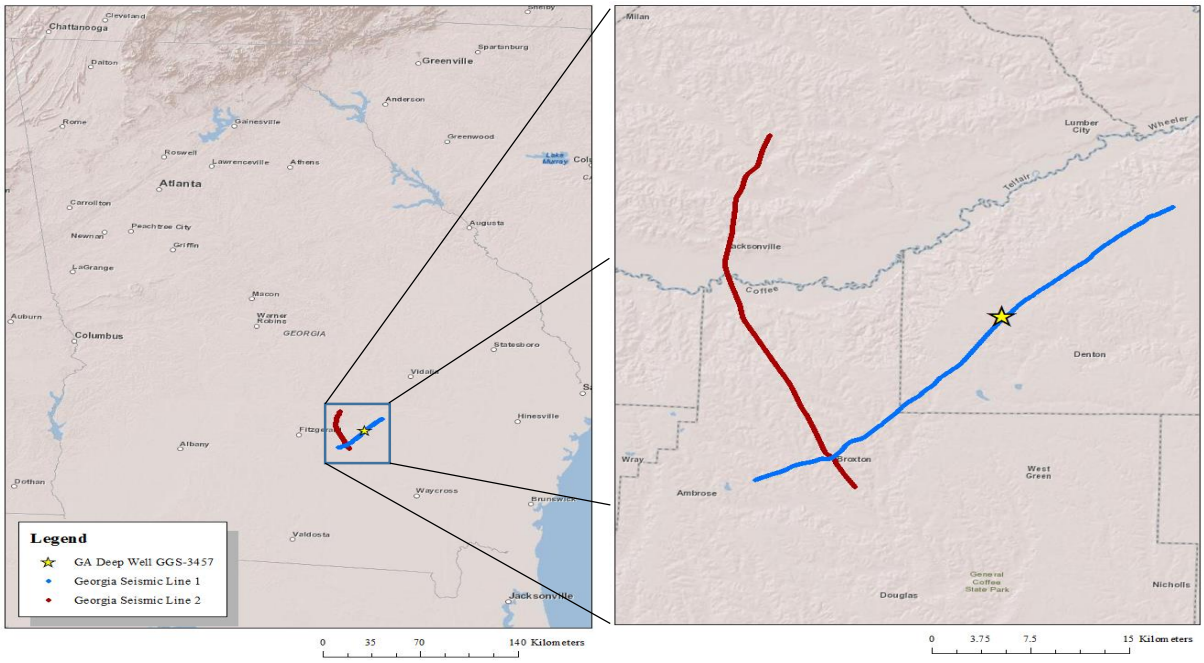

Figure 13. Location map of southern Georgia study area. Map on the left shows the relative location of the new seismic data with respect to state boundaries and cities such as Atlanta, Columbus, and Jacksonville (FL) to name a few. The map on the right is a close up of the two seismic lines and the one well. The map on the right shows topography, cities, and the Ocmulgee River. The GGS-3457 well is denoted as a yellow star in both maps and Georgia Seismic Line 1 is blue while Georgia Seismic Line 2 is red.

South Carolina Acquisition

The seismic acquisition parameters were determined after analysis of the existing seismic data and well data. Seismic acquisition parameters are listed in Table 4. The South Carolina seismic acquisition of the new 2-D and 3-D reflection seismic was conducted by Bay Geophysical, Inc. (Figure 14). Seismic line SCO2-1, was first line because it tied into the Norris Lightsey #1 well.

Table 4. Shows the seismic acquisition parameters used for the new 2-D survey in South Carolina.

Number of Channels	240 Channels
Group Interval	52 meters
Source Interval	52 meters
Spread	Symmetrical Split spread Maximum offset 6,240 meters
Source	3 Litton 315 Vibrators (42,000 force lbs with advance torque amp control system
Record Length Sample Rate Geophone Array	6 Seconds 2 ms 12 (each) Oyo GeoSpace Geophones- 10Hz over 52 meters

Seismic Processing

Two dimensional seismic reflection data processing workflow follows a conventional CDP data processing. Listed below is workflow that was used to process the 2-D seismic data. This processing workflow was applied to both the SC and GA seismic data sets.

2-D Processing Workflow

- Reformat field data – SEG-
- Vibroseis correlation – with synthetic sweep Output SEG-Y Disk
- Trace edit/ First break mute
- True amplitude recovery – T**n power scaling
- Crooked line geometry definition & assignment
- Surface consistent amplitude scaling – source & receiver
- Wavelet extraction / Minimum phase conversion
- Surface consistent deconvolution
- Spectral whitening
- 2-D Spatial
- Refraction
- CMP sort
- Velocity analysis (constant velocity stacks & velocity spectra)
- NMO – (NMO datum)/ Bandpass filter/Time variant scaling
- Stretch mute CDP stack w/root n scaling for QC
- 2nd Calculation of residual statics applied to trace headers
- Velocity analysis with statics
- Final stack with trace mix -5pt., weight 1, 2,7,2,1
- Finite difference migration with Bandpass (5-10-50-60) & mean scaling (entire trace)
- Display

Figure 14. This figure is showing the three 42,000 lbs peak force Litton Vibrators on seismic line SCO2-4.

3-D Seismic Survey

The 3-D seismic survey was conducted in the area surrounding the proposed location of the characterization boring site (Figure 15). The primary purpose of the 3-D was to verify the diabase units observed in the Norris Lightsey # 1 well that were present at the proposed drilling site. Unlike the 2-D seismic surveys that were conducted along public roads, the 3-D seismic survey is located entirely on private land. Therefore, the footprint of the 3-D seismic survey was dictated by our ability to obtain the land access permits to conduct the survey. The 3-D grid (Figure 15) is located on land for which we were able to obtain the landowner permission to access their property.

The survey design is to acquire 3-D seismic data over an area approximately 2.6 km2 (1 mi^2) in size with a target depth of 3,000 m (~9842 ft). The receiver and shot lines are 156 m (~ 511 ft) apart and the individual shots and receivers are 52 m (~170 ft) apart. Based on this configuration, the subsurface bin size is 25 by 25 m (~82 ft). Due to the relative small size of the survey it was decided to add additional shots farther away from the grid (Figure 15). Northwest of the 3-D grid is a series of shot points (red circles), these shots are placed so as to generate long shot to receiver offsets so that in the data processing we will have long offsets for possible seismic attribute analysis.

The 3-D seismic survey provided the project with 3-D data on the subsurface structure and the continuity of various diabase intrusions that were observed on seismic line SCO2-1 and in the Norris Lightsey #1 well prior to drilling the characterization borehole. Figure 16 shows the fold plot of the planned 3-D seismic survey.

3-D Processing Flow

Listed below is the processing workflow used to process the 3-D seismic data.

- Data QC/QA
- 3-D geometry definition and assignment
- Amplitude scaling: automatic gain control
- Bandpass filtering
- Decon
- Elevation and refraction statics
- Initial velocity analysis
- Brute stack generation
- residual statics
- Velocity analysis
- NMO – (NMO datum)/ Bandpass filter/Time Stretch mute CDP stack w/root n scaling
- CDP stack w/root n scaling – adjustment to final
- Display

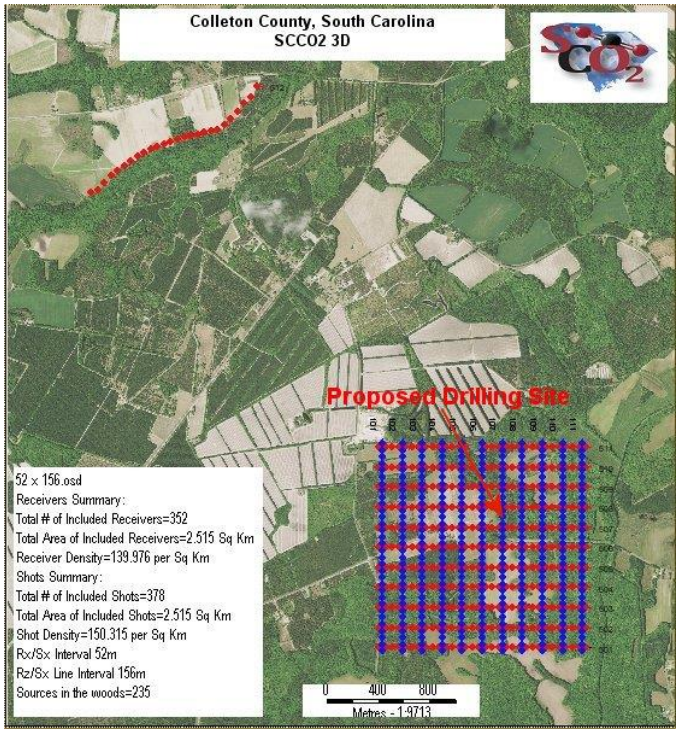

Figure 15. The proposed 3-D survey is approximately 2.6 square kilometers in area. The survey is designed in such a way so that all 352 receivers (geophones - blue circles) are live for the entire survey. The planned survey has a total of 378 shots (red circles). The red arrow is pointing to the proposed location of the characterization boring.

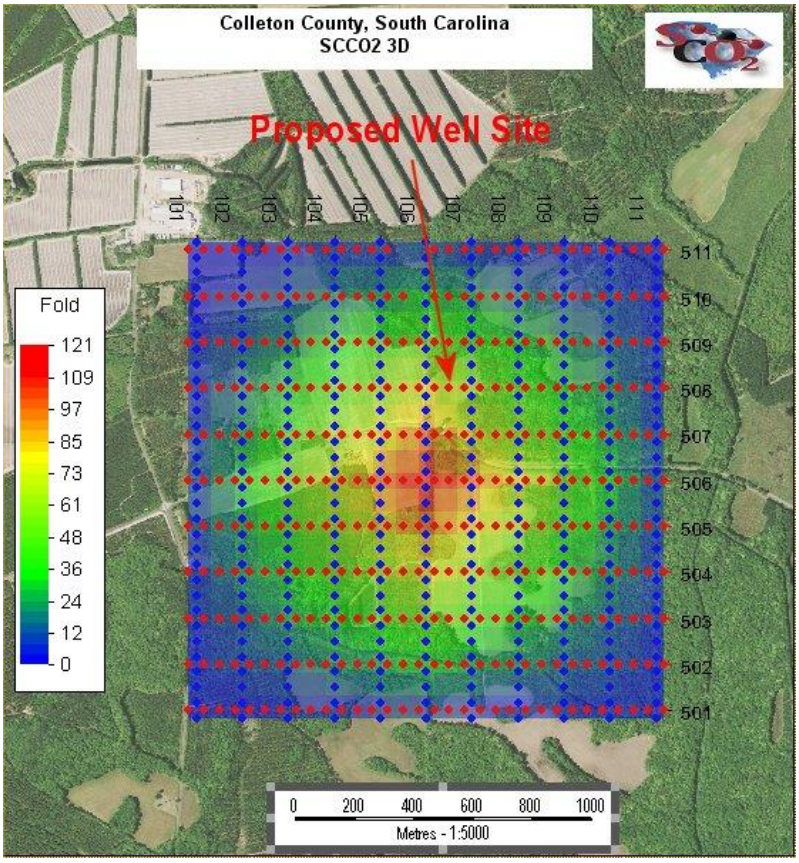

Figure 16. This figure is a fold plot of the 3-D seismic survey. The color scale indicates the number of traces in each subsurface bin. Based on the survey design the subsurface bin at 3,000 meters is approximately 25 by 25 meters. At the proposed characterization boring site the subsurface fold is between 50 and 80 traces.

Georgia Seismic Acquisition

The 81.3 km (50.5 mi) were divided into two lines approximately 40.5 km (~25 mi) each, with Line 1 intersecting Georgia well GGS 3457 (Figure 13). Line 2 intersects Line 1 at the southern portion of Line 1 to maximize the extent of coverage away from GGS-3457 (Figure 13).

The seismic data was collected using Wireless Seismic™ system, which is a cable-less acquisition system. In conjunction with the wireless system we used two INOVA UNIVIB vibrator with a peak ground force of 26,000 lbs. (Figure 17). The deployment of the wireless

seismic system reduced seismic acquisition costs by using less personnel and time to deploy the equipment. Reducing the number of vibrators further reduced acquisition costs. Table 5 shows the acquisition parameters for the Georgia 2-D survey.

Table 5. Shows the seismic acquisition parameters used for the new 2-D survey in Georgia.

Number of Channels	240 Channels
Group Interval	52 meters
Source Interval	52 meters
Spread Type	Symmetrical Split Spread Maximum Offset 6249 m
Source Type	2 Inova Vibrator 26,000 Force Pounds
Sweep Parameter	8 Hz to 70 Hz, 8 stacks per location
Record Length Sample Rate Geophone Array	6 Seconds 2 ms 6 (each) Oyo GeoSpace 10 Hz over 52 meters

Figure 17. Two INOVA UNIVIB was used to acquire the Georgia data. These two 26,000 lbs peak force vibrators produced the same energy and frequency bandwidth as the three 42,000 lbs peak force vibrators that were used to acquire the SC data with less impact on the roads.

The Georgia and South Carolina seismic data were processed using the same 2-D workflow.

South Carolina Interpretation

In the South Carolina portion of the SGR basin, a total of seven new 2-D seismic lines and a 3-D seismic survey were acquired, process and interpreted (Figure 12, 18, 19, 20, 21, 22, 23, 24 and 28). After the acquisition, processing and interpretations of the new seismic data, it became abundantly clear that the SGR basin in SC has had a very complex structural history. The project team concentrated the majority of their efforts on seismic lines SCO2-1 and SCO2-3 because of the proximity to the Norris Lightsey # 1 well and the location of our deep characterization boring the Rizer #1 (Figure 12 and 25).

Seismic lines SCO2-1 (Figure 18) and SCO2-3 (Figure 19) were reexamined to verify faulting imaged by the initial interpretations appear to be valid. A literature review of the reactivation of faulting and partitioned deformation also was done to support interpretations of faulting styles. Three types of faults were identified on SCO2-1 (Figure 18): 1) early extension faulting; 2) reverse reactivation inversion; and 3) transpressional overprinting (Each of these types of faults has a distinct, recognizable structural style. Although sub-vertical strike-slip faulting was not recognized on SCO2-3 (Figure 19), evidence for the three fault styles was identified on line SCO2-1(C. W. Clendenin, *et al*. 2011, C. W. Clendenin *et al*, 2012, and. C. W. Clendenin, 2013).

Interpretations of lines SCO2-1, and SCO2-3 (Figure 189) suggest that this portion of the basin has gone through an initial extensional phase during the Mesozoic. Later, after rifting ceased, the basin underwent at least one period of compression. The youngest faulting is interpreted to be transpressional overprinting. This faulting produced both sub-vertical strike-slip flower structures and a complicated, sub-horizontal thrust system that tends to mask the earlier two fault styles. Transpressional overprinting is interpreted to have been produced by an oblique NE-SW stress which could be the present stress field the continental margin is under today (Clendenin *et al*. 2011). Strain produced by this stress field was partitioned into fault-parallel strike-slip and orthogonal pure-shear components. The pure-shear component produced the sub-horizontal thrust system. This thrust system is localized in a zone of closely spaced diabase sills, and rheology differences between the mafic rocks and interlayered sediments may have influenced deformation location. The juxtaposition of sub-horizontal thrusts and mafic sills may act as an effective seal for any vertical movement of injected CO_2.

Our initial geologic conceptual model only considers stratigraphic traps for CO_2 storage. Based on the new seismic data it now appears the abundant faulting that occurred during the basin

inversion (compression) appears to be a detriment to CO_2 storage by increasing the number of possible potential pathways for uncontrolled CO_2 migration. The premise at the beginning of the project was that the 'J" basalt covers the majority of the SGR basin and would act as the caprock. With the additional seismic data it became clear that in portions of the basin, the "J" basalt is not present. For example, the "J" is not present on seismic lines SCO2-1, SCO2-2, and SCO2-3 but appears to be present on lines SCO2-4 SCO2-5, SCO2-6 and SCO2-7 (Figures 18, 19, 20, 21, 22, 23, 24, and 25). The present or absent of the "J" basalt is based on refraction velocities analyses along the contact of the Coastal Plain sediments and the underlying Triassic rocks (Figure 25) (J. Buckner, 2011 and M. Sims. 2012). On SCO2-7 and there appears to be "J" basalt at the bottom of the SSW-6 well located adjacent to line SCO2-7. Finally, determining the presence or absent of the "J" basalt seismically is based on the seismic resolution. The diabase units less than 10 m (33 ft) in thickness most likely will not be resolved (imagined) by the seismic data. There were diabase units identified in the seismic and correlated to the diabase units mapped in the Norris Lightsey # 1 and the Rizer #1 wells (Figure 26). There were also diabase units identified in the Norris Lightsey and Rizer wells that were not image with seismic because they were below the resolution of the data.

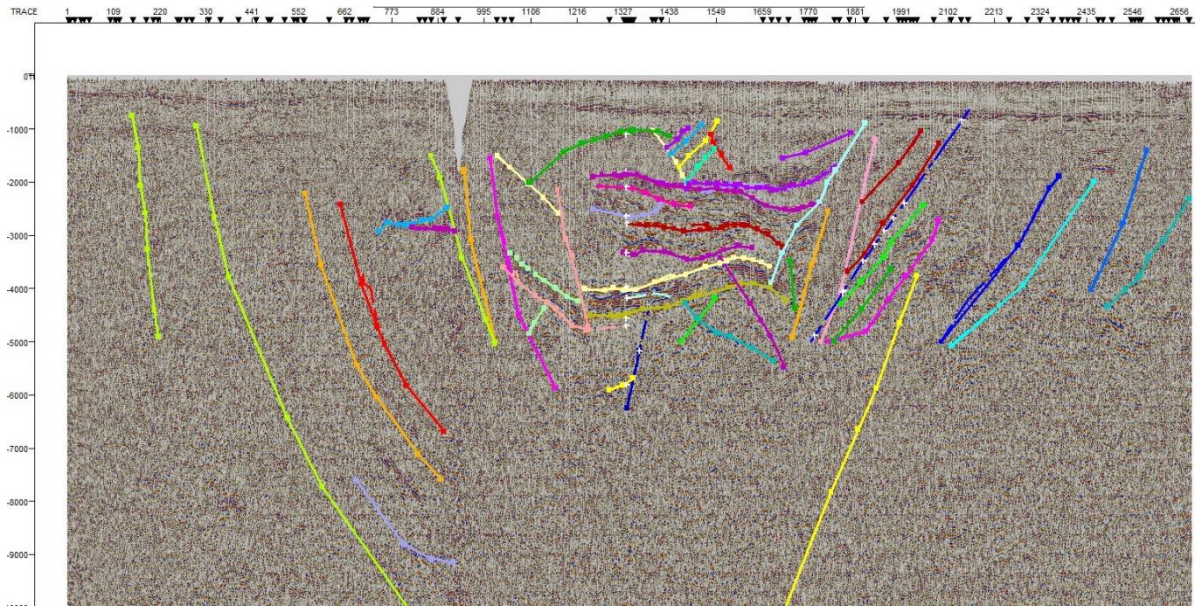

Figure 18. Seismic line SCO2-1 showing the complex faulting resulting from an initial extensional structural style that occurred during Triassic and Jurassic to a compressional structural style that most likely occurred sometime between the Jurassic and Early Cretaceous time. Faults on the left side of the figure appear to have been normal faults that were associated with the initial basin formation. The remaining faults identified so far appear to be related to the later compressional phase of the structural history of the basin. The vertical scale is meters and the line length is 51.5 km (32 Mi).

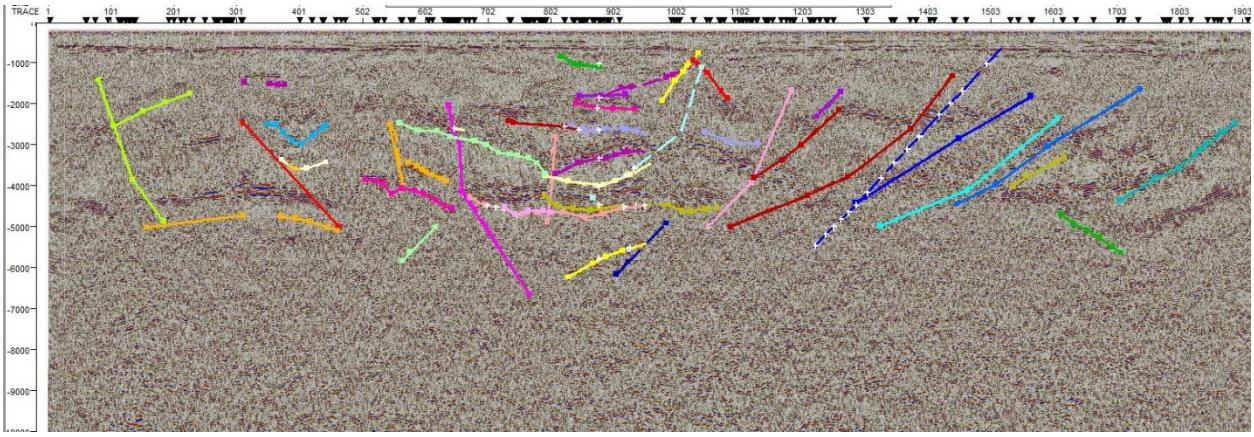

Figure 19. Seismic line SCO2-3 showing the complex faulting resulting from an initial extensional structural style that occurred during Triassic and Jurassic to a compressional structural style. The sub horizon faults that appear on both seismic line SCO2-1 and SCO2-3 appear to thrust faults associated with compressional "flower structural" The remaining faults identified so far appear to be related to the later compressional phase of the structural history of the basin. The vertical scale is in meters and the line length is 53.4 km (33.1 mi).

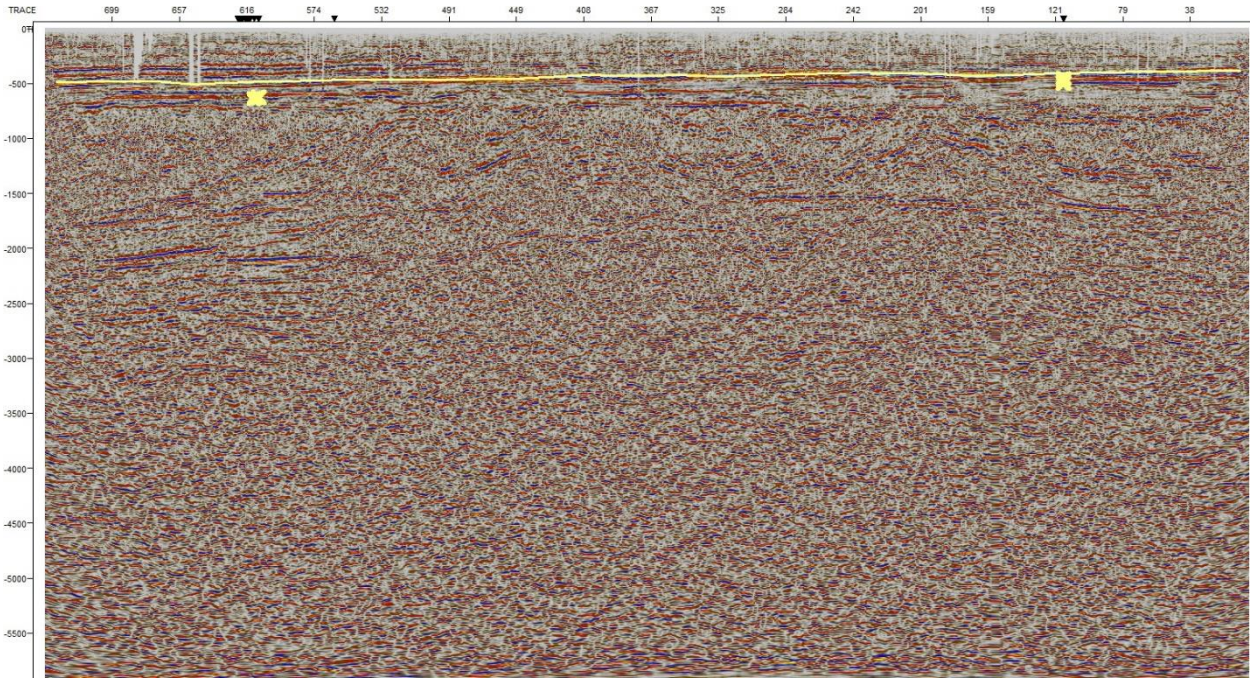

Figure 20. Seismic Line SCO2-2 showing the contact between the unconsolidated Coastal Plain sediments and Triassic rock (yellow). Base on refraction analysis of velocities along this contact the "J" basalt is absent.

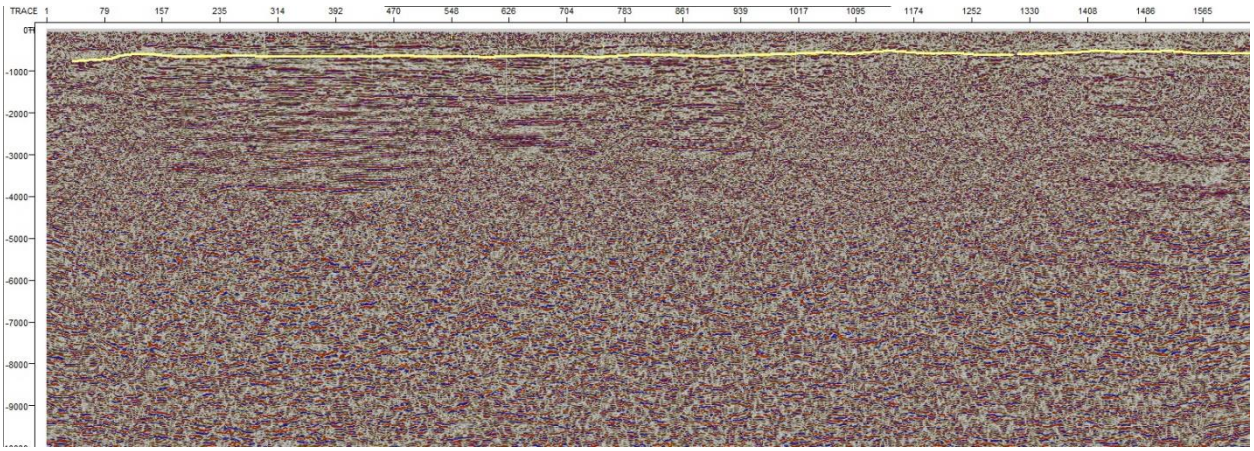

Figure 21. Seismic Line SCO2-4 showing the contact between the unconsolidated Coastal Plain sediments and Triassic rock (yellow). Base on refraction analysis of velocities along this contact the "J" basalt is present starting (left) at the beginning line until CDP 600.

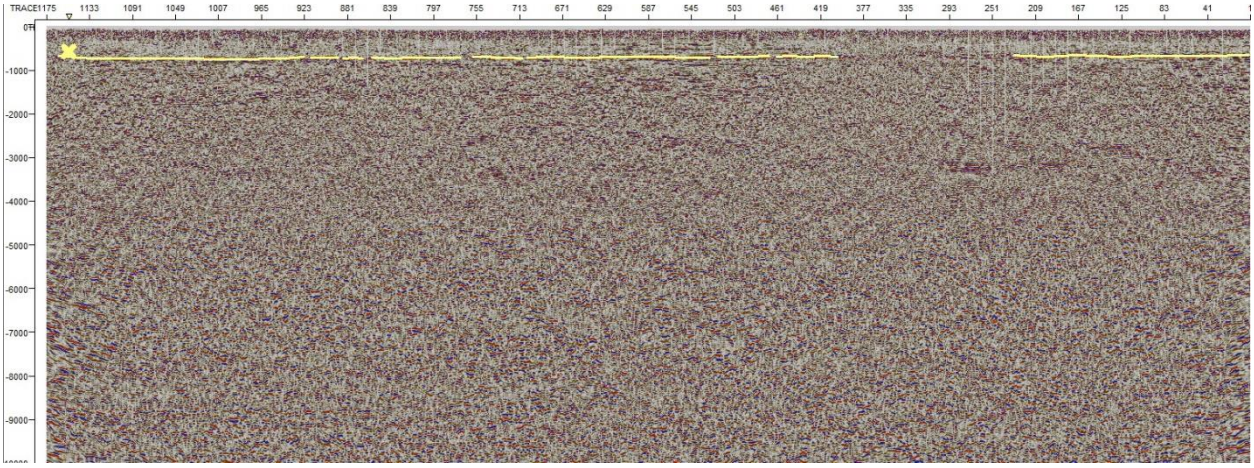

Figure 22. Seismic Line SCO2-5 showing the contact between the unconsolidated Coastal Plain sediments and Triassic rock (yellow). Base on refraction analysis of velocities along this contact the "J" basalt is present on most of the line except where the yellow horizon could not be mapped

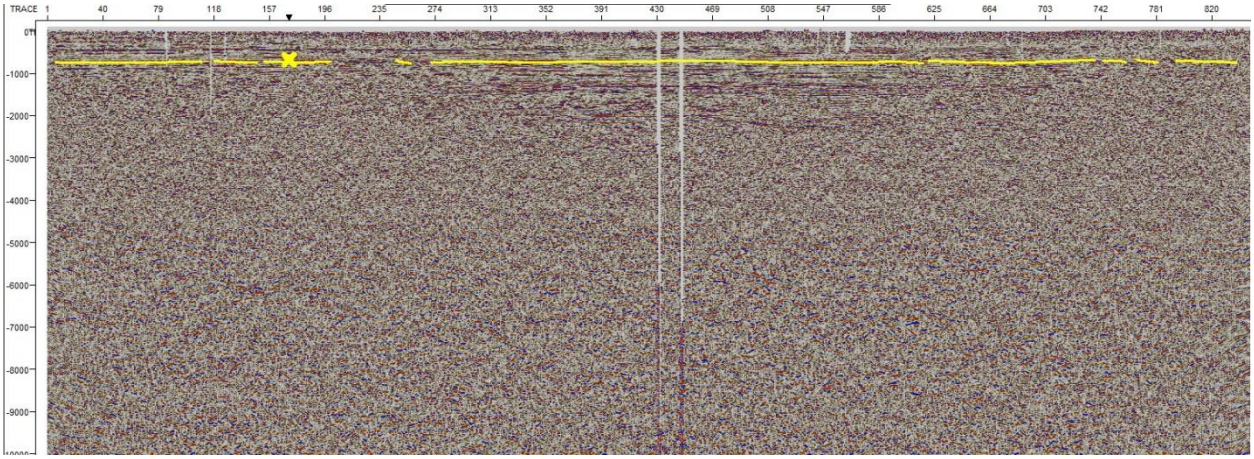

Figure 23. Seismic Line SCO2-6 showing the contact between the unconsolidated Coastal Plain sediments and Triassic rock (yellow). Base on refraction analysis of velocities along this contact the "J" basalt is present on entire line. This line also ties our lines to the legacy seismic data. The yellow X is where line SCO2-7 ties with this line.

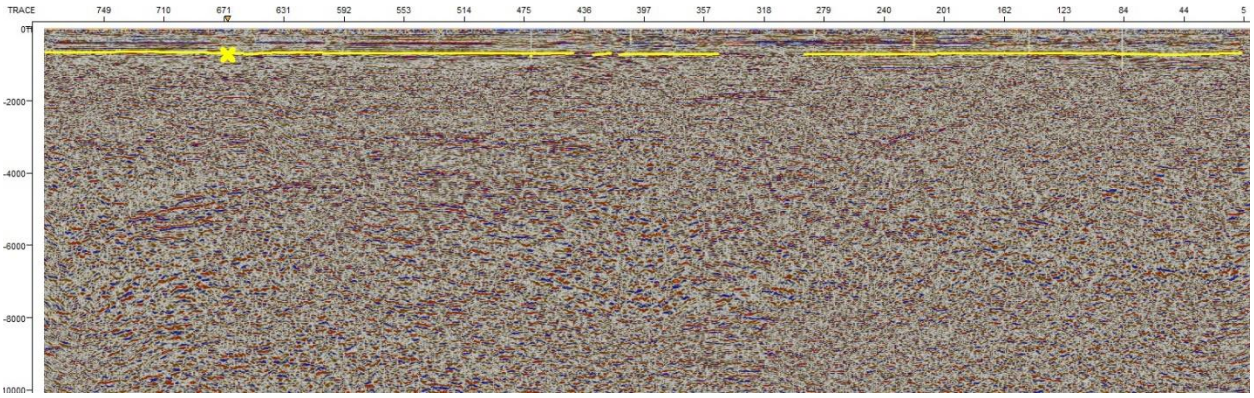

Figure 24. Seismic Line SCO2-7 showing the contact between the unconsolidated Coastal Plain sediments and Triassic rock (Yellow). Base on refraction analysis of velocities along this contact the "J" basalt is present on entire line. Near where this line ties with line SCO2-6 (yellow X) is well SSW-6. Base on the gamma log it appears to have "J" Basalt present in the bottom of the well.

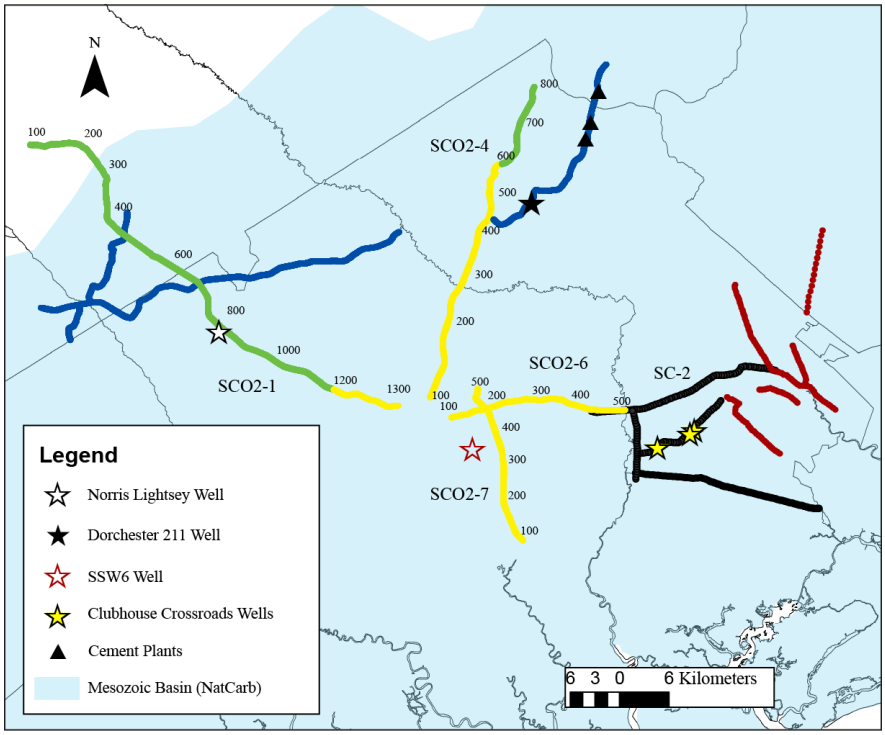

Figure 25. Location map of all the seismic lines used in the study. The blue, green, and yellow are the newly acquired seismic data and the black and red are legacy seismic data. The areas in yellow suggest the present of the "J" Basal base of refraction velocities (M. Sims, 2012 and J. Buckner, 2011).

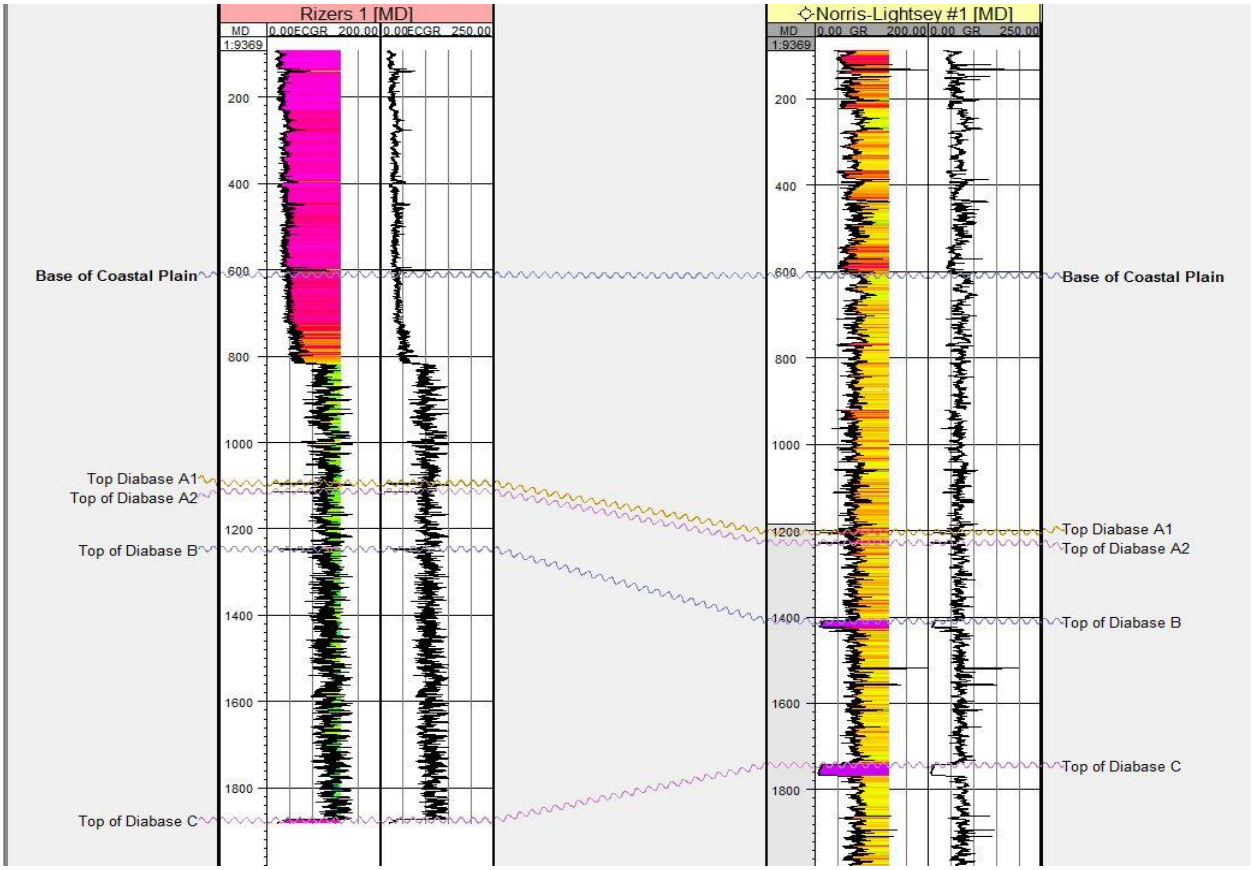

Figure 26. Gamma and lithologic log for the Rizer #1 and Norris Lightsey #1 well. The units label A-F are the Diabase layers. Scale is in meters. Distance between the two wells is approximately 1.5 km (.93 mi).

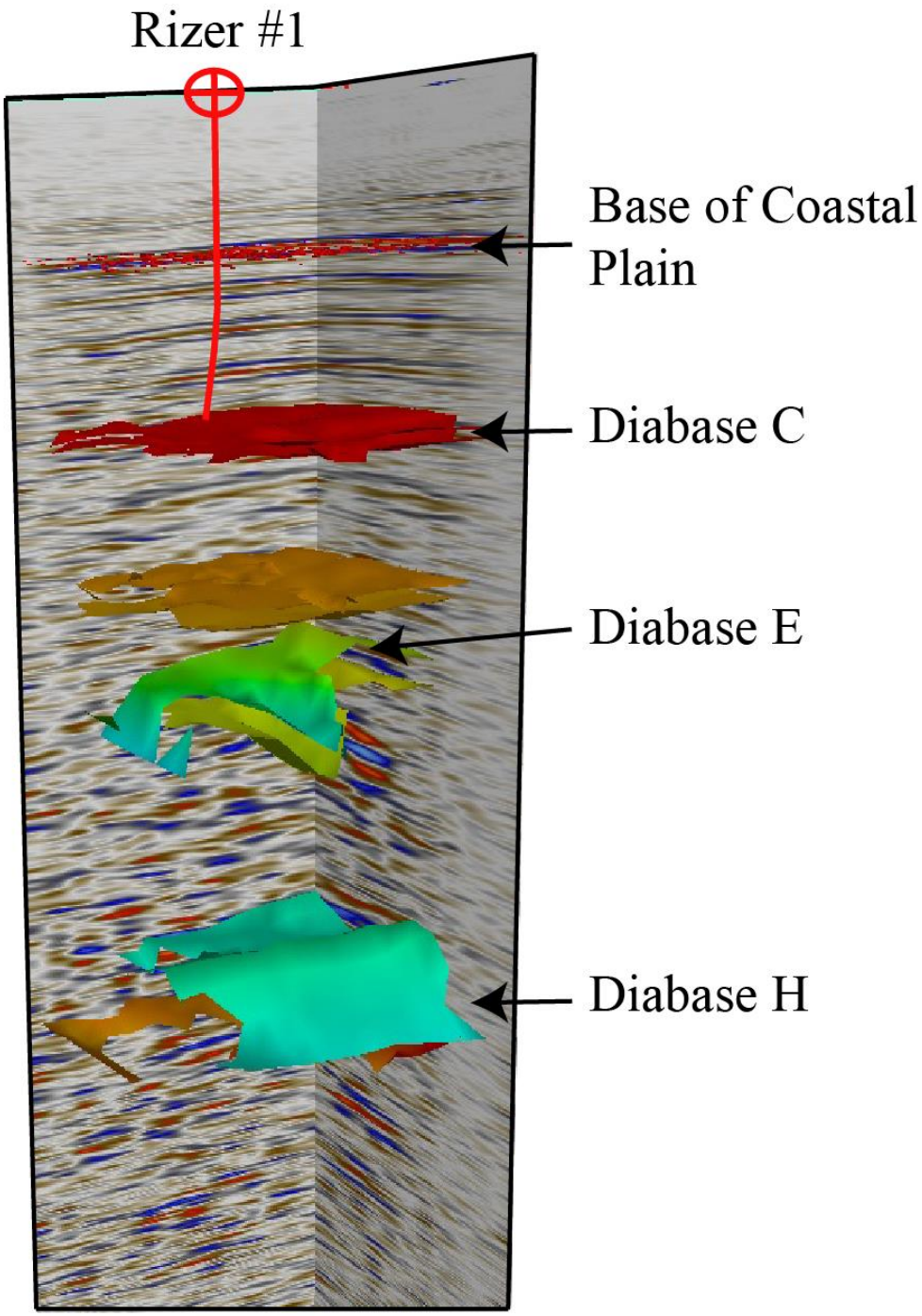

Figure 27. One inline and crossline from the 3-D cube. The base of coastal plain horizon was present on the SCO2 lines as well as the 3-D survey. Two prominent diabase units are label. Diabase C is where the Rizer #1 terminated in and Diabase E is the unit that the reservoir simulations are being run on.

Georgia Interpretations

Interpretation of the Georgia seismic reflection data (Figure 13) was the first step in building the Petrel geological model. Figure 28 is a map of the regional magnetic data. Georgia seismic line GA-1 is located so that the seismic data could be correlated to well GA-3457 (Figure 10). Line GA-2 was oriented parallel to structural dip base on the aero-magnetic map. The initial interpretation was the magnetic low (red) was the SGR basin and the magnetic high (white) was basement that has a high magnetic signature. The seismic lines were also located either in or near the Brunswick Magnetic Anomaly (BSMA) (McBride and Nelson, 1988) and a proposed transfer fault by Heffner, 2013. With this knowledge, there was a question of whether the seismic line would be located in the SGR basin or in one of the numerous sub-basins constitute the SGR system.

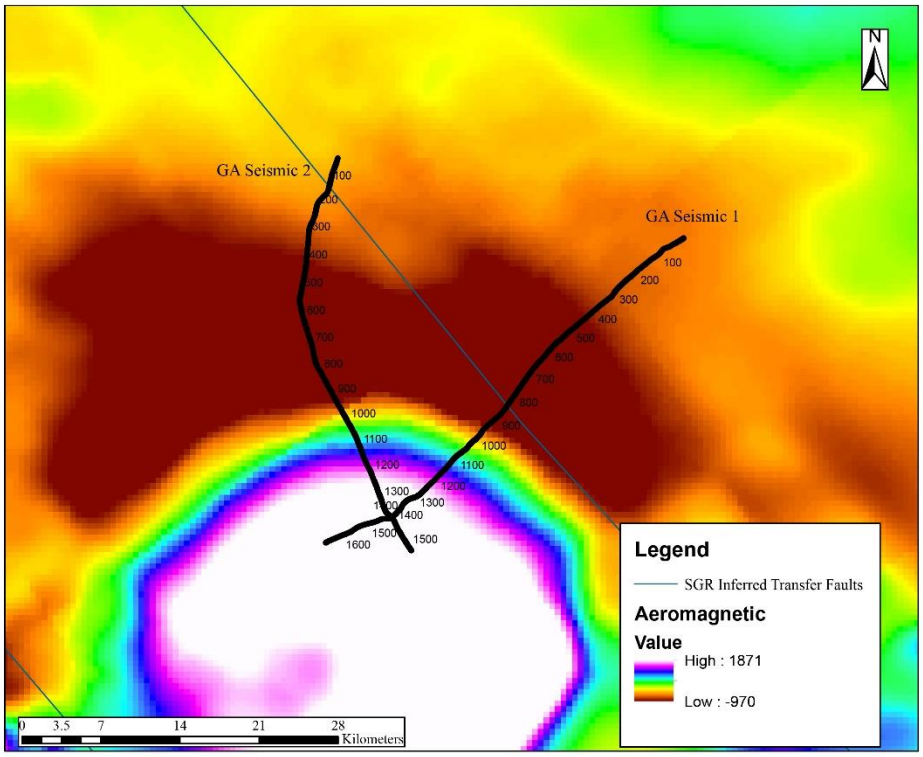

Figure 28. Aero Magnetic data with the Georgia's seismic lines overlain the magnetic data. The white areas are high magnetic values and the red to orange are magnetic lows. The line cuts the figure diagonally is an inferred transfer fault (Heffner, 2013).

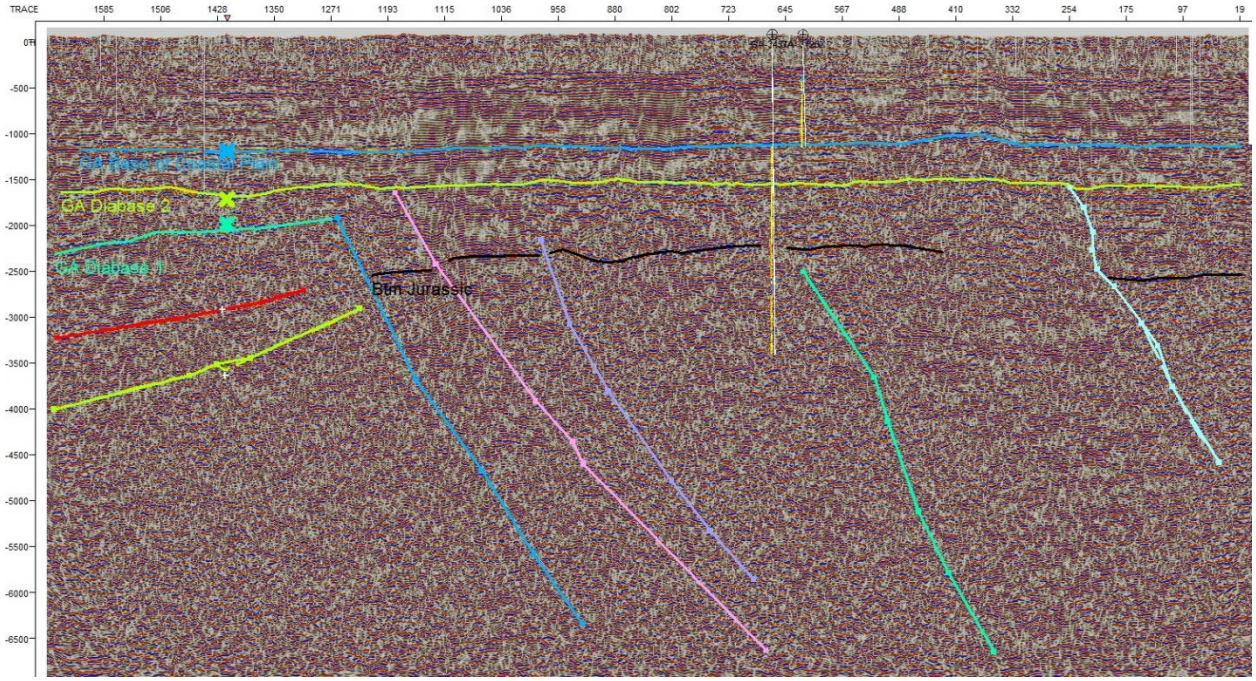

Figure 29. The blue horizon is the base of the Atlantic Coastal Plain (ACP), the green horizon is a diabase and the black is possible the base of the Jurassic section. The sub vertical lines are interpreted as faults to left of the blue fault. Wells GA-3457 and GA-3128 are both located on the GA-1 seismic line.

Georgia Seismic Line 1

GA-1 seismic line is orientated northeast to southwest and ties into the GA-3457 well. The orientation is highly oblique to the structural dip. On both Georgia lines there are three mappable horizons. The blue horizon is base of Coastal Plain sediments, green horizon was interpreted to be a diabase or basalt horizon and the black horizon is interpreted as the base of Jurassic (Figure 29). The "J" basalt equivalent appears to be at the base of the coastal plain. Well GA-3128, located ~2.0 km (1.2 mi) northwest of well GA-3457, terminated into a black igneous rock at the base of coastal plain. Unfortunately the geophysical logs in GA-3457 start slightly below the Coastal Plain missing the contact between the Coastal Plain sediments and underlying Mesozoic section so the "J" basalt maybe present at the contact. The majority of the faulting (blue, pink, green, and light blue, (Figure 29) appear to be dipping to the northeast. On the left side of the blue

fault (Figure 29) there are faults dipping to the southeast. This feature appears to be another asymmetrical sub-basin that is located above the magnetic high (Figure 28). There also appears to be a diabase (light green) (Figure 29) based on seismic amplitudes dipping to the south.

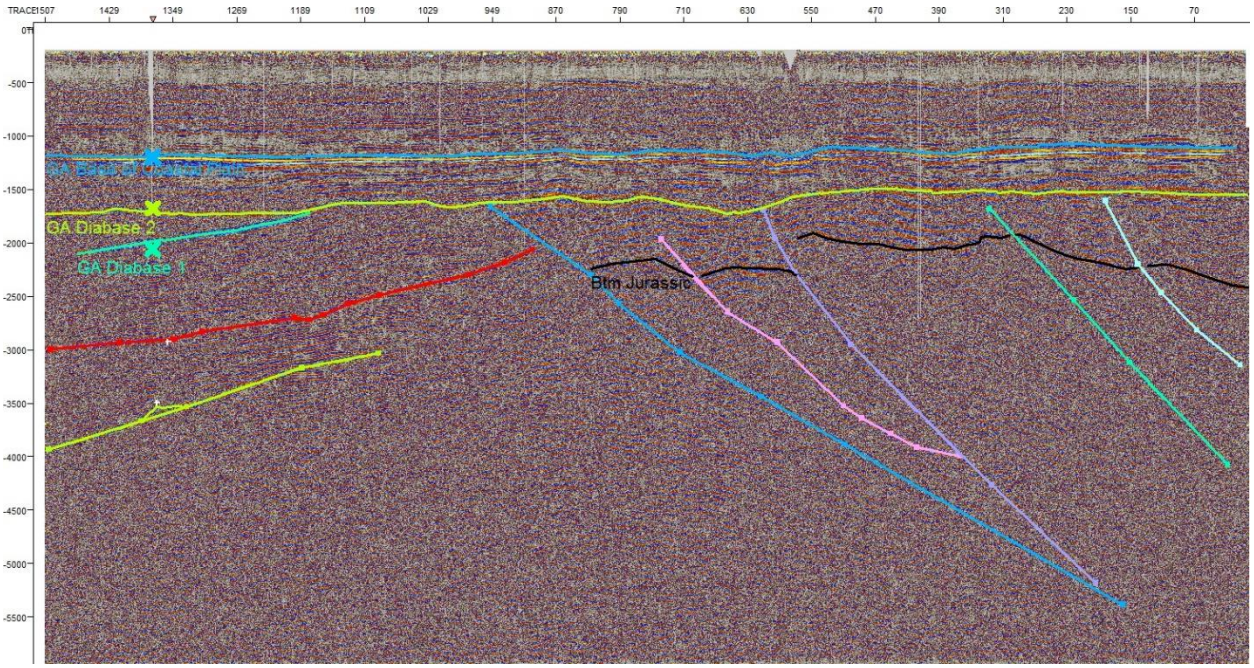

Figure 30. GA-2 is essentially a north to south seismic line that parallels structural dip. The color scheme for the faults and horizons are the same as on line GA-1. The "x" denotes tie points with GA-1.

GA-2 was acquired parallel to structural dip (Figure 30). The faults to the right of the blue fault (Figure 30) exhibit characteristics of reverse faulting associated with compression. It appears the amount of compression is less than what is observed in the South Carolina portion of the SGR basin. Three major horizons are mapped on this line, bottom of Coastal Plain (Blue), continuous diabase (green), bottom of Jurassic (black). The proposed lower Jurassic section (below Diabase 2) abruptly terminates against the blue fault and cannot be mapped into the adjacent sub-basin to the left of the blue fault. Diabase 2 is interpreted as a sill or flow basalt and Diabase 1 exhibits

characteristics of a dike. Some of the faulting (purple) may extend up to the base of the Coastal Plain and possibly into the Coastal Plain.

In the southern Georgia portion of the SGR basin, the sub-basins that are imaged by the additional seismic data suggest the basins have gone through some compression but not the magnitude observed in the southern part of the SGR in South Carolina. Heffner, 2013 postulated that there was a transfer fault in the area of investigation in southern Georgia. Generally a transfer fault system would infer basin polarity change in the structural characteristics. The blue fault (Figure 30) maybe the transfer fault. The basin to right of the blue fault structure is dipping north to northeast while the basin to the left of the blue fault is dipping south to southwest. The probability of storing CO_2 in this area is low. Even though there is approximately 120 meters of sandstone (determine from geophysical logs) with porosity values greater than 10% there is a strong possibility CO_2 may migrate upward into the Coastal Plain aquifer via conductive faulting.

Phase III Drilling

Drilling

Drill/Core Caprock(s) and Formation(s)

In May of 2012 the project team began the drilling, coring, and wireline logging the deep characterization borehole located in Colleton County, South Carolina. The initial drilling plan was to drill to 2750 m (9022 ft) below ground surface (bgs), core 36.6 m (120 ft) of caprock and 109.7 m (360 ft) possible reservoir rock. (Figure 31) It must be noted that the goals listed above were not obtained. From the commencement of drilling operations the project team started having drilling problems. The drilling contractor disregarded the warning of using air to drill through the Coastal Plain sediments which resulted in losing circulation of the drilling fluids for 4 days. Once

surface casing was set to 818 m (2683 ft) bgs the operation switched over from mud to air. Drilling with air improved our drilling rate substantially. At 1112 m (3648 ft) bgs we drilled into a diabase and encountered saline water flowing into the borehole at a rate of 200 gallons per minute. Air drilling ceased and drilling operations switch over to a mud system. Drilling rate drop dramatically using the mud system. Approximately 1890.0 m (6201 ft) bgs drilling encountered another diabase unit that was faulted. Once we drilled into the faulted diabase the diabase unit would slip along the fault causing the hole to collapse around the drill pipe. After a week of trying to ream the drill hole it was decided cease drilling and plug and abandon the test boring. We were able to obtained one 17.68 m (58 ft) whole core and one hundred and six 2.54 cm (1 inch) rotary sidewall core. We never reach the proposed total depth of 2,744 m (9002 ft).

The following section summarizes the results of the Rizer #1 borehole drilling:

Borehole Construction:

1. 20" grouted conductor casing to 17.07 meters KB
2. 13 3/8" steel casing to 818 meters (KB)
3. Open hole to 1891 meters (KB)

Whole Core: 17.68 from 1829.27 meters to 1846.95 meters (KB)

Sidewall Cores: 106 2.54 cm rotary sidewall cores between the interval 868.9 meters and 1,871.95 meters (KB)

Wireline Logs:

1. TVD (true vertical depth) array induction resistivity (815.55 meters to 1,882.93 meters KB)

2. TVD depth compensated neutron, litho-density, gamma ray, caliper (100 feet to 6,176 feet KB)

3. Mechanical sidewall coring tool log, gamma ray (868.9 meters to 1882.93 meters KB)

4. Cement bond, gamma ray (15.85 meters to 1912.28 meters KB)

5. NMR, gamma ray 815.55 meters to 1882.93 meters KB)

6. Spectral gamma ray (815.55 meters to 1882.93 meters KB)

7. FMI, rock mechanical properties, litho-log from spectral gamma ray log

8. VSP (701.22 meters to 1871.95 meters KB), check shots (91.46 meters intervals from 60.98 meters to 701.22 meters KB)

9 Formation tester tool attempted sample 6 intervals to obtain in situ water samples but due to the low porosity and permeability values no water samples were collected for analysis.

Note all the wireline logs and core data is loaded onto the NATCARB site.

One "near-offset" vertical seismic profile (VSP) was collected in the Rizer #1. The primary propose was to collect time-depth values for converting our seismic profiles from two-way travel time to depth. Figure 32 is the front corridor stack which is a one dimensional image of reflectors in one-way time near the well bore.

Table 6 shows the time-depth values from the Rizer #1, with depths ranging from 792.68 to 1875 m and TWT ranging from 700.1 to 1150 ms.

Table 6. Shows the time depth values from the Rizer #1.

Depth (m)	TWT (ms)	Depth (m)	TWT (ms)
792.68	700.1	1341.46	941.6
807.93	707.4	1356.71	947.4
823.17	715.2	1371.95	953.5
838.41	722.7	1387.20	959.2

Depth (m)	TWT (ms)	Depth (m)	TWT (ms)
853.66	729.3	1402.44	965.6
868.90	736.8	198.17	971 4
884.15	743.7	1432.93	977.9
899.39	750.9	1448.17	983.7
914.63	756.9	1463.41	989.9
929.88	763.8	1478.66	995.6
945.12	770.3	1493.90	1002
960.37	776.7	1509.15	1008
975.61	784.2	1524.39	1014
990.85	792.7	1539.63	1021
1006.10	797.6	1554.88	1027
1021.34	804.5	1570.12	1033
1036.59	810.5	1585.37	1039
1051.83	817.1	1600.61	1045
1067.07	823.8	1615.85	1051
1082.32	830.5	1631.10	1057
1097.56	837.2	1646.34	1063
1112.80	843.2	1661.59	1068
1128.05	850.5	1676.83	1075
1143.29	857.2	1692.07	1081
1158.54	864.1	1707.32	1087
1173.78	870.7	1722.56	1092
1189.02	876.9	1737.80	1098
1204.27	883.7	1753.05	1104
1219.51	890.1	1768.29	1110
1234.76	896.3	1783.54	1116
1250.00	903 4	1798.78	1122
1265.24	909.1	1814.02	1128
1280.49	915.4	1829.27	1134
1295.73	922 4	1844.51	1140
1310.98	928.6	1859.76	1146
1326.22	934.9	1875.00	1150

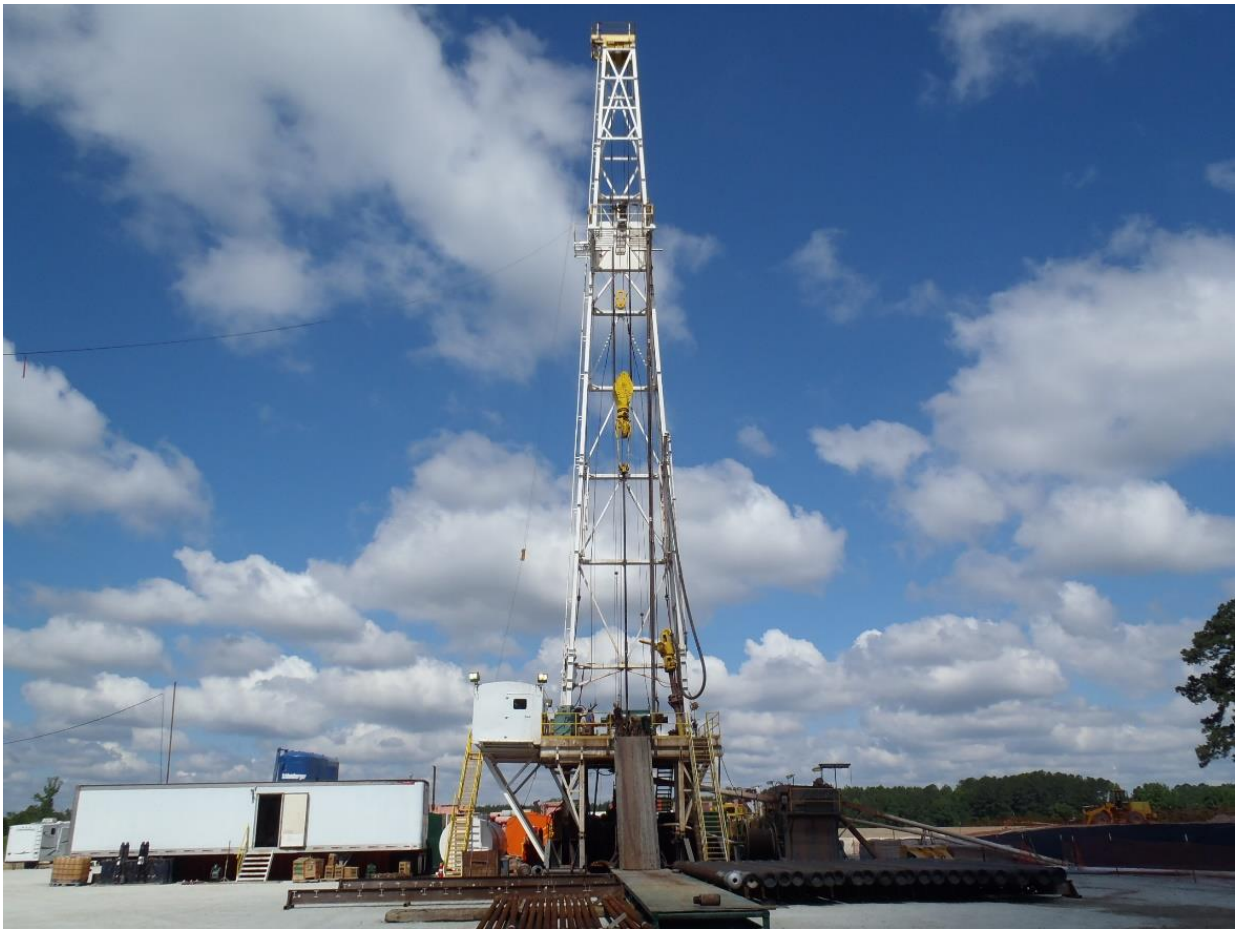

Figure 31. Picture of the Pollister Rig #3 during drilling of the Rizer #1 characterization boring.

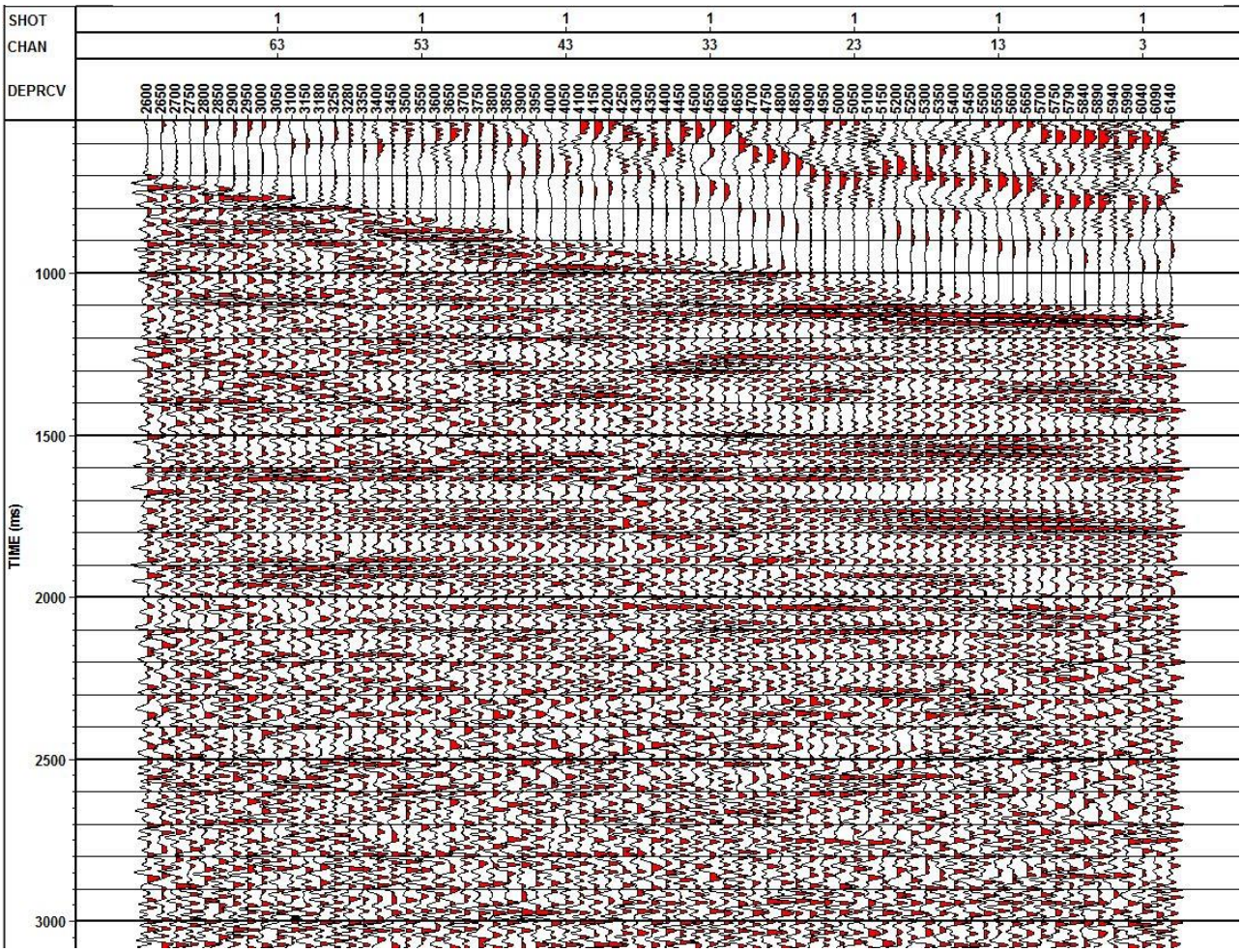

Figure 32. Front Corridor Stack using the VSP data from Rizer #1. The vertical axis is in milliseconds and the horizontal axis is depth in feet. Each trace represents a geophone level in the well.

The borehole was plugged (Figure 33) according to the abandonment requirements of the South Carolina Department of Health and Environmental Control. The land owner (lessee) released the University of South Carolina from any further liability regarding the drill site on

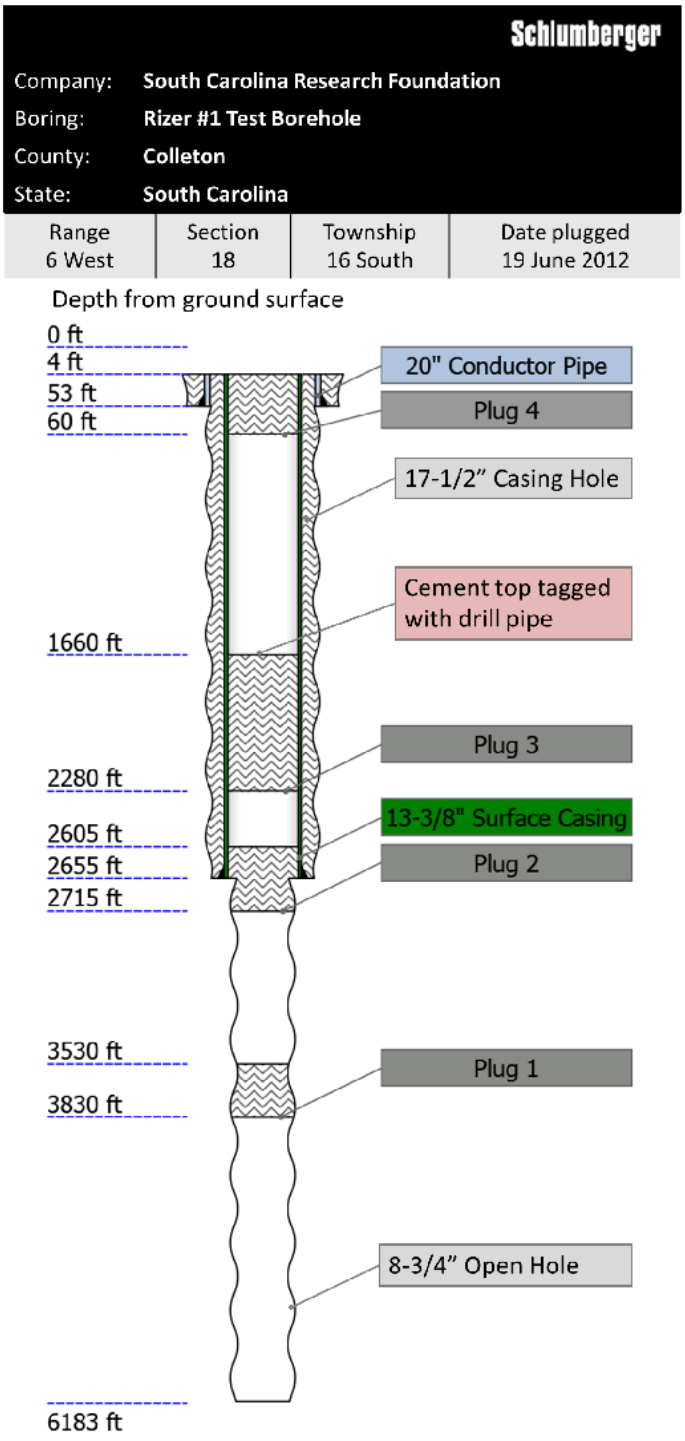

August 7, 2012.

Figure 33. Diagram showing the depth and location of the cement plugs in the Rizer #1. Plug #3 was tagged which means once the cement had cured the drill pipe was lower down to the top of the plug and 10,000 lbs. of weight was applied to the plug make sure the plug would not collapse. Plug #3 isolated the coastal plain aquifers from the underlying Triassic.

Wellbore Management and Risk Plan

One of the subtask in this phase is to determine possible drilling risk and mitigate those risks. Our data suggest that the two sites that were investigated during this project are unsuitable for CO_2 storage. The project team believes the SGR has potential to store 30 million tonnes of CO_2, just not in our study area(s) Table 7 below shows the possible risks and possible mitigation solutions to those risks for an idealized site in the SGR.

Table 7. Possible risk and mitigation solutions for an idealized site within the SGR.

Possible Risks		Mitigation
Geologic Conditions	High	Conduct detailed site characterization study The site needs to be located a minimum of 30 km (18.6 mi) from any transfer faults identified in Heffner, 2013
CO_2 Leakage into potable water aquifers	High	A detailed site characterization study which includes a 3-D seismic survey over the entire area of review
CO_2 leakage adjacent wells	Low	In SC there are only 5 wells that penetrate to sediments below the Coastal Plain. In GA there are approximately 150 wells in the SGR that penetrated below the coastal plain sediments.
Proximity to Populations centers	Low	Educate the general public and dispel public perception of high risk.
Pipelines Environment Impacts	High	Located CO_2 pipelines along existing pipeline right of ways,
Pipelines leakage	Low	
Earthquakes	Low/ medium	There is a low to medium risk in SC, low risk in GA
Hurricanes	Low	Emergency equipment to maintain operations

Wellbore Management-Risk Plan

It is difficult to come up with a wellbore management plan when at the present time we have no possible locations to drill. In both Georgia and South Carolina agriculture and numerous public water supply systems rely on groundwater. At a minimum the monitoring, verification, and accountability will require monitoring two wells at the injection depth, cluster of monitoring wells completed at the base of the coastal plain aquifers, soil gas survey prior to injection, during injection, periodically after injection has been completed. The Area of Review (AOR) can only be determined once a site has been selected and the geological and hydrological characterization and CO_2 injection simulations are complete. At this time we do not know what the States of South Carolina and Georgia are going to require for a Class VI injection well permit. All of the EPA Class VI administration and over site is being performed by the EPA, no state has been granted primacy.

Petrographic and Reservoir Analysis

This section summarizes the results of the examination of core and cutting samples from Rizer #1 test borehole. Rizer #1(For a detail discussion see Appendix 1). Since no conventional core of caprock was obtained from Rizer #1 for the contracted mechanical and other physical property tests, it was decided to obtain portions of conventional core from the nearby USGS Clubhouse Crossroads Test Hole No. 3 from Dorchester County, SC. This section describes the results from phase 3 of the project. The original objective of phase 3**,** which was to create an accurate model to predict long-term CO_2 storage capacity of the Jurassic to Late Triassic aged strata within SGR basin, had to be modified because of operational issues and geologic characteristics of the study interval. After it was determined that the poor reservoir quality (very

low permeability and porosity) (see Appendix 1 for details) throughout the study interval (between the depths 2016.0ft (614m) and 6140.0ft (1872m) did not allow further physical and geochemical testing of the recovered conventional core, efforts were diverted to the determination of the geologic conditions that resulted in the destruction of porosity and permeability within the proposed CO_2 sequestration interval.

Petrographic analyses of the conventional core and 106 rotary sidewall cores indicate that reservoir properties of the study sandstone (specifically permeability and porosity) were substantially diminished by a complex series of diagenetic events largely driven by regional tectonics. Consequently, the geologic history of the SGR basin and how it fits into the regional tectonics of central eastern North America during the Triassic and Jurassic.

Individual portions of the petrologic and reservoir/storage characterization of Rizer #1 Test Borehole are presented in Appendix 1, each with its own descriptions of methodology, results, and discussions. These sections are briefly described as follows.

Petrologic Results

This section presents the results of the petrologic, sedimentolologic, and paleontologic analyses of the rotary sidewall cores (RSWC), conventional core (CC), and cuttings from Rizer #1 and discusses how these data sets inter relate. Conclusions reached are as follows:

- The depositional setting for the conventionally core interval of test borehole Rizer #1 and probably the majority of the pre-Cretaceous strata penetrated is primarily alluvial associated with lacustrine coastal deposits.

- The sandstone samples recovered are generally lithic arkoses to arkosic litharenites with lithics comprised primarily of metamorphic rock fragments.
- The sandstones are predominantly cemented with quartz or calcite cements, with lessor abundances of authigenic sphene, and pyrite and isolated occurrence of evaporite cement.
- Based on modal analysis, total porosity averages 3.2%.
- Detrital matrix based on modal analysis of RSWC and CC sandstone samples only comprises an average of 2.9%.
- The igneous bodies encountered are classified as altered alkali olivine basalts or diabases.

Diagenetic Study

This Diagenetic study presents data sets, such as modal analysis of compaction indices and paleotemperatures of quartz and calcite cements to determine the burial and diagenetic history of the Rizer #1 study interval. Conclusions reached in this section are as follows:

- Reservoir quality of the study sandstone was substantially diminished by a complex series of diagenetic events, which include early cementation by chlorite, calcite, and sphene, followed by evaporates and multiple stages of quartz overgrowth and calcite cements during rapid subsidence of the basin.
- Based on modal analysis of compaction indices indicate a majority of the Rizer #1 sandstones appear to have been buried 2000ft to 6000ft (610m to 1823m) deeper than present day at some point in their burial history.
- Based on results of SIMS analysis of δ^{18}O within quartz cements, the study sandstones were buried approximately 8200ft (2500m) deeper than present burial depths at some point in their burial history.

- Sandstones within Rizer #1 test borehole and those laterally equivalent sandstones within the same fault block are not suitable candidates for CO_2 sequestration.
- Regarding reservoir properties for sandstones deeper within the Rizer #1 fault block, unless they experienced early cementation and subsequent dissolution of those cements to create secondary porosity or were over pressured early in their burial history, it is unlikely they possess reservoir properties to be suitable candidates for CO_2 sequestration.

Elemental Analyses Elemental analyses by X-ray fluorescence (XRF) of samples from test borehole interval 2660ft to 6200ft (810.8m to 1890.0m) (see Appendix 1 for details)Conclusions reached in this section are as follows:

- Present are six (6) chemostratigraphic zonations, which are characterized by compositional shifts between more-mafic and more-felsic input over vertical intervals ranging from 200 feet to over 1000 feet. These shifts are interpreted to be controlled by the erosion of different source rocks, possibly terranes associated with the Carolina Zone.
- The elemental data are consistent with only limited weathering and chemical modification of detritus during most of sedimentation. This may be due to relatively rapid erosion and deposition or accumulation during arid conditions. Whatever the cause, significant modification of sediments did not occur
- The elemental data alone cannot unequivocally establish whether basalts present are extrusive or intrusive. Only metasomatism is likely with lower-most Basalt, constrained by petrology and geochemistry.

Geocellular Earth Model

The ultimate goal of this project is to simulate CO_2 injection into the Jurassic/Triassic sediments within the South Georgia Rift basin (SGR). Building a geocellular model is a three-

step process: 1) build a solid earth model, 2) generate a 3-D grid with faults and horizons, and 3) incorporate the grid into a 3-D flow simulations using CO_2. We are using Petrel's structural framework module instead of the standard pillar gridding process due to the complexity of the faulting. Figure 34 is the workflow to create a geocellular model using Petrel's Structural Framework.

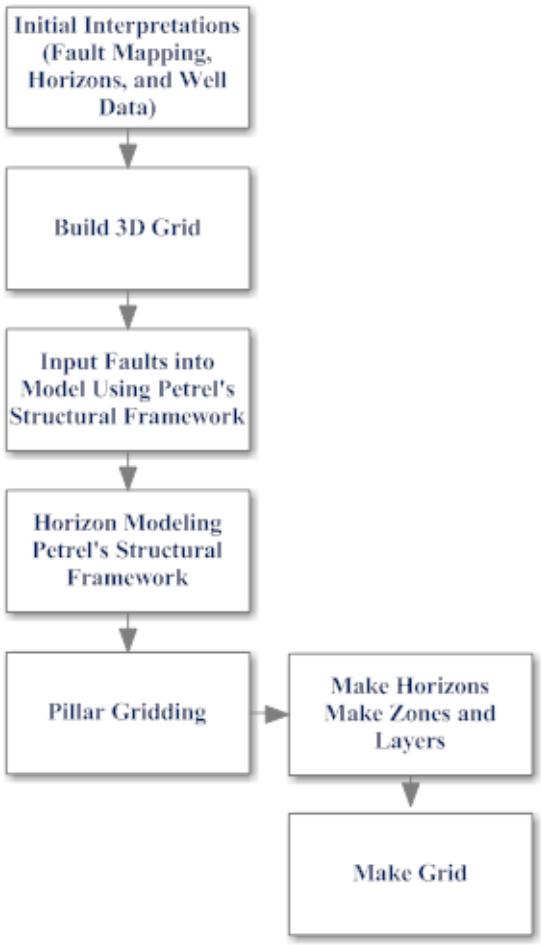

Figure 34. Geocellular modeling Workflow used to create the SC and GA models.

South Carolina SGR Basin Model

The first step in building the geocellular model workflow is to finalize all the fault and horizons interpretations (Figure 35). In the two areas in the SGR that were studied, the project has very complex structure styles (i.e. faulting) encountered in the Jurassic/ Triassic section. At this

stage in the modeling workflow it is essential, prior to converting the selected faults into a structural model, that the interpreter has assigned the correct type of fault e.g. listric or S-shape faults in flower structures (Figure 36). If the faults are not assigned the correct geometry this will affect the results from the flow simulations. During this phase of the workflow the project team had to make decisions on which faults would be used in the final fault model. In the initial interpretation of the seismic data over hundred faults were observed and 66 were interpreted. Listed are the criteria used for selecting which faults to use: 1) are the faults within the model boundary, 2) if the faults are within the model boundary do they affect horizons that will be model for injection, and 3) the geometry of the faults. In the South Carolina portion of the study area there were sub-horizontal to horizontal faulting. Petrel has problems modeling faults that do not cross horizons. Therefore some of the initial interpreted faults had to be eliminated from the final model. Using the above criteria eleven faults were selected (Figure 36)

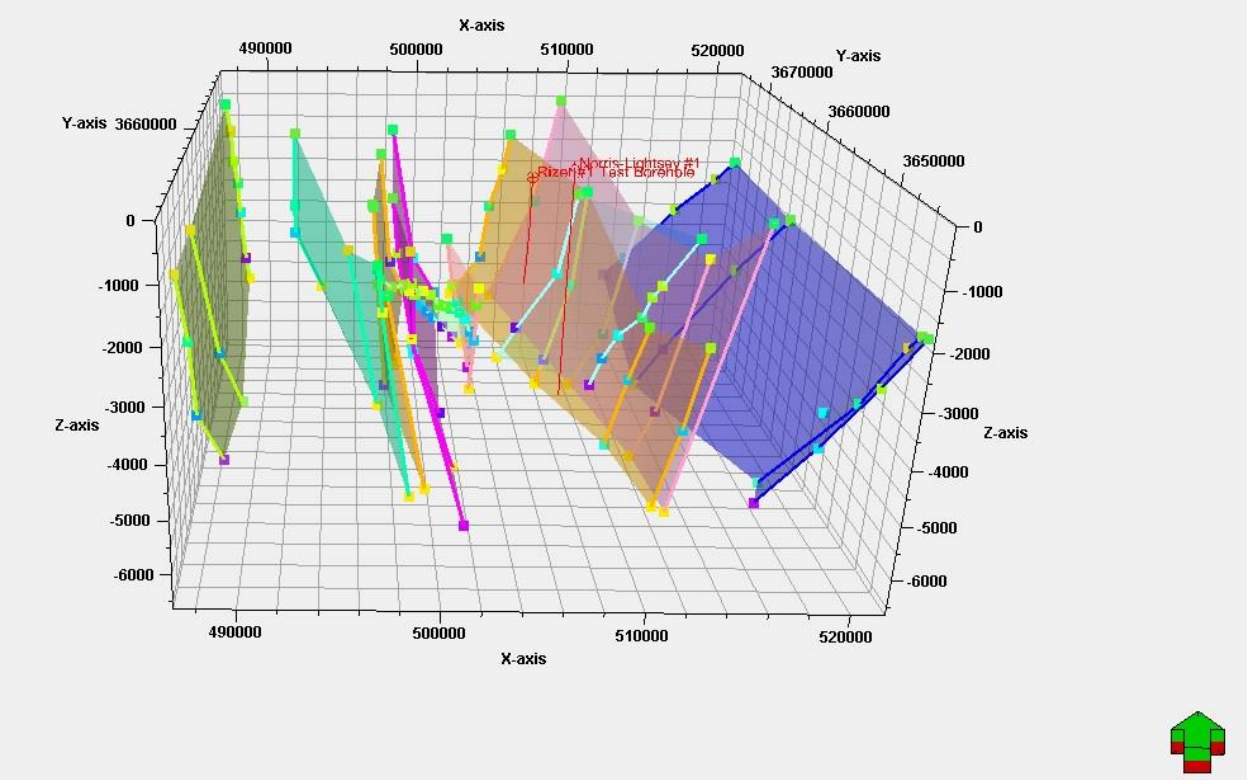

Figure 35. Figure showing the faults selected for creating the fault model for the SGR in the South Carolina study area.

The next step in the workflow is to take the seismic interpreted surfaces and any well data and convert the seismic surfaces into a horizon model. The horizon model has to also reflect the effects of faulting (Figure 35). The complexity of structure has made the correlation between sandstone units almost impossible. The only units that can be mapped between the Rizer #1 and Norris Lightsey #1 are the Diabase intrusive units. We modeled the following horizons: base of Coastal Plain, the top and base of Diabase units E, and F (Figure 27). The results from the petrographic and core analysis has ruled out using the sandstones as possible injection zones due to extremely low porosities and permeability's values. The average porosity value of the sedimentary material was 3.4% and the average permeability is 0.065 mD derived from whole core and 106 rotary sidewall cores analyzed by Weatherford Laboratories. The only possible porous zones are along the diabase units where water was flowing into the borehole during the drilling of

the Rizer #1. The diabase units selected for the geologic model can be mapped with the seismic data and with the well data from the Norris Lightsey # 1and/or in the Rizer #1 test boring. In this structural complex settings, fault modeling is the most important aspect of building a geocellular model.

In the Petrel geocellular workflow the structural fault modeling and horizon modeling are now incorporated into the Corner Point Gridding workflow to generate the final gridded geocellular model. The fault model derived from structural framework workflow is now converted into the pillar gridding module (Figure 36 and 37) thru the corner point gridding workflow. In this workflow the modeler has to establish the pillar spacing and the number of nodes on each pillar that will defined the shape of the fault.

The final step in building the geocellular model is incorporating the horizons into the pillar gridding workflow (Figure 34) building the different layers, zones and stair stepping faulting if necessary.

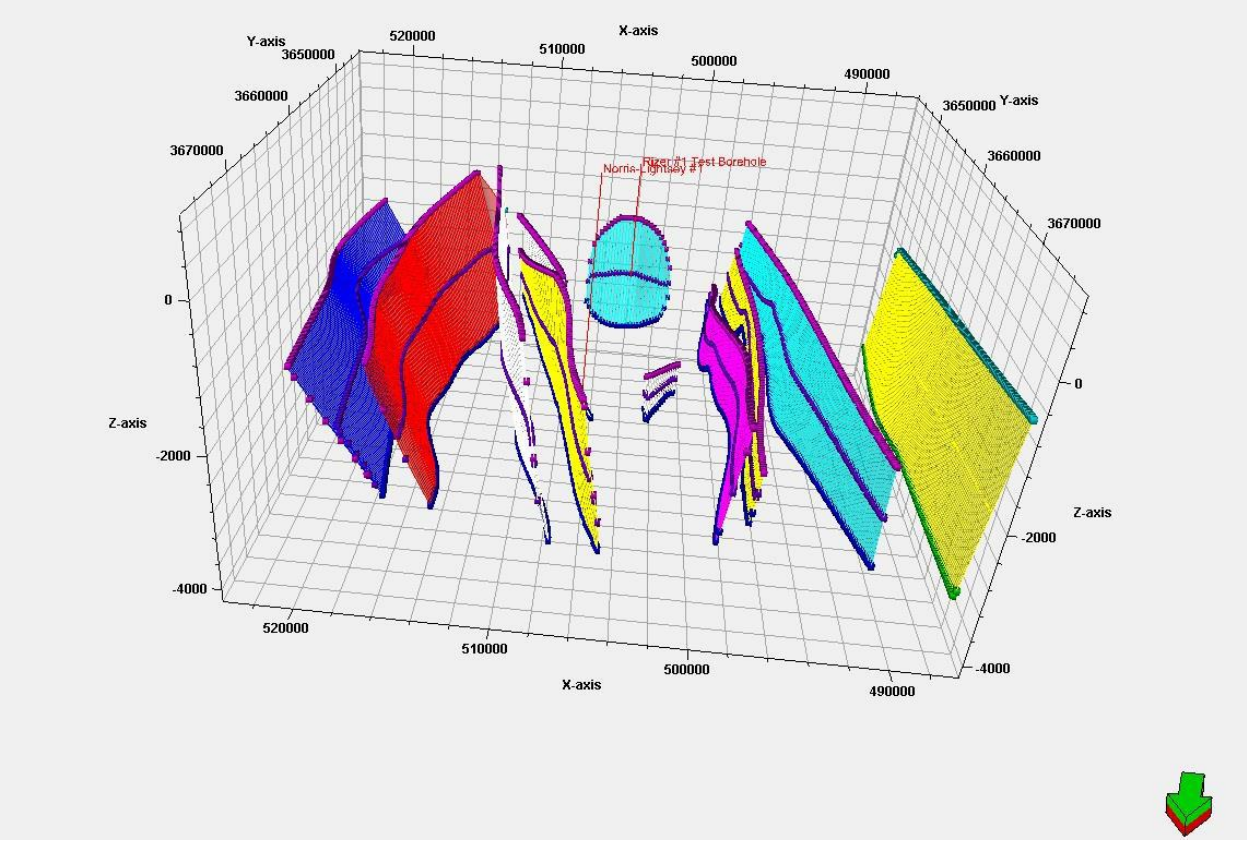

Figure 36. Final fault model after the pillar gridding workflow was completed in Petrel.

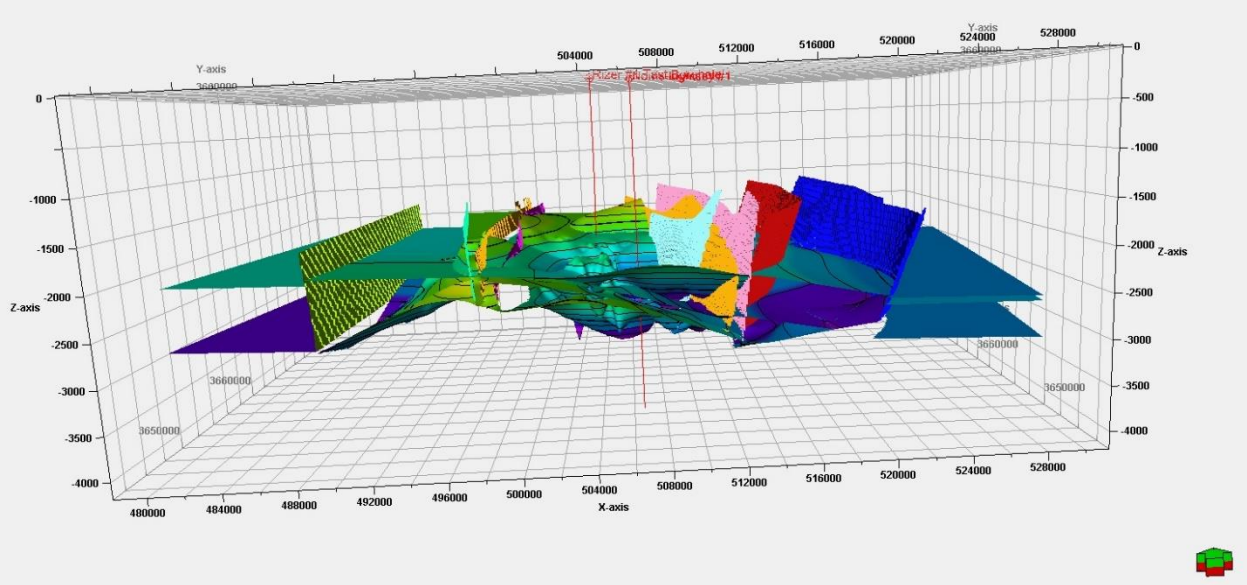

Figure 37. Final model with faults and horizons derived from the pillar gridding process.

Georgia SGR Basin Model

The Georgia study area consisted of two seismic lines and two wells that could be used to correlate the geology to seismic lines (Figures 13, 29, and 30). The study area in the southern Georgia portion of the SGR basin appears to have a less complex structural history. As stated in the interpretation section the seismic data appears to have image a transfer fault zone (Heffner, 2013) separating two sub-basins within the SGR. The seismic suggest that the sub-basin to the southeast is an asymmetrical half-graben type of basin (Figures 29 and 30). It was decided that the faults and diabase units mapped in the sub-basin would not be used since only a very small portion the basin was image with the seismic data.

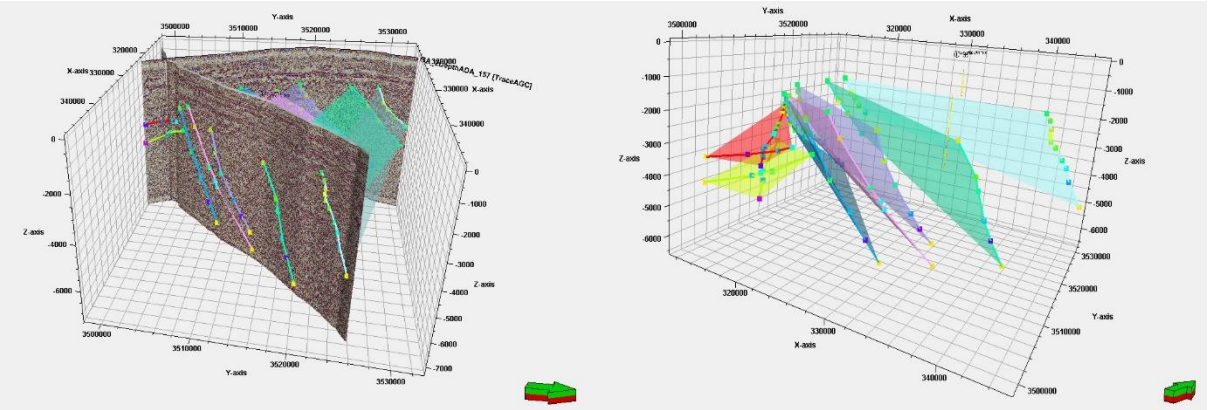

Figure 38. Three-dimensional view of seismic lines GA-1 and 2 with fault interpretations and without seismic lines. The red horizon is interpreted as a diabase dike and below the dike is a fault within the sub-basin. The dark blue fault defines the southern end of the transfer fault zone identified by Heffner, 2013.

In Figure 38 and 39, the fault model for southern Georgia study area is much less complex that the study area in South Carolina. Descriptions from the GA-3128 geologic log indicate that the well terminated in a diabase/ basalt unit at the base of the Coastal Plain sediments. This diabase unit may be equivalent to the "J" basalt found in SC. The geophysical log in well GA-3457 starts below the Coastal Plain so the presence of the basalt layer in this well cannot be confirmed. However the seismic amplitudes along the interface between the Coastal Plain and

Jurassic/Triassic suggest the diabase/basalt is present. Seismic interpretations suggest that may be a possible a Jurassic section (Figure 29 and 30). This unit was not recognized on any of the SC seismic data.

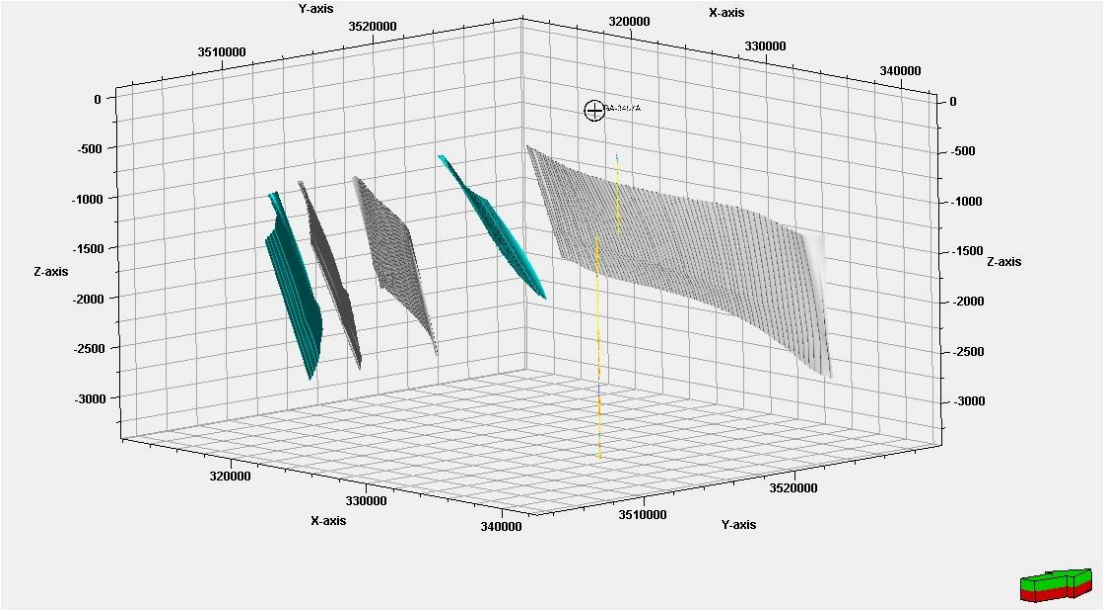

Figure 39. The final fault model for the Georgia portion of the SGR.

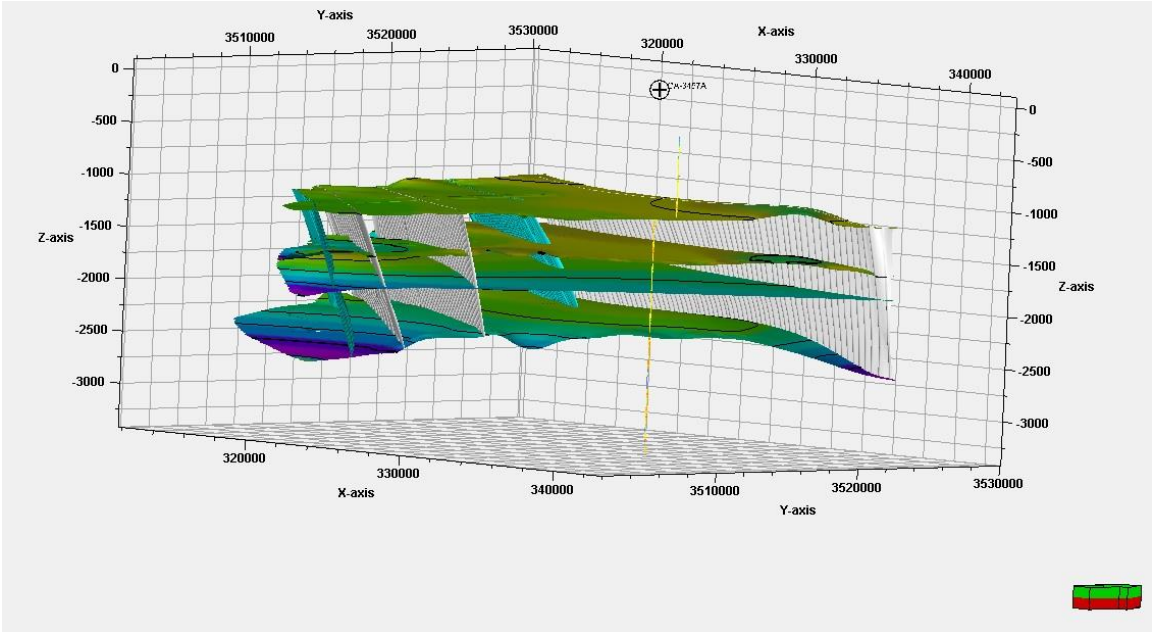

Figure 40. Three-dimensional view of the faults and the three horizons to generated the geocellular model for GA. The top horizon is base of the Coastal Plain (basalt?), diabase layer (top of Jurassic?), and base of Jurassic?

The final model incorporates the faults and horizons mapped on the seismic data (Figure 40). The adjacent sub-basin was excluded from the final model because so little of the basin was covered by the seismic data. The majority of the porous zones identified on the well log are below the resolution of the seismic data therefore we can only estimate the extent of these porous zones. Figure 40 shows a 3-D view of the faults and the three horizons to generate the geocellular model for GA. The top horizon is base of the Coastal Plain which maybe basalt, the next horizon is diabase layer 2 (which we believe to be the top of Jurassic), and the lower most horizon is believed to be base of Jurassic.

The newly acquired data in the southern Georgia portion of the SGR basin appears to have high potential for sequestering CO_2. The limited well data suggests that within the Jurassic/Triassic section there are porous zones that could be potential reservoirs. As in the SC study area there is evidence that faulting may continue upward into the Coastal Plain sediments causing upward migration of CO_2 and potential contamination of potable water sources. We think that any potential sites for CO_2 would have be a significant distance away from these transfer fault zones which increase the risk of CO_2 migration up into the Coastal Plain aquifers. We think other sub-basins that comprise the SGR basin can safely store CO_2 in Georgia.

Simulate Injectivity into Target CO2 Storage Formation

Injection Phase One: Injection Simulation Using Postulated Reservoir Data

Our study investigates the feasibility of injection and long-term CO_2 storage in the northern portion of the SGR basin (Figure 41). The Norris Lightsey #1 (N.L. #1) boring log indicates sequences of sandstone, diabase, and shale that could equate to a vertically stacked series of CO_2 reservoirs and seals, which would provide multiple reservoir CO_2 storage capability within the same injection well. The vertically stacked reservoir/seal combinations are ideal because they

potentially reduce the CO_2 footprint for large volumes of CO_2 injection by using the same well to inject CO_2 into a series of vertically stacked reservoir horizons (Shafer and Brantley, 2011). With conservative porosity and permeability estimates, the U.S. DOE capacity equations (U.S. DOE, 2006) indicate the SGR basin has massive potential (> 100 million tonnes) for CO_2 storage. The large CO_2 storage volume estimates, combined with the vertically stacked storage potential and lack of deep wells that could serve as potential leakage pathways, make the SGR basin unique and potentially very attractive for long term CO_2 storage. The southeastern U.S. contributes a large portion of our nation's total CO_2 (Figure 42). More than half of all (stationary and non-stationary) CO_2 emissions in South Carolina are from electric power plants and industrial manufacturing facilities. Permanently storing CO_2 in close proximity to the sources will provide economic efficiencies and reduce risks associated with transporting CO_2 long distances from source to sink. This research will ultimately aid in the determination of the extent to which the SGR is a suitable basin for long-term storage of supercritical CO_2. The objectives of this research were to simulate CO_2 injection, plume migration, and long-term fate of supercritical CO_2 in the SGR basin. The injection simulation will be assist in determining the suitability of the SGR basin for long-term geologic carbon sequestration. For this study, long-term is defined as 1000 years and over pressured is defined as pressure that would cause upward leakage of CO_2 through the igneous seal or pressure that exceeds lithostatic pressure, which is ~65 megapascals (MPa) [9,427 pound force per square inch (psi)].

Criteria for suitability are:

1. Meet U.S. DOE's minimum required injection rate and capacity of 1 million tonnes annually over 30 years.
2. The process of CO_2 injection does not over-pressurize the system.

3. The CO_2 does not migrate unexpectedly, particularly through the seal.

The CO_2 injection simulation will:

1. Forecast the reservoir conditions and the system's response to the stress of CO_2 injection.
2. Forecast the fate and transport of the CO_2 during injection as well as a prescribed time post-injection.
3. Aid as a decision support tool in determining if the SGR basin is suitable for long-term geologic storage of supercritical CO_2.
4. Aid as a decision support tool in the design of CO_2 injection field studies and full scale implementation.

Due to (1) the depth of the SGR basin combined with (2) the lack of interest from the petroleum exploration industry, only sparse drilling and geophysical research has been conducted. Previous to this study, the structure of the SGR basin had only been speculated from scattered drilling and potential field (gravity and magnetics) interpretation, leaving the internal boundary and the deep structure unknown (McBride, 1991). Chowns and Williams (1983) completed a comprehensive study of deep wells in Georgia, Florida, and Alabama to assess the extent of the SGR basin and relied on interpretations of gravity and magnetic surveys for determining the boundaries where little to no well control was available (Hefner, 2013). There are less than ten boreholes that were drilled into the Triassic-age sediments and only one wildcat well, the Norris Lightsey #1 (N.L.) drilled in the 1984, that penetrated a significant portion [~4,000 meters (m) (~13,123 feet)] of the SGR basin in our study area. Lack of data makes the SGR basin unique in

that unlike other U.S. DOE sponsored carbon capture and storage projects, the basin has yet to be studied. Further, there is so little currently known about the geology of the SGR basin that the formations have yet to be named. Nevertheless, the Carbon Sequestration Atlas of the United States and Canada (U.S. DOE NETL, 2008) identifies the Triassic basin in southern South Carolina as a saline formation suitable for CO_2 storage.

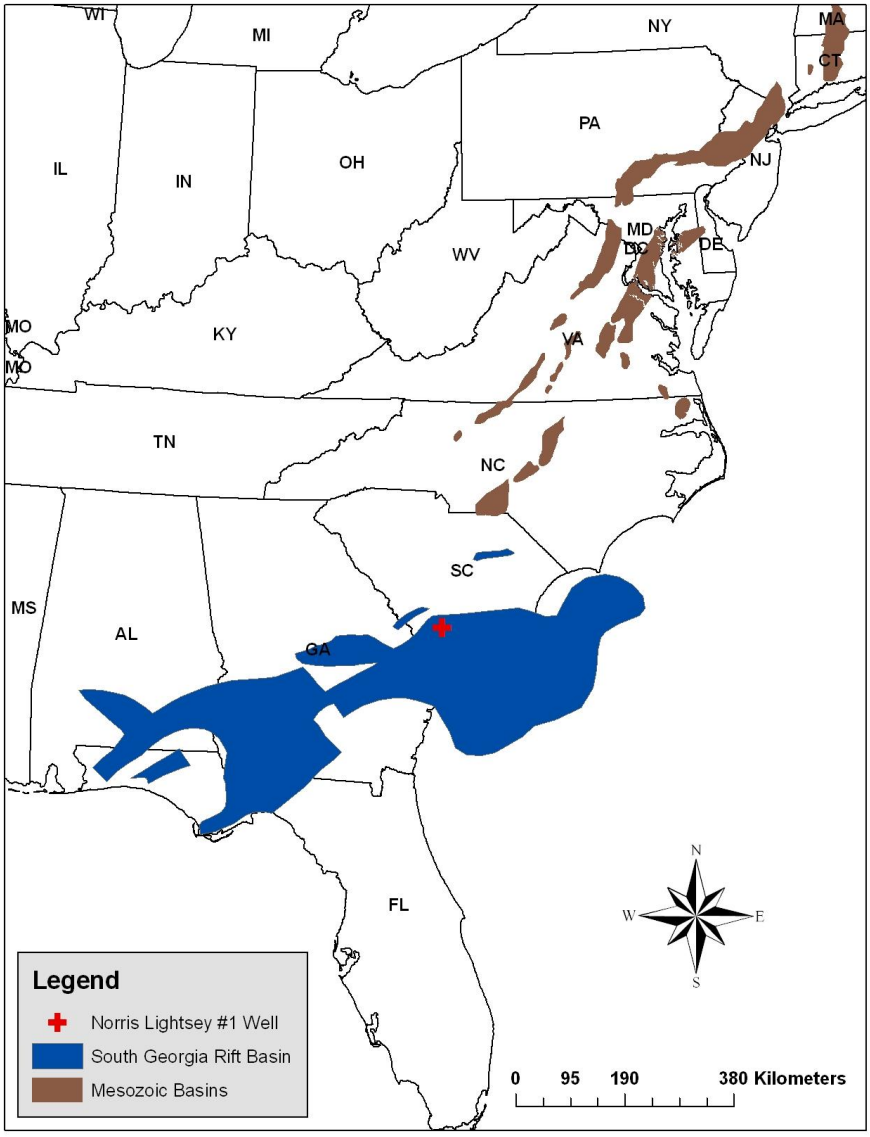

Figure 41 Eastern North American Rift System Mesozoic basins and the South Georgia Rift Basin.

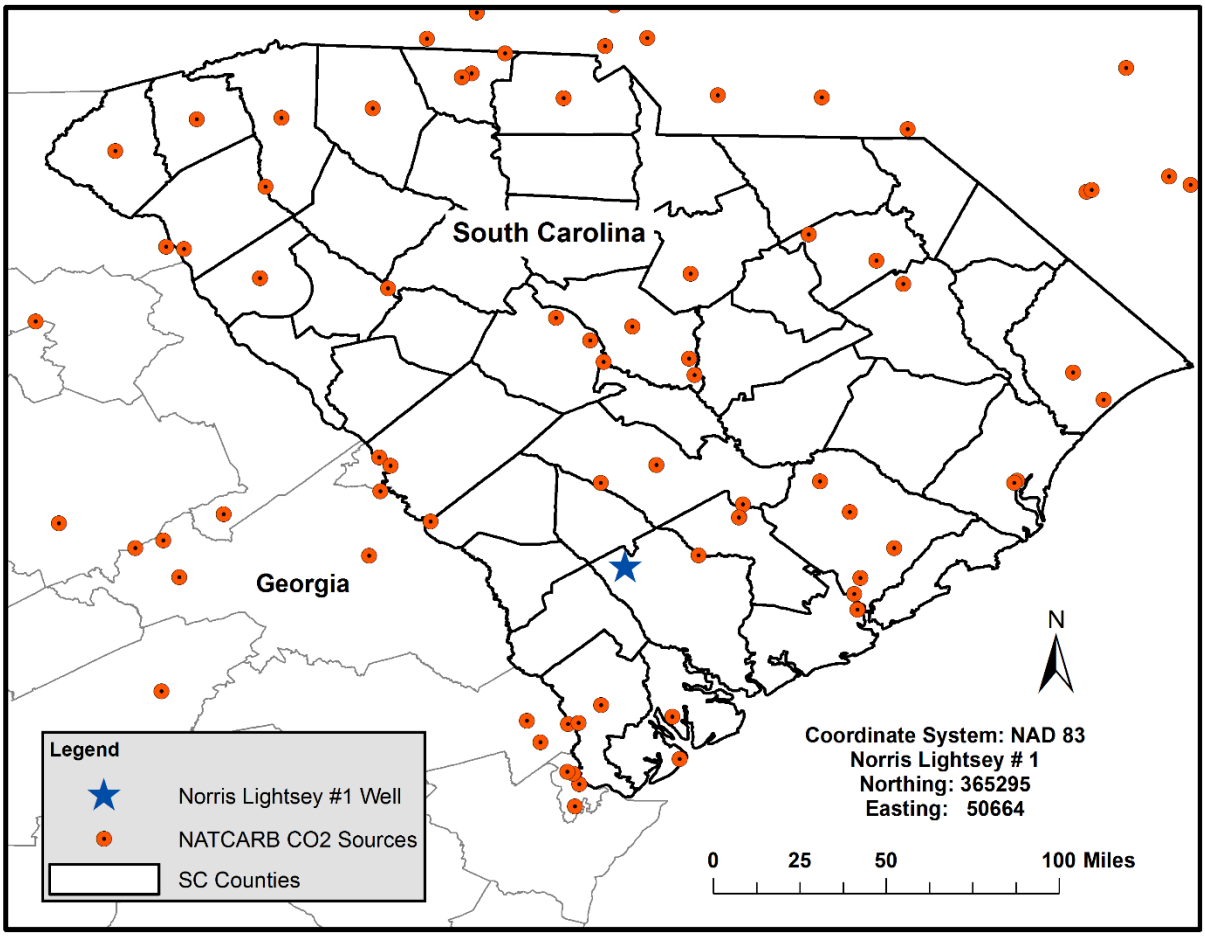

Figure 42. CO_2 Sources in South Carolina and Georgia proximal to the study area.

The long term fate of injected CO2 for geologic storage is broken up into four different storage modes: (1) free gas; (2) trapped gas; (3) dissolved in the formation brine, and (4) gas sequestered as solid minerals or mineralization trapping. Modes 1, 2 and 3 can be simulated with a multiphase flow simulator such as TOUGH2 and GEM. However, the mineralization trapping can only be done using a reactive transport model. For this study, we focused on the first, second and third modes using the multiphase simulators TOUGH2 and CMG-GEM. The next phase of the modeling is too procure a reactive transport model for the mineralization modeling. Unfortunately, due to the complexity of the geology and hence then 3-D geologic model, simulation time for each experiment was very long tedious with many iterations of trial and error just the get the model stable. Once the model was finally stable enough to converge, each

experiment took up a week to run. This was due to not only the complexity of the model, but also the size of the model. This phase two model, which was a Petrel™ export and contained basin structure, had over 1,100,000 cells. The size of the model combined with the juxtaposition of the faults verses the surrounding material made for very slow and tedious modeling.

CO_2 injection feasibility and CO_2 migration within (and out of) the target storage formations are key concerns of deep geologic sequestration. Safe and permanent underground storage of CO_2 must be certain before commercial development of a particular site can be undertaken. Numeric injection simulation models aid in addressing these concerns. The first step of the numeric modeling process is to create a Conceptual Site Model (CSM). A CSM is three-dimensional (3-D) geological model of the study site that is based on existing data and helps to better understand the physical conditions and behavior of the system being studied (Mercer and Faust, 1981). Using C-Tech Development Corporation's MVS software, a 3-D conceptual model was built to visualize the basic basin geology as indicated by the N.L. # 1 litho-stratigraphic log. MVS is state-of-the-art visualization software designed to aid engineers and environmental modelers in subsurface analysis, visualization, and animation (Copsey, 2014). For the MVS conceptual model, we used a simplified lithology of three different materials: unconsolidated coastal plain, igneous rock, and sandstone. Figure 43 illustrates the CSM and displays basic basin stratigraphy as well the stacked storage concept of injecting into the multiple horizons. Armed with a better understanding of the subsurface conditions, the next step was to construct a numerical model of the study area.

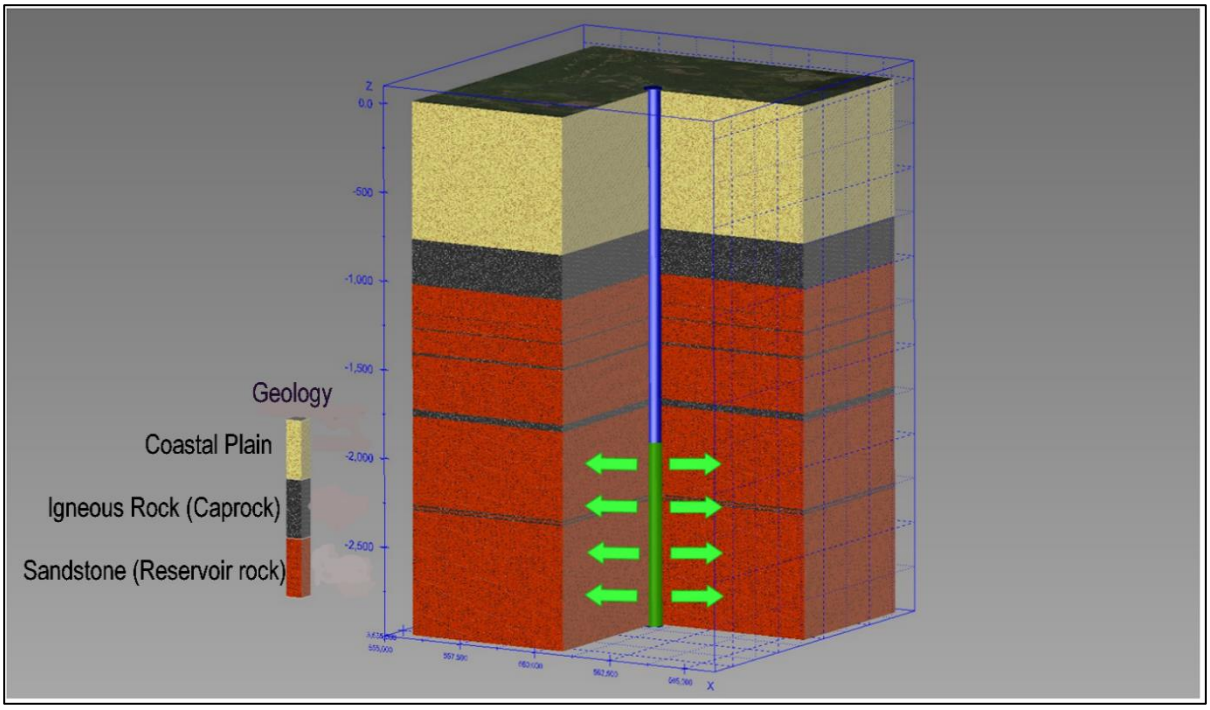

Figure 43. Conceptual solid earth model for the South Georgia Rift basin. The light brown represents the unconsolidated coastal plain sediments, red represents the sandstone reservoir material, and dark gray represents the diabase seals. Green represents the base of the injection well and the stacked series of injection zones.

Due to the deficiency of data in our study area, a two-pronged approach was taken to numerically simulate CO_2 injection and plume behavior in a target reservoir interval in the SGR basin's stacked reservoir stratigraphy. The SGR basin is a deep, variable-density groundwater flow, heat, and salinity transport system. However, hydrostatic pressure and brine concentration gradient are unknown. For this reason, the first step of the CO_2 injection simulation modeling was to establish pressure, temperature, and salinity regimes that are representative of the in-situ environment of the deep saline SGR basin using an equilibrium model. The results of the equilibrium model were then used as the initial conditions for the CO_2 injection simulation. Table 8 is a flowchart explaining the workflow for this two-pronged modeling approach to CO_2 injection simulation.

Table 8. Flow chart of the modeling steps taken in this study.

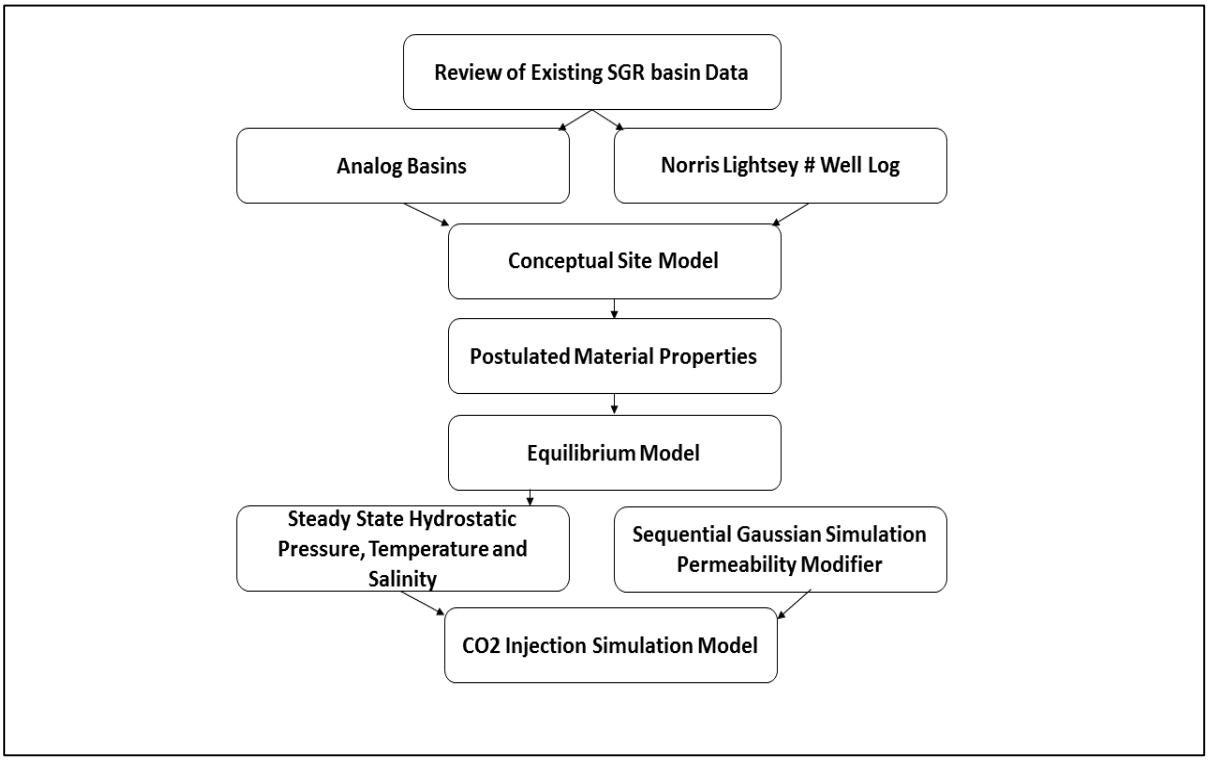

The initial conditions necessary for the injection simulation modeling using the TOUGH2 code require a hydrostatic pressure gradient, which is not known in the SGR basin. For this reason, we used USGS' SEAWAT to establish pressure, temperature, and salinity equilibrium conditions and thus, the initial hydrostatic pressure gradient. SEAWAT is an extension of the USGS-MODFLOW for numerical simulation of 3-D, variable density, transient groundwater flow integrated with MT3-DMS solute transport code. The advantages of using SEAWAT over traditional analytical methods are that it's readily available, easy to use, and considers density effects in the flow calculation. For the SEAWAT equilibrium model, a 100 x 100 x 100 grid was created that represents a 10 km (~6.2 mi) x 10 km (~6.2 mi) x 3 km (~1.9 mi) (x,y,z) spatial extent of the model domain. This grid size was selected to balance the size of the domain with the desired resolution. To the extent of what is known about the subsurface of the study area and in accordance with the conceptual site model, the layers are one of three materials: unconsolidated Coastal Plain

sediment, Triassic lithified sediments, or J/T_r mafic material. The model domain vertical discretization is variable to coincide with the litho-stratigraphy of the N.L. # 1 well (Figure 44).

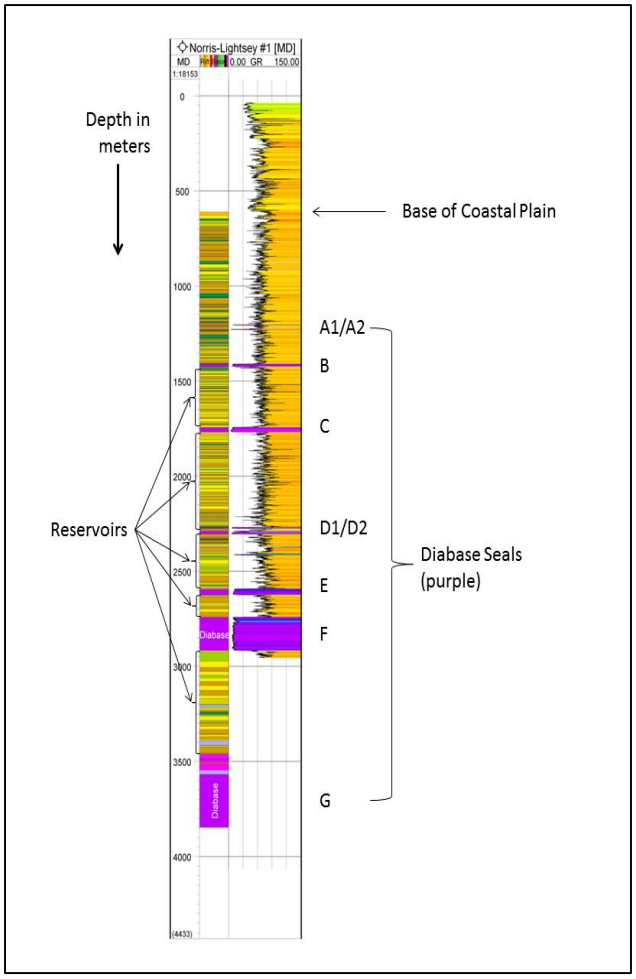

Figure 44. Norris Lightsey #1 lithostratigraphic well log with gamma-ray curve. Injection simulation took place in the reservoir between Diabase E and Diabase F.

The thermal gradient was derived from the bottom-hole temperature of the N.L. #1 well log. The salinity gradient was presupposed from the Department of Energy's National Energy Technology Lab's identification of the SGR basin as being a hyper-saline system. Storativity and porosity parameters were derived from relevant literature and the N.L. # 1 well log (Nelson and Kibler, 2003; Ryan *et al.*, 2002). The elevation of the water table in the study area is approximately -10 m (~32.8 ft), therefore an initial head of -10 m (32.8 ft) was assigned to the entire domain.

The surface layer of the domain was assigned -10 m (32.8 ft) as a fixed boundary head, for every cell below a continuously saturated system was assumed. The equilibrium model was run to steady state with only fixed top (i.e., water table) boundary hydraulic heads.

The model output is a steady-state equilibrium volume that represents the hydrostatic pressure as a function of depth, temperature, and salinity in the SGR basin. Table 9 shows the hydrostatic pressure vs. depth considering temperature and salinity for every 10 horizons within the full vertical dimension of the domain. As expected, the pressure gradient increases with depth, as the salinity increases. As the basin becomes hyper-saline near its modeled base, the hydrostatic pressure non-linearly increases with depth. The results of the SEAWAT equilibrium model were then used as the initial conditions for the CO_2 injection simulation modeling.

Table 9. Results of the equilibrium model showing hydrostatic pressure vs. depth considering temperature and salinity for every 10 horizons within the full vertical dimension of the domain. (Pa - Pascal; C - Celsius)

Layer	Top	Bottom	Pressure, Pa	Temperature Degrees C	Salt Mass Fraction
1	0	-40	97981	15.5	5.20E-05
10	-360	-400	3618651	24.5	1.07E-04
20	-760	-800	7508566	34.5	2.38E-04
30	-1160	-1200	11366485	44.5	5.29E-04
40	-1560	-1600	15185285	54.5	1.18E-03
50	-1960	-2000	18960265	64.5	2.62E-03
60	-2339.95	-2400	22598440	74.25	5.69E-03
70	-2760	-2800	26391763	84.5	1.28E-02
80	-3160	-3200	30112647	94.5	2.81E-02
90	-3534	-3582	33769369	103.95	5.80E-02
100	-3944.66	-4000	38539006	114.31	1.24E-01

TOUGH2-ECO2N, as implemented in PetraSim® is the software platform that was used for CO_2 injection simulation. ECO2N is the fluid property module for the TOUGH2 simulator

that is designed for applications to geologic sequestration of CO_2 in saline formations. It addresses the thermodynamics and thermophysical properties of H_2O – NaCl – CO_2 mixtures, reproducing fluid properties largely within experimental error for the temperature, pressure, and salinity conditions of interest (Pruess, 2005; Pruess and Spycher, 2006). For this study, it was assumed that the CO_2 being injected is in supercritical phase. Due to the depth of the injection horizon, the pressure and temperature of the geologic strata far exceeds what is necessary to maintain this phase (i.e., T_{crit} = 31.04 ^oC (87.9 ^oF), P_{crit} = 7.382 MPa [(1,071 psi); (Vargaftik, 1975)]. For the TOUGH2 injection simulation model, a variable grid was created that represents a 10 km (~6.2 mi) x 15 km (~9.3 mi) x 3 km (~1.9 mi) (x,y,z) domain (Figure 45). Variable grids are used to allow incorporation of more spatial information in a computationally efficient way. This approach creates a hierarchal concept of space that creates a grid with much smaller cells (Voronoi cells) centered on and around the injection well, with the smallest cell being approximately the size of the injection well for a realistic injection representation. The variable grid is capable of simulating regional as well as local dynamics simultaneously (Vleit *et al*., 2009).

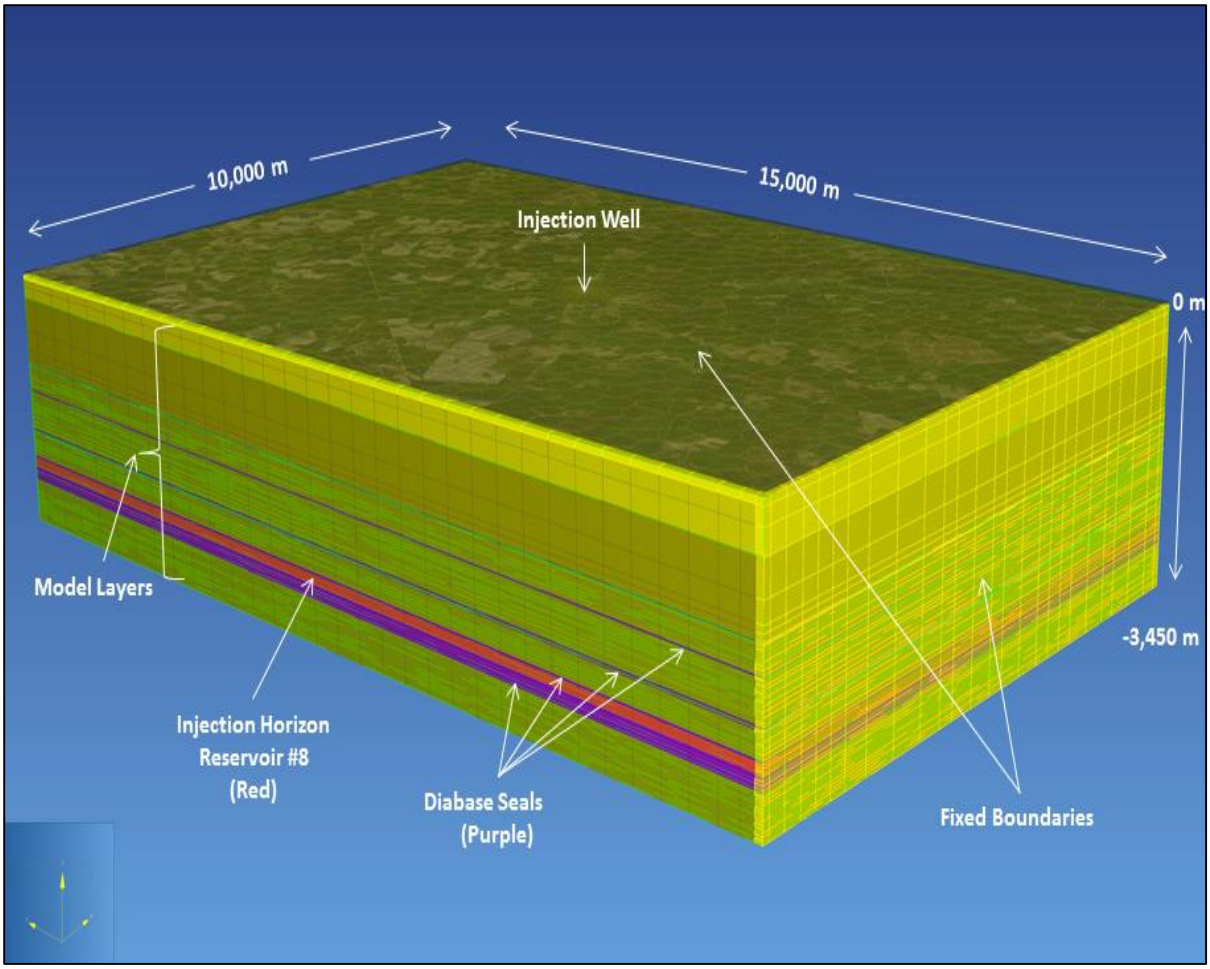

Figure 45. CO_2 injection simulation model domain based on Norris Lightsey #1 well lithology. The simulated injection well is located coincidently with the Norris Lightsey #1 well location and injection simulation in the red horizon. (between Diabase E and Diabase F in Figure 44).

As with the SEAWAT model, the TOUGH2 model domain vertical discretization is variable to agree with the lithostratigraphy of the N.L. # 1 well and each cell was assigned a material and populated with that materials postulated hydrogeologic properties determined from N.L. # 1 geophysical log and relevant literature. The largest database of siliciclastic porosity and permeability data found was an assimilation done by the U.S. Geologic Survey (USGS) in Open-file Report 03-420. This report consist of over 70 datasets taken from published data and all measurements were taken from core samples. From this report, all of the data on Triassic-aged sediments were filtered out and the porosity and permeability data were plotted. Each dataset

contained (1) a minimum of 20 porosity and permeability values, (2) a description of the depositional setting, (3) method of measurement, (4) referenceable source, and (5) the formation name, again, depth, and location of each sample taken (Nelson and Kibler, 2003). Figure 46 is a scatterplot of all datasets from the USGS that contain porosity and permeability data for cored samples of Mesozoic sandstone throughout the world. The porosity dataset is normally distributed and permeability dataset ranges over six orders of magnitude and log normally distributed. The dissolution of CO_2 in the formation water, also known as solubility trapping, is an important CO_2 migration and trapping mechanism in the post-injection period of geologic storage in deep saline formations. Capillary pressure (P_c) and relative permeability are two major driving forces of fluid migration in CCUS; therefore, an accurate representation of the each is crucial for modeling solubility trapping, and hence long term CCUS (Boxiao *et al.*, 2012; Bachu and Bennion, 2008). To address capillary pressure and relative permeability, the van Genuchten Function (Pruess, 2005) and Corey's curves (Pruess, 2005) were used respectively in accordance with the ECO2N user manual's default values.

For both the equilibrium and the injection simulation, it was assumed that the permeability of the mostly unconsolidated material of the South Carolina coastal plain of (SGR basin overburden) was anisotropic and that the sandstone and mafic material within the SGR basin was isotropic. Table 10 is a summary of the parameters used for SGR basin CO_2 injection simulation.

Table 10. Material properties of the three major rock types used in the injection simulation. Sources include Norris Lightsey #1 well log, relevant literature and TOUGH2 Manual default data for material type. [(mD - milliDarcy; S_{gr} - residual gas saturation; S_{lr} - residual liguid saturation; P_o - cappilary pressure; λ - pore distribution parameter (used for relative permeability calculations)]

Property	Units	Coastal Plain	Reservoir	Seal
XY Permeability	m^2/mD	3.60e-12/3650	9.87e-15/10	1.00e-20/1.00e-5
Z Permeability	m^2/mD	3.60e-13/365	9.87e-15/10	1.00e-20/1.00e-5

Property	Units	Coastal Plain	Reservoir	Seal
Porosity	%	20	6	0.1
Rock Density	kg/m^3	2,400	2700	2,933
Corey S_{gr}	-	0.05	0.05	0.05
Corey S_{lr}	-	0.17	0.15	0.20
van Genuchten P_o	kPa	2.10	1.50	337.00
van Genuchten λ	-	0.46	0.46	0.46
van Genuchten S_{lr}	-	0.17	0.15	0.20

Material property information (i.e., porosity and permeability) for CO_2 injection simulation in data-deficient geologic environments is sparse. Therefore, the material properties between and among data points must be determined through interpolation if the assumption of a homogeneous environment is unrealistic, which is usually the case. For this reason, stochastic simulation techniques have become the method of choice for generating numerical models that represent subsurface heterogeneities (Doyen, 2007). A commonly applied technique is Sequential Gaussian Simulation (SGS), which is a method for simulating spatially continuous properties (e.g., permeability) requiring knowledge of a variogram and histogram. In SGS, numerous equally probable and spatially correlated realizations are created to incorporate uncertainty in the model parameter. Throughout the history of spatial stochastic modeling, Gaussian random fields are probably the oldest and the most commonly used models to represent spatial distributions of continuous variables (Damsleth, 1994). To demonstrate the effect of uncertainty in permeability heterogeneity in the injection reservoir on simulated CO_2 plume migration, a spatially correlated random field of permeabilities ranging from 10 millidarcy (mD) to 100 mD was created using the Stanford Geostatistical Modeling Software (SGeMs) (Remy *et al.*, 2007) for SGS. The mean permeability of eight realizations was 23.4 mD, and the mean of the standard deviation of the eight realizations was 5.02 mD.

For this study, we used the sedimentary section between igneous seals E and F for the CO_2 injection simulation reservoir and the basalt horizon E as the top seal (Figure 44). The depth range of the target injection sedimentary section is between 2,476 m (8,123 ft) – 2,588 m (8,491 ft) below land surface, or well below the 1km (~0.62 mi) critical depth to maintain CO_2 as a supercritical fluid. Using the TOUGH2 preconditioned bi-conjugate gradient solver, multiple iterations of injection simulation were performed. The simulations began with a simple layer cake geologic representation of the basin and progressed into a more complex geology as confidence in the simulation approach was gained. For example, a 45º azimuth was applied to the permeability field to better represent the postulated SGR reservoir conditions. Also, to illustrate the significance of adding noncomplex, yet realistic geologic structure to the CO_2 injection simulation process, a 2% dip, trending in a southerly direction, was added to the entire model domain. This is the approximate dip of the base of the Coastal Plain. For the CO_2 injection simulation an injection rate of 1 million tonnes per year for 30 years was established. In addition to this requirement, a 970 year shut-in time (no injection) was also simulated to better determine the long-term fate and migration of the injected CO_2 and to ensure that the SGR basin could effectively contain the 30 million tonnes of supercritical CO_2.

Many numerical experiments were conducted using the TOUGH2-ECO2N simulation code. Reservoir parameters were varied along with injection zone, injection time and shut-in time.

Table 11 is a summary of the parameters that were adjusted for various simulation scenarios. The simulations were conducted to evaluate model robustness and the effects of different modeling scenarios and assumptions on the injection and resulting supercritical CO_2 plume dynamics. For example, experiments were run with reservoir porosity ranging from 1% to

25%. Due to uncertainty of the rock properties and hydrodynamics, an average of 6% porosity was used for the input of the modeling results discussed in this paper. This was an intentionally conservative approach as the USGS assimilated database suggest the average porosity for analog basin sandstone is ~ 15% (Figure 46). Throughout the preliminary injection simulation, many experiments were conducted using the range of input parameters discussed above, however, the results discussed in this paper are the results of the final and most progressed experiments of the preliminary modeling process.

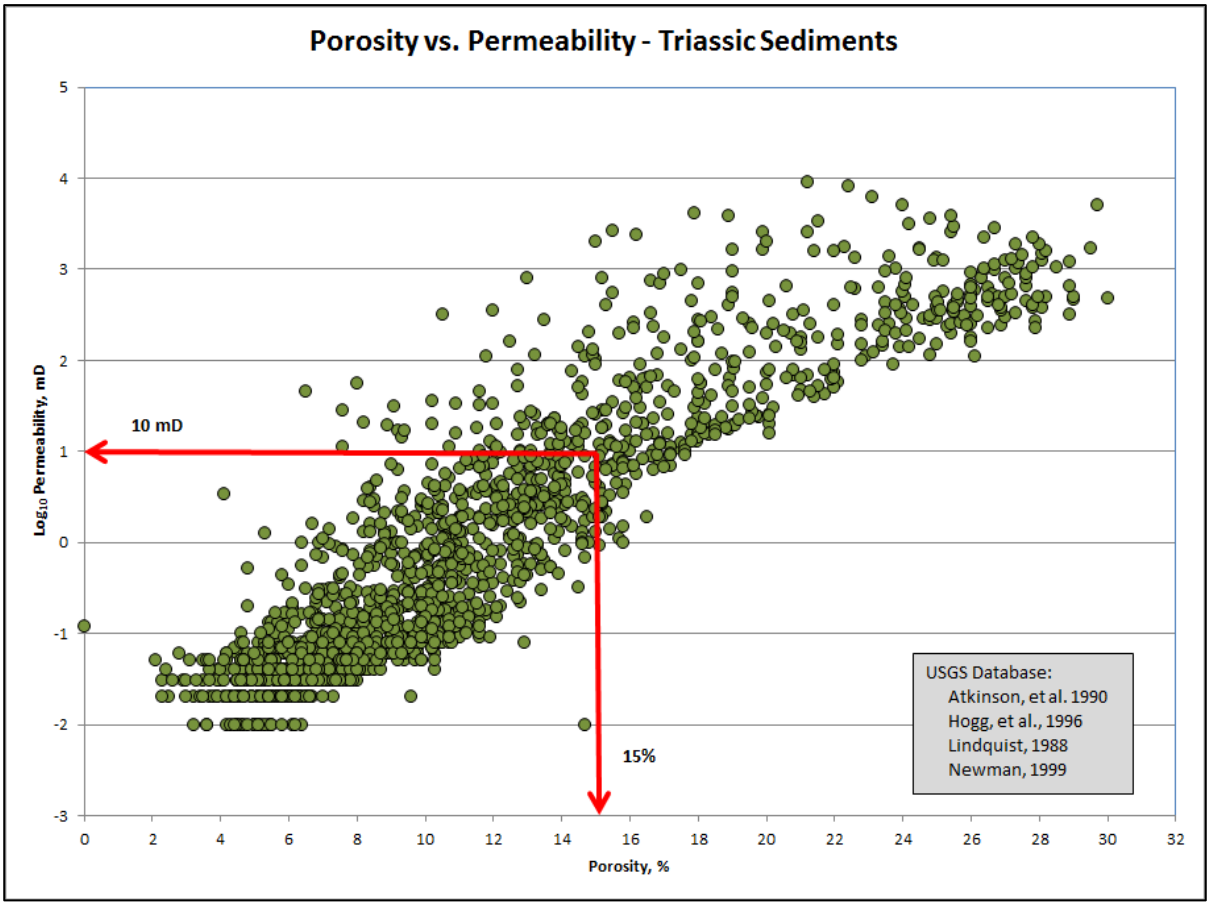

Figure 46. Scatterplot of USGS international database of porosity and permeability of Triassic Sediments. The mean porosity and permeability was used to postulate the reservoir data. Source: USGS Open-file Report 03-420.

Table 11. Parameters that varied to experiment with different modeling scenarios. (mD - millidarcy).

Parameters that were varied		
Material	**Porosity Range (%)**	**XY Permeability (mD)**
Reservoir	0.01 - 0.25	1 mD - 1000 mD
Sill	0.001 - 0.25	0.00001 mD - 1000 mD
Solution Controls	Years	
Injection Time	30 - 1000	
Shut-in Time	0 - 9,700	
End time	30 - 10,000	

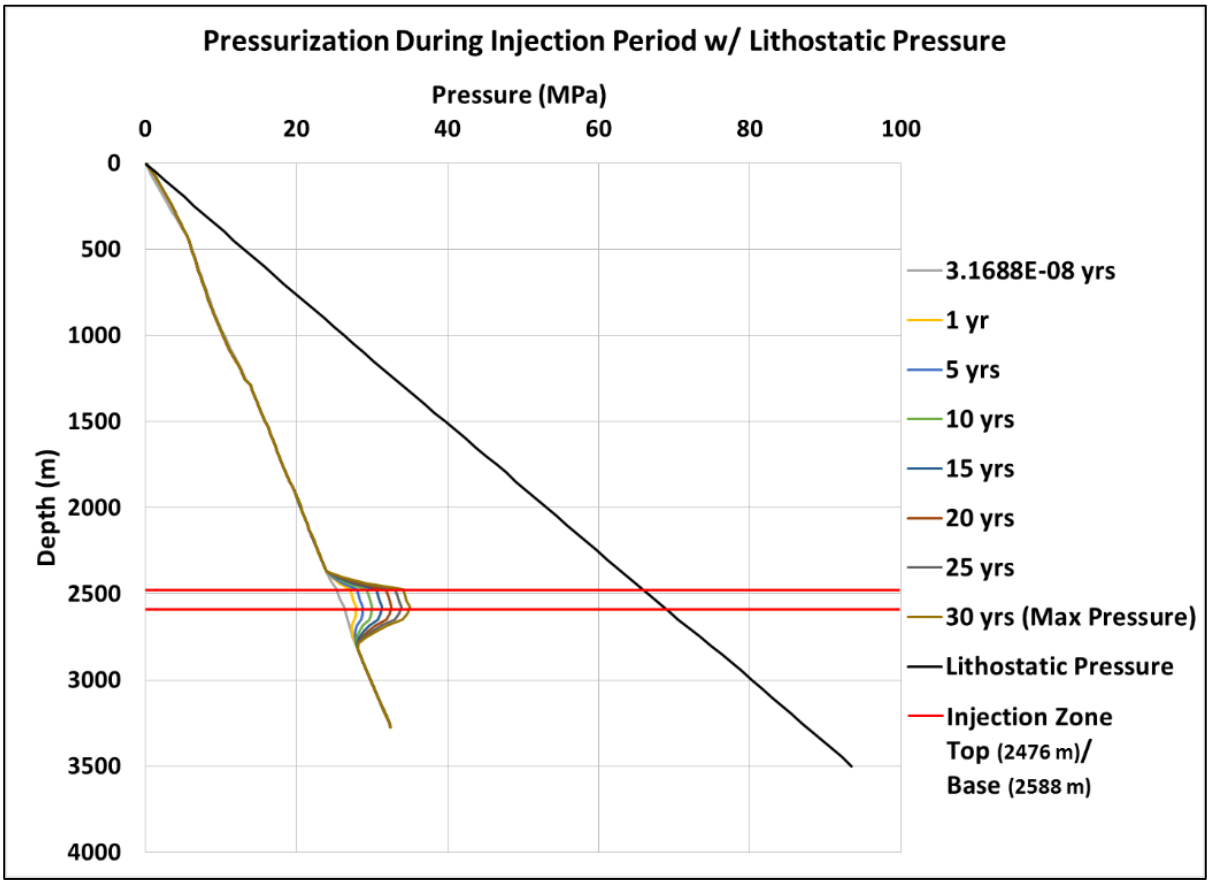

Figure 47. Pressure build-up adjacent to the injection well during injection compared to the lithostatic pressure (black line). Injection rate is 1 million tonnes of CO_2 per year for 30 years.

Figure 47 shows the maximum pressure build-up at the injection wellhead as compared to the lithostatic pressure and demonstrates that the maximum injection pressure stays well below the injection zone lithostatic pressure, therefore insuring that the system does not become over-pressured due to CO_2 injection. Figure 48 shows the dissipation of the pressure back towards basin equilibrium during the subsequent 970 year shut-in period. Figure 48 suggests that the pressure recovery takes significantly more time than build-up due to injections. Note that the basalt seal horizon tightly holds the injection pressure and only during the shut-in period does it slightly increase in response to the pressure increase due to CO_2 injection. This slight increase in pressure in the basalt seal indicates that the simulation is working correctly and that the seal easily keeps the increased system pressure from propagating upwards. In other words, the seal adequately contains not only the supercritical CO_2, it also contains the pressure increase resulting from the injection. Figure 49 shows the effect of uncertainty in permeability (k) heterogeneity in the injection reservoir after a 1,000 year simulation. The image on the left assumes homogenous conditions with a constant k (10 mD), while the image on the right show the results of the same simulation with k ranging from 10 mD to 100 mD. In comparing the two Figure 49 images, the addition of a heterogeneous permeability distribution to the injection reservoir did not significantly change the radial extent of the injected CO_2, however a permeability modifier did provide a reasonable way to address in-situ permeability heterogeneity and therefore this approach should be used in all future CO_2 injection simulation of the SGR basin.

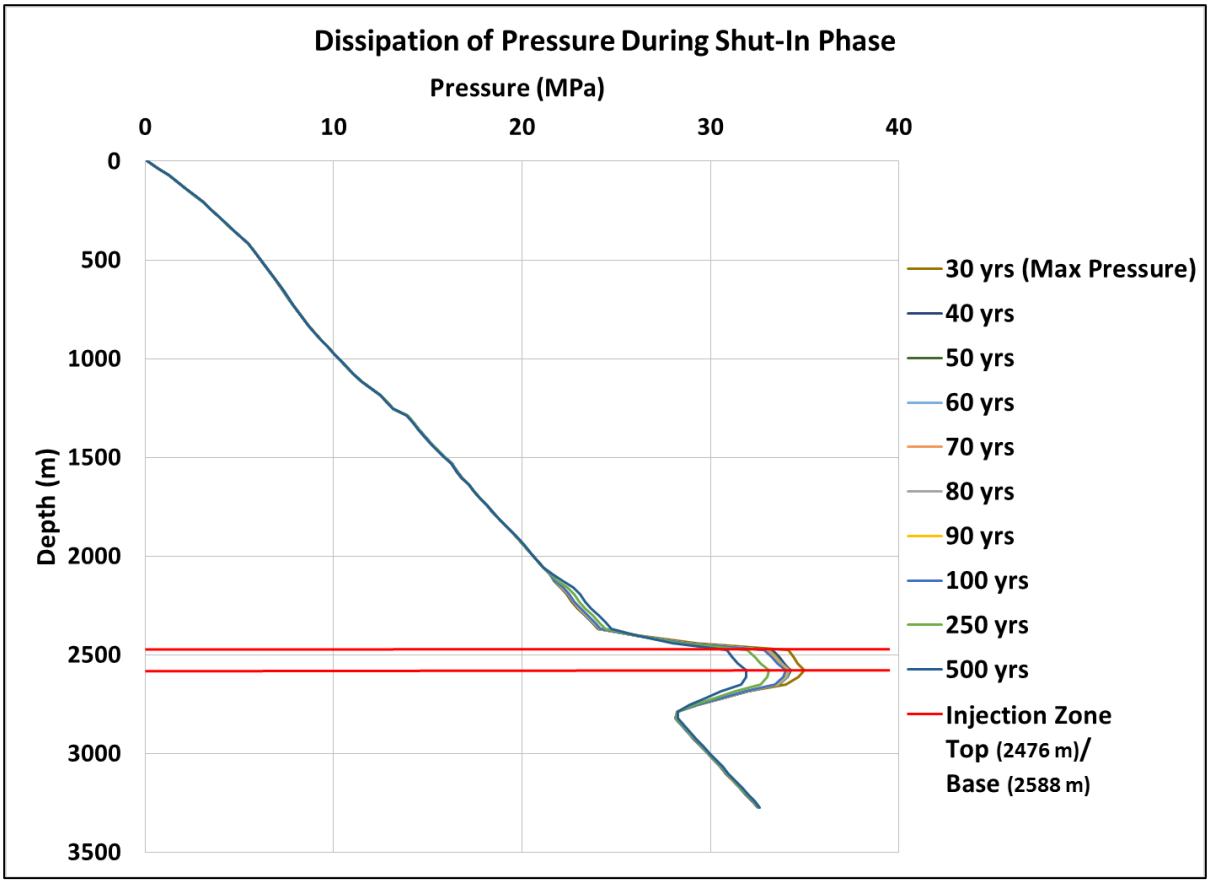

Figure 48. Dissipation of pressure during the 970-year post injection shut-in period

Figure 49. Effect of uncertainty in permeability heterogeneity in the injection reservoir on CO_2 plume footprint after 1,000 year simulation with 30 years injection of 1 million tonnes CO_2 and 970 years of shut-in. Left image assumes homogeneous conditions with a constant k (10 mD) while the right image shows the results of the same simulation with a k modifier ranging from 10 mD to 100 mD.

Figure 50. Effect of geologic structure (2% southerly trending dip) on CO_2 plume footprint after 1,000 year simulation with 30 years injection of 1 million tonnes CO_2 and 970 years of shut-in. Left image shows the results of the simulation with a spatially k in the range 10 mD to 100 mD but no dip. The right image shows the up-dip migration of the CO_2 plume as a result of the 2% dip in the reservoir strata.

In contrast to the results illustrated in Figure 49 pertaining to heterogeneity, Figure 50 illustrates the importance of adding structural geology to the CO_2 injection simulation process. As in Figure 49, both Figure 50 images are the result of simulating the injection of CO_2 into the SGR reservoir at a rate of 1 million tonnes per year for 30 years with a 970 year shut-in. The left image in Figure 50 is the result of using the previous 10 mD to 100 mD heterogeneous permeability field

for the injection reservoir. To illustrate the significance of adding simple, yet realistic, geologic structure to the CO_2 injection simulation process, a 2% dip was added to the entire model domain. As can be seen on the right of side of Figure 50, a 2% dip has a dramatic effect on the resultant morphology of the injected CO_2 plume. Being buoyant, the injected supercritical CO_2 rises until it hits the seal, and then slowly migrates up-dip along the bottom of the seal for the entire 1,000 year simulation. This simulation demonstrates that adding structural geology to the simulation can have a dramatic (and realistic) effect on the simulation outcome, resulting in a much larger areal footprint of the injected CO_2, particularly up-dip of the injection well. However, even with the geological structure added, the CO_2 still did not migrate more than 5 km (~3.2 mi) away from the injection well. Figures 49 and 50 are both from a top view looking straight down on the simulated injection site. The CO_2 plume seen in the both figures is in the injection reservoir, and none of the CO_2 penetrated the seal for the entire simulation period (Figure 51). Figure 51 is a slice plane of saturated CO_2 directly through the center of the injection well at the end of a 1,000 year simulation.

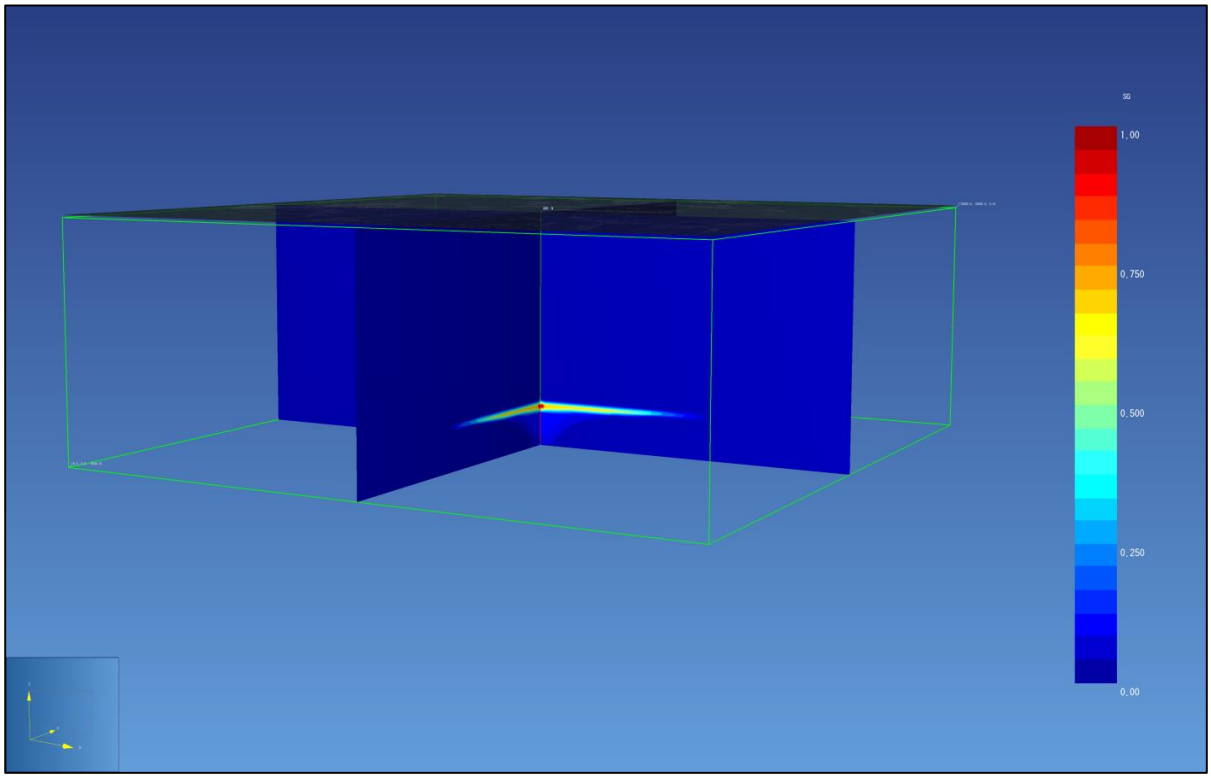

Figure 51. Results of simulation of 1 million tonnes CO_2 injection per year for 30 years after 1000 years (i.e., 970 years post injection).

Table 12. Maximum pressure at the well head as a result of CO_2 injection at a rate of 1 million tonnes per year for 30 years. Lithostatic pressure at the injection depth is ~ 65 MPa. (MPa - megaPascal).

Time Step (yrs)	Maximum Pressure (MPa)	Injection Horizon Litho-Static Pressure (MPa)
3.1688E-08	32.49	~65.00
1	32.49023	~65.00
5	32.49545322	~65.00
10	32.499372	~65.00
15	32.5013673	~65.00
20	32.61847671	~65.00
25	33.8951342	~65.00
30	34.9798193	~65.00

Time Step (yrs)	Maximum Pressure (MPa)	Injection Horizon Litho-Static Pressure (MPa)
40	34.21795855	~65.00
50	34.25720533	~65.00
60	34.18094097	~65.00
70	34.11525042	~65.00
80	34.05397069	~65.00
90	34.04202138	~65.00
100	33.98237462	~65.00
250	33.08928793	~65.00
500	32.60085565	~65.00

Using the parameters discussed above the SGR basin could easily handle the U.S. DOE minimum requirement of 30 million tonnes of CO_2. The plume footprint is minimal even with conservative estimates for porosity (6%) and permeability (10 - 100 mD) (Figure 49). At the end of the 30 year injection, the areal extent of the CO_2 footprint was <20 square km (~7.7 square mi) and the maximum migration of CO_2 away from the injection well was < 5 km (~3.2 mi) (up-dip). Further, the pressure build-up at the well-head is much less than half of the calculated lithostatic pressure, which at the injection depth is approximately 65 MPa (9,427 psi) (

Table 12). In the suitability criteria, over pressured is defined at (1) pressure that causes upward leakage of CO_2 through the caprock, and (2) injection pressure staying below the lithostatic pressure. When compared to numerical simulations of investigations from other saline basins, the plume size, pressures, and CO_2 saturation results of this SGR basin study are in range with their results (Zhuo *et al*., 2007; Yamamoto *et al*., 2009; Bacon *et al*., 2009; Sasaki *et al*., 2008; Omambia and Li, 2010).

Injection Phase Two: Injection Simulation Using Newly Acquired SGR Basin Data and a 3-D Geologic Model

Using newly acquired data, phase two of the injection simulation modeling was to create a more realistic CO_2 injection simulation model for the SGR basin. For phase two, an entire new domain was created using 1) the 3-D grid from Petrel that includes basin structure, and 2) parameterization using newly acquired SGR basin material data received from Weatherford's petro-physical analyses and the Rizer # 1 borehole geophysical logs. The 3-D grid created in Petrel has provided a more refined stratigraphic, volumetric and structural domain, including faults (Figure 52). These grid revisions along with the geologic property data provided by Weatherford® Laboratories have provided us with a working model more realistic to SGR basin conditions than the phase one modeling effort, which mostly used postulated basin data. Faults, fractures and deteriorated abandoned drill holes or wells comprise primary risk factors for leakage in engineered CO_2 injection systems (Rutqvist *et al*., 2007). Risk assessments of potential sequestration site leakage should consider faults and fracture zones to evaluate the potential for premature failure of a designed system (Deng *et al*. 2012). Faults can either serve as high permeability by-pass conduits that allow CO_2 to escape out of the target reservoir or they can act as low permeability seals that can aid in the compartmentalization of CO_2 in the target reservoir. During the phase two experiments, we estimated a permeability range from the Rizer # 1 borehole logs and used this range to investigate the impact of faults on the flow of supercritical CO_2 into the fractured diabase injection zone.

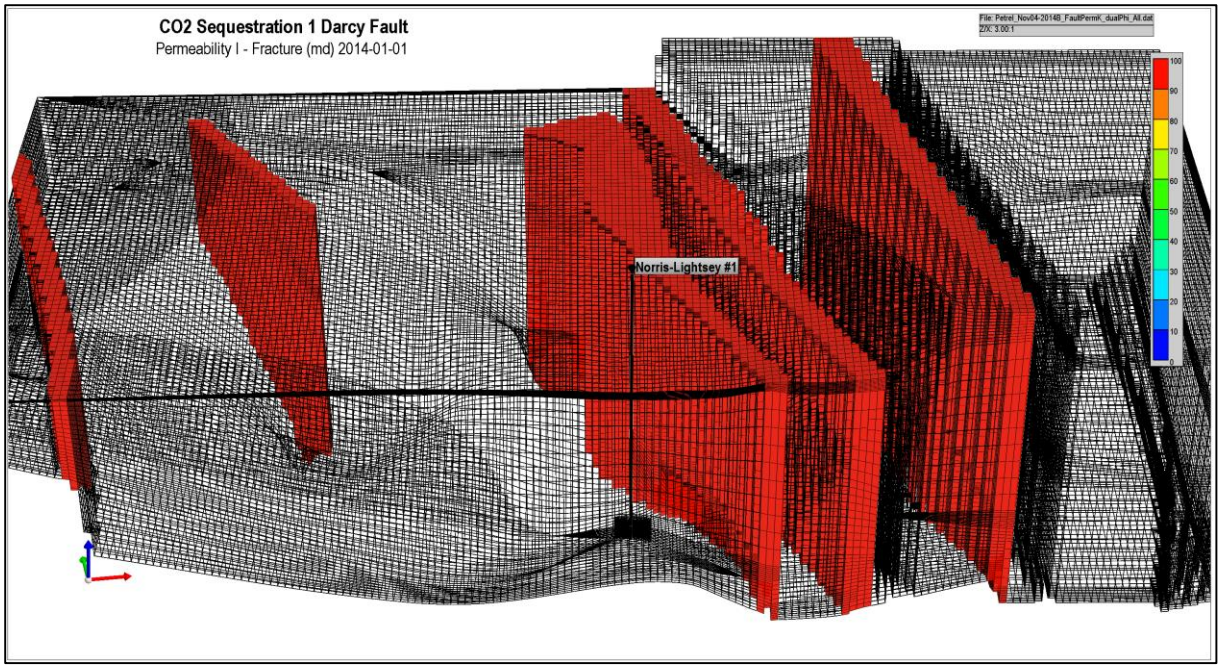

Figure 52. 3-D volume of the injection simulation model highlighting the faults.

During the second phase of project (DE-FE0001965), ~ 386 km (~240 miles) of seismic data were collected, processed and interpreted. During the third phase of the project, the characterization borehole Rizer # 1 was drilled to a depth of ~1889 m (~ 6,200 ft.). Core from this borehole were sent to Weatherford® Laboratory for petro-physical analyses. The results from the Weatherford Laboratory analyses indicates that the SGR basin was once buried up to 5 km (3.1 mi) deeper than previously known. For the reason, the postulated porosity and permeability data used in phase one of the injection simulation modeling were severely over estimated. Newly analyzed data suggest average ambient porosities for rotary and conventional core samples are 3.4% and 3.1%, respectively, and average permeability to air for rotary and conventional core samples are 0.065mD and 0.0049mD

Using these data, along with the newly acquired seismic data, a 3-D geologic model of the study area has been created using Schlumberger's Petrel. Petrel is a state-of-the-art industry grade

reservoir engineering software platform that enables collaboration of scientist and engineers to develop and contribute to a single dynamic earth model. The results of these studies have drastically changed what was once thought about the SGR basin, in particular, about the efficacy of using the Triassic sandstone horizons for permanent geologic storage. The complexity of the SGR basin structure made building the geologic model an extremely difficult and tedious task. The complexity of the structure made correlation between sandstone units almost impossible. The only units that can be mapped between the Rizer #1 borehole and the Norris Lightsey #1 borehole are the diabase intrusive units. The following horizons were mapped: base of the Coastal Plain, the top and base of diabase units C, E, and F. The results from the petrographic and core analyses ruled out using the sandstone as possible injection zones due to the aforementioned porosity and permeability values. The only possible porous zones that could be used for injection simulation are along the diabase units. These diabase are highly fractured and Rizer #1 geophysical log indicated the average porosity to be ~10% and the average permeability to be ~10mD. During the drilling of Rizer # 1, water flowed into the borehole from one of the diabase horizons which corroborates the log data.

For the phase two of the injection simulation modeling, two software packages were employed to build the dynamic simulation model. Schlumberger's Petrel platform was used to build the 3-D geologic model and resultant grid. The CO_2 injection simulation modeling was achieved using the compositional reservoir simulator CMG-GEM. GEM is the Computer Modeling Group (CMG) advanced equation-of-state compositional simulator which includes options such as CO_2, miscible gases, volatile oil, gas condensate, horizontal wells, well management, complex phase behavior among others (CMG user's guide).

Using the revised geocellular model, numerical solutions were carried out taking into consideration the injection rates described in Brantley et. al. (2014). The goal of these simulations were to (1) create a new dynamic model of the SGR basin for CO2 injection simulation and (2) test the feasibility of the SGR basin being suitable for the long term storage of .003 billion tonnes of supercritical CO2.

The model volume used in all of the phase two simulations is 178 x 142 x 50 (I by j by k cells) for a total of 1,167,563 active cells. The typical cell size was 100m x 100m, however, there was grid refinement of the injection horizon surrounding the injection well. This area was refined into 3x3x1 for a total of 2700 refined cells. The k cells were divided into 50 layers as follows (Figure 53):

Layers 1 to 10: Diabase C

Layers 11 to 20: Sandstone 1

Layers 21 to 30: Diabase E

Layers 31 to 40: Sandstone 2

Layers 41 to 50: Diabase F

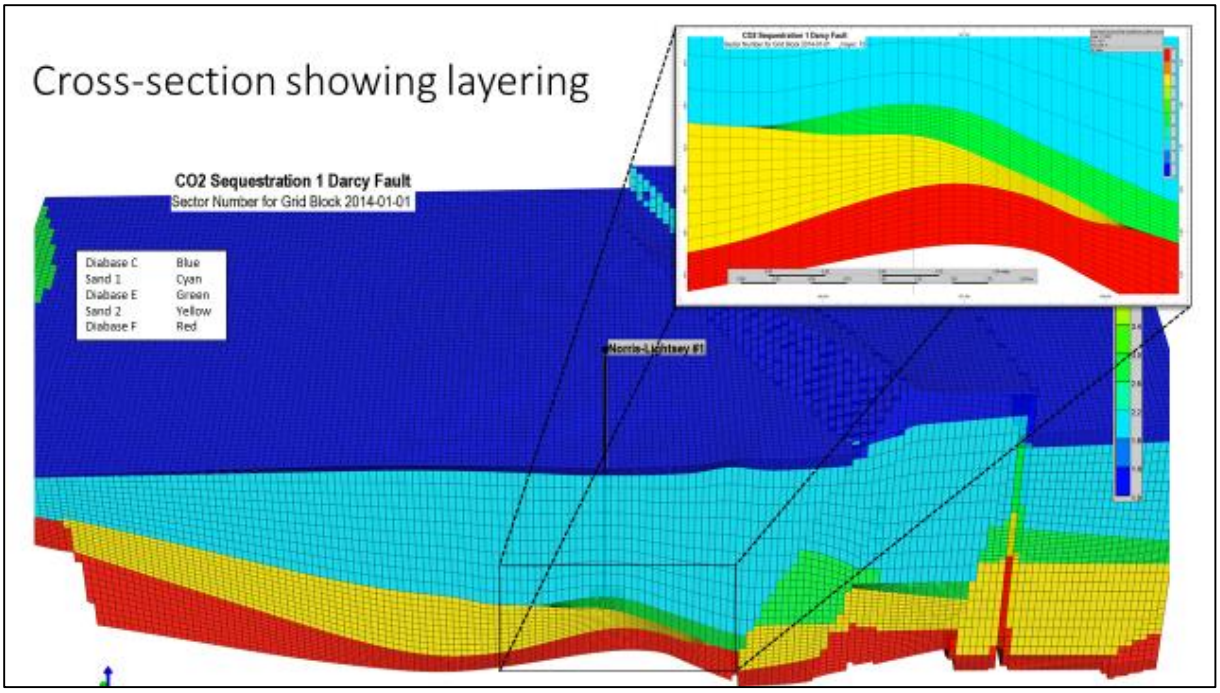

Figure 53. Cross section of the geocellular model. This image shows the layers and complexity of the geologic structure.

The horizons created in petrel were exported as zmap files and imported into CMG-GEM as isopachs. In order to maintain the grid resolution, only the horizons below the coastal plain were used in the simulation model. This included Diabase C, Sandstone1, Diabase E, Sandstone 2, and Diabase F. CO_2 was injected into Diabase E and Sandstone 1 served as the caprock seal. As with the preliminary assessment model (phase one), 30 million tonnes of CO_2 were injected at a rate of 1 million tonnes per year, which is the DOE's stated minimum capacity to be considered a viable basin for geologic storage.

Material properties were assigned based on the Weatherford Laboratory results. With the exception of the injection horizon (Diabase E), all of the diabase horizons were assigned a permeability of 10 mD and a porosity of 10%. The injection horizon was assigned permeability heterogeneity as shown in Figure 54. Diabase E permeability distribution was created from

random number generation of values between 0 and 200 mD. This range was derived due to the cracked nature of the diabase as seen in the geophysical logs taken in the Rizer # 1 well by Schlumberger. All sand horizons, now serving as caprock due to their low permeability and porosity, have a vertical and horizontal permeability of 0.0065 mD and porosity of 3.4% (Figure 55).

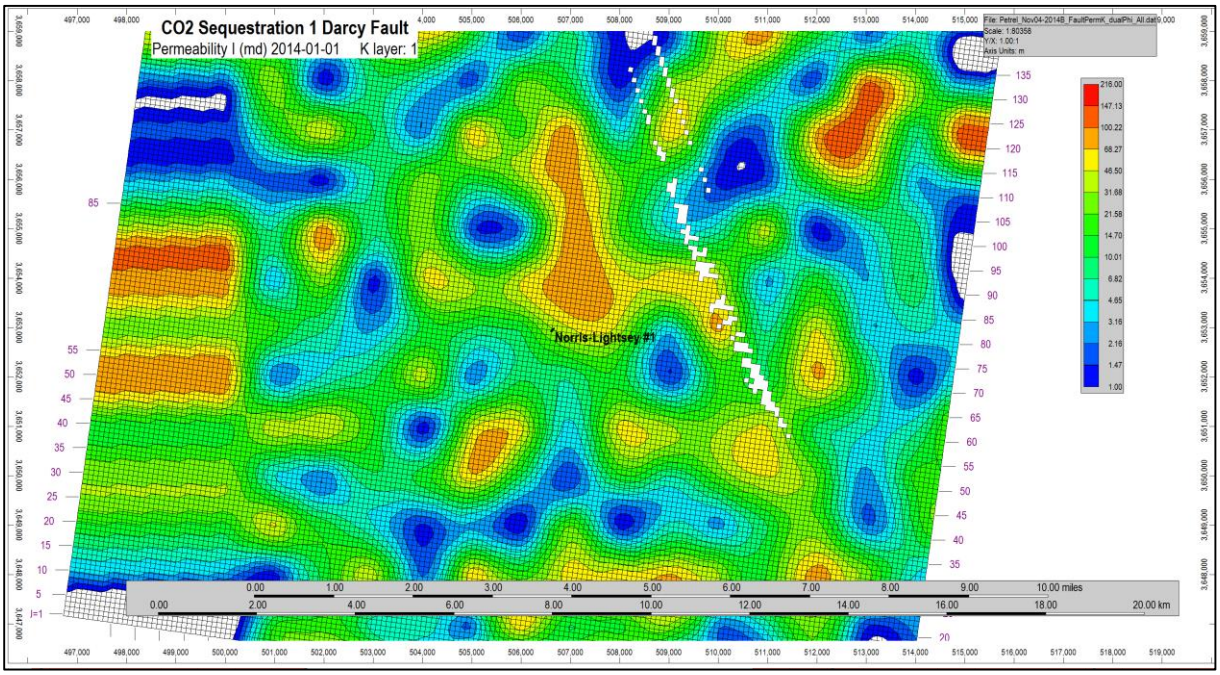

Figure 54. Diabase E permeability distribution. Created from random number generation values between 0 and 200 mD.

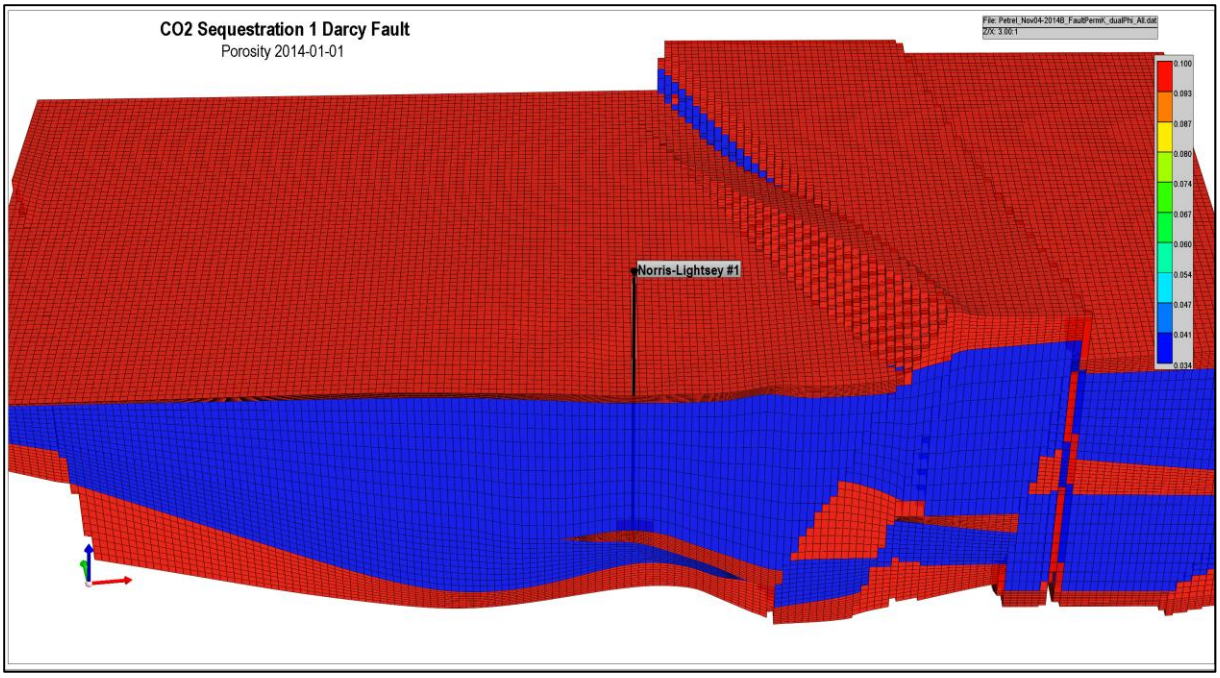

Figure 55. Simulation model porosity.

Due to the complexity of the geology, the run time for each experiment was weeks if not months for 1000 year simulations. For this reason, we chose 100 year simulations for phase two of the modeling. As with phase one, the first 30 years was CO_2 injection at a rate of 1 million tonnes per year (1.525E06 m^3 per day). However, instead of a 970 year shut-in as with phase one, there was only a 70 year shut-in with phase two. At the start of simulation 1/1/2014, all of 2014 was used as time to let them model equilibrate. Injection of 100% supercritical CO_2 then started on 1/1/2015 and continued for 30 years.

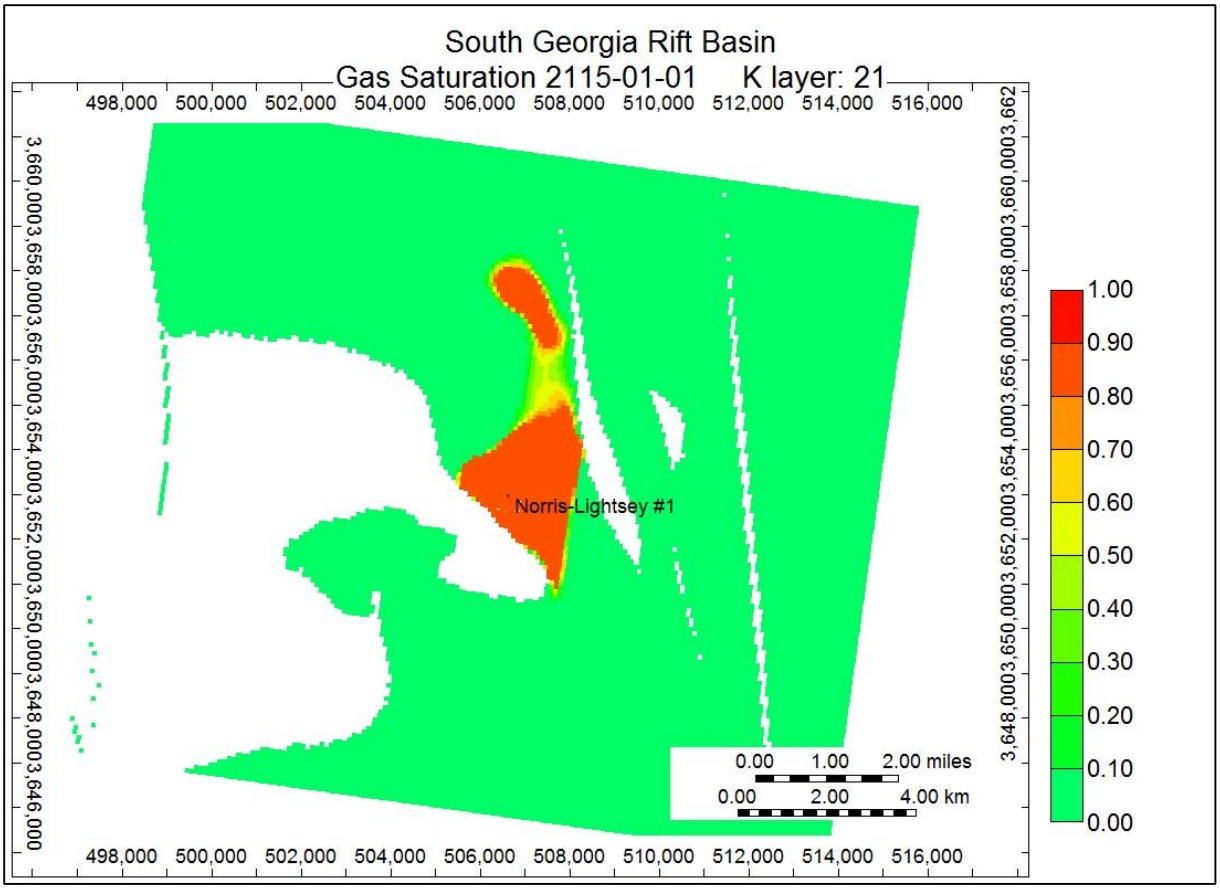

Figure 56. 2-D image of CO_2 saturation of the top layer of Diabase E showing the areal extent of the CO_2 plume as a result of 30 millions tonnes of CO_2 injected for 30 years with a 70 year shut-in. In this experiment, the faults transmissivity was 0 and all of the injected CO_2 remained in Diabase E. This image displays the faults serving as horizontal and lateral seals.

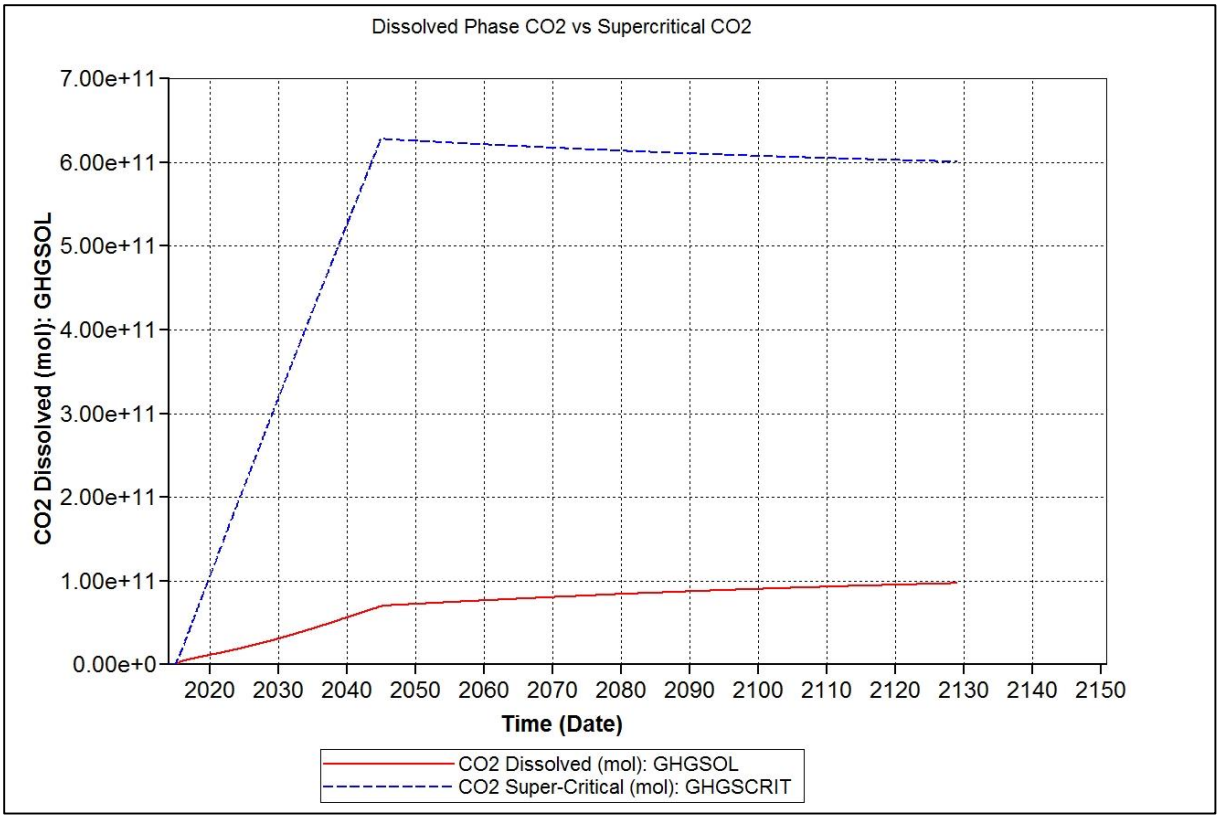

Figure 57. Plot of dissolved phase CO_2 vs supercricitical CO_2 in. In this experiment, the faults transmissivity was 0 and all of the injected CO_2 remained in Diabase E. The injection stopped and shut-in started 1/1/2045.

To examine the impact of potential fault leakage, numerous numerical simulations were conducted using different transmissivity multipliers in the fault zones identified in the 3-D geologic model. For the first experiment, a transmissivity of 0 mD was assigned to the faults. In this scenario, the fault served as a seal. As expected, the CO_2 was contained in the injection zone Diabase E and there was no CO_2 leakage or migration out of the target reservoir for the entire 100 year experiment (Figure 56). Figure 57 plots the dissolved phase CO_2 against the supercritical CO_2. The CO_2 is dissolving the fastest during the 30 year injection phase and slows as soon as the injection stops. However, CO_2 continues to dissolve for the entire 100 year experiment. This is corroborated by the supercritical CO_2 plot peaking at the end of the injection period and then trending in a steady decline as more CO_2 dissolves into the brine. For the second experiment, a

transmissivity of 1 mD was assigned to the faults. This scenario represents a leaky fault with small interconnected fractures. Figure 58 shows the top of Diabase E and the 2-D areal extent of the CO_2 plume migration at the top of the injection horizon. It closely resembles the plume extent in Figure 56, however as can be seen in Figure 59, even a permeability as low as 1 mD causes significant leakage and upward migration of CO_2 out of the target reservoir. Figure 59 is a 3-D image of the CO_2 migration over the 100 year simulation. The CO2 migrates up the faults and pools in Diabase C, which is the top of the model. For the third and last experiment, a transmissivity of 1 Darcy (1000 mD) was assigned to the faults. This experiment represents a highly fractured fault zone with a high leakage rate. Figure 60 is a 2-D image of the areal extent of the plume at the top of Diabase E. Note it has different shape than the previous experiments and has a much smaller areal footprint. This is because a large portion of the injected CO2 migrated up the faults and pooled in Diabase C, the upper most horizon of the model. Figure 61 is a 3-D image of this migration and shows the CO2 traveling up the fault and pooling in high concentrations on at the top of the model (Figure 62). It was determined that at injection depth, the lithostatic pressure ranges from ~60 – 65 MPa. The maximum injection pressure is ~31 Mpa, which is approximately half of the lithostatic pressure in the injection zone (Figure 63) thus indicating injecting activity would not induce seismicity and further fracturing. The results from these experiments stress the importance of (1) including accurate geologic structure (particularly faults) into injection simulation projects; (2) knowledge of whether the faults act as leaky conduits or seals; and (3) the importance of using correct reservoir data, in particular, porosity and permeability. The results from phase 1 suggest the SGR basin was not only suitable, but ideal for long term geologic storage of CO_2, which drastically differs from the phase two simulation results. The results from phase two of the modeling remains inconclusive due to lack accurate data on the

fault transmissivity and juxtaposition. If the faults act as seals, this portion of the SGR basin is suitable for CO_2 injection using the diabase layers as the reservoir horizons and the sedimentary sandstone layers as the seals. If the faults have even 1 mD of permeability, the seal is compromised and CO_2 will migrate upwards out of the intended reservoir and therefore deeming this portion of the SGR basin unsuitable for long term geologic storage of CO_2.

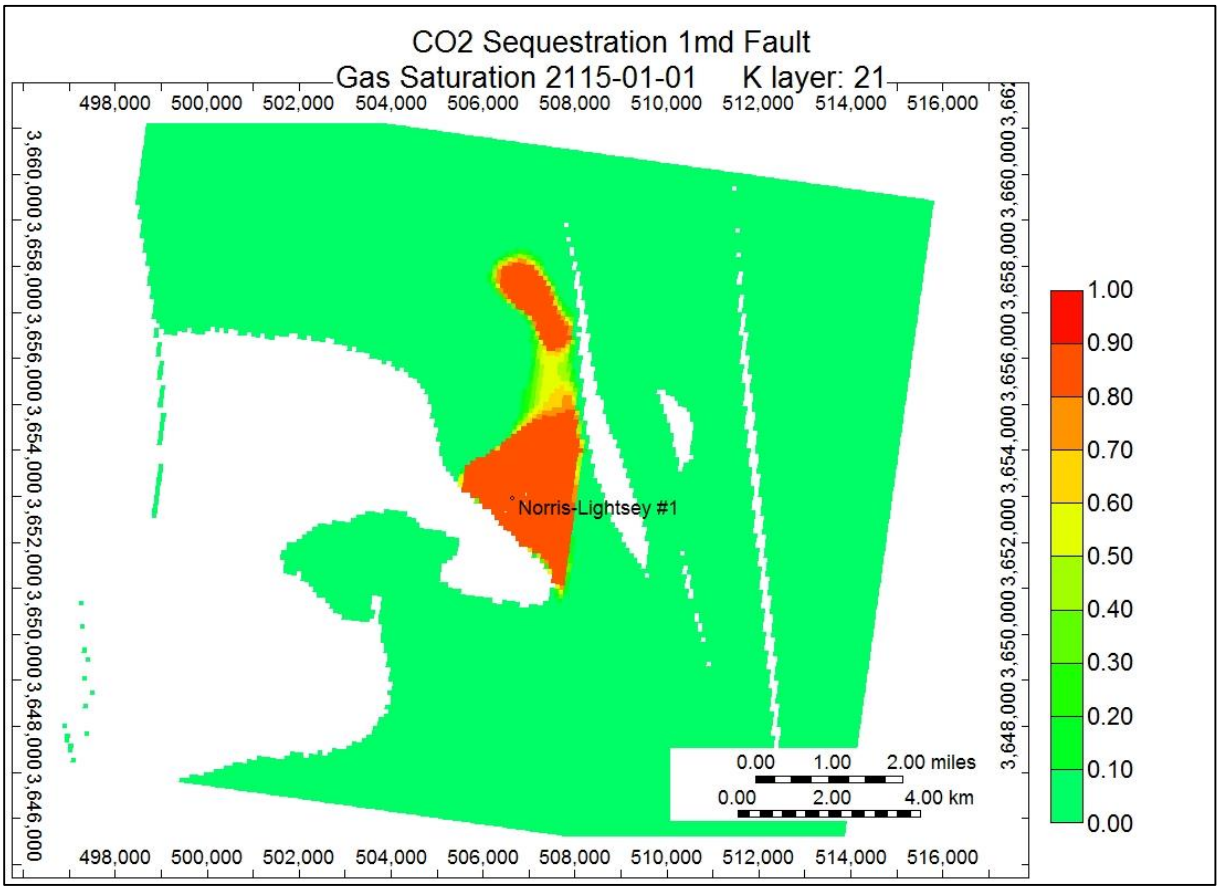

Figure 58. 2-D image of the CO_2 saturation of the top layer of Diabase E showing the areal extent of the CO_2 plume as a result of 30 millions tonnes of CO_2 injected for 30 years with a 70 year shut-in with a faults transmissivity of 1 mD.

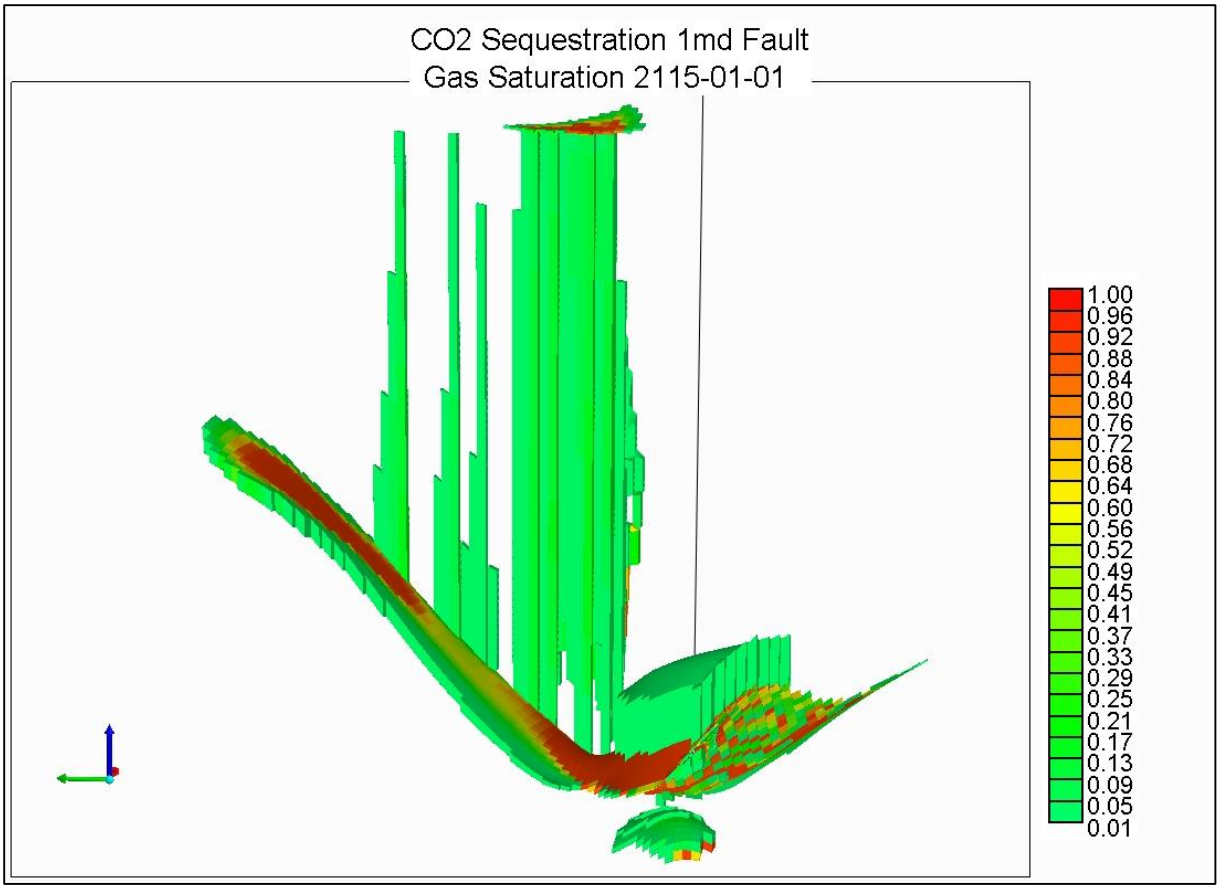

Figure 59. 3-D image of CO_2 saturation after 100 year experiment with the fault transmissivity set to 1 mD. This 3-D image displays (1) the complexity of the geology and (2) the leakeage up the faults into Diabase C, which is the top of horizon of the model.

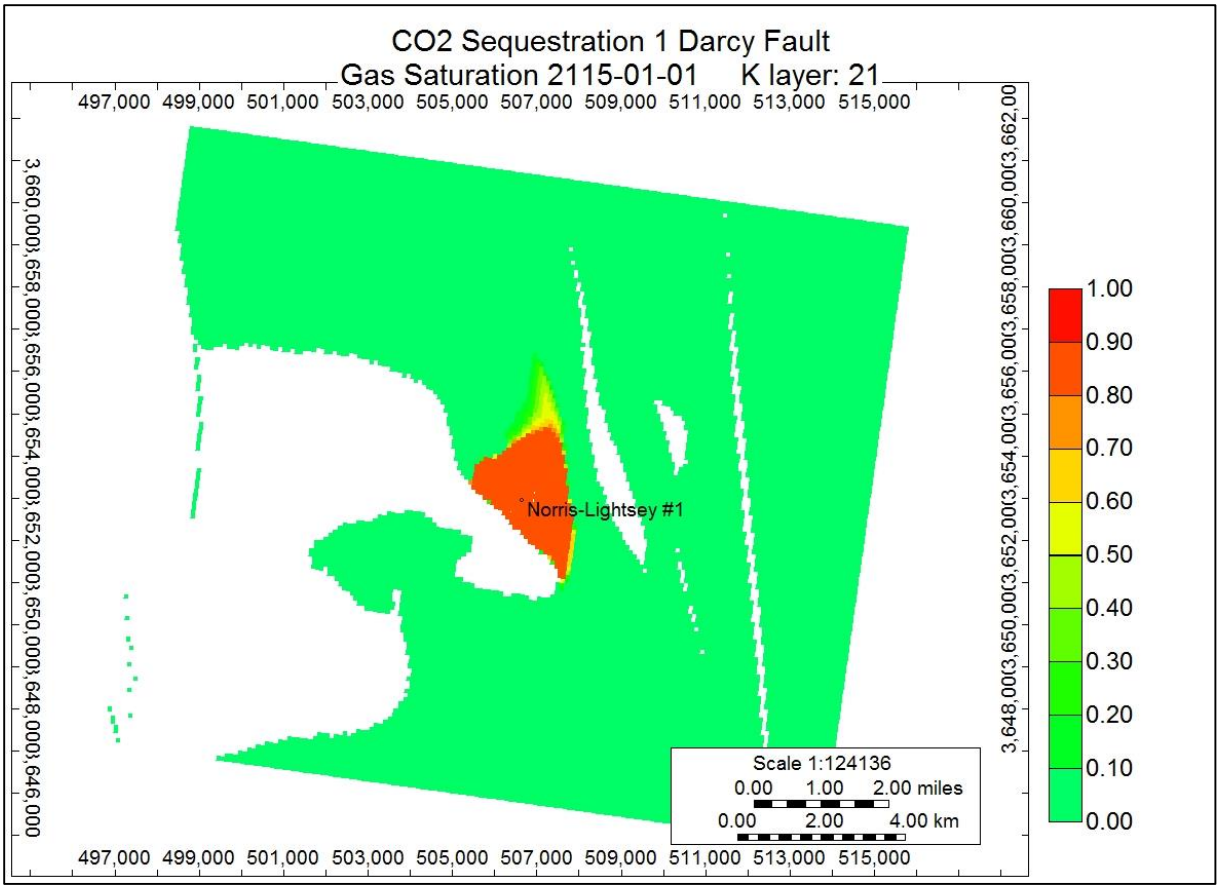

Figure 60. 2-D image of the CO_2 saturation of the top layer of Diabase E showing the areal extent of the CO_2 plume as a result of 30 millions tonnes of CO_2 injected for 30 years with a 70 year shut-in with a fault transmissivity of 1 Darcy (1000 mD). The plume is much smaller than previous experiments because a large portion of the CO_2 has migrated up through the faults into Diabase C, which is the top of the model.

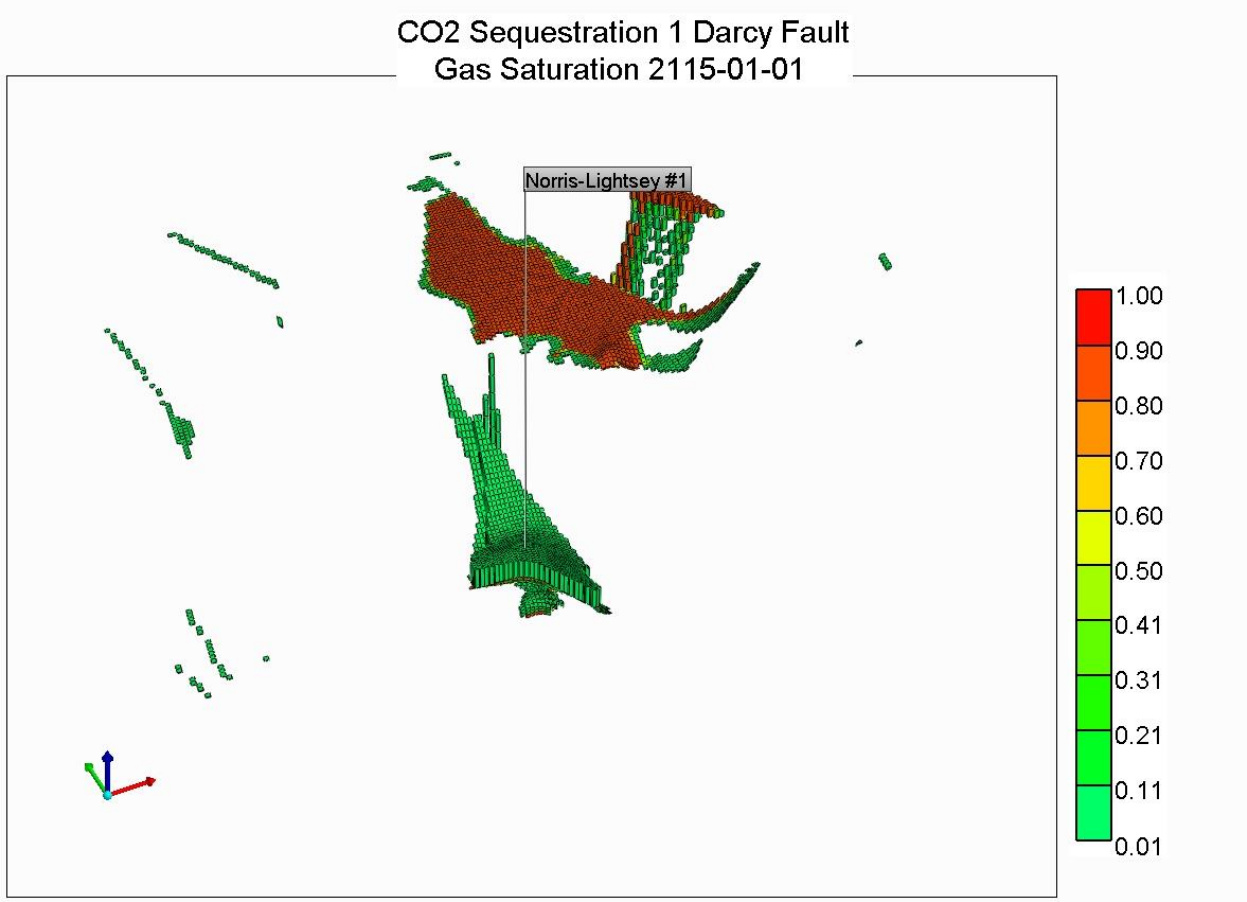

Figure 61. 3-D image of CO_2 saturation after 100 year experiment with the fault transmissivity set to 1 mD. This 3-D image displays (1) the complexity of the geology and (2) the leakeage up the faults into Diabase C, which is the top of horizon of the model. In the 100 year experiment, most of the CO_2 injected migrated up to the top of the model.

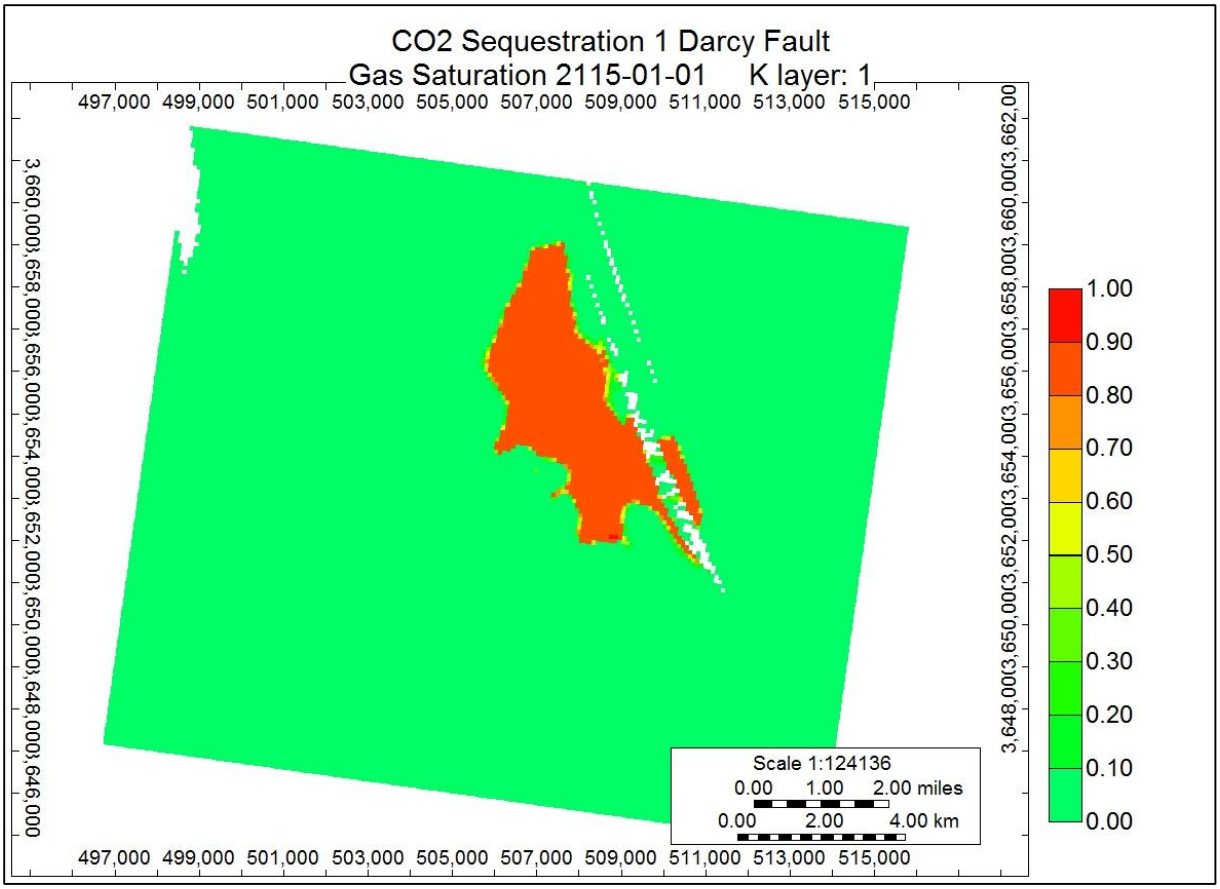

Figure 62. Pooling of the injected CO_2 at the top of Diabase C (top of the model) after a 100 year experiment with a 1 Darcy fault transmissivity assigned. A large portion of the CO_2 migrated out of the injection horizon.

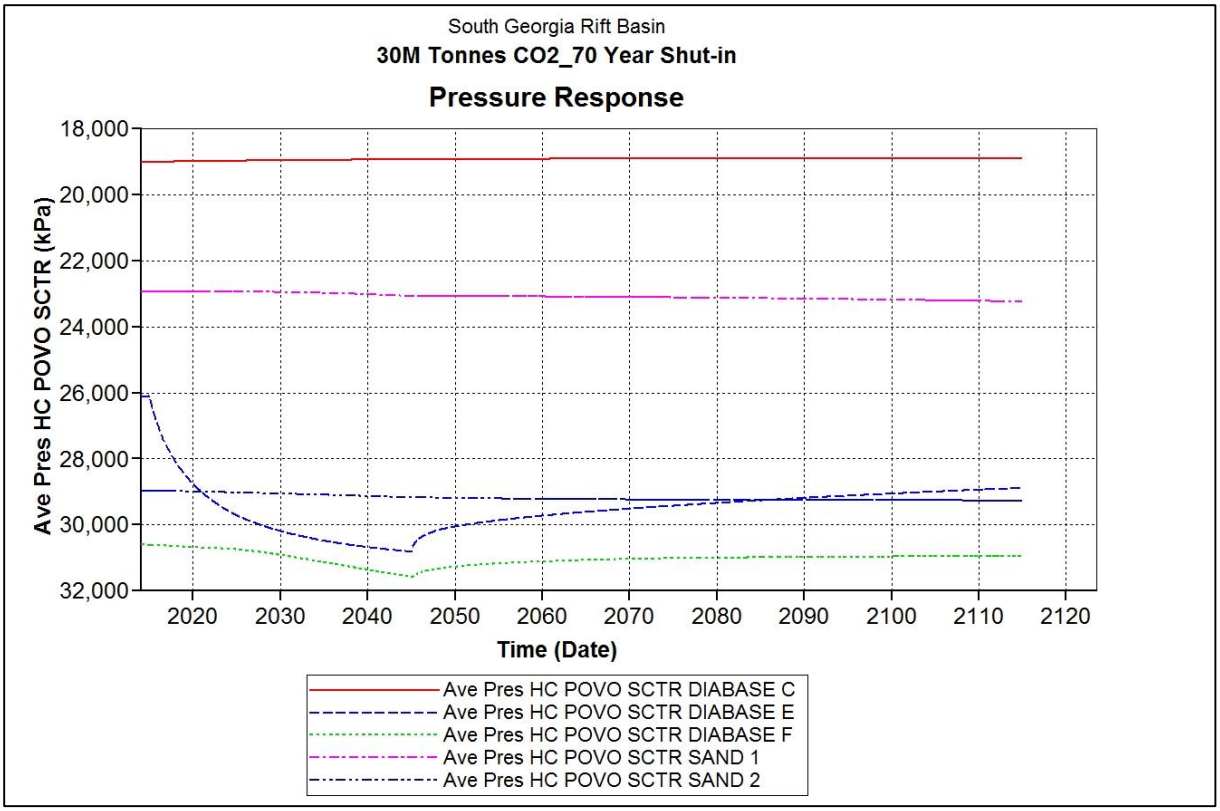

Figure 63. Plot of the basin response of each horizon at the injection well. Diabase E, the injection horizon, has the largest response. In this experiment, the faults transmissivity was 0 and all of the injected CO_2 remained in Diabase E.

Conclusions

Conclusion are: 1) the SGR basin is composed of numerous sub-basins, 2) this study only looked at portions of two sub-basins, 3) in SC, 30 million tonnes of CO_2 can be injected into the diabase units if the fracture network is continuous through the units, 4) due to the severity of the faulting there is no way of assuring the injected CO_2 will not migrate upward into the overlying Coastal Plain aquifers, 5) in Georgia there appears to porous zones in the Jurassic/Triassic sandstones, 6) as in SC there is faulting in the sub-basin and the seismic suggest the faulting extends upward into the Coastal Plain making that area not suitable for CO_2 sequestration, 7) the complex faulting observed at both study areas appear to be associated with transfer fault zones (Heffner 2013), 8) if sub-basins in the Georgia portion of the SGR basin can be located that are far

away from the transfer fault zones there is a strong possibility of sequestering CO_2 in these areas, and 9) the SGR basin covers area in three states and this project only studied two small areas so there is enormous potential for CO_2 sequestration in other portions the basin and further research needs to be done to find these areas.

References

Bachu, S., 2000, Sequestration of CO2 in geological media in response to climate chang: road map for site selection using the transform of geological space into the CO2 phase space: Energy Conversion and Management, v. 43, p. 87-102.

Bachu, S., and B. Bennion, 2008, Effects of in-situ conditions on relative permeability characteristics of CO2-brine systems: Environmental Geology, v. 54, p. 1707-1722.

Bacon, D.H., M. D. White, N. Gupta, J. R. Sminchak, and M. E. Kelley, 2009, CO2 sequestration potential in the Rose Run Formation at the Mountaineer Power Plant, New Haven, West Virginia, in M. Grobe, J. C. Pashin, and R. L. Dodge, eds., Carbon dioxide sequestration in geological media—State of the science: AAPG Studies in Geology 59, p. 553–570.

Behrendt, J.C., Hamilton, R.M., Ackermann, H.D., and Henry, V.J., 1981, Cenozoic faulting in the vicinity of the Charleston, South Carolina, 1886 earthquake: Geology, v. 9, p 117-122.

Behtham, M., and G. Kirby, 2005, CO2 Storage in Saline Aquifers: Oil & Gas and Technology - Rev. IFP, v. 60, no. 3, p. 559-567.

Benson, R.N., 2003. Age estimates of the seaward-dipping volcanic wedge, earliest oceanic crust, and earliest drift-stage sediments along the North Atlantic continental margin. In: Hanes, W.E., McHone, J.G., Renne, P.R., Ruppel, C. (Eds.), The Central Atlantic Magmatic Province, Insights from Fragments of Pangea, Geophysical Monograph, vol. 136. American Geophysical Union, Washington, D.C., pp. 61–75.

Boden, T.A., D.P. Kaiser, R.J. Sepanski, and F.W. Stoss, 1994, Trends '93: A compendium of Data on Global Climate. Oak Ridge, Tennessee 37831: Oak Ridge National Laboratory - Sponsored by DOE - Environmental Sciences Division.

Boldreel, L.O., and Andersen, M.S., 1993, Late Paleocene to Miocene compression in the Faero-Rockall area, in Parker, J.R. (ed.), Petroleum Geology of Northwest Europe: Geological Society of London, pp 1025-1034.

Bott, M.H.P., 1992, The stress regime associated with continental break-up, *in* Storey, B.C., Alabaster, T., and Pankhurst, R.J., eds., Magmatism and the causes of continental break-up: Geological Society Special Publication, 68, p 125-136.

Boxiao, L., H.A. Tchelepi, and S.M. Benson, 2012, The Influence of Capillary Pressure Entry Pressure Representation on the Rate of CO2 solubility Trapping: Proceedings, TOUGH Symposium; September 17-19, 2012. Berkeley, California: Lawrence Berkeley National Laboratory, 1-8.

Brantley, D.T., Shafer, J.M, and V. Lakshmi, 2015, CO2 Injection Simulation into the South Georgia Rift Basin for Geologic Storage: A Preliminary Assessment, *Environmental Geosciences* (in press).

Canadell, J.G., C. Le Quere, and M.R. Raupach, 2007, Contributions to accelerating atmospheric CO2 growth from economic activity, carbon intensity, and efficiency of natural sinks: Proceedings of the National Academy of Sciences, U.S.A, v. 104, no. 47, 18866-70.

Clendenin, C.W., 2013. Insights into mode of the South Georgia rift extension in eastern Georgia, USA. Tectonophysics 608, p 613-621.

Colquhoun, D. J., Woollen, L. D., Van Nienwenhuise, D. S., Padgett, G. G., Oldham, R. W., Boylan, D. C., Bishop, J. W., and Howell, P. D., 1983, Surface and subsurface stratigraphy, structure and aquifers of the South Carolina Coastal Plain: Columbia, SC, State of South Carolina, Office of the Governor, 78 p.

Comisky, J.T., K.E. Newsham, and J.A. Rushing, and T.A. Blasingame, 2007. A Comparative Study of Capillary-Pressure-Based Empirical Models for Estimating Absolute Permeability in Tight Gas Sands: SPE 110050; 2007 SPE Annual Technical Conference and Exhibition: SPE, Texas A&M University, p. 1-18.

Costain, J.K., and Coruh, C., 1989, Tectonic setting of Triassic half-grabens in the Appalachians: seismic data acquisition, processing, and results, *in* Tankard, A.J., and Balkwill, H.R., eds., Extensional tectonic and stratigraphy of the North Atlantic margins: AAPG Memoir 46, p 155-174.

Damsleth, E., 1994, Mixed Reservoir Characterization Methods. Proceedings from the Centennial Petroleum Engineering Symposium, Tulsa, Oklahoma.

Daniels, D.L., I. Zietz, and P. Popenoe, 1983, Distribution of subsurface lower Mesozoic rocks in the southeastern United States as interpreted from regional aeromagnetic and gravity maps, in Gohn, G.S., ed., Studies Related to the Charleston, South Carolina Earthquake of 1886-Tectonics and Seismicity: United States Geological Survey Professional Paper 1313, p. K1-K24.

Deng H, Stauffer PH, Dai Z, Jiao Z, Surdam RC (2012) Simulation of industrial-scale CO2 storage: multi-scale heterogeneity and its impacts on storage capacity, injectivity and leakage. International Journal of Greenhouse Gas Control, 10, p. 397–418.

Dewey, J.F., 1988, Lithospheric stress, deformation, and tectonic cycles: the disruption of Pangaea and the closure of the Tethys, in Audley-Charles, M.G., and Hallam, A., eds., Gondwana and Tethys: Geological Society Special Publicaton 37, p. 23-40.

Doyen, P.M, 2007, Seismic Reservoir Characterization: An Earth Modelling Perspective: Houten, The Netherlands, European Association of Geoscientist and Engineers, p. 255.

Duan Z, Sun R (2003) An improved model calculating CO2 solubility in pure water and aqueous NaCl solutions from 273 to 533 K and from 0 to 2000 bar. Chemical Geology, 193, p. 257–71.

Duan Z, Sun R, Zhu C, Zhou I-M (2006) An improved model for the calculation of CO2 solubility in aqueous solution containing Na+, K+, Ca2+, Mg2+, Cl _ , and SO4 2_. Marine Chemistry, 98, p.131–9.

Foster, D.G., Robinson, A.G., 1993. Geological history of the Flemish Pass basin, offshore Newfoundland. AAPG Bull. V. 77, p. 588–609.

Gohn, G.S., ed., 1983, Studies related to the Charleston, South Carolina earthquake of 1886-Tectonics and Seismicity: U.S. Geological Survey Professional Paper 1313, p. 375.

Ghomian, Y., G.A. Pope, and K. Sepehrnoori, 2008, Reservoir Simulation of CO2 Sequestration Pilot in Frio Brine Formation, USA Gulf Coast: Energy, v. 33, p. 1055-1067.

Hamilton, R.M., Behrendt, J.C., and Ackermann, H.D., 1983, Land multichannel seismic-reflection evidence for tectonic features near Charleston, South Carolina, in Gohn, G.S., ed., Studies related to the Charleston, South Carolina, earthquake of 1886-tectonics and seismicity: Geological Survey Professional Paper 1313, p. 11-118.

Heffner, D.M., Knapp, J.H., Akintunde, O.M., and Knapp, C.C. 2011. Preserved extent of Jurassic flood basalt in the South Georgia Rift: A new interpretation of the J horizon. Geology Vol. 40 Issue 2, p. 167

Hefner, D.M., 2013, Tectonics of the South Georgia Rift, Doctoral dissertation, University of South Carolina, Columbia, SC, p. 178.

Hiatt, E.E., Kyser, T.K., Fayek, M., Polito, P., G.J., Holk, and Riciputi, L.R., 2007, Early quartz cements and evolution of paleohydraulic properties of basal sandstones in three paleoproterozoic continental basins: Evidence from *in situ* δ^{18} O analysis of quartz cements: Chemical Geology, v. 238, p. 19-37.

Hollon, B., Mainali, P, Dix, M., Fu, R., Houghton, N., and Waddell, M. 2014. Whole Rock Bulk Geochemistry in Evaluating a CO2 Injection Well. Proceedings from the AAPG Annual Convention and Exhibit 2014, Houston, TX.

Houghton, J., 1997, Global Warming: The Complete Briefing, 2nd ed.: Cambridge University Press, p. 267.

Hutchinson, D.R., and Klitgord, K.D., 1988, Evolution of rift basins on the continental margin off southern New England, *in* Manspeizer, W., ed., Triassic-Jurassic rifting, continental breakup and the origin of the Atlantic Ocean passive margins, part A: New York, Elsevier, p. 81-98.

International Panel on Climate Change, 2007, Climate Change 2007: The physical science bases: Summary for policy makers: IPCC 2007a, Geneva, Switzerland: IPCC Secretariat.

International Panel on Climate Change, 2007, Climate Change 2007: Climate change impacts, adaptation and vulnerability: IPCC 2007b, Geneva, Switzerland: IPCC Secretariat.

Keeling, C.D., and T.P. Whorf, 2004, Atmospheric CO2 from Continious Air Samples At Mauna Loa Observatory, Hawaee, U.S.A.: Oak Ridge, Tenn. U.S.A., Carbon Dioxide Information Center, Oak Ridge National Laboratory.

Kempka, T. and M. Kuhn. 2013. Numercal Simulations of CO2 arrival times and reservoir pressure coincide with observations from the Ketzin pilot site, Germany. Environmental Earth Science 70(8), p. 3675-3685.

King, P.B., 1971, Systematic pattern of Triassic dikes in the Appalachian region-second report: U.S. Geological Survey Professional Paper 750-D, p. D84-D88.

Klitgord, K.D., P. Popenoe, and H. Schouten, 1984, Florida: A Jurrasic transform plate boundary: Journal of Geophysical Research, v. 89, p. 7753-7772

Manspeizeer, W., and Cousminer, H.L., 1988, Late Triassic-Early Jurassic synrift basins of the U.S. Atlanitc margin, in Sheridan, R.E., and Grow, J.A., eds., The geology of North America, v I-2, the Atlantic continental margin, U.S.: Geological Society of America, p. 197-216.

Mercer, J.W., and R. F. Faust, 1981, Ground-Water Modeling: P.O. Box 2550, Reston VA 22090, GeoTrans, Inc., National Water Well Association.

McBride, 1991, Constraints on the structure and tectonic development of the Early Mesozoic South Georgia Rift, southeastern United States; Seismic Reflection Data Processing and Interpretation: Tectonics, v. 10, no. 5, p. 1065-1083.

Micheal, K., A. Golab, V. Shulakova, J. Ennis-King, G. Allinson, S. Sharma, and T. Aiken, 2010, Geological Storage of CO2 in saline aquifers - A review of the experienece from exiting storage operations: International Journal of Greenhouse Gas Control, v. 4, p. 659-667.

McBride, E.F., Diggs, T.N., and Wilson, J.C., 1991, Compaction of Wilcox and Carrizo Sandstones (Paleocene-Eocene) to 4420 M, Texas Gulf Coast: Journal of Sedimentary Petrology, v. 61, p. 73-85.

McBride, J.H., Nelson, K.D., Brown, L.D., 1989, Evidence and implications of an extensive early Mesozoic rift basin and basalt/diabase sequence beneath the southeast Coastal Plain: Geological Society of America Bulletin, v 101, p. 512-520

McHone, J.G., 1996, Broad-terrane Jurassic flood basalts across northeastern North America: Geology, v 24, p. 319-322.

McHone, J.G., 2000. Non-plume magmatism and rifting during the opening of the central Atlantic Ocean. Tectonophysics 316, p. 287–296.

McHone, J.G., Anderson, D.L., Fialko, Y.A., 2004. Giant Dikes: Patterns and Plate Tectonics.http://www.mantleplumes.org/.

Mohammed, A., Ekoja, G.A., Adeniyi, A.A., Hassan, A.B. 2012. Modelling Long Term CO2 Storage in Saline Aquifers. International Journal of Applied Science and Technology. Vol. 2 No. 10. p. 5362.

Mukhopadhyay, S., Doughty, C., Bacon, D., Bacci, G., Govindan, R., Shi, J., Gasda, S., Ramanathan, Nicot, J-P., Hosseini, S., Birkholzer, J.T. 2012. Preliminary Model-Comparison.

Neftel, A., H. Friedli, E. Moor, H. Lotscher, H. Oeschger, U. Siegenthaler, and B. Stauffer, 1994, Historical CO2 record from the Siple Station ice core, In Trends: A Compendium of Data on Climate Change: Oak Ridge, Tenn. U.S.A., Oak Ridge National Laboratory, U.S. Department of Energy - Carbon Dioxide Information Analysis Center.

Nelson, P.H., and J.E. Kibler, 2003, A Catalog of Porosity and Permeability from Core Plugs in Siliciclastic Rocks, U.S.G.S. open file report 03-420: Denver, CO, Department of the Interior.

Oh, J., Austin, J.A., Phillips, J.D., Coffin, M.F., Stoffa, P.L., 1995. Seaward-dipping reflectors offshore the southeastern United States: Seismic evidence for extensive volcanism accompanying sequential formation of the Carolina trough and Blake Plateau basin. Geology 23, 9–12. Olsen, P.E., 1997, Stratigraphic record of the early Mesozoic breakup of Pangea in the Laurasia-Gondwana rift system: Annual Reviews of Earth and Planetary Science, v 25, p. 337-401.

Olsen, P.E., Schische, R.W., and Gore, P.J.W. (Eds.), 1989, Tectonic, depositional, and palaoecological history of early Mesozoic rift basins, eastern North America: International Geological Congress Field Trip T351: American Geophyscial Union, Washington, D.C., p. 174.

Olsen, P.E., Schische, R.W., and Fedosh, M.S., 1996, 580 kyr duration of the Early Jurassic flood basalt event in eastern North America estimated using Milankovitch cyclostratigraphy, in Morales, M. (ed.), The Continental Jurassic: Museum of Northern Arizona Bulletin, v 60, p. 11-22.

Olsen, P.E., and Kent, D.V., 2000, High resolution early Mesozoic Pangean climatic transect in lacustrine environments, *in* Bachmann, G., and Lerche, I.(eds.), Epicontinental Triassic: Zentrablatt fur Geologie und Palaontologie, v 3, VIII, p. 1475-1496.

Olsen, P.E., 1997, Stratigraphic record fo the early Mesozoic breakup of Pangea in the Laurasia-Gondwana rift system: Annual Review of Earth and Planetary Sciences, v. 25, p. 337-401.

Omambia, A.N., and Y. Li, 2010, Numeric modeling of carbon dioxide sequestration in deep saline aquifers in Wangchang Oilfield-Jianghan Basin, China: Journal of American Science, v. 6, p. 178-187.

Pruess, K., and N. Spycher, 2006, ECO2N - A New TOUGH2 Fluid Property Module for Studies of CO2 Storage in Saline Aquifers: University of California, Berkeley, CA 64720, Lawrence Berkeley National Laboratory - Earth Sciences Division.

Pettijohn, F. J., Potter, P. E., and Siever, R., 1973, Sand and Sandstones: Springer- Verlag; New York, Heidelberg, Berlin, Heidelberg, London, Paris, Tokyo, p. 618.

Ragland, P.C., Cummins, L.E., and Arthur, J.D., 1992, Compositional patterns for early Mesozoic diabases from South Carolina to central Virginia, in: Puffer, J.H., and Ragland, P.C., eds., Eastern North American Mesozoic Magmatism: Geological Society of America Special Paper, v. 268, p. 301-331.

Rankin, D.W., 1977. ed., 1983, Studies related to the Charleston, South Carolina earthquake of 1886-A Preliminary Report: U.S. Geological Survey Professional Paper 1028, p. 276.

Rankin, D.W., 1994, Continental margin of the eastern United States: past and present. In: Speed, R.C. (Ed.), Phanerozoic Evolution of North American Continent-Ocean Transitions, Geological Society of America, DNAG Continent-Ocean Transect Volume, p. 129–218.

Ryan, M.P., D.M. Stuphin, D.L. Daniels, H.A. Pierce, and J.P. Smoot, 2002, Three Dimensional Compartmentalization on Subsurface Ground Water Flow in Eastern North American Mesozoic Basins: American Geophysical Union, Spring Meeting: Washington, DC, AGU, Abstract # H22C-09.

Sasaki, K., T. Fujii, Y. Niibori, T. Ito, and T. Hashida, 2008, Numerical simulation of supercritical CO2 injection into subsurface rock masses: Energy Conversion & Management, v. 49, p. 54-61.

Solomon, S., G.K. Plattner, R. Knutti, and P. Friedlingstein, 2009, Irreversible climate change due to carbon dioxide emissions: Proceedings of the National Academy of Science U.S.A, v. 106, no. 6, p. 1704-9.

Schlische, R.W., Withjack, M.O., and Olsen, P.E., 2003, Relative timing of CAMP, rifting, continental breakup, and basin inversion: tectonic significance, in Hanes, W.E., McHone, J.G., Renne, P.R., and Ruppel, C. (eds.), The Central Atlantic Magmatic Province, insights from fragments of Pangea, Geophysical Monograph, v. 136: Washington, D.C., American Geophysical Union, p. 33-60.

Shafer, J.M., and D.T. Brantley, 2011, Characterizing a Geologic Formation: Chemical Engineering Progress, p. 50-52.

Tseng, Hsin-Yi, Onstott, T.C., Burruss, R.C., and Miller, D.S., 1996, Constraints on the thermal history of Taylorsville Basin, Virginia, U.S.A., from fluid-inclusion and fission-track analyses: implications for subsurface geomicrobiology experiments: chemical Geology, v. 127, p. 297-311.

United States Department of Energy, 2006, 2008, 2010, Carbon Sequestration Atlas of the United States and Canada. Pittsburg, PA, National Energy and Technology Laboratory.

Vargaftik, N.B., 1975, Tables on the Thermophysical Properties of Liquids and Gases, 2nd Ed: New York, John Wiley & Sons.

Venkatakrishnan, R., and Lutz, R., 1988, A kinematic model for the evolution of the Richmond basin, in Manspeizeer, W. (ed.), Triassic-jurassic Rifting, Continental Breakup and the Origin of the Atlantic Ocean Passive Margins, Part A: New York, Elsevier, p. 445-462.

Vleit, J. van, R. White,and S. Dragicevic, 2009, Modeling urban growth using a variable grid cellular automaton: Computer, Environment and Urban Systems, v. 33, no. 1, p. 35-43.

Welsink, H.J., Dwyer, J.D., Knight, R.J., 1989. Tectono-stratigraphy of the passivemargin off Nova Scotia. In: Tankard, A.J., Balkwill, H.R. (Eds.), Extensional Tectonics and Stratigraphy of the North Atlantic Margins, American Association of Petroleum Geologists Memoir, vol. 46, p. 215–231.

Wilson, J.C. and McBride, E.F., 1988, Compaction and Porosity evolution of Pliocene sandstones, Ventura Basin, California: American Association of Petroleum Geologists Bulletin, v. 72, p. 664-681.

Withjack, M. O., Olsen, P. E., and Schlische, R.W., 1995, Tectonic evolution of the Fundy rift basin, Cana: evidence of extensions and shortening during passive margin development: Tectonics, v. 14, p. 390-405.

Withjack, M.O., Schlische, R.W., and Olsen, P.E., 1998, Diachronous rifting, drifting, and inversion on the passive margin of central eastern North America: An analog for other passive margins: AAPG Bulletin, v. 82, p. 817-835.

Withjack, M. O., Schlische, R.W., and Olsen, P. E., 2012, Development of the passive margin of eastern North America: Mesozoic rifting, igneous activity, and breakup. In: Bally, A. W. & Roberts, D. G. (eds), Principles of Phanerozoic Regional Geology, v. 1, Elsevier, Amsterdam, p. 301–335.

Yamamoto, H., K. Zhang, K. Karasaki, A. Marui, H. Uehara, and N. Nishikawa, 2009, Numerical investigation concerning the impact of CO2 geologic storage on regional groundwater flow: International Journal of Greenhouse Gas Control, v. 3, p. 586-599.

Zhuo, Q., J.T. Birkholzer, J. Rutqvist, and C.F. Tsang, 2007, Sensitivity Study of CO2 Storage Capacity in Brine Aquifers with Closed Boundaries: Dependence on Hydrogeological Properties: Sixth Annual Conference on Carbon Capture and Sequestration; University of California, Berkeley, Berkeley CA 64720, DOE-NETL Earth Sciences Division, Lawrence Berkeley National Laboratory.

List of acronyms and abbreviations

M - Meters

Pa - Pascal;

C – Celsius

KB - Kelly Bushing

mD - milliDarcy

ms - milliseconds

SGR – South Georgia Rift

SGRB – South Georgia Rift Basin

S_{gr} - residual gas saturation

S_{lr} - residual liguid saturation

P_o - capilary pressure

λ - pore distribution parameter

Appendix 1: Weatherford Laboratories Full Report

-FINAL REPORT- GEOLOGIC CHARACTERIZATION OF A PORTION OF THE SOUTH GEORGIA RIFT BASIN FOR SOURCE PROXIMAL CO_2 STORAGE BASED ON ANALYSIS OF SAMPLES FROM RIZER #1 TEST BOREHOLE, COLLETON COUNTY, SC AND USGS CLUBHOUSE CROSSROADS TEST HOLE NO. 3, DORCHESTER COUNTY, SC

WEATHERFORD LABS JOB NUMBERS: HH-57745 & HH-59364

Weatherford®
LABORATORIES

Weatherford LABORATORIES

(832) 375-6800
5200 N Sam Houston Parkway W, Suite 500 • Houston, Texas 77064

June 25, 2014

Michael Waddell
Earth Sciences and Resources Institute
University of South Carolina
1233 Washington St.
Suite 300
Columbia, SC 29208

SUBJECT: *Final Report* - Geologic Characterization of a Portion of the South Georgia Rift Basin for Source Proximal CO_2 Storage based on Analysis of Samples from Rizer #1 Test Borehole, Colleton County, SC and USGS Clubhouse Crossroads Test Hole No. 3, Dorchester County, SC WFT Labs Files: HH-57745 and HH-59364

Dear Mr. Waddell:

This report presents and summarizes the results of the examination of core and cutting samples from the Rizer #1 test borehole. Rizer #1 was drilled in Colleton County, SC in the spring of 2012. Since no conventional core of caprock was obtained from Rizer #1 for the contracted mechanical and other physical property tests, it was decided to obtain portions of conventional core from the nearby USGS Clubhouse Crossroads Test Hole No. 3 from Dorchester County, SC. This report describes results of phase 3 of a larger study, *Geologic Characterization of the South Georgia Rift Basin for Source Proximal CO_2 Storage* funded by the U.S. Department of Energy's National Energy Technology Laboratory (DOE NETL). Original objectives of phase 3**,** which were to create an accurate model to predict long-term CO_2 storage capacity of the Jurassic to Late Triassic aged strata within the South Georgia Rift Basin, had to be modified because of operational issues and geology of the study interval. After it was determined that the poor reservoir quality of the recovered interval did not allow further physical and geochemical testing, efforts were diverted to determination of the factors which resulted in the destruction of porosity and permeability within the proposed CO_2 sequestration interval.

This report is divided into five sections: 1. Introduction; 2. Petrologic Results; 3. Diagenetic Study; 4. Elemental Analyses; 5. Caprock and CO_2 Storage Assessment; 6. Appendices. This report includes five (5) USB flash drives with a digital version of report and all data generated for the geologic characterization portion of this study.

Thank you for the opportunity to participate in this study with your institute. Please feel free to contact us if you have any questions concerning this report or if we can be of further service.

Sincerely,
Weatherford Laboratories

Keith E. Goggin, R.P.G.
Sedimentology Manager

James M. Rine, Ph.D.
Principal Geologist / Geologic Advisor

EXECUTIVE SUMMARY: ***Final Report*** **- Geologic Characterization of a Portion of the South Georgia Rift Basin for Source Proximal CO_2 Storage based on Analysis of Samples from Rizer #1 Test Borehole, Colleton County, SC and USGS Clubhouse Crossroads Test Hole No. 3, Dorchester County, SC**

This report presents and summarizes the results of the examination of core and cutting samples from Rizer #1 test borehole. Rizer #1 was drilled in Colleton County, SC in the spring of 2012. Since no conventional core of caprock was obtained from Rizer #1 for the contracted mechanical and other physical property tests, it was decided to obtain portions of conventional core from the nearby USGS Clubhouse Crossroads Test Hole No. 3 from Dorchester County, SC. This report describes the results of phase 3 of a larger study, *Geologic Characterization of the South Georgia Rift Basin for Source Proximal CO_2 Storage* funded by the U.S. Department of Energy's National Energy Technology Laboratory (DOE NETL). The original objective of phase 3**,** which was to create an accurate model to predict long-term CO_2 storage capacity of the Jurassic to Late Triassic aged strata within SGRB, had to be modified because of operational issues and geologic characteristics of the study interval. After it was determined that the poor reservoir quality (very low permeability and porosity) throughout the study interval (between the depths 2016.0ft [0.61km] and 6140.0ft [1.87km]) did not allow further physical and geochemical testing of the recovered conventional core, efforts were diverted to determination of the factors which resulted in the destruction of porosity and permeability within the proposed CO_2 sequestration interval.

It is hypothesized that reservoir properties of the study sandstone were substantially diminished by a complex series of diagenetic events largely driven by regional tectonics. Consequently, the geologic history of the SGRB and how it fits into the regional tectonics of central eastern North America during the Triassic and Jurassic is presented in Section 1.0.

Individual portions of the petrologic and reservoir/storage characterization of Rizer #1 Test Borehole are presented in separate sections, each with its own descriptions of methodology, results, and discussions. These sections are briefly described as follows.

2.0 Petrologic Results: This section presents the results of the petrologic, sedimentolologic, and paleontologic analyses of the rotary sidewall cores (RSWC), conventional core (CC), and cuttings from Rizer #1 and discusses how these data sets inter relate. Conclusions reached in this section are as follows:

- The depositional setting for the conventionally core interval of test borehole Rizer #1 and probably the majority of the pre-Cretaceous strata penetrated is primarily alluvial associated with lacustrine coastal deposits.
- The sandstone samples recovered are generally lithic arkoses to arkosic litharenites with lithics comprised primarily of metamorphic rock fragments.
- The sandstones are predominantly cemented with quartz or calcite cements, with lessor abundances of authigenic sphene, and pyrite and isolated occurrence of evaporite cement.
- Based on modal analysis, total porosity averages 3.2%.

- Detrital matrix based on modal analysis of RSWC and CC sandstone samples only comprises an average of 2.9%.
- The igneous bodies encountered are classified as altered alkali olivine basalts or diabases. Due to the high dip angles of these bodies, they are interpreted to be intrusive dikes. These features also coincide with high angle fractures.
- Paleontological examination of RSWC, CC, and selected cuttings samples found no Triassic- or Jurassic-aged fossils.

3.0 Diagenetic Study: This section presents data sets, such as modal analysis of compaction indices and paleotemperatures of quartz and calcite cements to determine the burial and diagenetic history of the Rizer #1 study interval. Conclusions reached in this section are as follows:

- Reservoir quality of the study sandstone was substantially diminished by a complex series of diagenetic events, which include early cementation by chlorite, calcite, and sphene, followed by evaporates and multiple stages of quartz overgrowth and calcite cements during rapid subsidence of the basin.
- Based on modal analysis of compaction indices indicate a majority of the Rizer #1 sandstones appear to have been buried 2000ft to 6000ft (0.61km to 1.82km) deeper than present day at some point in their burial history.
- Based on results of SIMS analysis of δ^{18} O within quartz cements, the study sandstones were buried approximately 8200ft (2.50km) deeper than present burial depths at some point in their burial history.
- Sandstones within Rizer #1 test borehole and those laterally equivalent sandstones within the same fault block are not suitable candidates for CO_2 sequestration.
- Regarding reservoir properties for sandstones deeper within the Rizer #1 fault block, unless they experienced early cementation and subsequent dissolution of those cements to create secondary porosity or were over pressured early in their burial history, it is unlikely they possess reservoir properties to be suitable candidates for CO_2 sequestration.

4.0 Elemental Analyses: This section presents results of elemental analyses by X-ray fluorescence (XRF) of samples from test borehole interval 2660ft to 6200ft (810.8m to 1890.0m) and discusses the implications of the resulting chemostratigraphy. Conclusions reached in this section are as follows:

- Present are six (6) chemostratigraphic zonations, which are characterized by compositional shifts between more-mafic and more-felsic input over vertical intervals ranging from 200 feet to over 1000 feet. These shifts are interpreted to be controlled by the erosion of different source rocks, possibly terranes associated with the Carolina Zone.
- The elemental data are consistent with only limited weathering and chemical modification of detritus during most of sedimentation. This may be due to relatively rapid erosion and deposition or accumulation during arid conditions. Whatever the cause, significant modification of sediments did not occur.

- The elemental data alone cannot unequivocally establish whether basalts present are extrusive or intrusive. Only metasomatism is likely with lower-most Basalt I, constrained by petrology and geochemistry.

5.0 Caprock and CO_2 Storage Assessment: This section presents results of analyses of caprock lithologies from the nearby USGS Clubhouse Crossroads Test Hole No. 3 (Gohn, 1983; because whole core cap rock was not recovered from Rizer #1) and extrapolates CO_2 storage capacities for other portions of the SGRB based on Rizer #1 study interval characteristics. Conclusions reached in this section are as follows:

- Sandstone intervals present within recovered study interval of test borehole Rizer #1 are not suitable for the storage of CO_2.
- The presence of numerous dikes within the Rizer #1 fault block combined with the lack of a basalt flow cap rock at the top of the Triassic sequence indicates that portion of the of the SGRB is not structurally competent enough to prevent injected CO_2 from migrating upward into the overlying Coastal Plain aquifers.
- It can be assumed that laterally equivalent sandstones within the same fault block as Rizer #1 test borehole underwent the same degree of compaction and cementation and, consequently, are not suitable candidates for the storage of CO_2.

TABLE OF CONTENTS

5.0 Caprock and CO_2 Storage Assessment of a Portion of the South Georgia Rift Basin Based on Examination of Samples from Rizer #1 Test Borehole , Colleton County, SC and USGS Clubhouse Crossroads Test Hole No. 3, Dorchester County, SC

6.0 APPENDICES

SECTION 1

1.0 Introduction to Geologic Characterization of a Portion of the South Georgia Rift Basin for Source Proximal CO2 Storage Based on Analysis of Samples from Rizer #1 Test Borehole, Colleton County, SC and USGS Clubhouse Crossroads Test Hole No. 3, Dorchester County, SC

1.1 INTRODUCTION

This report describes results of the petrologic and reservoir/storage characterization portion of a larger study, *Geologic Characterization of the South Georgia Rift Basin for Source Proximal CO_2 Storage.* The lead organization for the overall project is the Earth Sciences & Resources Institute at the University of South Carolina. This project is one of numerous projects funded by the U.S. Department of Energy's National Energy Technology Laboratory (DOE NETL) around the country to identify options for carbon storage. The South Georgia Rift Basin (SGRB) was investigated because of its proximity to numerous coal-burning power plants in South Carolina and Georgia. The overall project was divided into three phases. The first phase provided an evaluation of the existing geologic data pertaining to the SGRB. The second phase collected new seismic data and evaluated the optimum location for drilling a deep test borehole. The third phase drilled the test borehole (Rizer #1), performed petrophysical and geochemical tests within the borehole, and petrologically examined core and cuttings samples from the borehole. This report presents and summarizes the results of the examination of core and cutting samples from Rizer #1. Rizer #1 Test Borehole was drilled in Colleton County, SC in the spring of 2012 (Figure 1.1) within 3 miles (5 km) of the Norris Lightsey well. This well, which recorded over an 8200ft (2.50km) sequence of pre-Cretaceous sandstone, was cored but the core was subsequently discarded.

Original objectives of phase 3 of the study had to be modified because of operational issues and geology of the study interval. The original objective of the geologic characterization was to create an accurate model to predict long-term CO_2 storage capacity of the Jurassic to Late Triassic aged strata within SGRB using samples of caprock, host formation, and formation brine. When the hole was abandoned at 6200.0ft (1.90km), some 2800.0ft (0.85km) short of the proposed sequestration interval, it became necessary to design analyses to help predict the reservoir quality of SGRB sandstones that are lateral to or deeper than the interval recovered. Objectives were altered further, however, after it was determined that the poor reservoir quality of the recovered interval did not allow further physical and geochemical testing. Consequently, study efforts were diverted to determination of the factors which resulted in the destruction of porosity and permeability within the proposed CO_2 sequestration interval.

The history of the geologic characterization portion of this study is described in more detail in the sub-section 1.2: Project History.

It is hypothesized that reservoir properties of the study sandstone were substantially diminished by a complex series of diagenetic events largely driven by regional tectonics.

Consequently, the geologic history of the SGRB and how it fits into the regional tectonics of central eastern North America during the Triassic and Jurassic is presented in the sub-section 1.3: Geologic Setting.

Individual portions of the petrologic and reservoir/storage characterization of Rizer #1 Test Borehole are presented in separate sections, each with its own descriptions of methodology, results, and discussions. These sections are briefly described as follows.

2.0 Petrologic Results: This section presents the results of the petrologic , sedimentolologic, and paleontologic analyses of the rotary sidewall cores (RSWC), conventional core (CC), and cuttings from Rizer #1 and discusses how these data sets interrelate.

3.0 Diagenetic Study: This section presents data sets, such as modal analysis of compaction indices and paleotemperatures of quartz and calcite cements to determine the burial and diagenetic history of the Rizer #1 study interval.

4.0 Elemental Analyses: This section presents results of elemental analyses (XRF) of samples from test borehole interval 2660ft to 6200ft (810.8m to 1890.0m) and discusses the implications of the resulting chemostratigraphy.

5.0 Caprock and CO_2 Storage Assessment: This section presents results of analyses of caprock lithologies from nearby Clubhouse Crossroads Test Hole No. 3 (cap rock was not recovered from Rizer #1) and extrapolates CO_2 storage capacities for other portions of the SGRB based on Rizer #1 study interval characteristics.

6.0 Appendices: All data generated for the geologic characterization portion of this study are included in this portion of the report.

1.2 Project History

Initial CC and RSWC samples were obtained from the Rizer #1 site in June 2012 and transported to the Weatherford Laboratories (WFT Labs) location in Houston, Texas. Only 57.20 linear feet of CC was recovered out of the originally proposed 720ft (660ft of reservoir and 60ft of caprock) because the borehole was abandoned at approximately 6200.0ft due to technical difficulties. The borehole, which was abandoned at the top of an igneous sill or dike (and possible fault), did not penetrate or core caprock and did not recover a conventional core of caprock (basalt) or sandstone from the interval originally hypothesized as most favorable for sequestration, which was hypothesized to be between well depth 6200.0ft (1.90km) and 9000.0ft (2.74km). Subsequently, 108 RSWC were obtained between the depths 2016.0ft (0.61km) and 6140.0ft (1.87km) for the purpose of adding to the petrologic data set and to determine if geologic characteristics significantly changed with depth. The study objectives were revised to collect data to be able to extrapolate rock character at depths below where Rizer #1 terminated. A listing of samples and the subsequent analyses performed on them is in Appendix A.

In addition, one container of produced formation water from 3651.0ft (1.11km) in Rizer #1 was also transported to the WFT Labs for salinity analysis.

Since no conventional core of caprock was obtained from Rizer #1 for the contracted mechanical and other physical property tests, it was decided to obtain portions of conventional core from the nearby USGS Clubhouse Crossroads Test Hole No. 3 from Dorchester County, SC (Figure 1.1B; approximately 38.5 miles [62.00km] from Rizer #1). The USGS Clubhouse Crossroads Test Hole No. 3 is one of three stratigraphic test wells completed in 1975 to study the Charleston, SC earthquake of 1886 (Rankin, 1977). These samples were obtained in July 2012 from the South Carolina Geological Survey and transported to WFT Labs. A listing of samples from USGS Clubhouse Crossroads Test Hole No. 3 and the subsequent analyses performed on them is in Appendix B.

Routine core analysis (RCA; September - October of 2012) showed average ambient porosities for RSWC and CC samples were 3.4% and 3.1%, respectively, and average permeability to air for RSWC and CC samples were 0.065mD and 0.0049mD (Appendices A and B). This poor reservoir quality made reservoir property measurements impractical. Special core analysis, such as mercury-injection capillary pressure, generally requires a minimum of 0.2mD permeability (Comisky et al., 2007). Consequently, the special core analysis portion of the study was abandoned. Instead, efforts were directed to determine why the reservoir properties of the proposed sequestration interval for are so poor and if scientifically supportable predictions of reservoir properties could be made for sandstones within the SGRB that are lateral to or deeper than the interval recovered.

In the fall of 2012, results of petrographic modal analyses and general descriptions of RSWC and CC samples not only confirmed the poor reservoir quality of the Rizer #1 sandstones but also indicated that the interval had at sometime in it's burial history undergone degrees of compaction and cementation typically associated with burial depths greater than the 2660ft to 6200ft (810.8m to 1890.0m) present-day depths of the study interval (Wilson and McBride, 1988). In order to test the hypothesis of deeper burial, dual lines of investigation were formulated. First, modal compaction analysis was performed on 12 thin section samples to determine their contact index (CI) and tight packing index (TPI) following the guidelines of Pettijohn et al. (1975), Wilson and McBride (1988), and McBride et al. (1991). The second path of investigation was to determine formation temperatures of the intergranular cements, quartz and calcite, to infer burial depths. This mode of investigation followed the methodology of Hiatt et al (2007), which incorporated δ^{18} O values obtained by secondary ion mass spectrometry (SIMS) of quartz overgrowths.

In addition to redirecting resources to determine the diagenetic history of the Rizer #1 study interval, it was decided to glean as much geologic information from the samples obtained from borehole as possible. The resulting data and analyses will hopefully aid future geologic research of the SGRB. Consequently, 299 cuttings samples from the interval 2660ft (below base of Coastal Plain aquifers) to 6200ft (0.81km to 1.90km) were analyzed for elemental composition (XRF) compiled with the thirty-one (31) RSWC and ten (10) CC samples already completed. Additional paleontologic samples were also selected. Appendix A lists all samples utilized for geologic analyses. The elemental

analyses, whose results are present in Section 3, were performed in the spring and summer of 2013.

Analyses for the diagenesis study were performed and completed in the late winter and spring of 2013. Initial efforts were directed at selecting a suite of six (6) samples for SEM CL examination. These examinations, which were performed with Dr. Robert Reed at the Bureau of Economic Geology at the University of Texas, Austin (BEG), were designed to delineate the presence or absence of multiple stages of cement growth. The scanned CL images indicted multiple stages of quartz overgrowth cement but were unable to delineate stages of calcite cement due to luminescence of the calcite. Subsequently, three (3) samples were selected for SIMS determination of δ^{18} O values of the quartz and calcite cements at the WiscSIMS laboratory at the University of Wisconsin in Madison, WI. The SIMS examinations were completed in June of 2013 with assistance of Dr. John Valley and Dr. Kouki Kitajima. Supporting elemental analyses were performed by Dr. John Fournelle at the University of Wisconsin Electron Microprobe Lab. Additional bulk δ^{18} O measurements were later obtained from WFT Labs on calcite cements that could not be analyzed with the SIMS.

More detailed descriptions of methodologies employed in this study are described in their respective sections.

1.3 GEOLOGIC SETTING

The overall regional geologic setting is a critical component to understanding the depositional and diagenetic history of the study interval in Rizer #1 because regional tectonic events were not only instrumental in creating the SGRB but were also critical in driving the post-burial processes that altered the SGRB strata. Although the study area is presently situated on the trailing edge of a passive continental margin, it experienced three regional tectonic stages since the break up of the Pangea supercontinent and the formation of the North Atlantic Basin (Withjack et al., 1998; Figure 1.2).

During early Mesozoic time a massive rift zone formed within the Pangea supercontinent (Figure 1.3; Olsen, 1997; Withjack et al. 2012). The North American portion of this rift zone, which was separated from other portions on the northwestern margins of Africa and Europe with the breakup of Pangea, is one of the world's largest rift systems being 500 km wide by 3000 km long (Withjack et al., 2012).

Rift basins, such as the SGRB examined in this study, formed in eastern North America from the Middle Triassic to Early Jurassic (Figure 1.3 and 1.4; Manspeizeer and Cousminer, 1988; Olsen et al., 1989; Withjack et al., 1998). Strata within southern basins (south of the Culpepper Basin in Virginia), however, are exclusively Late Triassic in age, whereas basins to the north contain strata ranging from Middle Triassic to Early Jurassic in age (Figure 1.4; Olsen et al., 1989; Olsen, 1997). Most rift basins are asymmetric, bounded on one side by a normal fault or faults that strike northeast- southwest (Figure 1.2) and have displacements that locally exceed 10 km (Hutchinson and Klitgord, 1988; Schische, 1992, 1993; Withjack et al., 1995). The Upper Triassic synrift basins in the southern and central segments of eastern North America (ENA) are thought to be thicker (5-10 km) than in the northern segment (Figure 1.3; Withjack et al., 2012).

Based on regional outcrop studies of south and central ENA basins, continental conditions

prevailed throughout their Late Triassic depositional histories (McAlpine, 1990; Olsen, 1997; Withjack et al., 2012). Paleoclimatic conditions are theorized to have varied from early Late Triassic (Carnian) to late Late Triassic (Norian) as Pangea and the low latitude southern segment ENA rift basins drifted northward (Withjack et al., 2012). This period is characterized by "apparent drying with shallow water cyclical lacustrine strata predominating in the southern and central basins (Withjack et al., 2012 after Olsen and Kent, 2000 and Olsen, 1997).

No sedimentary rocks of Early Jurassic age are present within any onshore rift basin south of the Culpeper Basin (Figure 1.5; Olsen et al. 1989; Olsen, 1997; Withjack et al.,1998). It is reported that an angular unconformity separates synrift and post rift strata in the subsurface of South Carolina (Behrendt, 1986; Costain and Coruh, 1989; Withjack et al., 1998). The oldest strata, which overlies the onshore South Carolina portion of the SGRB, is the Upper Cretaceous aged Middendorf Formation (Colquhoun et al., 1983). Offshore, however, "a thin package" of sedimentary rocks separates ENA basalts from the underlying postrift unconformity (Dillon et al., 1983; Withjack et al., 1998). According to Withjack et al. (1998), rifting ceased and erosion took place before eruption of the ENA basalts at approximately 200 Ma. (Findings from this study indicate a minimum of 4400ft [1.35km] of erosion from Rizer #1 portion of the SGRB.) During this same period preceding the ENA magmatic event, numerous basement-involved reverse faults formed, including the Cooke fault in South Carolina (Behrendt et al., 1981; Hamilton et al., 1983; Withjack et al., 1998) and numerous reverse faults with associated propagation folds in the Richmond rift basin of southern Virginia (Venkatakrishnan and Lutz, 1988; Withjack et al., 1998).

ENA magmatic activity, which during the Early Jurassic included inclusion of diabase dikes and sills and the extrusion of basalt flows (King, 1971; Olsen et al., 1989, 1996; McHone, 1996; Withjack et al., 1998), is part of one of the world's largest igneous provinces, the Central Atlantic Magmatic Province (CAMP; Figure 1.5). North of the Culpeper basin, basalt flows are intercalated with synrift strata but are not present within exposed rift basins to the south (Olsen, 1997). (A majority of igneous layers observed within the Rizer #1 study interval are at relatively high-angle, and, consequently, are interpreted as intrusive dikes.) Ragland et al. (1992) determined the age for the ENA magmatic activity (flows, dikes, and sills) was 200 $\pm$5 Ma (Figure 1.4), based on review of all geologic, paleomagnetic, and geochemical data available.

Postrift contractional deformation is recognized as pervasive within the ENA (Withjack et al. (2012). Many of these postrift contraction features are inversions or flower structures (such as the fault block penetrated by Rizer #1). The degree of inversion for Taylorsville basin in the southern segment of the ENA and the Fundy basin in the northern segment are both interpreted to be approximately 2 km (6600ft; Figure 1.6; as

is the Rizer #1 portion of the SGRB). Since no collision of subduction zones existed near the ENA during Mesozoic time "incipient ridge-push forces and/or an initial continental resistance to plate motion may produce shortening…" (Withjack et al., 2012 after Boldreel and Andersen, 1993; Bott, 1992; Dewey, 1988; Schlische et al., 2003; Withjack et al., 1995, 1998; Figure 1.7). In the southern segment of the ENA, postrift contractional deformation occurred both prior to and after the ENA magmatic event (Figure 1.8), including approximately 460ft (140m) of reverse displacement along the Cooke fault in South Carolina preceding the magmatic event (Behrendt et al., 1981; Hamilton et al., 1983; Withjack et al., 1998).

As previously mentioned, the CAMP basalt flows, encountered within the Clubhouse Crossroads No. 3 borehole, are unconformably overlain by Upper Cretaceous, Santonian- to Turonian-aged Middendorf Formation. The missing section spans over a 100 Ma period.

1.4 CITATIONS

Behrendt, J.C., Hamilton, R.M., Ackermann, H.D., and Henry, V.J., 1981, Cenozoic faulting in the vicinity of the Charleston, South Carolina, 1886 earthquake: Geology, v. 9, p 117-122.

Benson, R.N., 2003. Age estimates of the seaward-dipping volcanic wedge, earliest oceanic crust, and earliest drift-stage sediments along the North Atlantic continental margin. In: Hanes, W.E., McHone, J.G., Renne, P.R., Ruppel, C. (Eds.), The Central Atlantic Magmatic Province, Insights from Fragments of Pangea, Geophysical Monograph, vol. 136. American Geophysical Union, Washington, D.C., pp. 61–75.

Boldreel, L.O., and Andersen, M.S., 1993, Late Paleocene to Miocene compression in the Faero-Rockall area, in Parker, J.R. (ed.), Petroleum Geology of Northwest Europe: Geological Society of London, pp 1025-1034.

Bott, M.H.P., 1992, The stress regime associated with continental break-up, *in* Storey, B.C., Alabaster, T., and Pankhurst, R.J., eds., Magmatism and the causes of continental break-up: Geological Society Special Publication, 68, p 125-136.

Colquhoun, D. J., Woollen, L. D., Van Nienwenhuise, D. S., Padgett, G. G., Oldham, R. W., Boylan, D. C., Bishop, J. W., and Howell, P. D., 1983, Surface and subsurface stratigraphy, structure and aquifers of the South Carolina Coastal Plain: Columbia, SC, State of South Carolina, Office of the Governor, 78 p.

Comisky, J.T., K.E. Newsham, and J.A. Rushing, and T.A. Blasingame, 2007. A Comparative Study of Capillary-Pressure-Based Empirical Models for Estimating Absolute Permeability in Tight Gas Sands: SPE 110050; 2007 SPE Annual Technical Conference and Exhibition: SPE, Texas A&M University, p. 1-18.

Costain, J.K., and Coruh, C., 1989, Tectonic setting of Triassic half-grabens in the Appalachians: seismic data acquisition, processing, and results, *in* Tankard, A.J.,

and Balkwill, H.R., eds., Extensional tectonic and stratigraphy of the North Atlantic margins: AAPG Memoir 46, p 155-174.

Dewey, J.F., 1988, Lithospheric stress, deformation, and tectonic cycles: the disruption of Pangaea and the closure of the Tethys, *in* Audley-Charles, M.G., and Hallam, A., eds., Gondwana and Tethys: Geological Society Special Publicaton 37, p 23-40.

Foster, D.G., Robinson, A.G., 1993. Geological history of the Flemish Pass basin, offshore Newfoundland. AAPG Bull. V. 77, p. 588–609.

Gohn, G.S., ed., 1983, Studies related to the Charleston, South Carolina earthquake of 1886-Tectonics and Seismicity: U.S. Geological Survey Professional Paper 1313, 375 p.

Hamilton, R.M., Behrendt, J.C., and Ackermann, H.D., 1983, Land multichannel seismic-reflection evidence for tectonic features near Charleston, South Carolina, in Gohn, G.S., ed., Studies related to the Charleston, South Carolina, earthquake of 1886-tectonics and seismicity: Geological Survey Professional Paper 1313, p 11-118.

Hutchinson, D.R., and Klitgord, K.D., 1988, Evolution of rift basins on the continental margin off southern New England, *in* Manspeizer, W., ed., Triassic-Jurassic rifting, continental breakup and the origin of the Atlantic Ocean passive margins, part A: New York, E;sevier, p 81-98.

Hiatt, E.E., Kyser, T.K., Fayek, M., Polito, P., G.J., Holk, and Riciputi, L.R., 2007, Early quartz cements and evolution of paleohydraulic properties of basal sandstones in three paleoproterozoic continental basins: Evidence from *in situ* δ^{18} O analysis of quartz cements: Chemical Geology, v. 238, p. 19-37.

King, P.B., 1971, Systematic pattern of Triassic dikes in the Appalachian region-second report: U.S. Geological Survey Professional Paper 750-D, p D84-D88.

Manspeizeer, W., and Cousminer, H.L., 1988, Late Triassic-Early Jurassic synrift basins of the U.S. Atlanitc margin, in Sheridan, R.E., and Grow, J.A., eds., The geology of North America, v I-2, the Atlantic continental margin, U.S.: Geological Society of America, p 197-216.

McBride, E.F., Diggs, T.N., and Wilson, J.C., 1991, Compaction of Wilcox and Carrizo Sandstones (Paleocene-Eocene) to 4420 M, Texas Gulf Coast: Journal of Sedimentary Petrology, v. 61, p 73-85.

McBride, J.H., Nelson, K.D., Brown, L.D., 1989, Evidence and implications of an extensive early Mesozoic rift basin and basalt/diabase sequence beneath the southeast Coastal Plain: Geological Society of America Bulletin, v 101, p 512-520

McHone, J.G., 1996, Broad-terrane Jurassic flood basalts across northeastern North America: Geology, v 24, p 319-322.

McHone, J.G., 2000. Non-plume magmatism and rifting during the opening of the central Atlantic Ocean. Tectonophysics 316, 287–296.

McHone, J.G., Anderson, D.L., Fialko, Y.A., 2004. Giant Dikes: Patterns and Plate Tectonics.http://www.mantleplumes.org/.

Pettijohn, F. J., Potter, P. E., and Siever, R., 1973, Sand and Sandstones: Springer- Verlag; New York, Heidelberg, Berlin, Heidelberg, London, Paris, Tokyo, pp. 618.

Oh, J., Austin, J.A., Phillips, J.D., Coffin, M.F., Stoffa, P.L., 1995. Seaward-dipping reflectors offshore the southeastern United States: Seismic evidence for extensive

volcanism accompanying sequential formation of the Carolina trough and Blake Plateau basin. Geology 23, 9–12.

Olsen, P.E., 1997, Stratigraphic record of the early Mesozoic breakup of Pangea in the Laurasia-Gondwana rift system: Annual Reviews of Earth and Planetary Science, v 25, p 337-401.

Olsen, P.E., Schische, R.W., and Gore, P.J.W. (Eds.), 1989, Tectonic, depositional, and palaoecological history of early Mesozoic rift basins, eastern North America: International Geological Congress Field Trip T351: American Geophyscial Union, Washington, D.C., pp 174.

Olsen, P.E., Schische, R.W., and Fedosh, M.S., 1996, 580 kyr duration of the Early Jurassic flood basalt event in eastern North America estimated using Milankovitch cyclostratigraphy, in Morales, M. (ed.), The Continental Jurassic: Museum of Northern Arizona Bulletin, v 60, p 11-22.

Olsen, P.E., and Kent, D.V., 2000, High resolution early Mesozoic Pangean climatic transect in lacustrine environments, *in* Bachmann, G., and Lerche, I.(eds.), Epicontinental Triassic: Zentrablatt fur Geologie und Palaontologie, v 3, VIII, p 1475-1496.

Ragland, P.C., Cummins, L.E., and Arthur, J.D., 1992, Compositional patterns for early Mesozoic diabases from South Carolina to central Virginia, in: Puffer, J.H., and Ragland, P.C., eds., Eastern North American Mesozoic Magmatism: Geological Society of America Special Paper, v. 268, p 301-331.

Rankin, D.W., 1977. ed., 1983, Studies related to the Charleston, South Carolina earthquake of 1886-A Preliminary Report: U.S. Geological Survey Professional Paper 1028, 276 p.

Rankin, D.W., 1994, Continental margin of the eastern United States: past and present. In: Speed, R.C. (Ed.), Phanerozoic Evolution of North American Continent-Ocean Transitions, Geological Society of America, DNAG Continent-Ocean Transect Volume, pp. 129–218.

Schlische, R.W., Withjack, M.O., and Olsen, P.E., 2003, Relative timing of CAMP, rifting, continental breakup, and basin inversion: tectonic significance, in Hanes, W.E., McHone, J.G., Renne, P.R., and Ruppel, C. (eds.), The Central Atlantic Magmatic Province, insights from fragments of Pangea, Geophysical Monograph, v. 136: Washington, D.C., American Geophysical Union, p 33-60.

Tseng, Hsin-Yi, Onstott, T.C., Burruss, R.C., and Miller, D.S., 1996, Constraints on the thermal history of Taylorsville Basin, Virginia, U.S.A., from fluid-inclusion and fission-track analyses: implications for subsurface geomicrobiology experiments: chemical Geology, v. 127, p. 297-311.

Venkatakrishnan, R., and Lutz, R., 1988, A kinematic model for the evolution of the Richmond basin, in Manspeizeer, W. (ed.), Triassic-jurassic Rifting, Continental Breakup and the Origin of the Atlantic Ocean Passive Margins, Part A: New York, Elsevier, p 445-462.

Welsink, H.J., Dwyer, J.D., Knight, R.J., 1989. Tectono-stratigraphy of the passivemargin off Nova Scotia. In: Tankard, A.J., Balkwill, H.R. (Eds.), Extensional Tectonics and Stratigraphy of the North Atlantic Margins, American Association of Petroleum Geologists Memoir, vol. 46, pp. 215–231.

Wilson, J.C. and McBride, E.F., 1988, Compaction and Porosity evolution of Pliocene sandstones, Ventura Basin, California: American Association of Petroleum Geologists Bulletin, v. 72, p 664-681.

Withjack, M. O., Olsen, P. E., and Schlische, R.W., 1995, Tectonic evolution of the Fundy rift basin, Cana: evidence of extensions and shortening during passive margin development: Tectonics, v. 14, p 390-405.

Withjack, M.O., Schlische, R.W., and Olsen, P.E., 1998, Diachronous rifting, drifting, and inversion on the passive margin of central eastern North America: An analog for other passive margins: AAPG Bulletin, v. 82, p. 817-835.

Withjack, M. O., Schlische, R.W., and Olsen, P. E., 2012, Development of the passive margin of eastern North America: Mesozoic rifting, igneous activity, and breakup. In: Bally, A. W. & Roberts, D. G. (eds), Principles of Phanerozoic Regional Geology, v. 1, Elsevier, Amsterdam, p. 301–335.

1.5 ACKNOWLEDGEMENTS

DOE/NETL Acknowledgment:
This material is based upon work supported by the Department of Energy under Award Number DE-FE0001965.

A

B

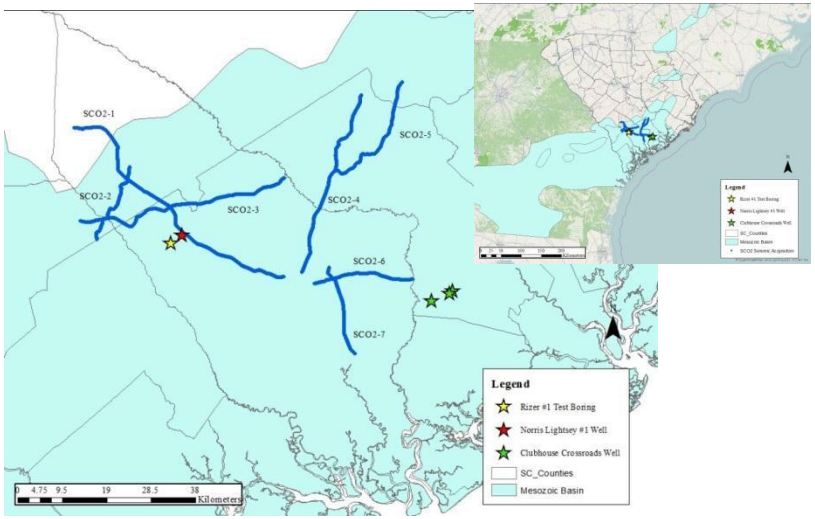

C

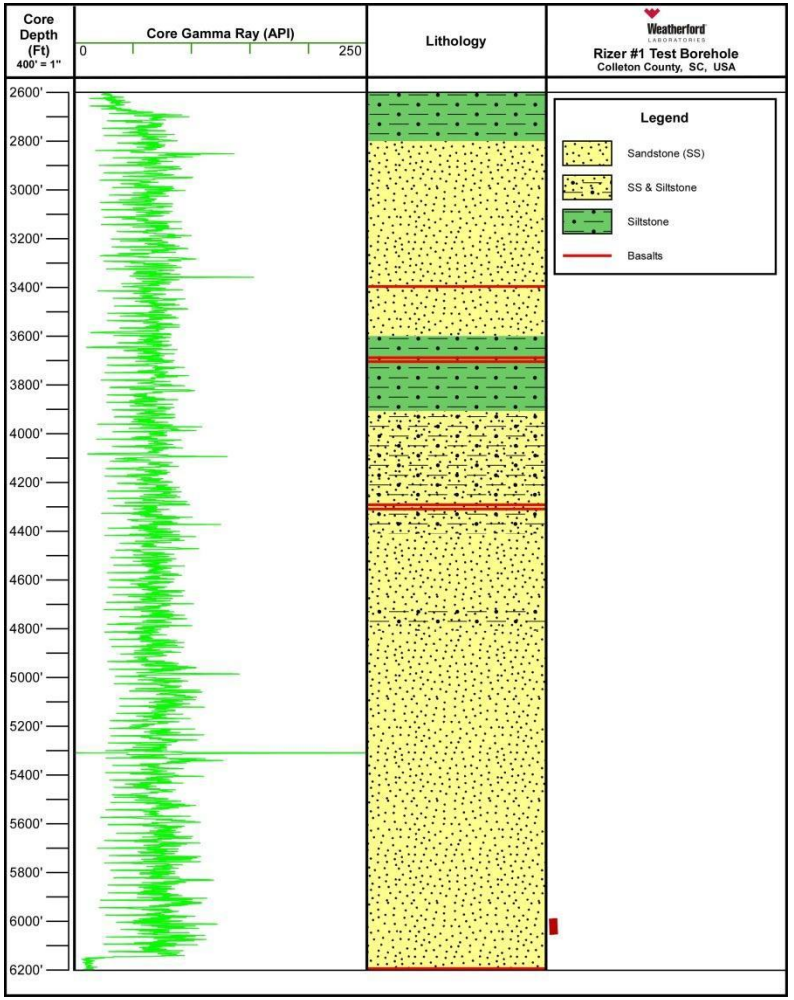

Figure 1.1 A. Drill rig operated by Schlumberger at the site of Rizer # 1 test borehole in Colleton County, South Carolina from June 2012. B. Location of Rizer #1 and neighboring boreholes and seismic lines utilized in the overall project. Samples from USGS Clubhouse Crossroads Test Hole No. 3 in Dorchester County were utilized for caprock studies. C. Graphic lithic log of study interval within Rizer #1 based on cuttings.

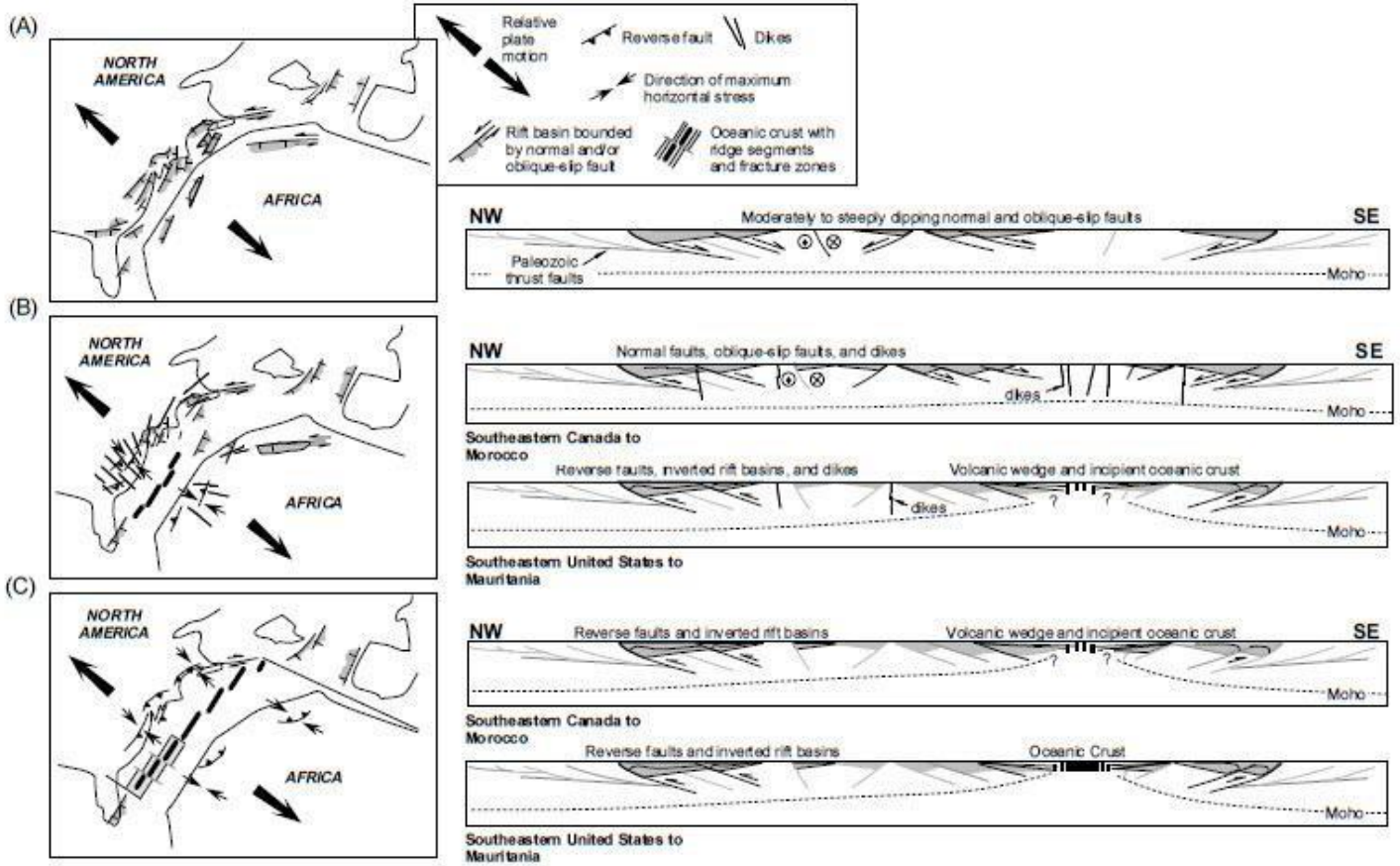

Figure 1.2 Graphical model by Withjack et al. (1998) showing evolution of central eastern North America in map and cross-sectional views. (A) Shows Middle to Late Triassic activity with northeast striking rift basins subsiding and filling with sediment. (B) Shows late Triassic to Early Jurassic activity which includes basin inversion in the south and is shortly before or after eastern North America (ENA) magmatic activity with northwest-striking dikes. (C) Shows Early Jurassic (post ENA magmatic activity) to Early Cretaceous when rifting ceased. (From Withjack et al., 1998).

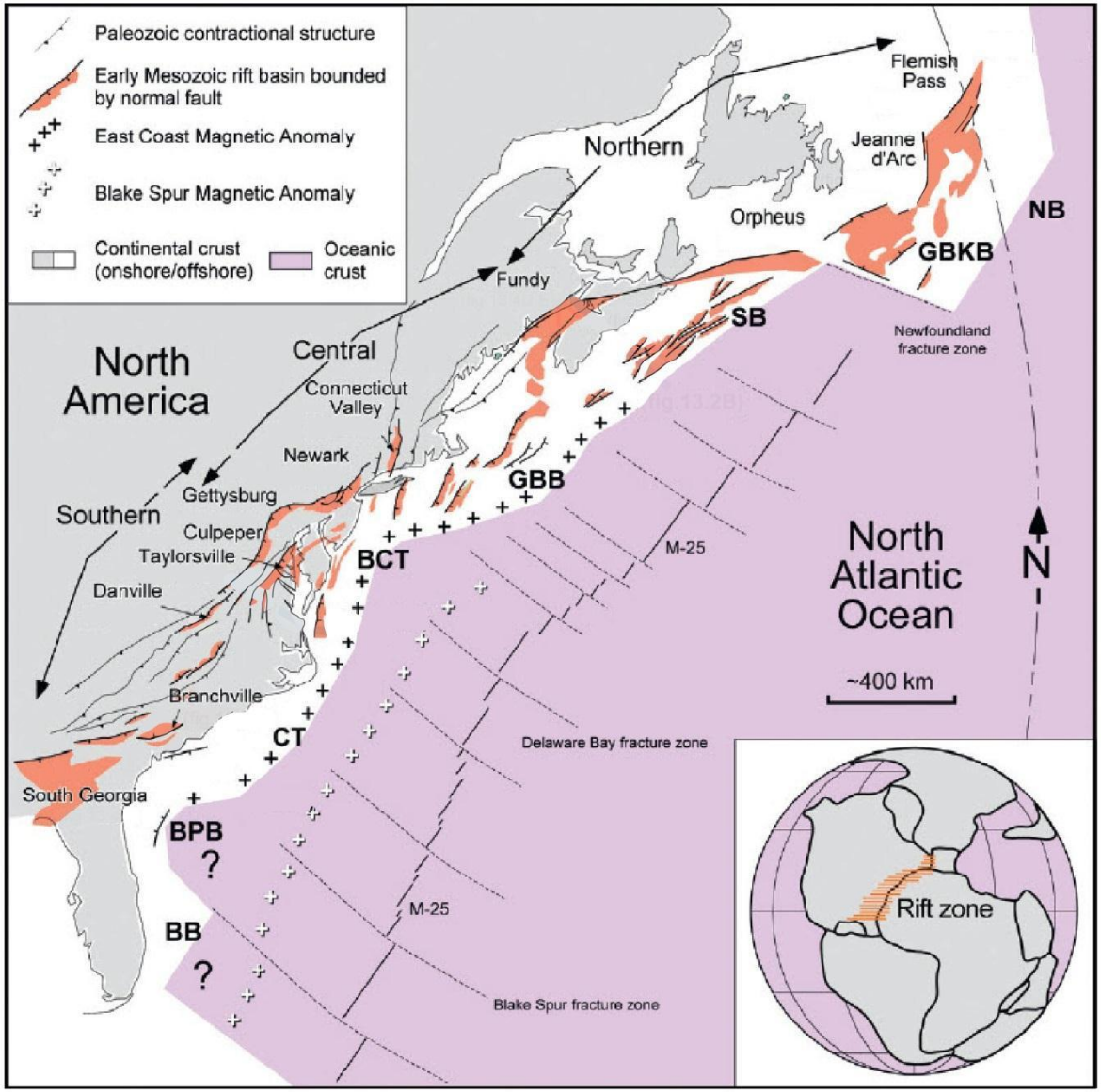

Figure 1.3 Major Paleozoic contractional structures and early Mesozoic rift basins of eastern North America with key tectonic features of the eastern North Atlantic as synthesized by Withjack et al. (2012) from Benson (2003), Foster and Robinson (1993), Klitgord et al. (1988), Olsen et al. (1989), Rankin (1994) and Welsink et al. (1989).
The South Georgia Rift Basin (SGRB) is the southernmost basin identified in the system. Mesozoic/Cenozoic postrift basins are: BB, Bahamas basin; BPB, Blake plateau basin; CT, Carolina trough; BCT, Baltimore Canyon trough; GBB, Georges Bank basin; SB, Scotian basin; GBKB, Grand Banks basin; NB, Newfoundland basin. Pangaean supercontinent during the Late Triassic is based on a reconstruction of Olsen (1997) and shows the approximate extent of rift zone between the eastern edge of the North American plate and the northwestern edge of the African plate (Withjack et al., 2012). Figure is modified from Withjack et al. (2012).

Figure 1.4 Graphic, which is modified from Withjack et al. (1998), shows the spatial and temporal distribution of central eastern North American rift basins starting with the SGRB in the south to the Fundy rift basin in the north. Also depicted are associated synrift basin / trough deposits and associated eastern North America (ENA) magmatic activity.

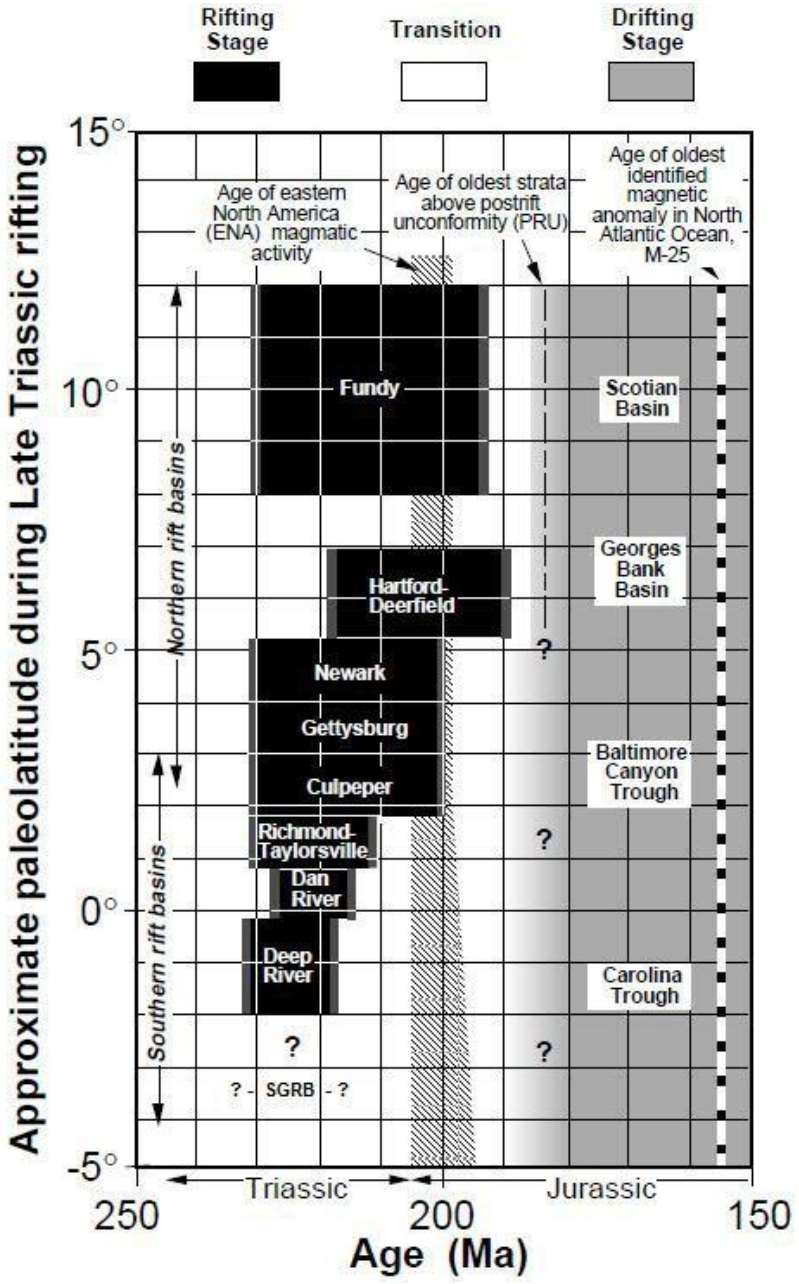

Figure 1.5 Figure from Withjack et al. (2012), showing early Jurassic-age dikes (thin lines) in ENA and the possible extent of the Clubhouse Crossroads Basalt (after Oh et al., 1995; McHone, 2000; and McHone et al., 2004).

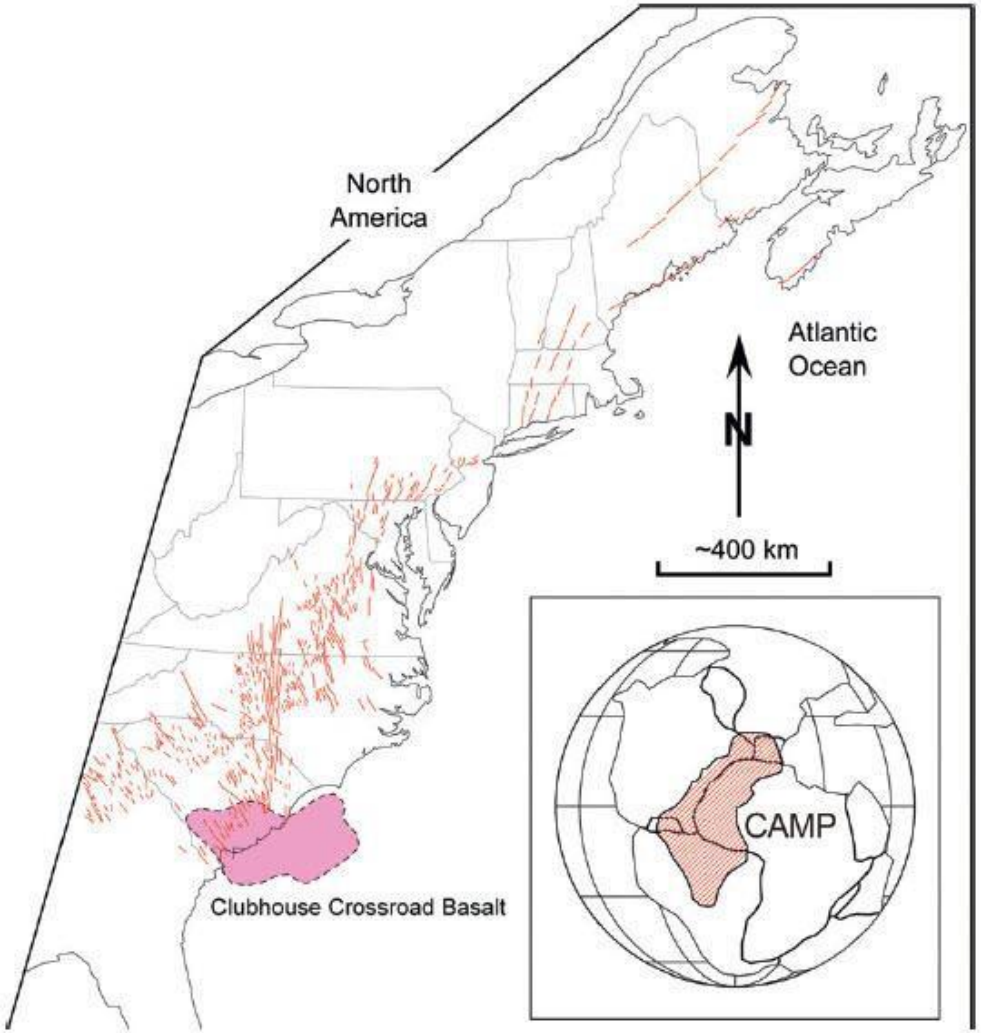

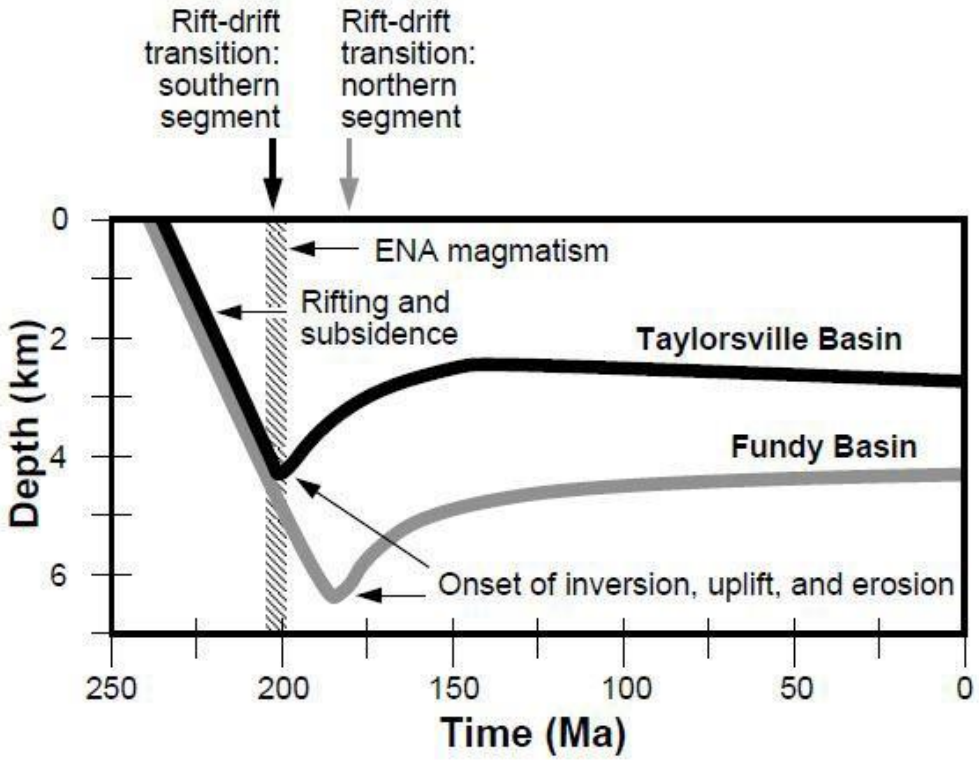

Figure 1.6 Subsidence histories of the Taylorville and Fundy rift basins (Tseng et al., 1996; Withjack et al., 1998). Figure is from Withjack et al. (1998).

Figure 1.7 A graphic representation of the three stage rift-drift tectonic model for eastern North America (ENA) from Withjack et al. (1998). The first stage of early rifting (A) creates a setting of widespread extension, which produces the rift basins within the ENA. Late rifting (B) is a period when lithospheric displacement near the upwelling exceeds displacement far away, resulting in "compensating shortening" in the intervening zone. The final stage of drifting (C) is a period of uniform lithospheric displacement with most inversion activity ceasing. Figure from Withjack et al. (1998).

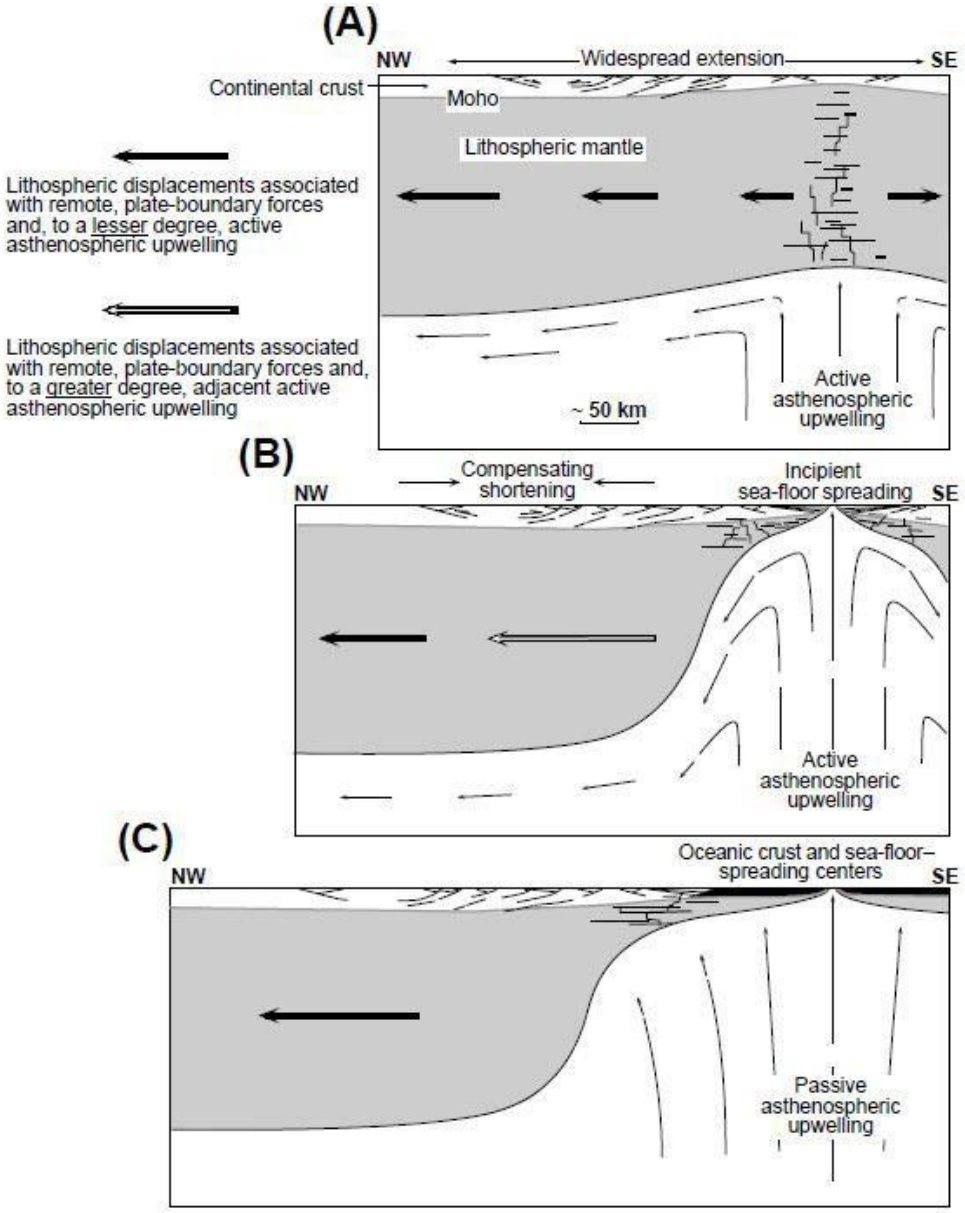

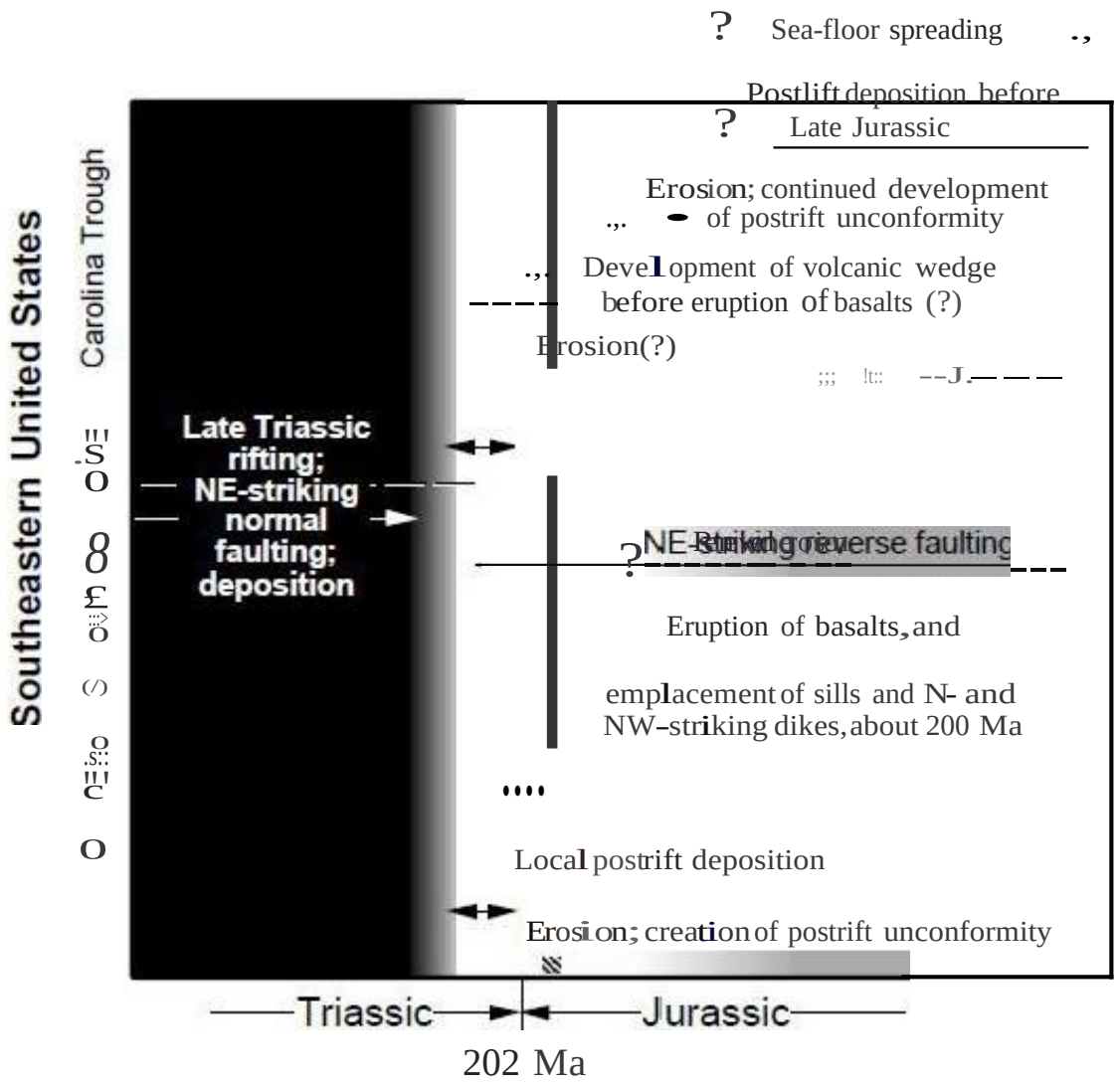

Figure 1.8 Graphical depiction of sequence of events during rift-drift transition in southeastern United States. Figure is frorn Withjacket al. (1998).

SECTION 2

2.0 Petrologic Characterization of a Portion of the South Georgia Rift Basin Based on Examination of Samples from Rizer #1 Test Borehole, Colleton County, SC

2.1 INTRODUCTION

This section of the report describes results of the petrologic characterization of samples obtained from Rizer #1 test borehole drilled in Colleton County, SC. In sub-section 2.2 the methods employed in this portion of the study are summarized. In sub-section 2.3 the sedimentologic character and general lithology of the conventional core (CC) are described. In sub-section 2.4 and petrologic characteristics of the sedimentary strata recovered by CC, rotary sidewall cores (RSWC), and one cuttings sample are described. In sub-section 2.5 the petrologic characteristics of the igneous rocks encountered with the borehole are described. Sub-section 2.6 describes the results of the paleontological examinations of the study interval.

2.2 METHODS

The petrologic aspects of this study are based on examination of 57.20ft of CC and analyses of selected samples from 108 RSWC within the depth interval 2850.0ft to 6140.0ft in Rizer #1 test borehole. From a total of seventy-eight (78) thin sections prepared and photographed (30 from CC and 48 from RSWC), detailed (modal) analysis was completed on thirty-four samples (10 from CC and 24 from RSWC) and thirty (30) general thin section descriptions were completed (2 from CC and 28 from RSWC samples). A brief examination of the cuttings from 2630ft-2640ft determined the character and origin of the limestone fragments recovered. XRD analysis was performed on forty-three (43) samples (10 from CC and 33 from RSWC). Standard SEM analyses were performed on twenty-four (24) samples (2 from CC and 22 from RSWC). Paleontologic examinations were performed on a total of nine (9) sample sets (3 from CC and 6 cuttings intervals). A complete listing of all the analyses performed on RSWC and CC samples from Rizer #1 test borehole are in Appendix A. Detailed procedures utilized with these analyses are described in Appendix C. Additional procedures, which were conducted for the diagenesis and compaction study, are summarized in Section 3.

2.3 SEDIMENTOLOGY OF CONVENTIONAL CORE (6000.00FT – 6057.20FT)

The core consists primarily of thick bedded sandstones, ranging in grain-size from very fine grained- to coarse grained sandstone with the basal unit a mudstone and the top unit with interbedded mudstones and sandstones (Figure 2.1; Appendix D). The depositional setting is interpreted to be primarily alluvial associated with lacustrine coastal deposits. The alluvial facies are comprised of braided and meandering channel fill or lacustrine delta deposits. The braided channel fill sequences are comprised of fine- to coarse-grained sandstones with abundant pebbles and intrabasinal clasts generally within large-scale cross-bedded beds (6002.90ft to 6014.70ft, 6039.90ft to 6049.60ft; Figure 2.1 and 2.2; Appendix D). The intrabasinal clasts consist of claystone,

clayey siltstone, micrite, and micrite-bound sand (Figure 2.3; Appendix I). The relatively thick meandering channel or lacustrine delta channel-fill deposit (Figure 2.1, 6014.70ft to 6031.40ft) is comprised of very fine- to medium-grained sandstone. This package is interpreted to be a fluvial/deltaic because of the presence of burrow traces (*Scoyenia* and *Chondrites*) within the sequence (6014.70ft to 6031.40ft; Figures 2.1, 2.4) and the moderately well sorted character of the sandstone within this fining upward unit (Appendix D). Other alluvial packages are a small fluvial channel-fill (6049.60ft to 6054.10ft) overlying an erosion surface at the top of a weathered package of sandy mudstone alluvium (6054.10ft to 6057.20ft; Figure 2.5) and sandy overbank deposits (6031.40ft to 6039.90ft). The cored interval is capped with interbedded mudstones and sandstones with ripple bedding and burrow traces (Figure 2.6A). Flaser bedding and composite ripple bedding (current and wave ripples; 6002.10ft to 6002.90ft; Figure 2.6) indicate fluctuating flow intensities and the presence of wave energy. These features are commonly associated with tidal flats (Reineck, 1975) but can probably be found in lacustrine sand-flats or mud-flats influenced by periodic, wind-induced seiches (water- level surges). At the base of the cored interval, the sandy mudstone unit appears to be overbank alluvium altered by soil formation (6054.10ft to 6057.20ft; Figure 2.5).

The interpretation that the cored interval was associated with a lacustrine and not a coastal marine setting, is based on paleogeographic reconstructions which indicate no marine influence on the SGRB (Olsen, 1997; Olsen and Kent, 2000; Withjack et al., 2012). Consequently, the presence of micrite clasts (Figure 2.3) and phosphatic fish bones (Figure 2.7) indicate proximity to a lacustrine setting. The occurrence of lacustrine carbonate deposits associated with rift basins is not uncommon (Harris et al., 2013).

2.4 PETROLOGIC CHARACTERISTICS OF SEDIMENTARY STRATA

2.4.1 Lithostratigraphy

The Late Triassic-Early Jurassic strata penetrated by Rizer #1 is sandstone-rich and mudstone-poor. The lithology log for the recovered portions of the study interval 2660ft to 6200ft (810.8m to 1890.0m; Figure 1.1C) found only 6% identified as "shale, clay, interbedded shale and sandstone," or "silty clay." Only 28% of the interval is classified as "siltstone" or "interlayered siltstone and sandstone" or "siltstone stringers." Except for a few ten's of feet (1%) of interval identified as "diabase" or "no sample" (6%), the remainder is identified as fine to coarse-grained sandstone (59%). Photomicrographs of the few mudstone or siltstones sampled by RSWC and CC are shown in Figure 2.9.

2.4.2 Framework Grains

The majority of sandstones are lithic arkoses or feldspathic litharenites based on the classification of Folk (1968; Figure 2.10A). The ternary diagram of lithic fragments (Figure 2.10B) indicates the majority of rock fragments are metamorphic (MRF). Many of the grains classified as sedimentary rock fragments (SRF), however, are actually intrabasinal clasts of lacustrine micrite. Plutonic rock fragments are not included in the

ternary diagram of lithic fragments. According to XRD analysis of RSWC samples (33) plagioclase feldspar is twice as abundant as potassium feldspar (average of 9 wt% versus 20 wt%; Appendix F). This ratio is the same for modal analysis of thin sections (10 CC and 24 RSWC; average 6.7% potassium feldspar versus 14.2% plagioclase). Based on modal analysis, potassium feldspar grains range in abundance from 1.0% to 17.3% and plagioclase grains range from 4.7% to 24.3%. The most abundant MRF are of schists and phyllites (Figure 2.11). Granule-sized gneiss and plutonic rock fragments were also observed (Figures 2.12 and 2.13). Other lithics include sedimentary rock fragments, such as from siltstones (Figures 2.14), and volcanic rock fragments (Figure 2.15A). Two samples from the CC (thin sections from 6007.60ft and 6040.18ft) were examined with the objective of determining provenance. Both found ubiquitous monocrystalline quartz, potassium feldspar, and plagioclase feldspar. This assemblage is consistent with granitic source for much of the detrital minerals in samples. Rock fragments of quartzite, schist, gneiss, and meta felsic igneous rocks are also present.

2.4.3 Cements and Replacement Minerals

The most abundant cement present, based on modal analysis of 34 thin sections of RSWC and CC samples, is quartz overgrowth cement (Table 2.1). Quartz overgrowth cement averages 4.5% and ranges from absent to 14.0%. The second most abundant cement is calcite, which averages 2.5% and ranges from 0.3% to 19.0%. Intergranular calcite is comprised predominantly of poikilotopic cement (Figure 2.15) with some blocky calcite to microspar. Quartz overgrowth cement commonly occurs with calcite cement (Figure 2.15) and with authigenic clay, such as chlorite (Figure 2.16) and illite or illite/smectite. Other significantly occurring cements are plagioclase (albite), pyrite/titanium oxide, iron oxides, microquartz, sphene (Figure 2.17B), and anhydrite (Figure 2.18; Table 2.1). These minerals are also present as grain replacements (Appendix E).

2.4.4 Sedimentary Texture and Degree of Compaction of Sandstones

The sandstone sampled within Rizer #1 test borehole are generally moderate to moderately well sorted, very fine to medium-grained sandstone. Layering in the form of laminations or ripple bedding is common. Grain angularity is generally subangular to subrounded (Figure 2.18). Degree of compaction is generally moderate to high, with stylolite and pressure solution features common (Figure 2.12A and 2.19).

2.4.5 Porosity (from Modal Analysis)

Examination of the thin sections supports the results of the RCA (average ambient porosities for RSWC and CC samples were 3.4% and 3.1%, respectively, and average permeability to air for RSWC and CC samples were 0.065mD and 0.0049mD; Appendices E). Based on modal analysis of the 34 thin sections, total porosity averages 3.2% with the most common porosity types present being intergranular microporosity (1.8%) and intragranular microporosity (0.6%) with lesser amounts of primary or secondary inter- or intragranular porosity and grain fractures. Microporosity

is generally associated with authigenic clays both lining intergranular and secondary intragranular pores (Figures 2.11, 2.16, and 2.20A). Some of the intergranular porosity observed in the RSWC (4937.0ft) with the best porosity (12.4% ambient and 10.4% based on modal analysis) appears to be secondary based on the elongated nature of some pores (Schmidt and MacDonald, 1979; Figure 2.20B).

2.4.6 Detrital Matrix and Altered Grains

Detrital matrix based on modal analysis of RSWC and CC sandstone samples only comprises an average of 2.9% and ranges from absent to over 21.0% (fine-grained sandstone at 2890.0ft; Appendix G). Most of this clay is either pore filling clay, mica, or other silicates (the total averaging approximately 2%). A trace of this matrix material is concentrated along stylolites (Figures 2.12 and 2.19). There are also minor occurrences of infiltrated, pore-lining clays (average 0.1%; cutans) and detrital clay-rims (0.3%; Figure 2.15A). Some clay is due to alteration with the extreme example observed in the deepest RSWC recovered from 6140.0ft (Figure 2.21). In this sample it is difficult to distinguish detrital matrix from grains, possibly due to metasomatic alteration from an underlying dike or sill. (Rizer #1 test borehole was terminated at the top of an igneous body, which in the nearby Norris Ligthsey #1 well is relatively thick; Figure 1.1).

2.5 PETROLOGIC CHARACTERISTICS OF THE IGNEOUS BODIES

2.5.1 Classification and Geometry

The igneous bodies encountered within Rizer #1 test borehole were classified as altered alkali olivine basalts or diabases (Appendix F). Based on the Schlumberger FMI logs of Rizer #1, all the bodies, which coincided with RSWC's of igneous rocks, appear to dip at relatively high angles (50^o to 80^o) and strike in a variety of directions (Figures 2.22, 2.23, 2.24). Due to the high dip angles of these bodies, they are interpreted to be all intrusive dikes. These features also coincide with intervals of high angle fractures (Figures 2.22, 2.23, 2.24).

2.5.2 Rock Texture and Mineralogy

The sampled rocks are hypocrystalline to holocrystalline with generally subhedral to anhedral crystal geometries. Some of the fine groundmass or glass is replaced by authigenic chlorite. Detailed descriptions of and photomicrographs of these samples can be viewed in Appendix H (Plates 5, 6, 12, and 13). Primary minerals are plagioclase (Figures 2.22B and 2.23) with lesser abundances of pyroxenes, remnants of olivine (Figures 2.22A and 2.24C), sanidine, partially devitrified volcanic glass, and magnetite. Secondary minerals include fibrous amphibole replacing olivine, chlorite replacing volcanic glass, calcite, microcrystalline quartz, and a trace amount of pyrite or ilmenite replacing magnetite (Figure 2.24B). No porosity was observed within these samples in thin section, but measured porosity averages 3.9%, slightly higher than average porosity for all RSWCs analyzed.

2.5.3 Secondary Minerals

The major secondary minerals present appear to be fibrous amphiboles and chlorite clay generally replacing olivines, pyroxenes, and/or glassy matrix (Figures 22, 23, and 24). Also present is replacement by microcrystalline quartz, dolomite, and calcite (Figure 2.22A, 2.24B and 2.24C). Based on XRD analysis, RSWC of apparent basalts from 4091.0ft and 4113.0ft are comprised of 69 wt% and 21 wt% calcite and 19 wt% and 21 wt% chlorite, respectively (Appendix F).

2.6 PALEONTOLOGICAL RESULTS

2.6.1 Sample Analysis

Six cuttings samples in the interval of 2070ft to 5910ft, were analyzed for their palynological content in order to assess their age, environment of deposition, and organic matter typing as well as thermal maturity. The first sample (2070-2090ft) was quite productive of palynomorphs and appears to be Late Cretaceous and marine (nearshore). This interval was recovered from the Middendorf Formation, which is interpreted to be Santonian to Coniacian/Turonian in age (Colquhoun et al., 1983). The second sample (3225ft-3245ft) had little recovery of organic matter and a rather meager flora was recovered, characterized by rare occurrences of Late Cretaceous dinocysts indicative of a marine depositional setting. The third sample (4360ft-4380ft) showed little recovery of organic matter as well, with rare occurrences of Late Cretaceous spores (no younger than Latest Maastrichtian and no older than Turonian) suggesting, perhaps, a nonmarine to very nearshore/transitional depositional setting. Since both the samples from 3225ft-3245ft and 4360ft-4380ft were recovered well within the strata considered to be Late Triassic to Early Jurassic in age, the dinocysts and pores probably are from cavings. The last three samples were too thermally mature to be able to identify palynomorphs beyond spore sp. indeterminate. Three conventional core samples taken from 6000.70ft to 6057.00ft are barren of palynomorphs and therefore age indeterminate. For the most part, however, the organic matter suggests these samples represent a nonmarine setting, and where plant tissue is observed, the coloration (dark black-brown) indicates a Staplin TAI at approximately 4.4+. This is considered to be very mature and in the gas window (Staplin, 1969; Appendix L).

Petrographic examination of cuttings from 2630ft-2640ft also only found fossils from Cretaceous-age or younger. Limestone fragments, which were picked from an interval with largely well cemented sandstone fragments, are skeletal grainstones comprised of undifferentiated planktonic foraminifera tests (Appendix L).

Since all identifiable fossils recovered from the study interval fit the ages of the Upper Cretaceous portion of the overlying Coastal Plain sediments (Pee Dee to Middendorf formations; Colquhoun et al., 1983) they are judged to be derived from cavings.

2.7 DISCUSSION

Although it is difficult to accurately interpret the depositional history of a basin based on limited samples from a single borehole, the results appear to agree with interpretations from past paleogeography studies (Olsen, 1997; Withjack et al., 2012).

Post burial compaction and diagenesis will be discussed in the following section 3.0. The only post depositional features described in this section are the igneous bodies encountered within the study interval.

2.7.1 Sediment Source

The study interval is sand-rich with a majority of the framework grains subangular to subrounded grains. Along with the lack of detrital clays, the high feldspar content and abundance of large, subangular, labile metamorphic grains (phyllites, schists) indicate relatively short transport distances and not a great deal of reworking prior to deposition. Since there is only one borehole in the data set it is not possible to determine direction of transport. The western margin of the SGRB is interpreted to be relatively steep based on seismic data (Figure 1.1). The composition of the sand- to granule-sized grains is consistent with a hypothesis of sediment sourced from the Piedmont rocks to the immediate west.

Ubiquitous monocrystalline quartz, potassium feldspar, and plagioclase feldspar are consistent with granitic source such as the nearby Carolina Zone. The Carolina Zone is the eastern most belt of metamorphic and igneous rocks that is presently exposed west of the Atlantic Coastal Plain (e.g. Hibbard et al. 2002; Figure 2.25). The Carolina Zone is overlain by Mesozoic rift basins which are concentrated along its exposed eastern margin and extends in the subsurface under the Atlantic Coastal Plain eastward to the East Coast magnetic anomaly (e.g. Horten et al., 1989; Hall, 1990). There are a number of terranes which comprise the Carolina Zone, but two stand out as possible sources for igneous and metamorphic detritus within the South Georgia rift basin. These are the Carolina terrane and Charlotte terrane. The Carolina terrane is the eastern most belt in the Carolina Zone and consists of low-grade metamorphosed, sedimentary, and felsic intrusive and volcanic rocks. Igneous rocks in the Carolina terrane have been dated between 635 and 610 Ma. The Charlotte terrane is dominated by Neoproterozoic and late Paleozoic plutonic rocks that intrude metavolcanic rocks with minor quartzite, mica schist, phyllite and marble. The Charlotte terrane lies to the west of the Carolina terrane.

2.7.2 Depositional Setting

The overall interpretation of the deposition setting of the study interval is an alluvial system with fluvial braided to meandering channels with thin fine-grained overbank deposits intercalated with lacustrine coastal flats and deltas. Interpretation of the depositional setting of the study sequence in Rizer #1 is based on the sedimentary character of the conventional core recovered (6000.00ft–6057.20ft) and observation of

the fabric and composition of the RSWC samples recovered. The fluvial channel and lacustrine coastal deposit interpretations are based almost wholly on the CC description. The interpretation that lacustrine processes were present is partly based on the CC description (physical and biogenic structures observed) and the abundance of intrabasinal clasts of micrite in both the CC and RSWC samples (Figures 2.6 and 2.8). The preclusion of marine influence is based on numerous paleogeographic reconstructions which place the SGRB far inland within a still dividing Pangea (Figure 1.3; Olsen, 1997; Withjack et al., 2012) and on the lack of marine fossils recovered that are Jurassic or Late Triassic in age. The depositional setting interpreted in this study supports hypotheses of past regional studies who theorized "…Carnian through Norian- age strata is characterized by apparent drying with shallow-water cyclical lacustrine strata predominating in the southern and central basins" (Withjack et al., 2012 after Olsen and Kent, 2000; Olsen, 1997).

2.7.3 Igneous Intrusives

All the igneous bodies identified and examined from Rizer #1 test borehole are interpreted to be intrusive dikes based on their high angle of dip (50^o to 80^o) and thin character (2ft to 3ft [< 1m]; Figures 2.22, 2.23, and 2.24). Compositionally they classified as altered alkali olivine basalts or diabases (Appendix H). This appears to vary in composition from the slightly altered tholeiitic basalts present in the Clubhouse Crossroads Test Hole No. 3 (Appendix R) and reported by Gottfried et al. (1983). Without detailed elemental analysis of the Rizer #1 intrusive basalts, however, it is not possible to determine absolutely if they are related to the extrusive basalt flows cored in the Clubhouse Crossroads Test Hole No. 3. (Perhaps, future studies of the Rizer #1 intrusives could make this determination.) It is hypothesized in the literature that within the southern segment of the rift system, igneous sheets and NW and N-striking dikes are associated with CAMP event, essentially occurring around 200 Ma (Olsen, 1997; Withjack et al., 2012).

The prevalence of low-temperature secondary replacement by calcite, dolomite, and chlorite indicates deuteric alteration, possibly by groundwater flow through the numerous fractures associated with the dikes (Figures 2.22, 2.23, 2.24). Based on other studies of dikes within sedimentary strata, stress fractures and joints formed within the dikes and host rock due to the heating and cooling associated with the injection of the diabase/basalt (Keane et al., 2012; NCDENR, 2012). Studies of dikes within Triassic basins of North Carolina indicate "… the presence of dikes increases the probability of differential weathering, which could enhance groundwater movement along contact of the dike with adjacent country rock" (NCDENR, 2012).

2.8 CONCLUSIONS

1. The depositional setting for the conventionally cored interval of Rizer #1 test borehole, and probably the majority of the pre-Cretaceous strata penetrated, is primarily alluvial associated with lacustrine coastal deposits. The alluvial facies are comprised of braided and meandering channel-fill or lacustrine delta deposits.

2. The sandstone recovered within the RSWC are generally lithic arkoses to arkosic litharenites based on the classification of Folk (1980) with lithics comprised primarily of metamorphic rock fragments.
3. The sandstones are predominantly cemented with quartz or calcite cements, with lessor abundances of authigenic sphene, and pyrite and isolated occurrence of evaporite cement.
4. Based on modal analysis of the 34 thin sections, total porosity averages 3.2%, which supports the finding of the routine core analysis (103 RSWC and 41 CC samples).
5. Detrital matrix based on modal analysis of RSWC and CC sandstone samples only comprises an average of 2.9% and ranges from absent to over 21.0%.
6. The igneous bodies encountered are classified as altered alkali olivine basalts or diabases. Due to the high dip angles of these bodies, they are interpreted to be intrusive dikes. These features also coincide with intervals of high angle fractures.
7. Paleontological examination of RSWC, CC, and selected cuttings samples found no Triassic or Jurassic aged fossils. Since all identifiable fossils recovered from the study interval fit the ages of the Upper Cretaceous portion of the overlying Coastal Plain sediments (Pee Dee to Middendorf formations; Colquhoun et al., 1983) they are judged to be derived from cavings.

2.9 CITATIONS

Colquhoun, D. J., Woollen, L. D., Van Nienwenhuise, D. S., Padgett, G. G., Oldham, R. W., Boylan, D. C., Bishop, J. W., and Howell, P. D., 1983, Surface and subsurface stratigraphy, structure and aquifers of the South Carolina Coastal Plain: Columbia, SC, State of South Carolina, Office of the Governor, 78 p.

Folk, R. L., 1968, Petrology of Sedimentary Rocks: Austin, University of Texas Publication, 170 p.

Gottfried, D., Annell, C. S., and Byerly, G.R., 1983, Geochemistry and tectonic significance of subsurface basalts near Charleston, South CarolinaL Clubhouse Crossroads test holes #2 and #3, *in* Gohn, G.S., ed., Studies related to the Charleston, South Carolina earthquake of 1886-Tectonics and Seismicity: U.S. Geological Survey Professional Paper 1313, p. A1-A19.

Hall, D.J., 1990. Gulf Coast-East Coast magnetic anomaly I: Root of the main crustal decollement for the Appalachian-Ouachita orogen: Geology, v. 18, p. 862-865.

Harris, P.M., Ellis, J., and Purkis, S.J., 2013, Assessing the extent of carbonate deposition in early rift settings: American Association of Petroleum Geologists Bulletin, v. 97, p. 27-60.

Hibbard, J.P., Stoddard, E.F., Secor, D.T., and Dennis, A.J. 2002. The Carolina Zone: overview of Neoproterozoic to early Paleozoic peri-Gondwanan terranes along the eastern flank of the southern Appalachians. Earth-Science Reviews, v. 57, p. 299–339.

Horton, W., Drake, A., Rankin, D., 1989. Tectonostratigraphic terranes and their Paleozoic boundaries in the central and southern Appalachians. In: Dallmeyer, D. (Ed.), Terranes in the Circum-Atlantic Paleozoic Orogens. Geological Society of America Special Paper, v. 230, p. 213– 245.

Keane, J. and T. Gilstrap, 2012, Delineation of mafic intrusions near Bedford (Virginia, USA) using geological and geophysical methods: Environ Earth Sci., v 66, p 1393-1402.

NCDENR, 2012, Final North Carolina Oil and Gas Study: North Carolina Department of Environment and Natural Resources, pp. 327.

Olsen, P.E., 1997, Stratigraphic record of the early Mesozoic breakup of Pangea in the Laurasia-Gondwana rift system: Annual Reviews of Earth and Planetary Science, v 25, p 337-401.

Olsen, P.E., and Kent, D.V., 2000, High resolution early Mesozoic Pangean climatic transect in lacustrine environments, *in* Bachmann, G., and Lerche, I.(eds.), Epicontinental Triassic: Zentrablatt fur Geologie und Palaontologie, v 3, VIII, p 1475-1496.

Schmidt, V. and MacDonald, D.A., 1979, The role of secondary porosity in the course of sandstone diagenesis: Aspects of Diagenesis: SEPM Special Publication 26, p. 175-208.

Staplin, F.L., 1969, Sedimentary Organic matter, organic metamorphism and oil and gas occurrence. Bull. Can. Pet. Geology, 17:47-66.

Reineck, H.E., 1975, German North Sea tidal flats, in Ginsburg, R.N. (ed.), Tidal Deposits A Casebook of Recent Examples and Fossil Counterparts: Spring-Verlag, New York, Heidelberg, Berlin, p 5-12.

Withjack, M. O., Schlische, R.W., and Olsen, P. E., 2012, Development of the passive margin of eastern North America: Mesozoic rifting, igneous activity, and breakup. In: Bally, A. W. & Roberts, D. G. (eds), Principles of Phanerozoic Regional Geology, v. 1, Elsevier, Amsterdam, p. 301–335.

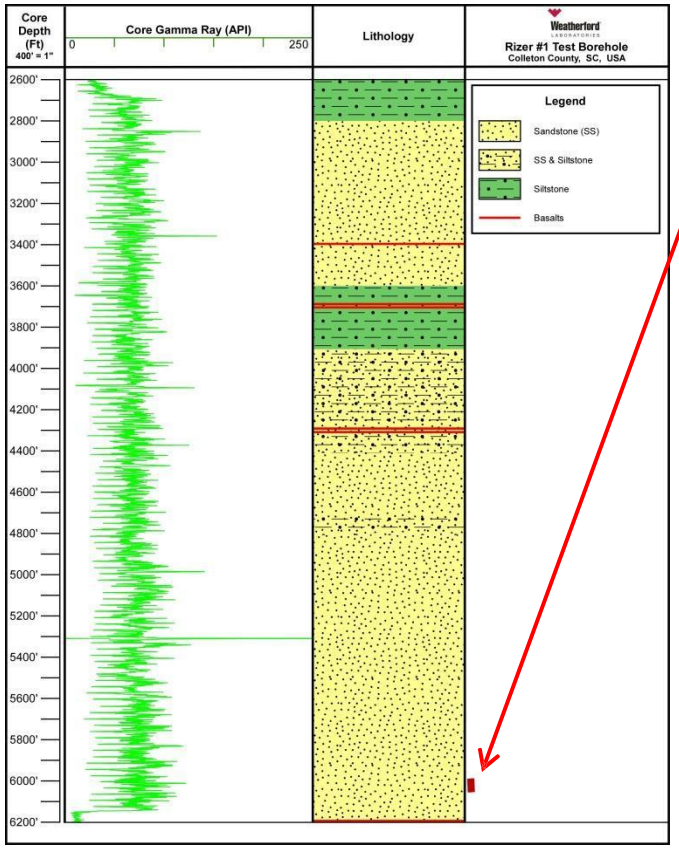

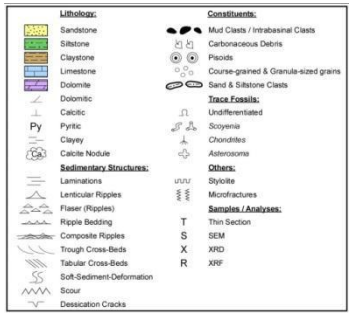

Figure 2.1 Graphic description of conventional core from Rizer #1 (6000.00ft – 6057.20ft) plotted with core gamma logs (total and spectral). Total Rizer #1 stratigraphy based on borehole lithology log.

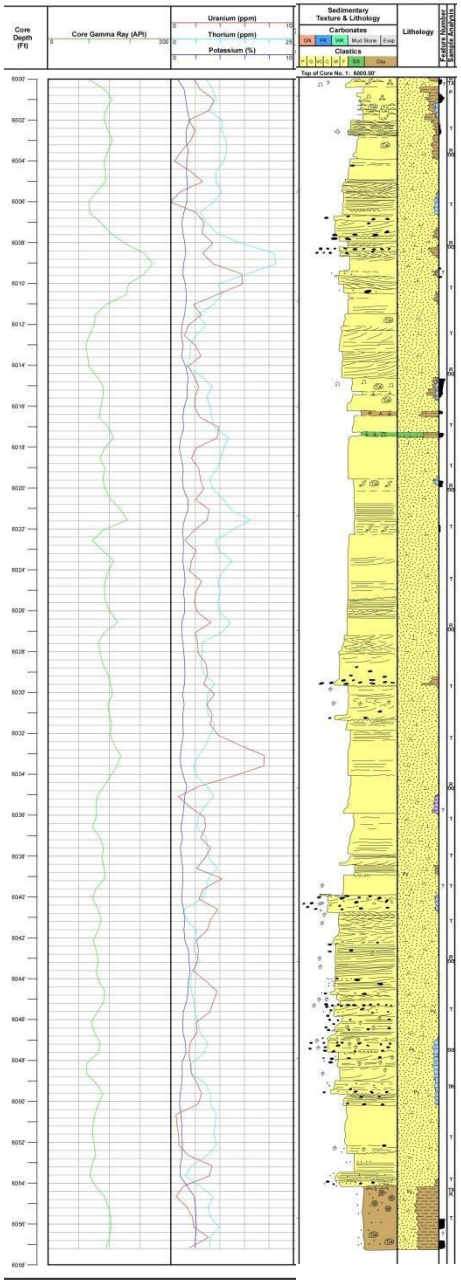

Interlayered Mudstones and Ripple-Bedded Sandstones (*Wind Tidal Flat;* 6000.00ft to 6002.90ft)

Stacked, Cross-Bedded, Medium- to Fine-Grained Sandstone Beds (*Braided Channel;* 6002.90ft to 6014.70ft)

Fining Upward, Large-scale Cross-bedded and Laminated to Burrowed, Medium- to Very Fine-Grained Sandstone (*Lacustrine Delta Channel;* 6014.70ft to 6031.40ft)

Stacked, Laminated, Very Fine- to Fine-Grained Sandstone (*Sandy Overbank Deposits;* 6031.40ft to 6039.90ft)

Stacked, Cross-Bedded, Medium- to Coarse-Grained Sandstone (*Braided Channel;* 6039.90ft to 6049.60ft)

Laminated to Cross-Bedded, Very Five to Medium-Grained Sandstone (*Fluvial Channel;* 6049.60ft to 6054.10ft)

Sandy Mudstone (*Overbank Alluvium;* 6054.10ft to 6057.20ft)

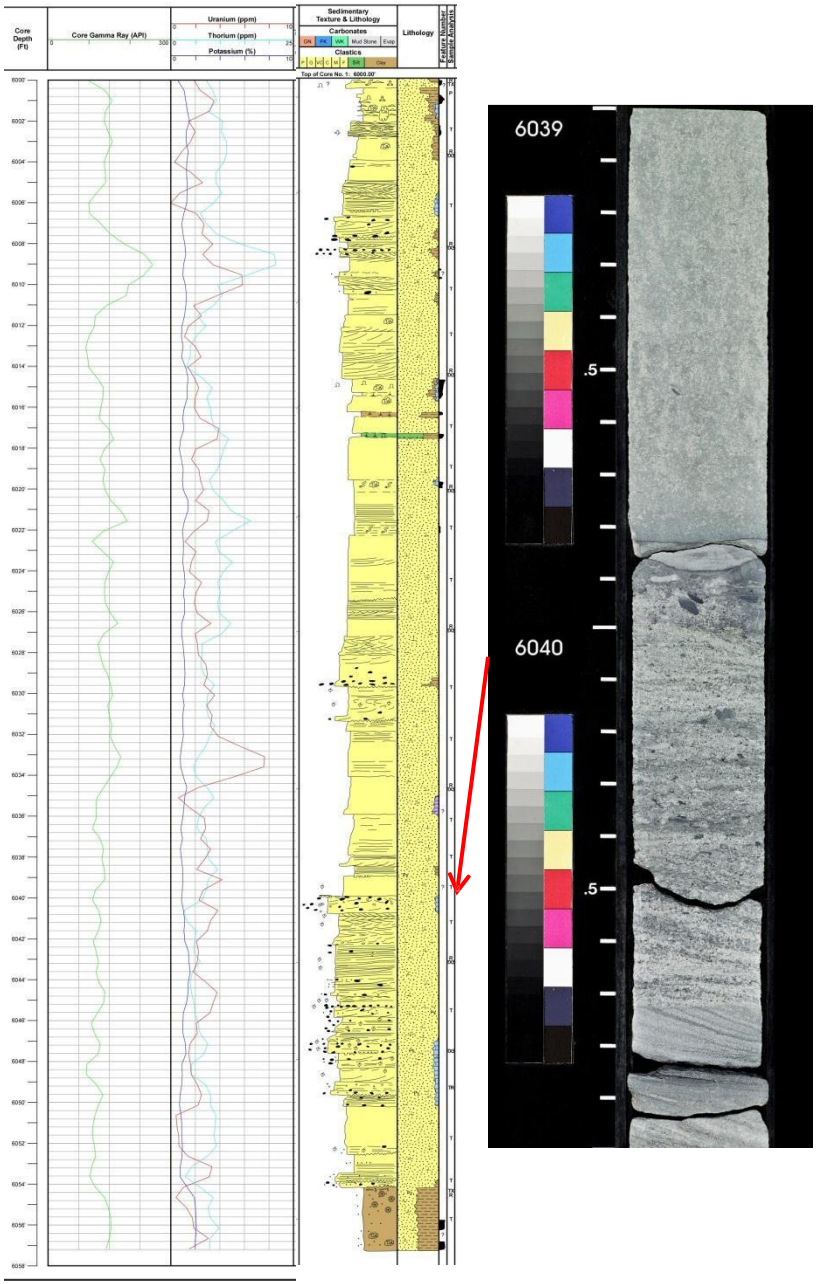

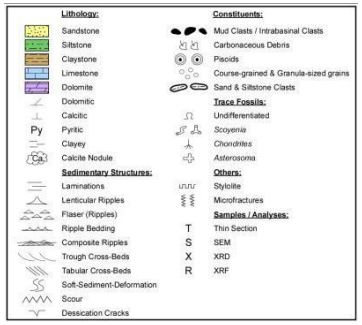

Very fine- to fine-grained sandstone within an alluvial overbank

Cross-bedded, medium to coarse-grained sandstone within a braided channel setting

Figure 2.2 Graphic description of conventional core from Rizer #1 test borehole (6000.00ft - 6057.20ft) with photograph of slabbed core between 6039.00ft and 6041.00ft. Photograph is of cross-bedded, medium to coarse-grained sandstone within a braided channel deposit abruptly overlain by very fine- to fine-grained sandstone apparently deposited within an alluvial overbank setting.

Figure 2.3 Macro photograph shows textural layering and inclined cross bedding. Potassium feldspar is stained yellow and calcite is stained pink. Irregular clay-lined stylolites are present throughout the thin section. Intrabasinal clasts are comprised of micrite (stained pink), clay (brown), and micrite-bound fine-grained sand clast (upper right quadrant). Sample is from CC at 6040.18ft.

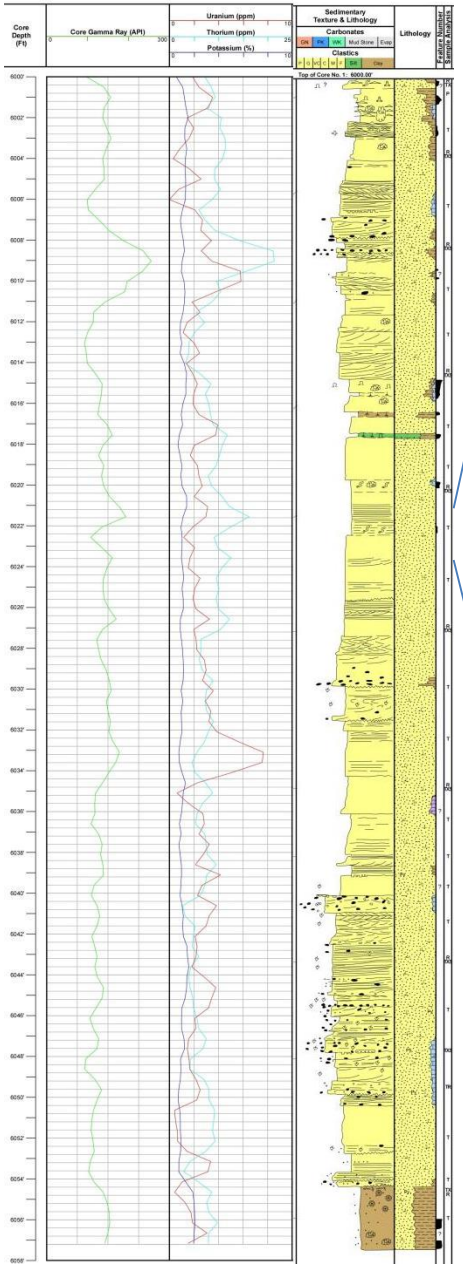

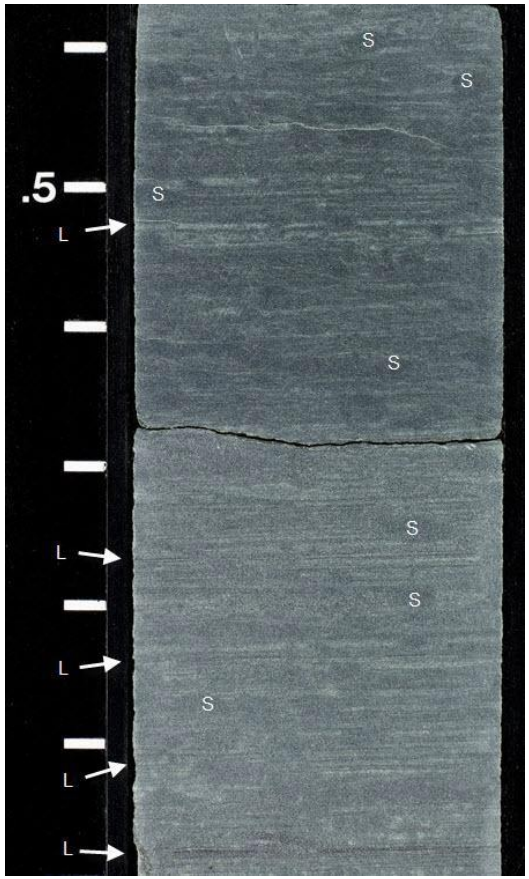

6021.40ft

6022.00ft

Figure 2.4 Graphic description of conventional core from Rizer #1 test borehole (6000.00ft – 6057.20ft) with photograph of slabbed core between 6021.40ft and 6022.00ft). This package is interpreted to be a fluvial/deltaic because of the presence of *Scoyenia*-like (S), which appear to disturb laminations (L).

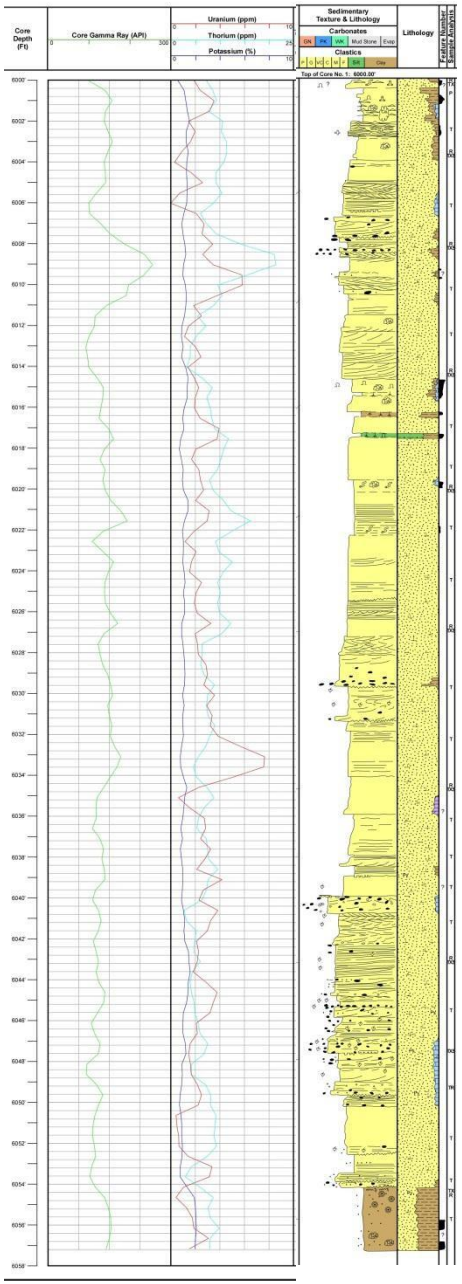

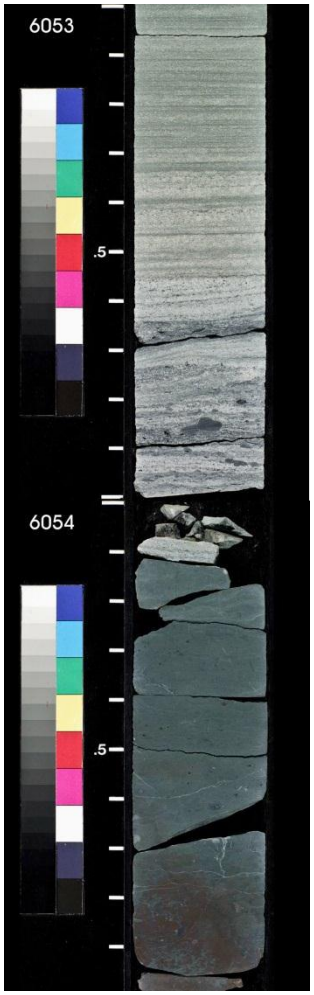

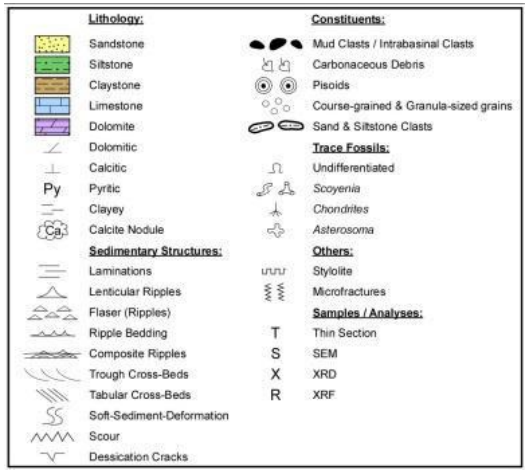

Figure 2.5 Graphic description of conventional core from Rizer #1 test borehole (6000.00ft – 6057.20ft) with photograph of slabbed core between 6039.00ft and 6041.00ft. Photograph is of the basal portion of a small fluvial channel-fill (6049.60ft to 6054.10ft) overlying an erosion surface at the top of a weathered package of sandy mudstone alluvium (6054.10ft to 6057.20ft).

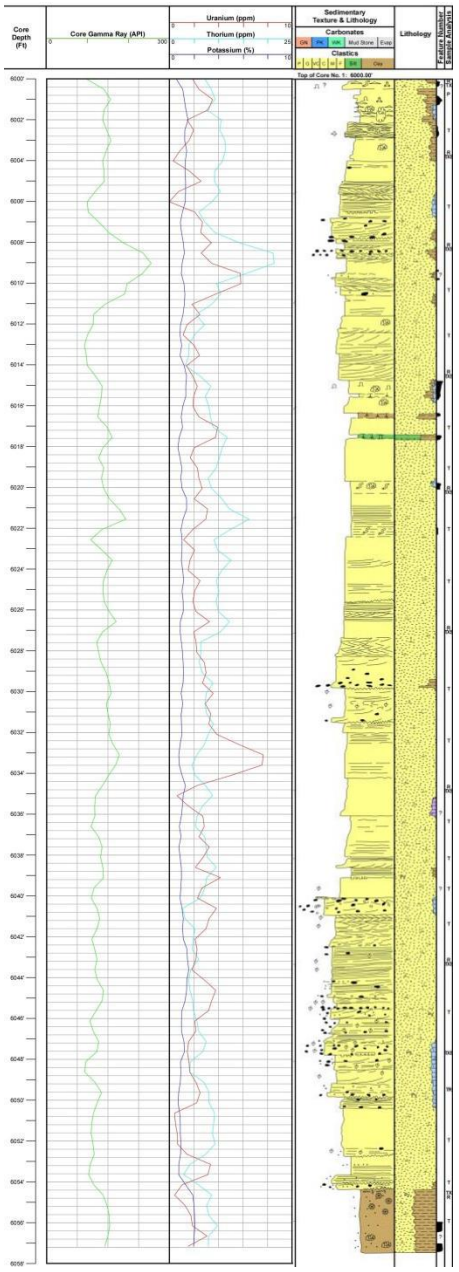

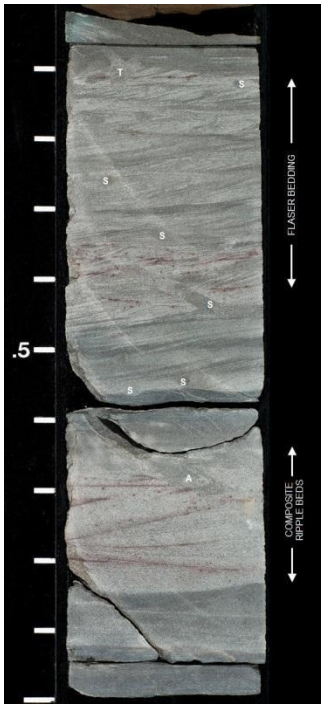

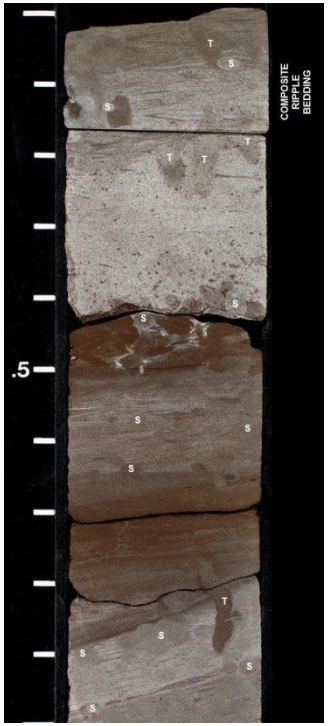

6000.00ft

6002.00ft

A

6001.00ft

B

6003.00ft

Figure 2.6 Graphic description of conventional core from Rizer #1 test borehole (6000.00ft – 6057.20ft) with photographs of slabbed core between 6000.00ft to 6003.00ft. A. The cored interval is interbedded mudstones and sandstones with some ripple bedding but more common burrow traces of horizontal *Scoyenia* (S) and near-vertical *Scoyenia* (T). B. Both flaser bedding and composite ripple bedding (current and wave ripples) are common. Also present are burrow traces of horizontal *Scoyenia* (S), near-vertical *Scoyenia* (T), and an *Asterosoma*- like burrow (A).

Figure 2.7 Photomicrograph of CC sample from 6045.50ft shows examples of lacustrine influence with the presence of phosphatic fish fragments (FP) and micritic intrabasinal clasts (CC). A majority of the grains in this moderately sorted sandstone are quartz and plagioclase (white) and potassium (stained yellow; K). Other grains are comprised of mica (M), schist fragments (S), altered plagioclase (P), and lithics (L). Calcite is present as intergranular cement and replacing some grains (C; stained pink). Secondary intergranular and intragranular porosity is blue.

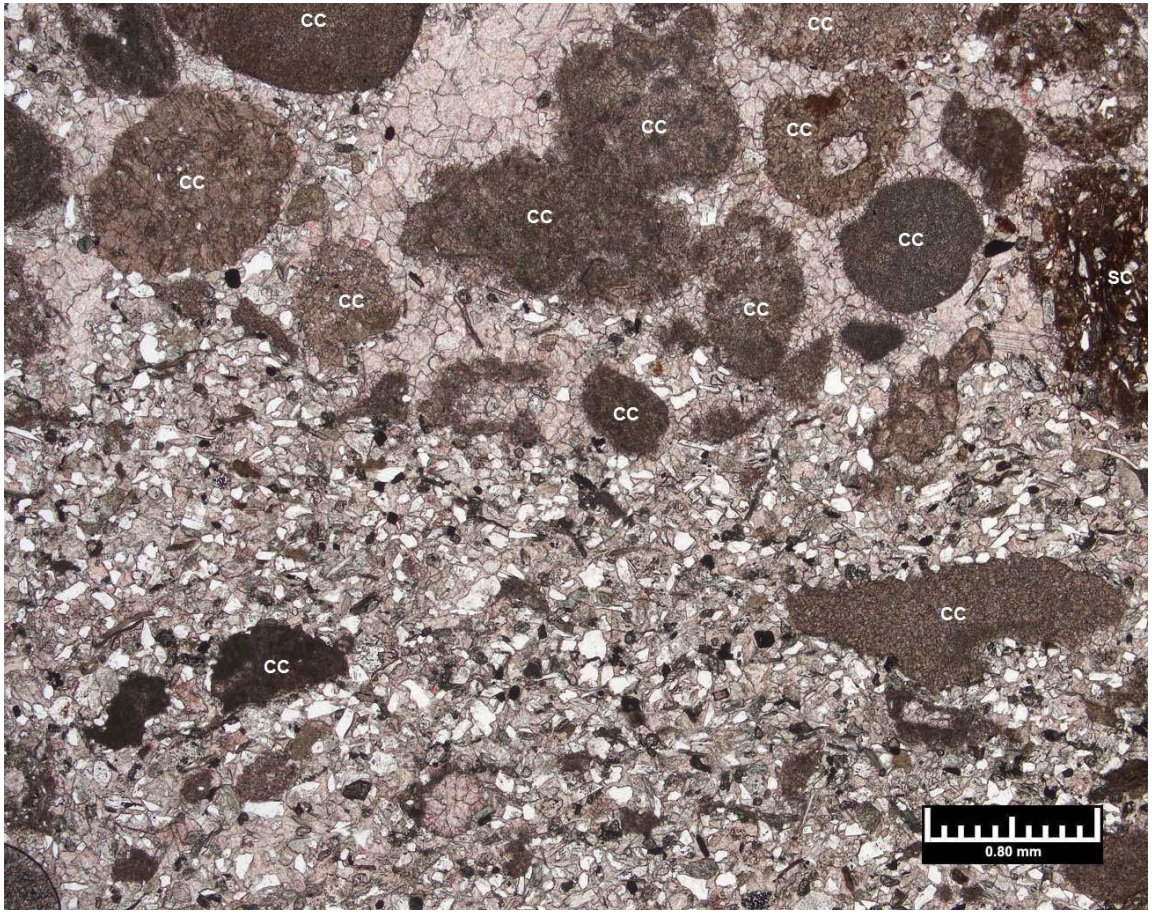

Figure 2.8 Photomicrograph of RSWC sample from 3845.50ft shows contact between very fine-grained sandstone layer (in lower 2/3's of field of view) with grainstone laminations of coarse-grained sand- to granule-sized micritic clasts (upper 1/3 of field of view). A majority of the clasts are comprised of micrite (CC) but some contain silt grains (SC). The rock is well cemented with calcite spar. Calcite is stained pink.

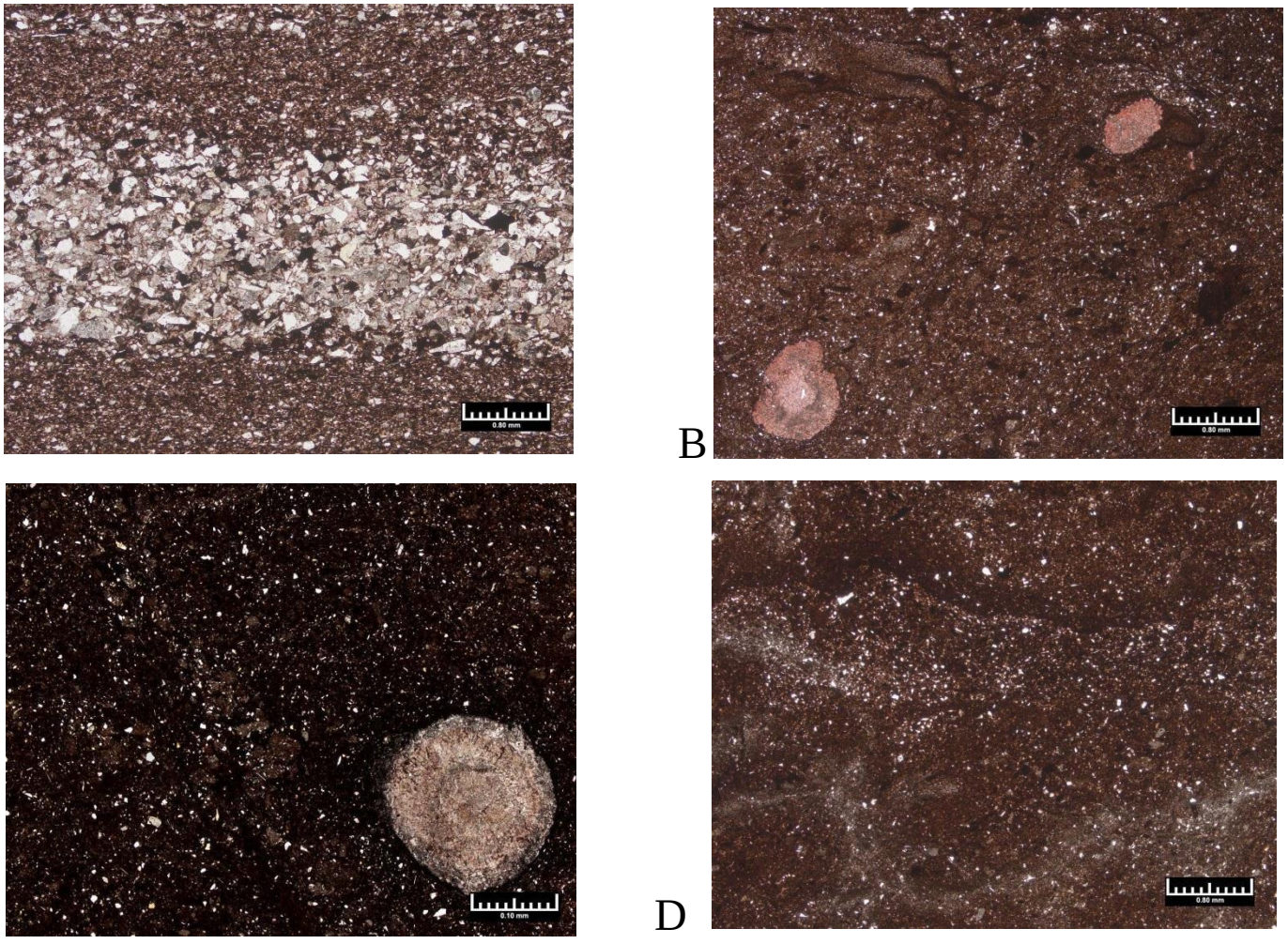

Figure 2.9 Photomicrographs of finer-grained strata within Rizer #1. A) A sandy siltstone from RSWC at 3916.5ft shows fine-grained sandstone lamination within a slightly clayey, siltstone. Lamination is cemented with calcite spar (stained pink). B) Very calcitic, clayey siltstone from RSWC at 5980.0ft with disturbed darker laminations with higher concentration of clay and carbonaceous debris and calcite spar infilling an irregular fracture, biogenic trace (root?), or a nodule. C) CC sample from 6055.10ft shows mottled texture of this silty clay with an incipient calcite nodule in lower right. D) RSWC from 6061.0ft shows mottled texture with clay-rich patches versus more silt-rich areas. Mottling is probably due to root disturbance and pedogenesis.

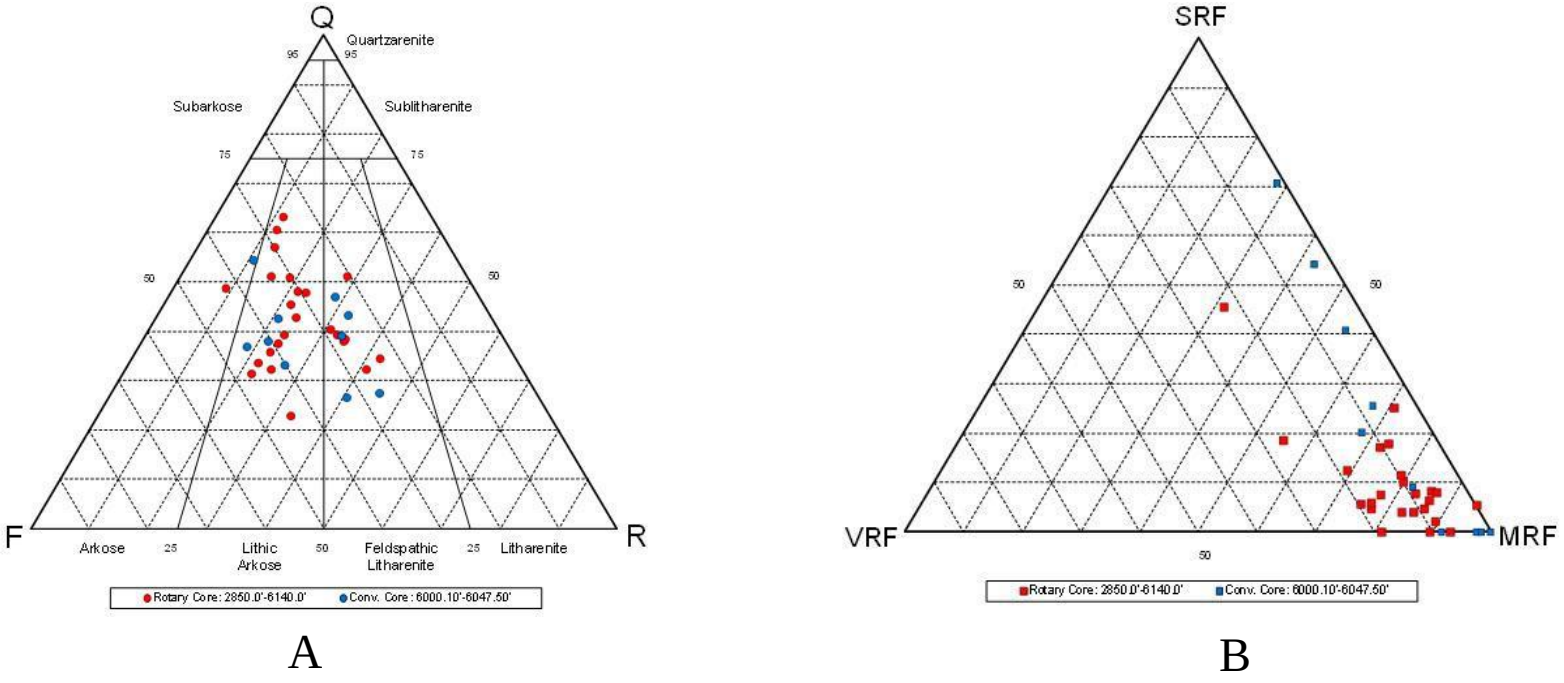

Figure 2.10 The ternary diagram (A) of relative abundances of quartz (Q), feldspar (F), and lithic fragments (L), which is based on modal analysis of twenty-four (24) RSWC and ten (10) CC samples, shows the majority of sandstones are lithic arkoses or feldspathic litharenites based on the classification of Folk (1980). The ternary diagram of lithic fragments (B) indicates the majority of rock fragments are metamorphic. Many of the grains classified as sedimentary rock fragments (SRF), however, are actually intrabasinal clasts of lacustrine micrite.

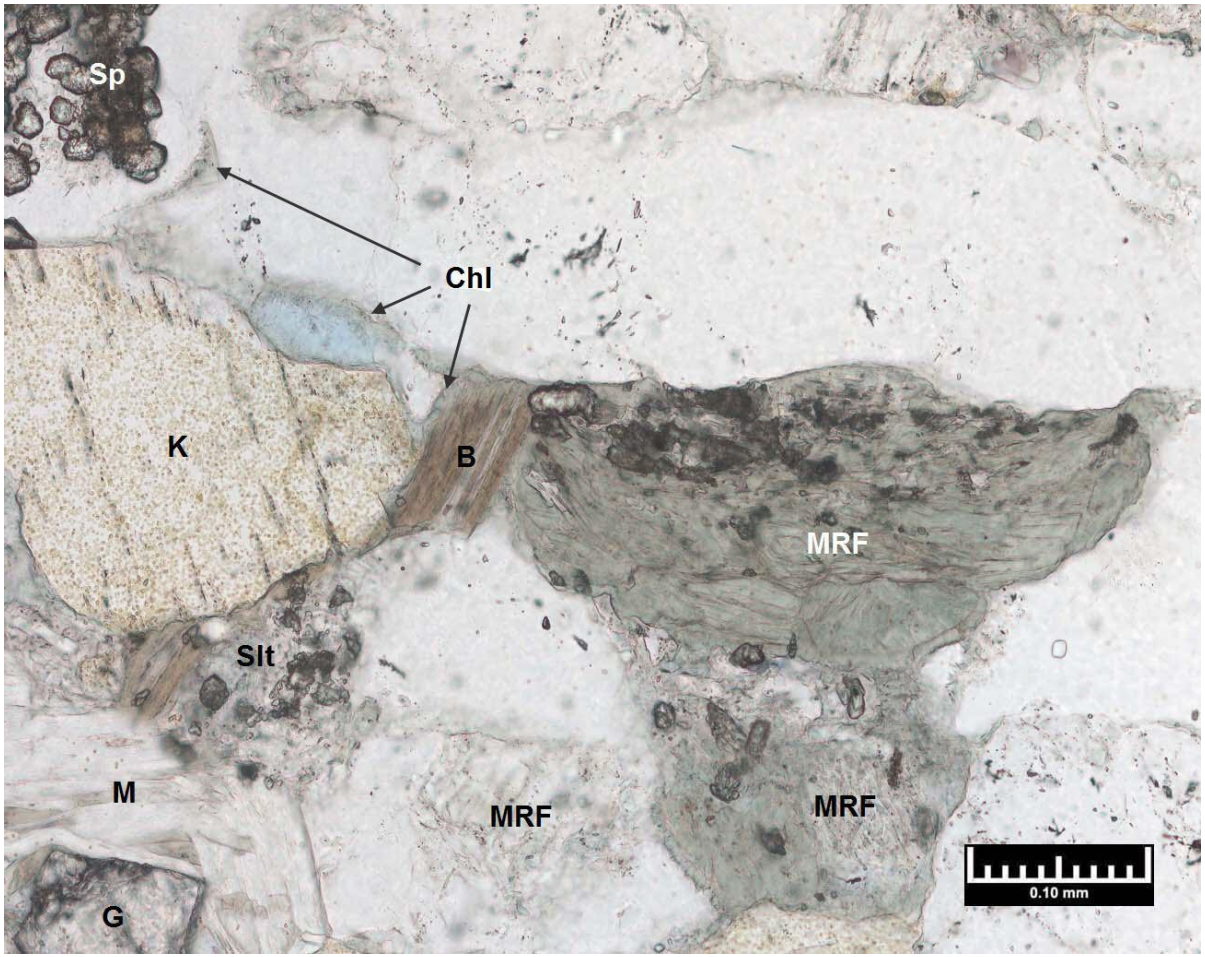

Figure 2.11 Photomicrograph of RSWC from 5775.0ft a moderately sorted, medium-grained sandstone show the abundance of lithic fragments, which are comprised of schistose metamorphic rock fragments (MRF), and biotite (B), deformed muscovite (M). Also common are grains of quartz (white), potassium feldspar (stained yellow; K), and heavy minerals (G; garnet). Platy chlorite (Chl) is lining intergranular pores (blue). Sphene (Sp) is engulfed within quartz overgrowth cement.

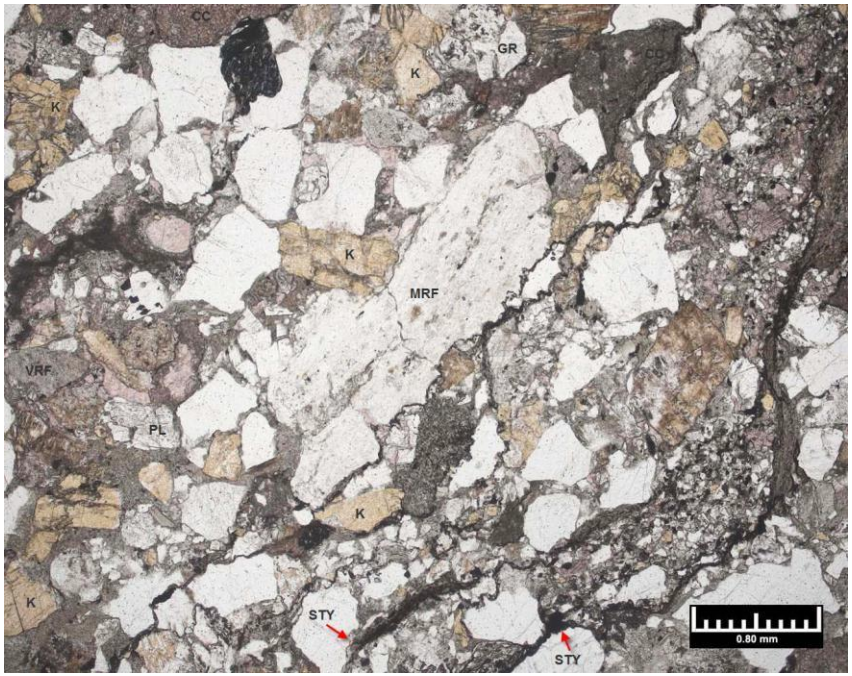

A

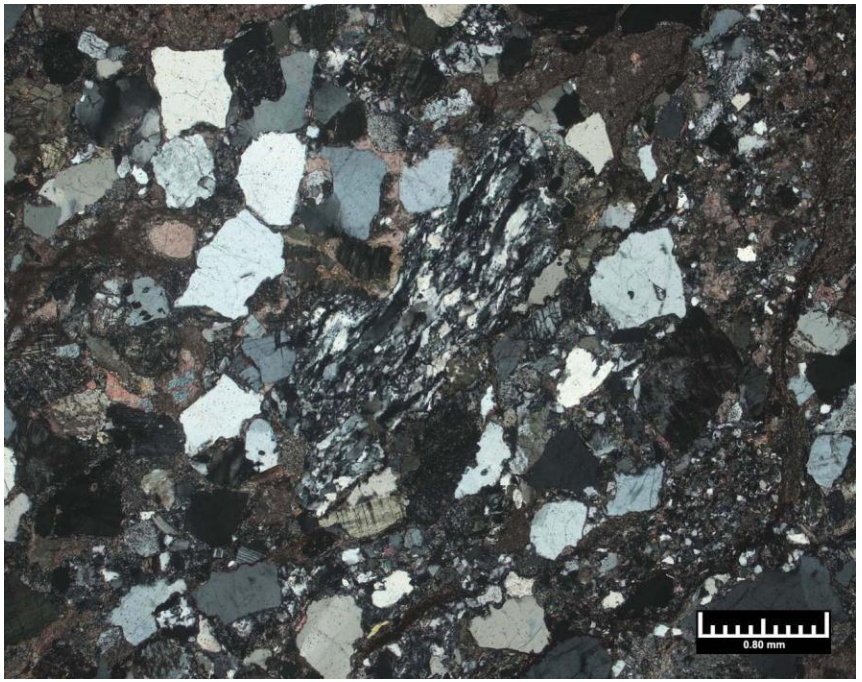

B

Figure 2.12 Photomicrographs from CC sample at 6040.18ft depict a slightly calcitic lithic arkose in plane white light (A) and crossed polarized light (B). Detrital minerals include monocrystalline quartz (white), metamorphic rock fragments (gneissic; MRF) volcanic (VRF), granite (or plutonic) rock fragments (GR), potassium feldspar (stained yellow; K), and plagioclase feldspar (PL). Clay, intrabasinal micrite, and siliciclastic mud clasts are compressed along the irregular surfaces of stylolites (STY).

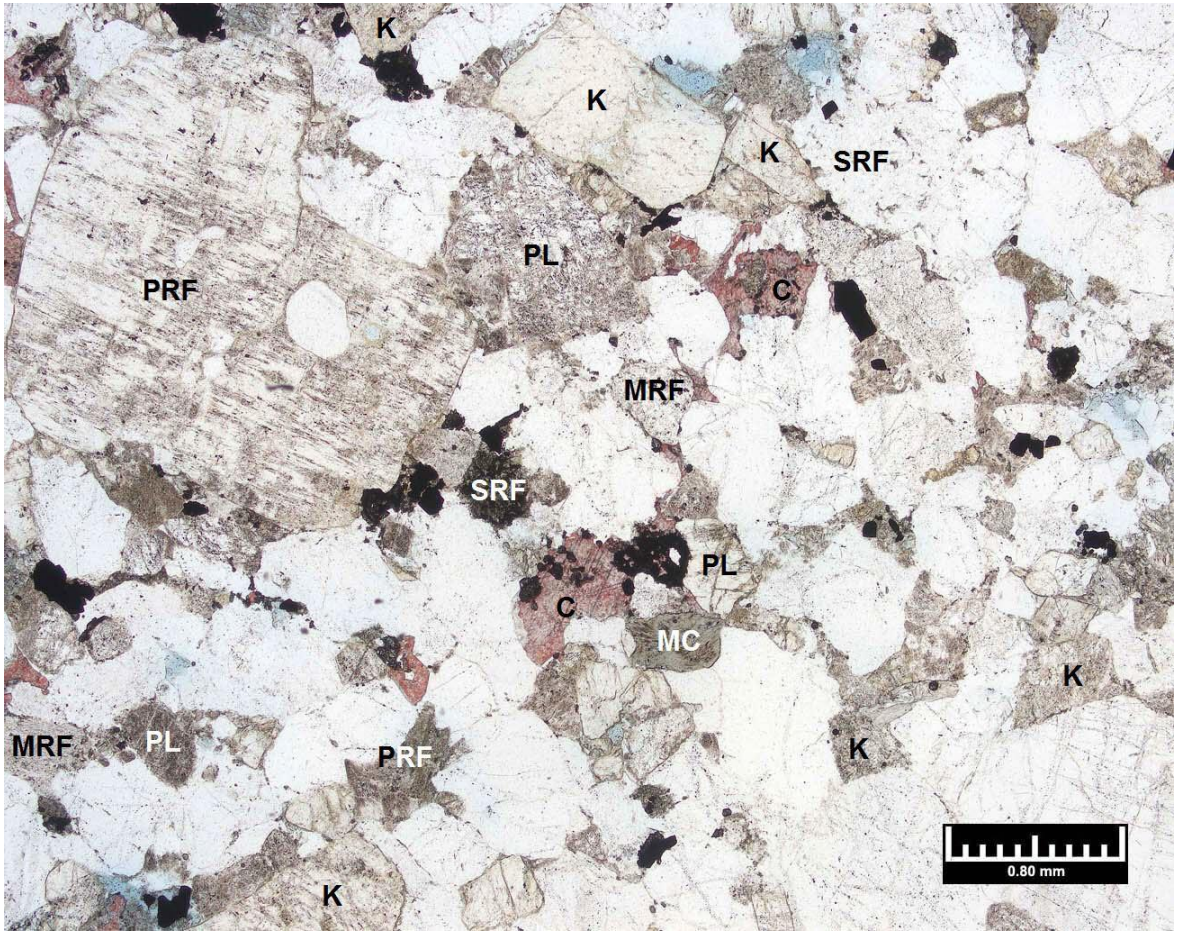

Figure 2.13 Photomicrograph of RSWC from 4788.0ft a poorly sorted, very coarse-grained sandstone show the abundance of lithic fragments, such as granule- to very fine-grained sand-sized plutonic rock fragments (PRF) and sand-sized metamorphic (MRF) and sedimentary rock fragments (SRF). Patches of calcite (C; stained pink) comprise intergranular cement and replacement of partial replacement of framework grains. Other detrital minerals include monocrystalline quartz (white), chlorite mica (MC), potassium feldspar (stained yellow; K), and plagioclase feldspar (PL). Porosity (blue) present in field of view is comprised of intergranular and secondary intragranular pores.

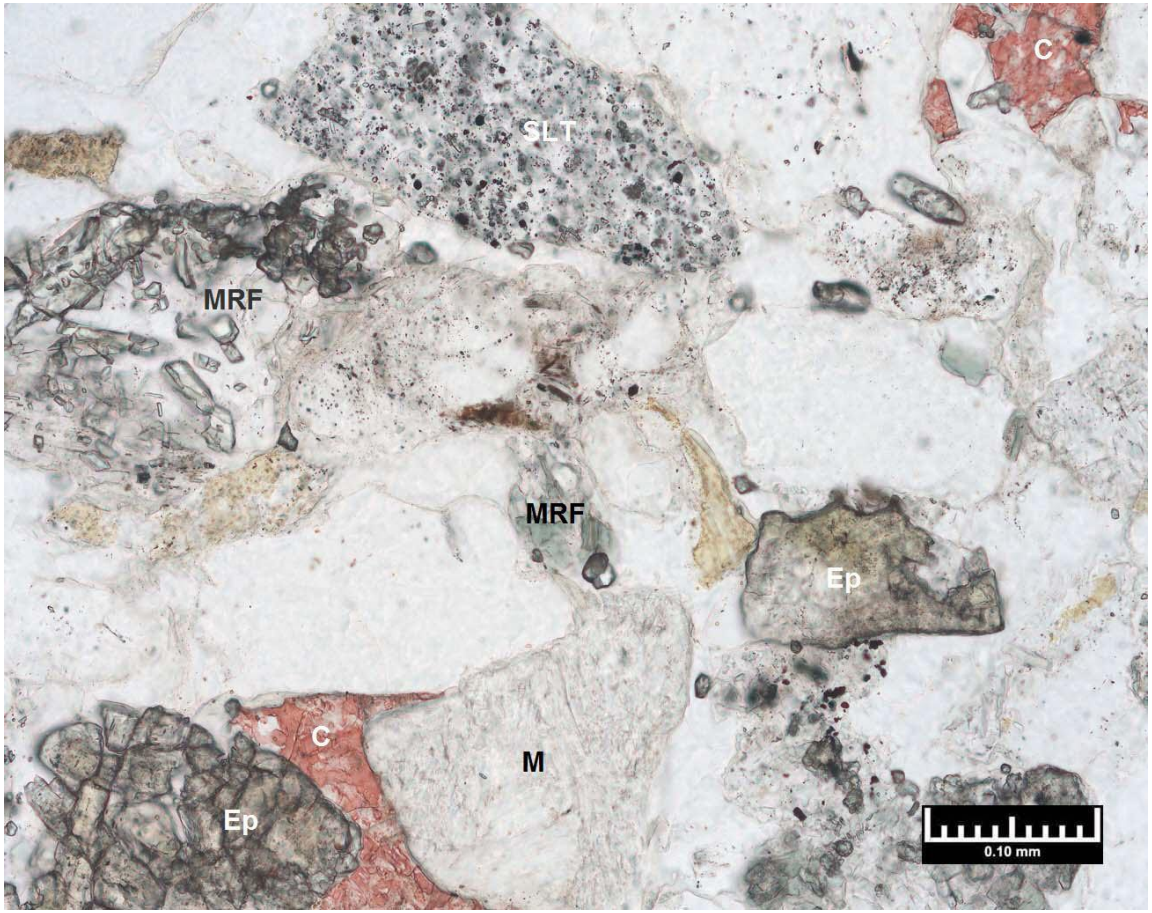

Figure 2.14 Photomicrograph of a RSWC from 5486.5ft, which is a moderately well sorted, fine-grained sandstone, shows the character of some of the lithic fragments present. In this field of view, lithics are comprised of fragments of siltstone (SLT) and metamorphic rocks (MRF). Also present are epidote (Ep) and muscovite mica (M). Grains of quartz (white) and potassium feldspar (stained yellow) are common. Intergranular pore spaces are infilled with calcite (stained red) or quartz (white).

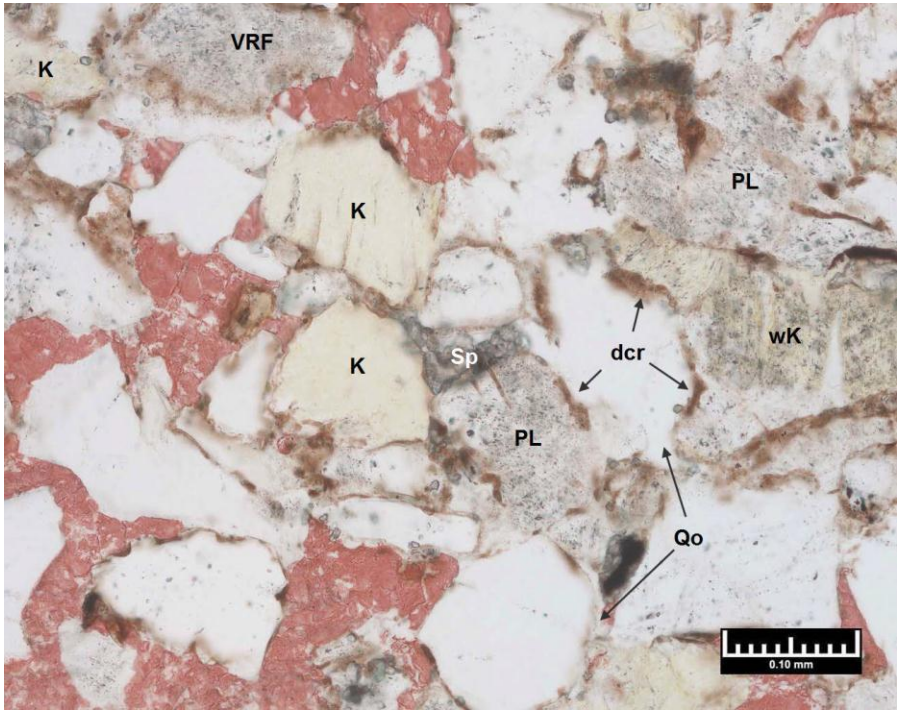

A

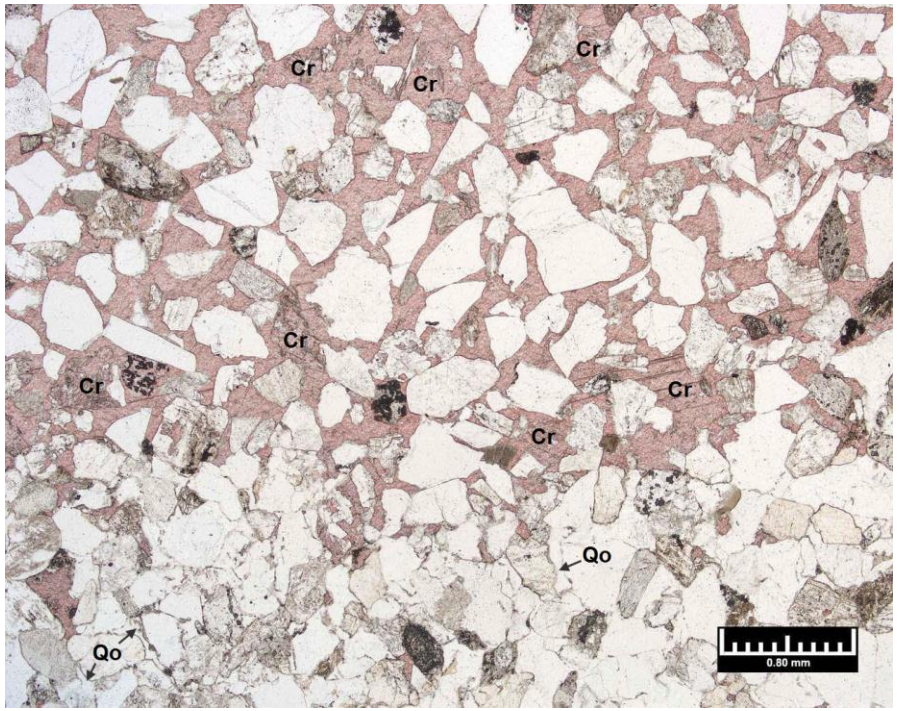

B

Figure 2.15 Photomicrographs show examples of calcite cement and grain replacement calcite (stained red) within selected samples. A. RSWC from 3674.0ft has abundant poikilitopic calcite cement (red) with only minor occurrences of quartz overgrowths (Qo) and sphene (Sp). Many quartz grains (white) are lined with detrital clay rims (brown, dcr). Other framework grains are potassium feldspar (K), weathered feldspar (wK), plagioclase (PL), and volcanic rock fragments (VRF). B. RSWC from 5338.0ft shows abundant poikilitopic calcite cement (red) in the upper two thirds of the field of view. Most of this calcite is infilling intergranular pores but some is replacing framework grains (Cr). Quartz overgrowth cement (Qo) is more common in the lower one third of the field of view. Degree of compaction appears to be greater in the lower one third of the field of view.

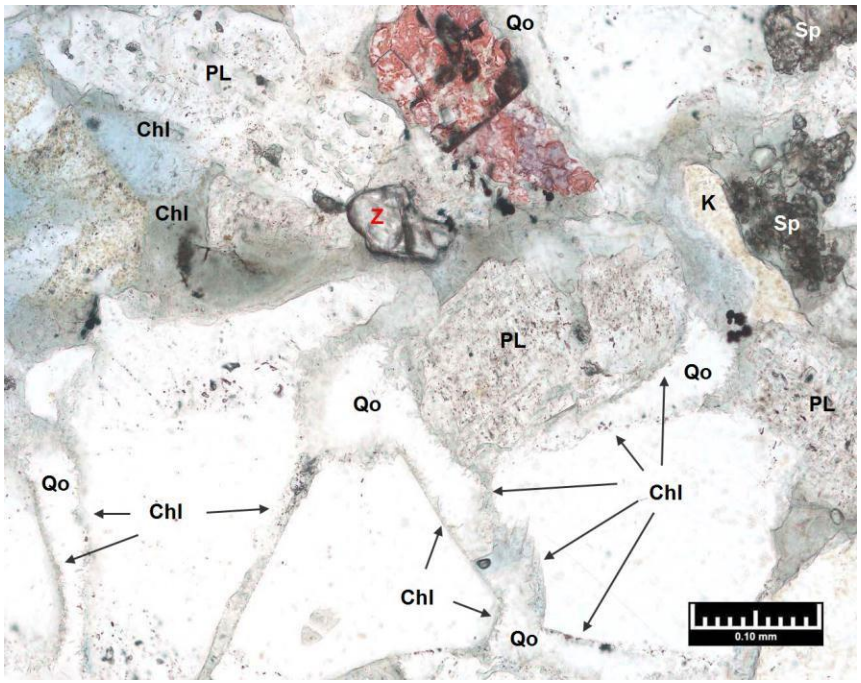

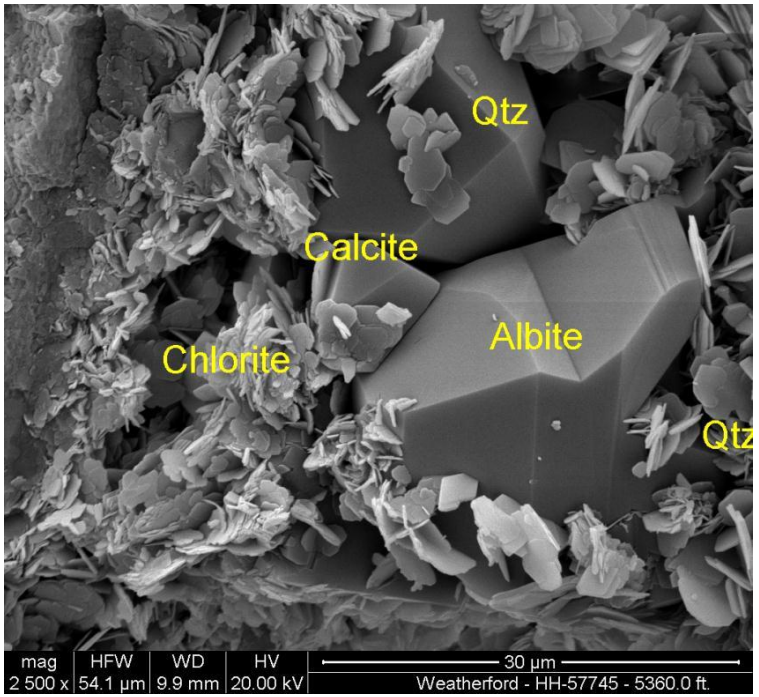

A B

Figure 2.16 A. Photomicrograph (with transmitted white light) of fine-grained lithic arkose in RSWC from 5360.0ft showing abundance of grain coating chlorite clay (Chl) with some being engulfed by quartz overgrowth cement (Qo). Patches of sphene cement are present (Sp). Calcite appears to be replacing a grain (stained red). Framework grains consist of quartz (white), plagioclase (PL), potassium feldspar (K), and zircon (Z). Porosity (blue) consists of secondary intragranular and microporosity associated with clays. B. SEM image of RSWC from 5360.0ft shows chlorite clay being engulfed by both albite and quartz overgrowth cements.

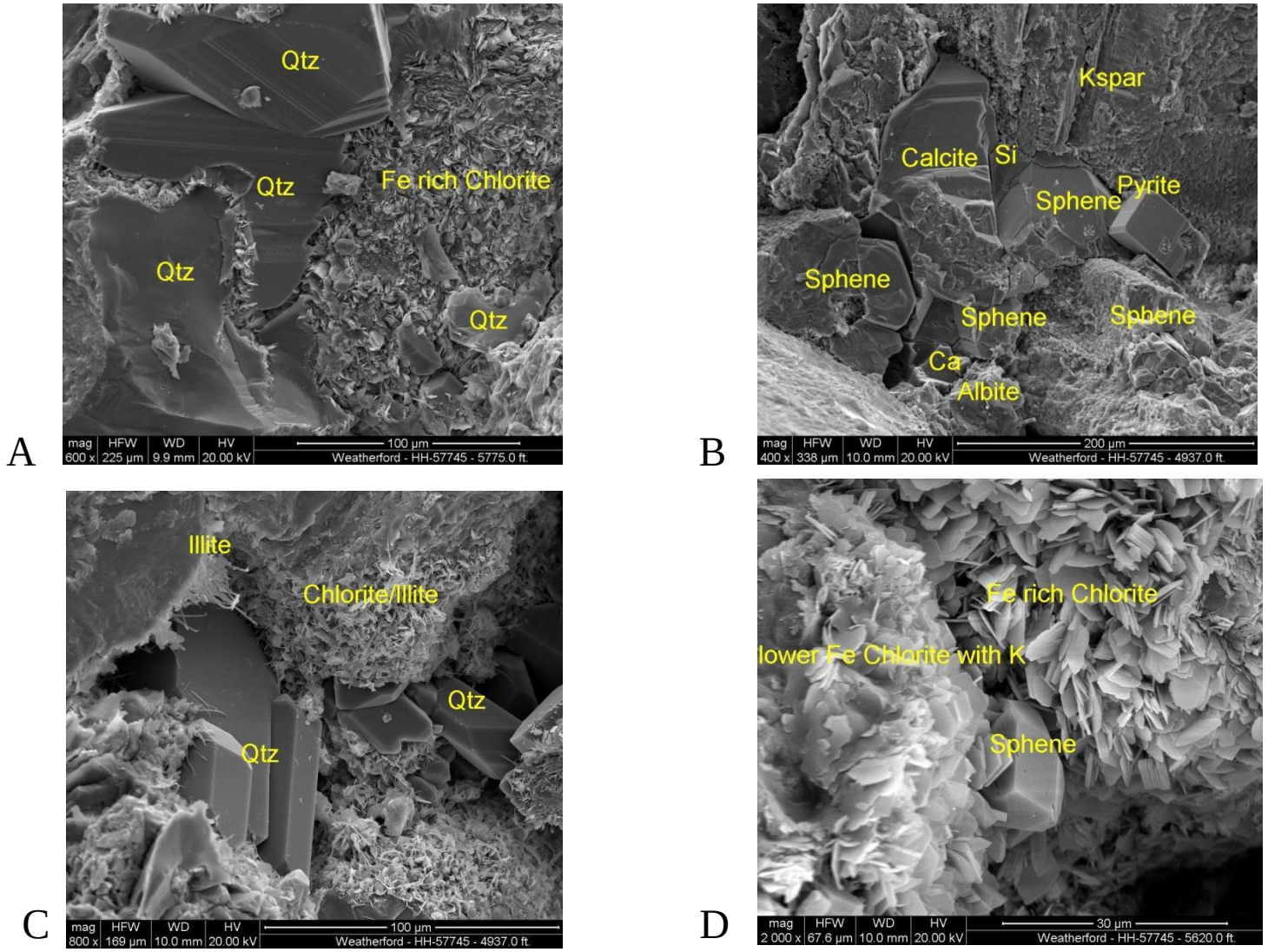

Figure 2.17 A. SEM image of RSWC from 5775.0ft shows Fe-rich chlorite (based on EDS) coating grain surfaces and being partially engulfed by quartz overgrowth cement. B. SEM image of RSWC from 4937.0ft shows the coincidence of authigenic sphene, calcite (Ca), and pyrite with framework grains of quartz (Si) and potassium feldspar (Kspar). C. SEM image of RSWC from 4937.0ft shows the coincidence of authigenic chlorite and illite clays with quartz overgrowth cement (Qtz). D. SEM image of RSWC from 5620.0ft shows the coincidence of two types of authigenic chlorite, one that is iron- rich (Fe rich chlorite) and one that is iron-poor with potassium (K). Also present is authigenic sphene.

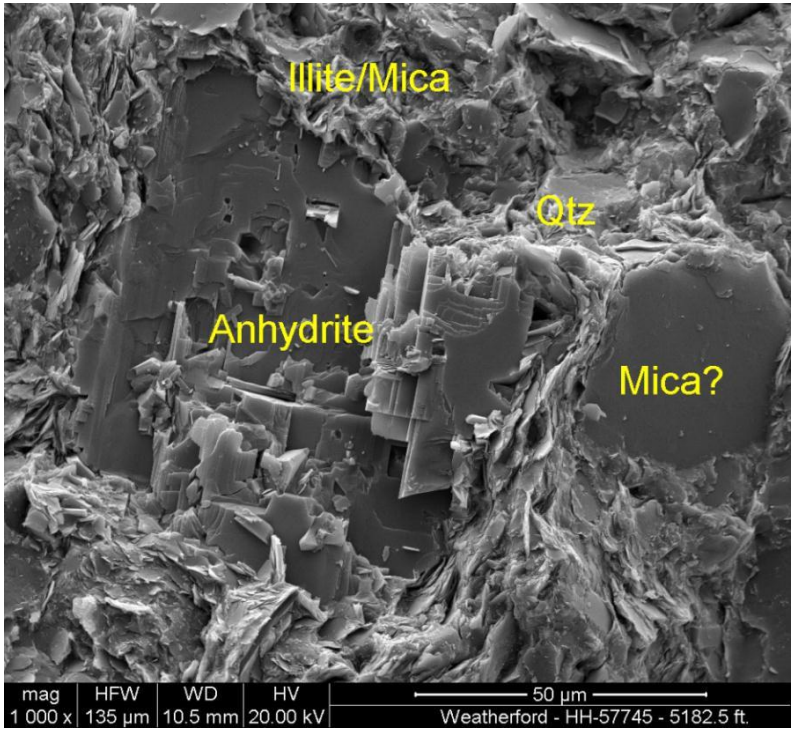

A

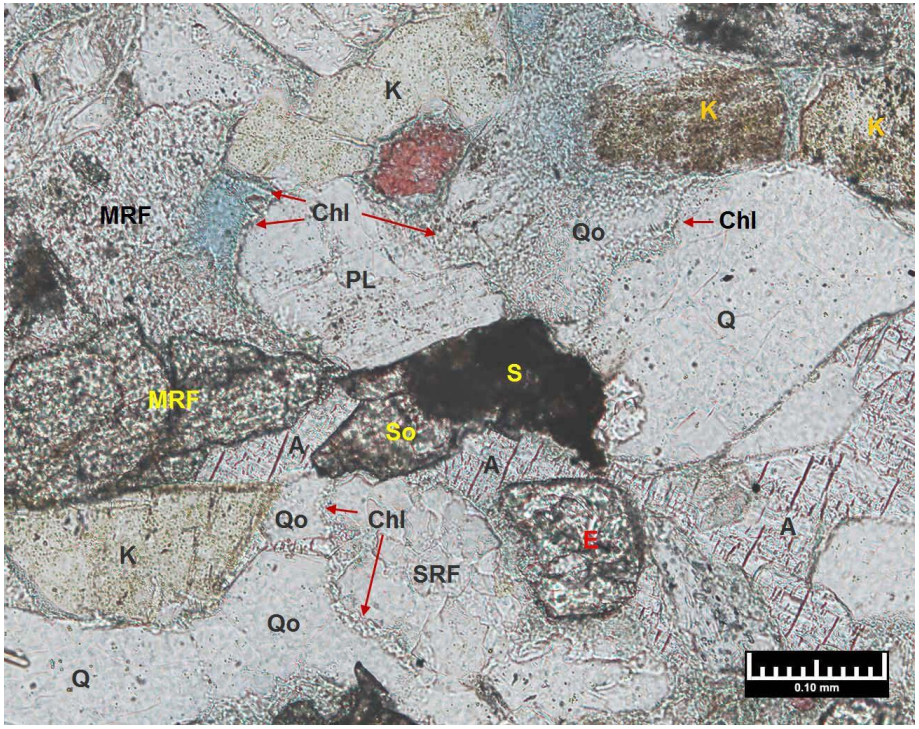

B

Figure 2.18 A. SEM image of RSWC from 5775.0ft shows anhydrite apparently replacing a framework grain. B. Plain light photomicrograph of sample from 5360.0ft (1-62R) shows relationship of anhydrite cement (A), sphene detrital grain (S) with extensive overgrowth (So), authigenic chlorite clay (Chl), and quartz overgrowth cement (Qo). Also present in the photomicrograph are detrital grains of quartz (Q), sedimentary rock fragments (SRF), metamorphic rock fragments (MRF), plagioclase (PL), epidote (E), and potassium feldspar (K).

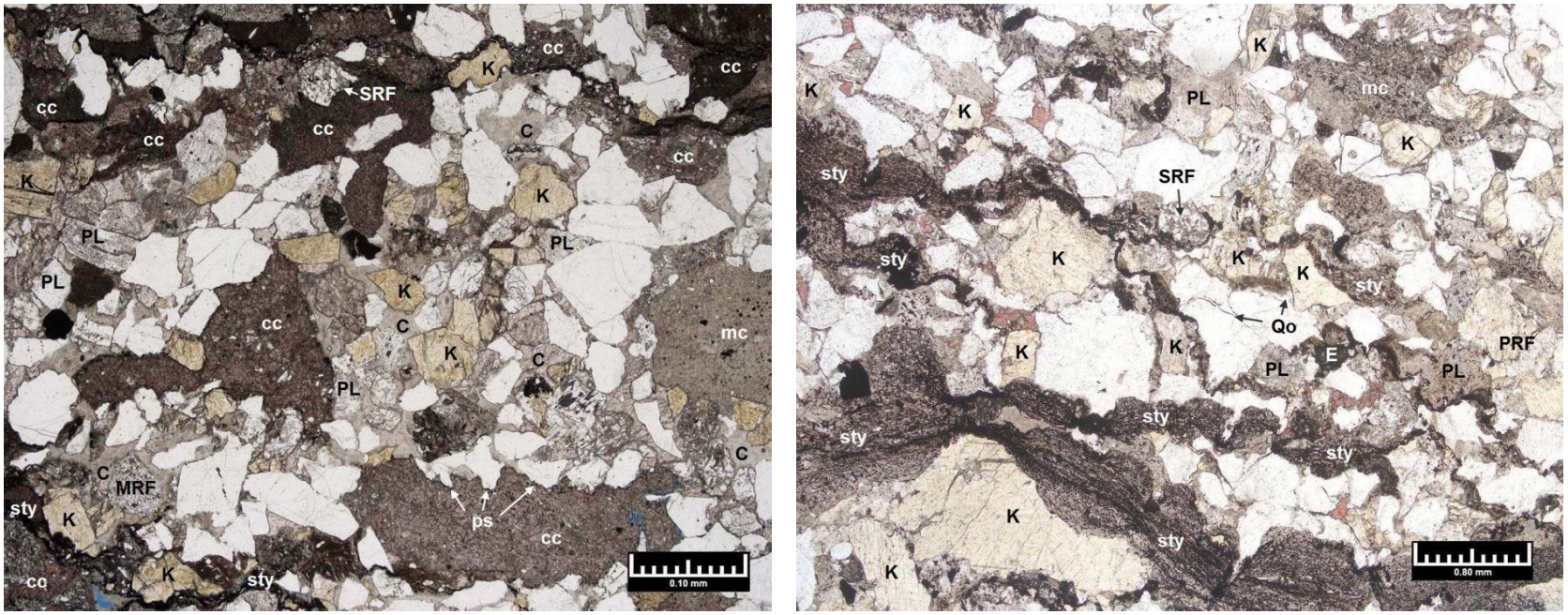

A B

Figure 2.19 Photomicrographs, which were taken with transmitted white, illustrating the high degree of compaction present within samples from test borehole Rizer #1. Both samples are rich in feldspar and lithic grains, such as potassium feldspar (K), plagioclase (PL), sedimentary rock fragments (SRF), metameophic rock fragments (MRF), and plutonic rock fragments (PRF). Also common are intrabasinal clasts comprised of micrite (cc) and siliciclastic mud (mc). White grains are generally quartz. A. CC sample from 6047.50ft is a moderately sorted, coarse- grained sandstone with highly compressed intrabasinal micrite clasts (cc) and mud clasts (mc). A stylolite is present along the base of the field of view (sty) and pressure solution (ps) along contacts of grains and micrite clasts. B. RSWC sample from 4610.5ft contains numerous stylolites (sty) with abundant irregularly shaped grains along the stylolites due to pressure solution.

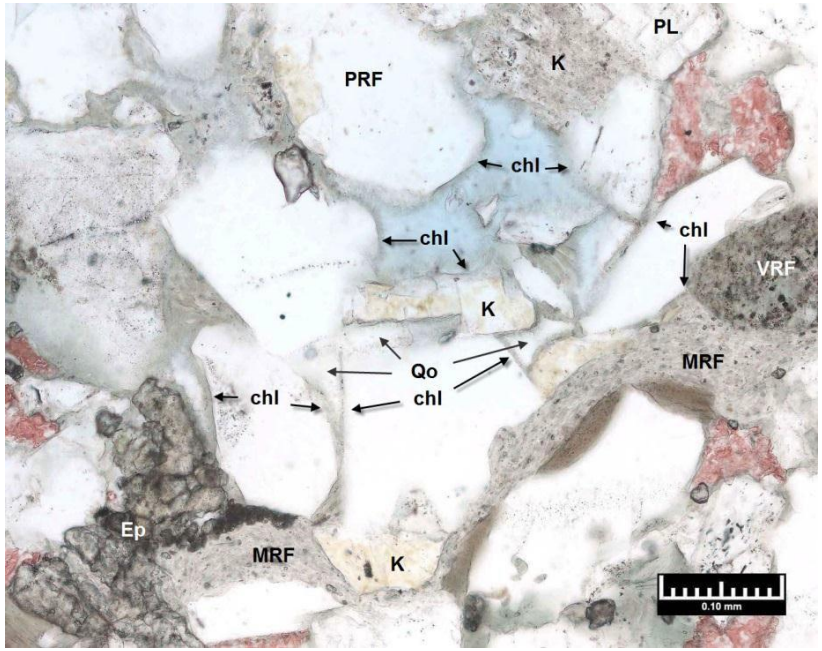

A

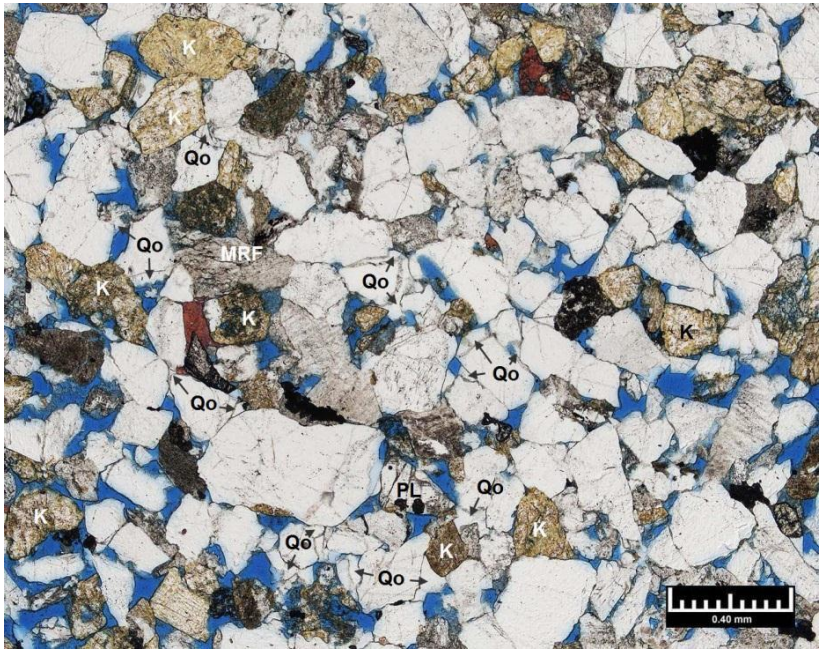

B

Figure 2.20 Photomicrographs (with white light) showing examples of types of porosity observed within Rizer #1 samples. A. RSWC from 5057.0ft shows occurrence of secondary intragranular pores (light blue area in upper center portion of field of view). This pore is lined with chlorite clay (chl) as are most of the grain surfaces. Quartz overgrowth cements (Qo) are also engulfing some of these clay-linings. Microporosity is also associated with these authigenic clays. In this view, a phyllite metamorphic rock fragment (MRF) is deformed by compaction. Other grain types present are quartz (white), potassium feldspar (stained yellow, K), volcanic rock fragments (VRF), plutonic rock fragments (PRF), plagioclase (PL), epidote (Ep), and volcanic rock fragments (VRF). Small isolated patches of calcite cement (red) are common. B. RSWC from 4037.0ft shows the occurrence of intergranular pores (blue), which due to the relative abundance of elongated pores, may be secondary. There is patchy distribution of quartz overgrowth cements (Qo) and calcite cement (red). Framework grains are comprised largely of quartz (white), potassium feldspar (stained yellow, K), metamorphic rock fragments (MRF) and plagioclase (PL).

A

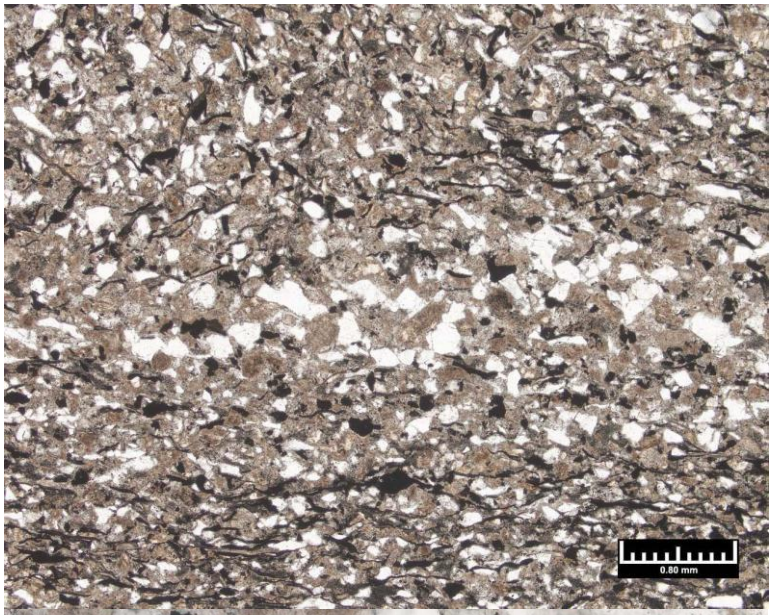

B

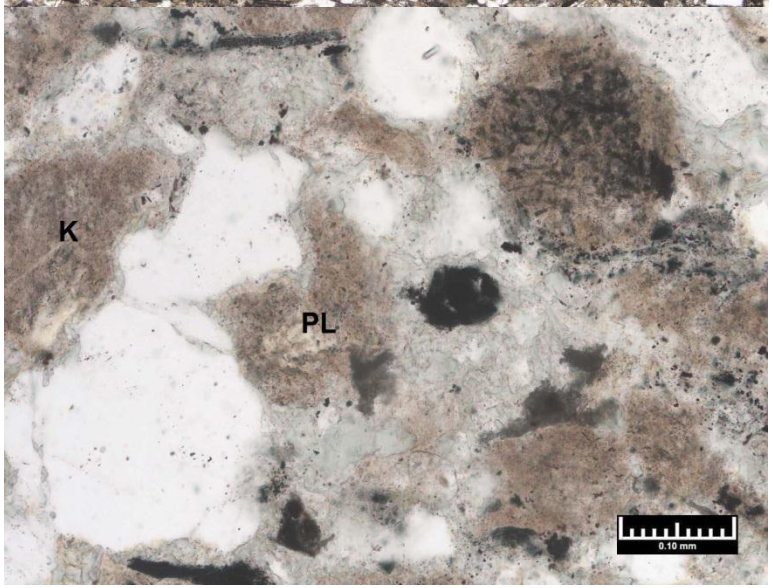

C

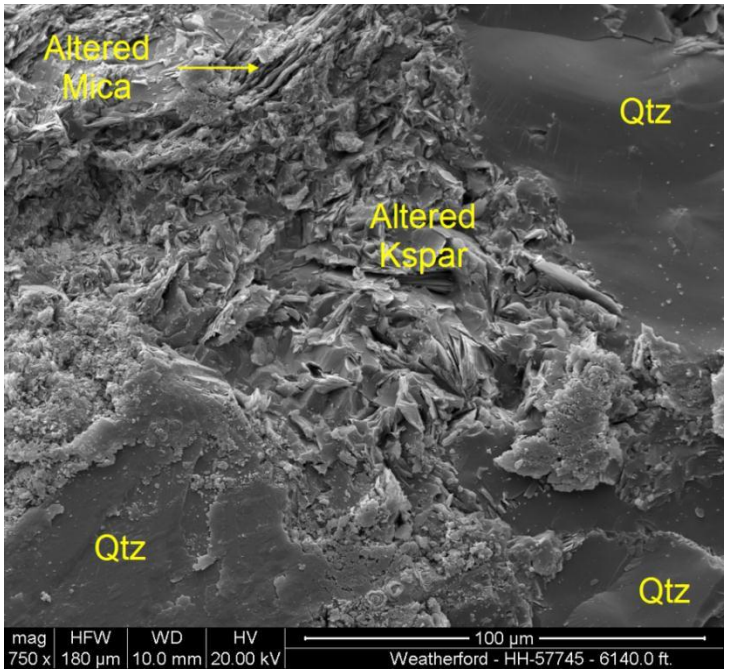

Figure 2.21 A. General view shows the abundance of altered grains (tan) and altered micas (black), which are concentrated in laminations. For the most part, only quartz grains appear white. XRD clay minerals and mica comprise only 22 wt% of this sample and feldspars comprise 40 wt %. B. Higher magnified view of an area in Figure 2.21A shows the character of partially altered framework grains. Some of these altered grains can be recognized as plagioclase (PL) or potassium feldspar (K). Pyrite and titanium oxide are replacing some particles and mica flakes (black). Quartz grains are white. C. SEM view of altered potassium feldspar grain and altered mica. Based on EDS, the clays within the feldspar grain appear to be either chlorite or illite.

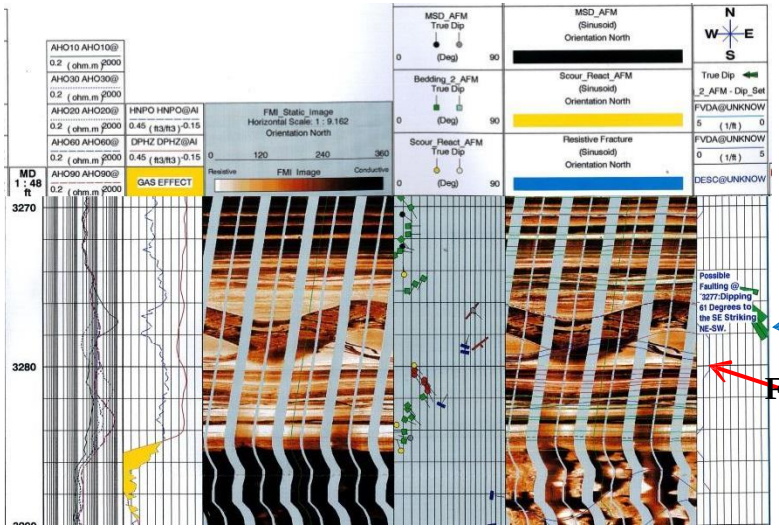

FRACTURES

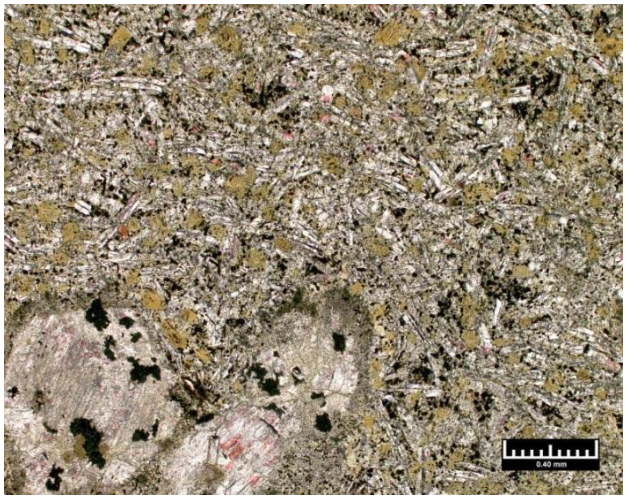

A. 3278.0ft (sample 1-5R)

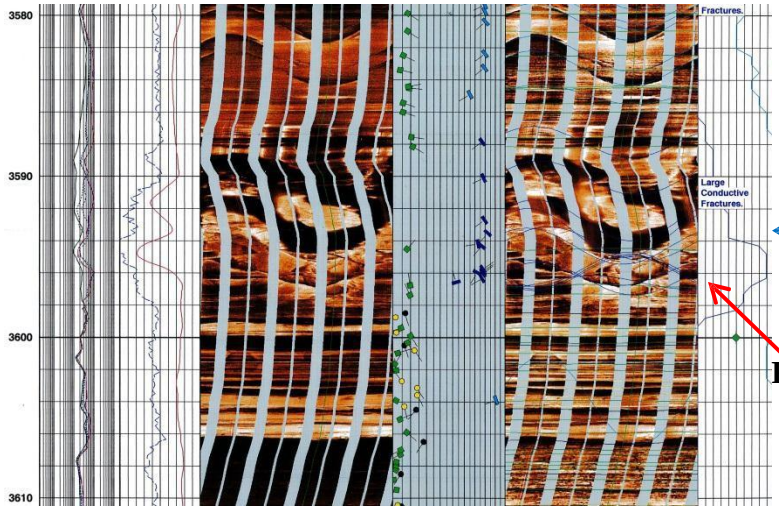

FRACTURES

B. 3593.0ft (sample 1-7R)

Figure 2.22

Figure 2.22 A. Photomicrographs of thin sections taken from altered olivine basalts at 3278.0ft and 3593.0ft with FMI logs from their corresponding depths indicating the samples came from steeply dipping features associated with fractures. A. Plain white light photomicrograph of hypocrystalline to holocrystalline basalt with numerous phenocrysts of plagioclase (white) comprised of euhedral, elongated laths and larger anhedral crystals (PL). Chlorite (yellow) is replacing phenocrysts of olivine and (glassy?) matrix. Replacement calcite (red) and titanium oxide (black) are dispersed throughout. B. Photomicrograph taken with crossed polarized light of hypocrystalline to holocrystalline basalt with numerous phenocrysts of plagioclase (white) comprised of euhedral, elongated laths, which commonly display Carlsbad twinning. Larger anhedral crystals of olivine and pyroxene are replaced with chlorite (yellow). General thin section descriptions and additional photomicrographs are in Appendix E.

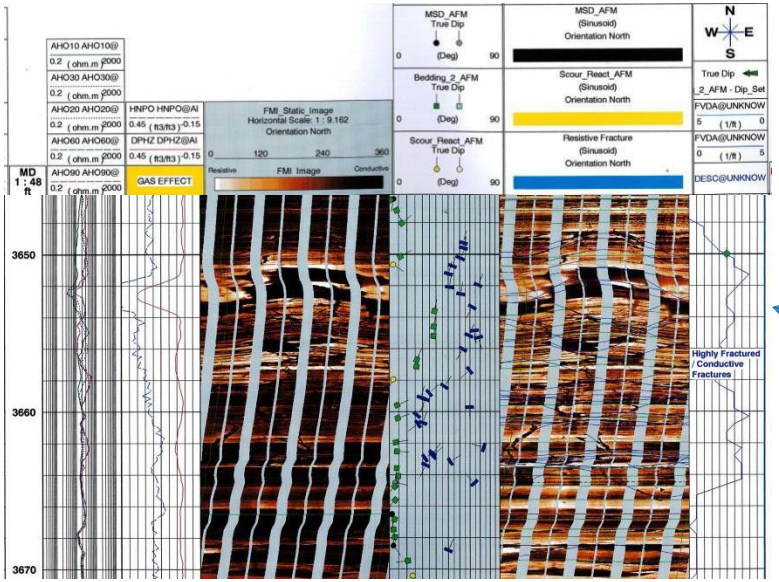

3654.0ft (sample 1-8R)

Figure 2.23 Photomicrograph of thin section is taken from an altered diabase or alkali olivine basalt at 3654.0ft with FMI logs from corresponding depths. FMI log indicates extensive fracturing above and below the steeply dipping igneous body from approximately 3649ft to 3665ft (log depth). Plain white light photomicrograph of hypocrystalline basalt with numerous euhedral phenocrysts of elongated plagioclase laths (white). Yellow brown fibrous amphiboles are replacing pyroxene crystals and some plagioclase. Also present are phenocrysts of augite (Ag). General thin section descriptions and additional photomicrographs are in Appendix E.

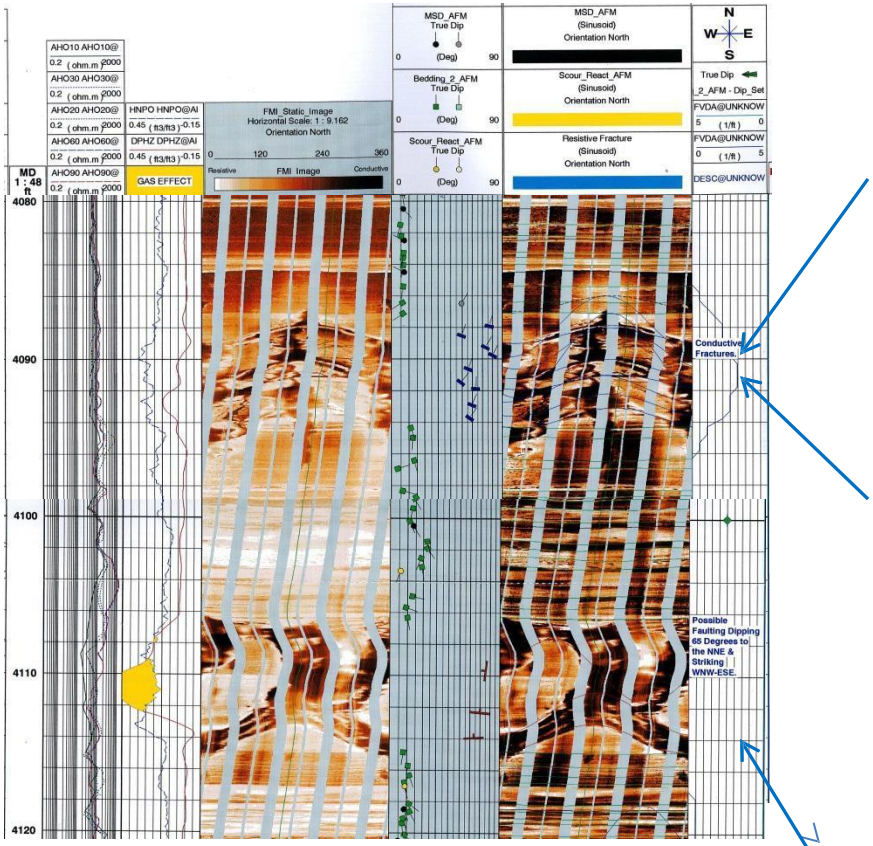

Figure 2.24

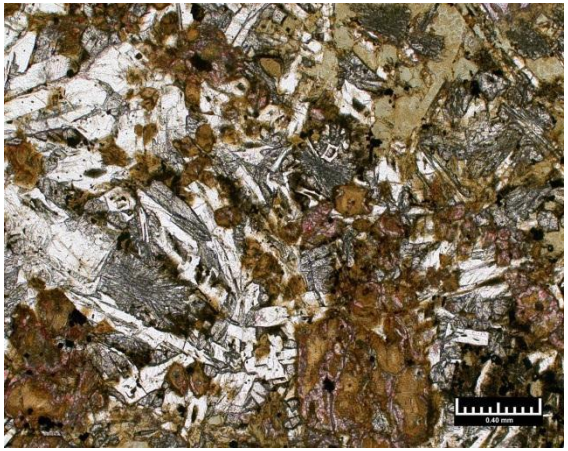

A 4090.0ft
(sample 1-17R)

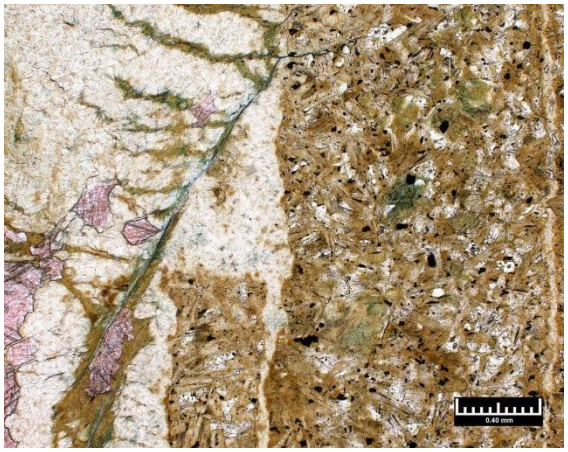

B 4091.0ft
(sample 1-18R)

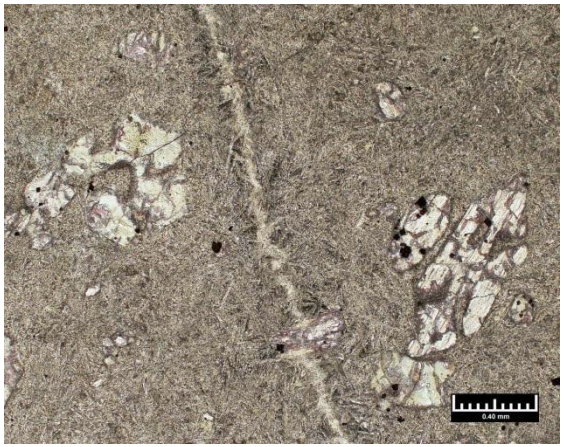

C 4113.0ft
(sample 1-19R)

Figure 2.24 Figure displays some high degrees of alteration experienced by igneous bodies encountered with test borehole Rizer #1. Photomicrographs are of three thin sections taken from two altered alkali olivine basalts bodies, which dip at relatively high angles in approximately the same dip direction (north- northeast) according to the corresponding FMI log. A. Plain white light photomicrograph hypocrystalline basalt with numerous euhedral and subeuhedral phenocrysts of plagioclase (white) and apparent anhedral phenocrysts of olivine and pyroxene replaced by fibrous amphibole (yellow brown) or chlorite (yellowish green) with only minor occurrence of chlorite replaced (glassey?) matrix. B. Plain white light photomicrograph of a hypocrystalline basalt. On the right half of the field of view is displayed dispersed subeuhedral laths of plagioclase (white) surrounded by clay-replaced matrix and phenocrysts of olivine and pyroxene (brown). On the left half of the photomicrograph, the majority of the rock is replaced by chert (white) or calcite spar (pink). C. Plain white light photomicrograph of hypocrystalline basalt with phenocrysts of olivine (OL) replaced by calcite of fibrous amphibole. Finely crystalline groundmass and bisecting fracture are largely replaced by chlorite clay. General thin section descriptions and additional photomicrographs are in Appendix E.

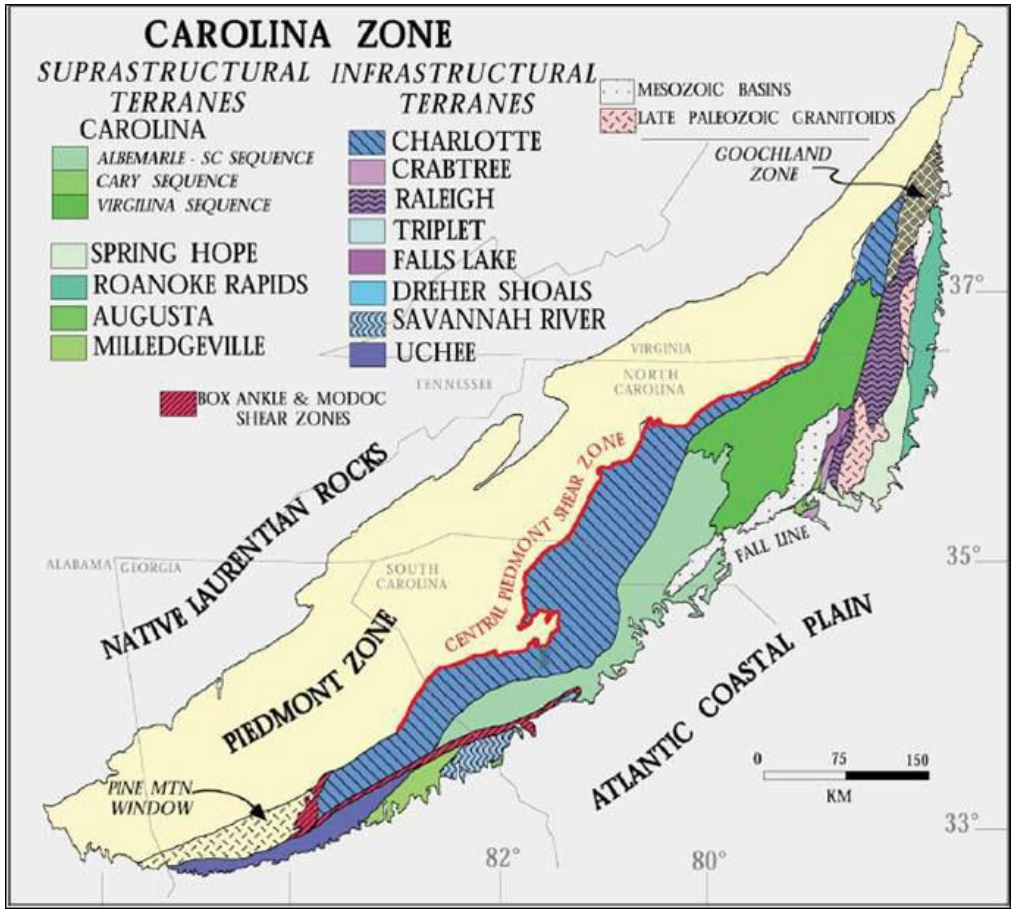

Figure 2.25 The mix of igneous and metamorphic rocks associated with the Carolina terrane and Charlotte terrane within the Carolina Zone represent likely source lithologies that match both the rock fragments and minerals observed in thin section and the mafic-elements and felsic-elements indicated in the chemostratigraphic zonation described in Section 4 of this report. Figure is modified from Hibbard et al, (2002).

SECTION 3

3.0 Depositional and Diagenetic History of a Portion of the South Georgia Rift Basin Based on Petrologic Examination of Samples from Rizer #1 Test Borehole, Colleton County, SC

3.1 INTRODUCTION

This section of the report concentrates on results of a study designed to determine the factors which destroyed porosity and permeability within the recovered interval in Rizer #1 test borehole in Colleton County, South Carolina. This study is concentrated on samples obtained between drilling depths 2600.0ft and 6200.0ft (0.79km and 1.89km) as a result of technical difficulties with the drilling of Rizer #1, which was abandoned at approximately 6200ft (1.90km) from ground surface.

Routine core analysis (RCA) shows average ambient porosities for rotary side wall core (RSWC) and conventional core (CC) samples are 3.4% and 3.1%, respectively and average permeability (to air) for RSWC and CC samples are 0.065mD and 0.0049mD (Appendix F). The poor reservoir quality makes reservoir property measurements impractical. Consequently, the special core analysis portion of the study was abandoned. Instead, efforts were directed to determine why the reservoir properties of the proposed interval for sequestration are so poor and if scientifically supportable predictions of reservoir properties can be made for sandstones within the South Georgia Rift Basin (SGRB) that are lateral to or deeper than the interval recovered.

3.1.1 Study Approach

Two approaches were employed to determine the causes of the reduction in porosity and permeability found within the sandstones recovered in Rizer #1 test borehole. Both approaches followed methodologies employed in previous published studies. The first approach was to quantify the degree of compaction experienced by the study interval in order to ascertain if the subject sandstone were buried deeper during their geologic history. This compaction study followed the procedures outlined and utilized by Pettijohn et al. (1973), Wilson and McBride (1988), and McBride et al. (1991). The second approach was to determine the precipitation temperatures of cements present within the study sandstone with the goal of ascertaining whether burial depth or metasomatism (due to proximity to an igneous intrusive) was more influential on degradation of reservoir properties. A study by Hiatt et al. (2007) of basal sandstones in three Proterozoic continental basins was used as a guide for an analytical approach.

3.1.2 Previous Related Studies of Cementation

Quartz and calcite are the more common cements present within Rizer #1 based on modal analysis. Consequently, this subsection will review applicable previous studies of quartz and calcite cements.

Numerous researchers have utilized geochemical studies of quartz cement to determine burial depth and pore water paleotemperatures (Hervig et al., 1995; Hiatt et al., 2007;

Harwood et al., 2013). The Hiatt et al. (2007) study, which reconstructed burial depths and pore water paleotemperatures for three Proterozoic continental basins (Figure 3.1), was judged most applicable to the examination of the SGRB. Consequently, it was utilized as a template for the SGRB study.

Although there are exceptions, the bulk of quartz cements form at pore-water temperatures greater than 60^{o}C and burial depths greater than 2 km (McBride, 1989; Bjørlykke and Egeberg, 1993; Hiatt et al., 2007). Consequently, unless other cement- forming minerals, such as calcite or gypsum/anhydrite, fill the intergranular pores, mechanical compaction will play a major role reducing porosity within the first kilometer or so of burial. Regarding sources of silica, precluding shallow groundwater transport of silica laden waters, the most likely source of silica is that released by stylolites or dissolution of quartz or feldspar grains (Hiatt et al., 2007). Since mud rocks are not abundant in the Proterozoic basins examined by Hiatt et al. (2007), they did not consider clay diagenesis to be a major source of silica for the rocks in their study. (The lack of a significant presence of mud rocks within the Rizer #1 borehole, may also preclude this silica source for the studied portion of the SGRB.) Using *in situ* ion microprobe analysis (SIMS), Hiatt et al. (2007) found δ^{18} O VSMOW values ranging from 3.0‰ δ^{18} O to 33.2‰ δ^{18} O with values generally below 15.0 δ^{18} O generally considered detrital grains (Figure 3.1). Other studies of quartz cements that were identified using SEM CL found similar ranges for δ^{18} O (20-34‰ δ^{18} O, Hervig et al., 1995; 20-28‰ δ^{18} O VSMOW, Harwood et al., 2013). A survey of δ^{18} O values in selected rock types by Blatt (1987) delineated average values for igneous rocks at 9‰ δ^{18} O, metamorphic rocks at 13 to 14‰ δ^{18} O, sandstones (detrital grains) at 11‰ δ^{18}O, and quartz cements at 20‰ δ^{18} O.

Calcite cemented sandstones are found at a variety of depths and temperatures. One study of the Frio Sandstone in Texas by Milliken et al. (1981) compared δ^{18} O values within calcite cements with depth (Figure 3.2). In the Milliken et al. (1981) study, δ^{18} O values of calcite cements within the sandstone samples range from -4.4‰ to -12.8‰ δ^{18}O PDB (Figure 3.2; 26.37‰ to 17.71‰ δ^{18} O VSMOW) while the current depths of these samples range from approximately 4500.0ft (1.37 km) to 18000 ft (5.49 km). Similar δ^{18} O values are found in calcite cements that were interpreted to have formed in relatively shallow burial depths (Parcerisa et al. 2005). This paper, which describes Neogene alluvial fan to lacustrine deposits, contains calcite cements with similar δ^{18} O values (-10.5‰ to -6.2 ‰ δ^{18} O PDB or 20.09‰ to 24.52‰ δ^{18} O VSMOW) as found in Milliken et al. (1981). Calcite cements found with lighter δ^{18} O values (<17.71‰ δ^{18} O VSMOW) than the deepest sandstone examined in the Milliken et al. (1981) study have been reported from cements associated with contact metamorphism (Ferry et al., 2011) or from cements interpreted to be derived from isotopically depleted hydrothermal fluids migrating along fault planes (Katz et al., 2006).

3.1.3 Previous Studies of Compaction

The compaction study of McBride et al. (1991) was utilized as a template for this study because the sandstones analyzed by McBride et al. (1991) more closely resemble the

Rizer #1 samples in grain-size and sorting. The McBride et al. (1991) study, which examined packing and porosity in 40 thin section samples from south Texas, USA Wilcox and Carrizo formation sandstones (2600.0ft (0.79km) to 14500.0ft [4.42km] burial depths), arrived at the following conclusions:

- Compaction was the major cause of porosity reduction.
- Rates of compaction and porosity reduction were greatest at burial depths less than 3940ft (1.20km), which is typical for lithic sandstones (Pittman and Larese, 1991).
- Cements were not introduced early enough or in enough quantities to halt compaction.
- No significant compaction occurred deeper than 9840.0ft (3.00km, which is 1640.0ft [0.50 km] shallower than present depth of hard overpressure).
- Total porosity loss by compaction ranges from 9% to 31% with grain rearrangement causing twice the porosity loss than by labile grain deformation or pressure solution.

Plots of the contact index (CI) and tight packing index (TPI) data derived from the McBride et al. (1991) study are shown in Figure 3.3. Also included in these plots are results of CI and TPI modal analyses of Rizer #1 samples.

3.2 METHODOLOGY

The methods employed for this study were done on a subset of samples (Appendix A, Table A1) on which detailed (modal) analysis was completed (10 from CC and 24 from RSWC) or general thin section descriptions were completed (2 from CC and 28 from RSWC samples). These examinations were used to select the optimum subset of samples for study. The specialized analyses are as follows:

- A modal compaction analysis was performed on 12 thin section samples to determine their contact index (CI) and tight packing index (TPI; Figure 3.3; Table 3.1; Appendix M).
- Cathodoluminescence scanning electron microscopy (CL SEM) examination was performed on four (4) samples at the Bureau of Economic Geology (BEG) at the University of Texas (Appendix N).
- Secondary ion mass spectrometry (SIMS) was performed on 3 RSWC samples at the University of Wisconsin SIMS laboratory (WiscSIMS) to determine δ^{18} O values of quartz and calcite cements (Table 3.2; Appendix O).
- Bulk analysis of δ^{18} O within calcite was done on the same 3 RSWC samples (Table 3.2; Appendix O).
- Electron Microprobe analyses were performed on the SIMS samples to aid in calibration of the results (Appendix O).

3.2.1 Modal Compaction Analysis

A total of twelve samples (10 RSWC and 2 CC) were modally analyzed to determine the contact index (CI) and the tight packing index (TPI). The contact index (CI) is the average number of contacts for each grain counted (200). The tight packing index (TPI)

identifies types of grain contacts as defined in Pettijohn et al. (1973) and follows the formula below as described in Wilson and McBride (1988).

TPI = the sum of the average number of long + concavo-convex + sutured contacts per grain

3.2.2 Determination of Precipitation Temperatures of Cements

The objective of this portion of the study was to determine the precipitation temperatures of cements present within the study sandstone with the goal of delineating whether burial depth or metasomatism was more influential on degradation of reservoir properties. Generally speaking, cement precipitation studies rely on both oxygen isotope analyses and on fluid inclusions. Unfortunately, sufficiently large fluid inclusions were not observed in either the quartz or the calcite cements.

Prior to performing *in situ* ion microprobe analysis of the quartz and calcite cements with the SIMS, it was necessary to identify quartz cements versus framework grains and to delineate if cements were formed in a single or multiple phases. This was accomplished via CL SEM on the quartz overgrowths cements but not with the calcite cements because of intense fluorescence of the calcite. Occurrences of multiple stages of quartz cement were bracketed with platinum-filled squares using a focus ion beam (FIB) SEM for later identification with the SIMS.

Calculations of paleo-pore water temperatures derived from the SIMS δ^{18} O values are based on the equation of Clayton et al. (1972) and use the VSMOW values of 0 (normal sea water), +1 and -1 (Table 3.2). These values were utilized, since this study could not determine the initial salinity of the SGRB pore waters and they approximated the Late Triassic sea water VSMOW of -1 utilized by previous studies (Gretz et al., 2013).

Since SIMS δ^{18} O values could only be obtained from calcite cements from one of the three samples examined with the SIMS (R8 from 3674.0ft [1.12km]), Bulk-rock δ^{18} O analyses of all three RSWC samples were done following the procedures of Epstein et al. (1964). The inability to obtain SIMS δ^{18} O from two of the samples (R26 from 5152.5ft [1.57km] and R37 from 5702.5ft [1.74km]) was due to polishing difficulties. The samples with a high degree of quartz cementation and relatively low abundances of calcite cement, did not acquire a smooth polish on the soft calcite cement surfaces. Consequently, accurate SIMS measurements could not be made.

3.3 RESULTS

3.3.1 Compaction Study

A total of twelve samples (10 RSWC and 2 CC) were modally analyzed and compared with results from a compaction study published by McBride et al. (1991), who examined well to very well sorted sandstones (Paleocene-Eocene) from the Texas Gulf Coast.

The CI and TPI analyses of the Rizer #1 samples indicate the sandstones were buried deeper than their current depth below the subsurface. This hypothesis is based on

comparing the Rizer #1 results with the results in the McBride et al. (1991) study (Figure 3.3). A majority of the Rizer #1 samples have CI numbers comparable to samples buried 2000ft to 4000ft (0.61km to 1.22km) deeper than the McBride et al. (1991) samples (Figure 3.3A). This additional burial depth value is estimated by comparing Rizer #1 sample depths with the depth of the trend line of the McBride et al. (1991) for the same CI value. Only one Rizer #1 sample (1-60R, from 5338.0ft [1.63km]; Figure 2.15B) plots at values significantly less the comparable McBride et al. (1991) values. This Rizer #1 sandstone sample 1-60R is well cemented with calcite (19% based on modal analysis; Figure 2.15B). Comparison of TPI results between Rizer #1 and the McBride et al. (1991) study indicates a 4000ft to 6000ft (1.22km to 1.83km) difference (Figure 3.3B).

3.3.2 Precipitation Temperatures of Cements

The δ^{18} O values obtained by SIMS analysis from the quartz overgrowth cements in the RSWC samples (R26 from 5152.5ft [1.57km] and R37 from 5702.5ft [1.74km]) show multiple groupings of quartz cements with significantly different δ^{18} O values (Table 3.2; Figure 3.4; Appendix M). All three groups are present within the sample R37 (5702.5ft) but only Group 3 quartz cements are present in sample R26 (5152.5ft [1.57km]). Within the Group 1 quartz cements from R37 the δ^{18} O values average 20.95‰ δ^{18} O based on four readings ranging from 20.26‰ to 21.82‰. The average Group 1 δ^{18} O value equates to a paleo-pore water temperature of approximately 101^{o}C, based on the equation of Clayton et al. (1972) and using a normal sea water VSMOW of 0 (Figure 3.8). Group 1 cements are from the fluorescent band of quartz overgrowth cement adjoining the detrital grain surfaces as recorded by CL SEM (Figure 3.5). Group 2, which is also only present in sample R37, has δ^{18}O values averaging 18.36‰ δ^{18}O based on four readings ranging from 17.93‰ to 18.71‰. The average Group 2 δ^{18} O value equates to a paleo-pore water temperature of approximately 123^{o}C (Group 2 in Figure 3.4). Group 3 has a broad range of δ^{18} O values ranging from a high of 16.58‰ δ^{18}O to a low of 12.98‰ δ^{18}O (Group 3 in Figure 3.4). This broad range of δ^{18} O values coincide with a precipitation temperature range of 140^{o}C to 183^{o}C based on the equation of Clayton et al. (1972) and using a normal sea water VSMOW of 0 (Figure 3.4). These high and low δ^{18}O values were obtained from sample R37 (5702.5ft [1.74km]) with the low value appearing to be within a quartz overgrowth (sample point #96 within Figure 3.5). The high and low δ^{18} O values obtained from sample R26 (5152.5ft [1.57km]) range from a high of 15.99‰ δ^{18} O (sample point #151 within Figure 3.6) to a low of 13.23‰ δ^{18} O (sample point #175 within Figure 3.6). An examination of sample R26 in Figure 3.6 shows that it is difficult to optically distinguish grains from cement (Figure 3.6B). Only by assuming that quartz cement is any quartz body with a δ^{18} O value of 12.98‰ or higher can one make the distinction (Figure 3.6A).

The quartz detrital grain with the highest δ^{18} O values appears to be fractured and subsequently infilled with quartz cement (Table 3.2; Figure 3.7). The grain pictured in Figure 3.7 is judged to have been fractured prior to deposition, since the quartz fracture- fill does not appear to exhibit a similar fluorescence as the adjoining intergranular quartz cement as viewed with CL SEM (Figure 3.9A).

Calcite cements also show a wide range of δ^{18} O values based on *in situ* SIMS analyses from RSWC R8 from 3674.0ft [1.12km] and bulk analyses of all three RSWC samples (R8, R26, and R37), which were performed because SIMS analyses could not be done on the deeper two RSWC samples due to rough calcite cement surfaces. The δ^{18} O SIMS values from calcite cements within R8 (3674.0ft [1.12km]; Table 3.2 and Figure 3.8 and 3.9) have two major groupings. (Values from replaced framework grains are not included because their rough surfaces prevented accurate SIMS measurements.) The calcite cement group with the highest average δ^{18} averages 27.68‰ δ^{18} O, which equates to a paleo pore water temperature of approximately 31^{o}C (88^{o}F) based on the equation of O'Neil, Clayton and Mayeda (1969) and using a normal sea water VSMOW of 0. The lower δ^{18} O value cement averages 22.46‰ δ^{18} O, which equates to a paleo pore water temperature of approximately 60^{o}C (140^{o}F). Bulk-rock δ^{18} O analyses of all three RSWC samples (R8, R26, R37; done following the procedures of Epstein et al. 1964) show two distinct groupings with a 20.95‰ δ^{18} value from R8 and a 13.34‰ δ^{18} value and 13.22‰ δ^{18} value from R26 and R37, respectively. Assuming a VSMOW of 0 these bulk-rock values equate to a low value of 62^{o}C (144^{o}F) and high values of 142^{o} to 143^{o}C (288^{o}F to 289^{o}F). It should be noted that these bulk values blend isotopes from possible early (shallow and low temperature) and late (deep and higher temperature) cement or grain-replacing calcite. In Figure 3.2B, the calcite δ^{18} O values for the Rizer #1 samples, which are plotted at their current depths, are compared with bulk δ^{18} O values of samples consisting primarily of cement from the Milliken et al. (1981) study of the Frio Formation in southeastern Texas. Based on their δ^{18} values, the Group I calcite cement values within Rizer #1 are isotopically similar to relatively shallow cements (less than 1.50km or 4921.0ft) documented by Milliken et al. (1981; Figure 3.2). Group II cements from Rizer #1 equate with cements from the Milliken et al. (1981) study that are greater than 3.00km depth (9842.0ft). Group III calcite cements from Rizer #1 are isotopically lighter than any calcareous samples encountered in the Milliken et al. (1981) study (Figure 3.2).

Although authigenic sphene is well documented by SEM examinations in other Rizer #1 samples (Figure 2.17A), the sphene analyzed by SIMS in samples R26 and R37 indicate they are all detrital grains of igneous origin with very low δ^{18} O values ranging from 1.50‰ to 5.21‰ (Figure 3.7 and 3.10). Based on modal analysis of the thin sections, sphene is a common cement (averaging is 0.4%) and a common replacement mineral (averaging 0.2%; Appendix G). Some of the authigenic sphene occurs as overgrowths on detrital sphene (Figure 3.11A). Sphene is thought to be relatively early cement, occurring contemporaneous or soon after pore-lining chlorite clay. Quartz overgrowth cements are commonly observed engulfing clay linings and sphene cements (Figures 3.11D and 2.17A), indicating quartz formed after both.

3.4 DISCUSSION

3.4.1 Compaction Study: Depth of Burial

Observations of the lack of porosity and the abundance of stylolites and related pressure/solution features made during the initial phases of the petrologic study, indicate the study interval had been buried deeper than its present depth. These findings support geophysical evidence that the Rizer #1 borehole penetrated an uplifted portion of the SGRB (Clendenin et al., 2011; Waddell et al., 2011). Since the extent of that inversion (or the degree of deeper burial) could not be determined seismically (Waddell, personnel communication), a primary objective of the petrologic study was to determine depth of burial. One methodology utilized to determine burial depth was modal analysis to determine the contact index (CI) and the tight packing index (TPI). Results from these analyses indicate the majority of Rizer #1 sandstones appear to have been buried deeper than comparable sandstones from the Texas Gulf Coast as examined by McBride et al. (1991). Comparison of the Rizer #1 modal CI analyses indicates a burial depth for most samples is approximately 2000.0ft to 4000.0ft (0.61km to 1.22km) deeper than samples with comparable CI values in the McBride et al. (1991) study (Figure 3.3A). Within the TPI plot, the maximum difference is approximately 4000.0ft to 6000.0ft (1.22km to 1.83km; Figures 3.3B). It should be noted, however, that the Rizer #1 study interval was probably deposited in a rapidly subsiding rift basin and was later subjected to intrusive igneous activity. Whereas the Gulf Coast sequence was accumulated in a relatively structurally inactive and geothermally cool setting. Whatever the scale, it is certain that the Rizer #1 study interval was buried deeper at some point in its post-depositional history.

3.4.2 Oxygen Isotopes of Cements and Depth of Burial

Determination of the depth of cement precipitation based on results of the δ^{18} O analyses of both quartz and calcite cements requires the assignment of a geothermal gradient. The Hiatt et al. (2007) study used a 30^{o}C/km geothermal gradient and an assumed surface temperature of 25^{o}C to determine the burial depths of the Proterozoic basins they investigated. Utilizing the highest average cement precipitation temperatures from this study, 153^{o}C (307^{o}F; Table 3.2) and a 30^{o}C/km geothermal gradient that would result in a burial depth 14010.0ft (4.27km). The plot shown in Figure 3.12, however, utilizes a geothermal gradient employed in the study of the Taylorsville Triassic rift-basin in Virginia (Tseng et al., 1996) study. The Tseng et al. (1996) study, which was based on fluid inclusion analyses, used a 40^{o}C/km gradient to determine their burial depths. Tseng et al. (2007) derived their gradient from a Tillman and Barnes (1983) study of the late Paleozoic or early Mesozoic-aged basins within the central and northern Appalachian basins. This study adopted the geothermal gradient of Tseng et al. (1996) because both the SGRB and Taylorville are tectonically similar, both are Late Triassic in age, and they are geographically close. In addition, the resulting depths more closely approximate the depths derived from the modal compaction study. The isotope study of Rizer #1 quartz cements indicates the cement with the lowest δ^{18} O formed at a pore water temperature of 183^{o}C at burial depths of

approximately 13000.0ft (3.96 km; Table 3.2; R37 from 5702.5ft [1.74km]) or approximately 7300.0ft (2.22 km) deeper than present burial depths assuming the cements with the lowest δ^{18} O were the last and deepest cements formed. The lowest bulk-rock calcite δ^{18} O results indicate a precipitation temperature of approximately 143^{o}C based on the equation of O'Neil, Clayton and Mayeda (1969) and using normal sea water VSMOW of 0. Assuming a 40^{o}C/km gradient, the calcite cements formed at a burial depth of 9710.0ft (2.96km).

3.4.3 Burial Model

The burial model hypothesized for the study portion of the SGRB is displayed in Figure 3.12A. Timing of the rifting and drifting phases is based on Withjack et al. (1998, 2012). Initial subsidence rates for the SGRF are relatively high at approximately 140mm/1000yr. This is a much higher subsidence rate than a typical passive margin, which ranges from 10 to 40mm/1000yr (Schwab, 1976; Rona, 1973), but it is less than the rate of subsidence since the Tertiary for portions of the Gulf coast of the USA (200mm/1000yr; Blatt et al, 1980). Age of end of uplift at 140 Ma BP is based on the model of Tseng et al. (1996) for the Taylorsville Basin in Virginia. The unconformity at the top of the Late Triassic/Early Jurassic is overlain by coastal plain strata ranging in age from Quaternary to the Turonian/Coniacian-aged (94 Ma BP) Middendorf Formation (Colquhoun et al., 1983). The burial curve in Figure 3.12A simulates the burial history of strata at a present day burial depth of 5000.0ft (1.52 km). This model projects that the strata at 5000.0ft (1.52 km) was buried approximately 8200.0ft (2.50km) deeper than today (Figure 3.12). Or in other words, the model indicates that approximately 11500.0ft (3.50km) of late Triassic strata overlaid the study interval at before the basin began to invert some 200 million years ago (Figure 3.12). Since approximately 2300.0ft (0.70km) currently overlies the model interval at 5000.0ft (1.52 km), this indicates 9200.0ft (2.8km) of Triassic section was eroded prior to deposition of the Cretaceous- age and younger coastal plain strata.

3.4.4 Diagenetic Model

It is hypothesized that reservoir quality of the study sandstone was substantially diminished by a complex series of diagenetic events (Figure 3.12B). Based on petrographic examination of RSWCs and the CC combined with published paleogeographic interpretations (Withjack et al., 1998, 2012), it is hypothesized that the study interval accumulated within an alluvial – lacustrine setting. After deposition and initial compaction, infiltrating clays formed cutaneous clay and/or hematitic coatings on some grains. Early cements consisted primarily of poikilotopic calcite spar. Within some portions of the sequence, these early calcite cements, which fill relatively large pre-compaction pores and precede other diagenetic minerals, occurred in significant volume to inhibit compaction (Figures 3.8 and 3.9). Feldspar grains were also replaced during these early stages of calcite cementation, a phenomenon that also occurs with late stage calcite cements. Sphene cements, which are in significant quantities (average 0.4% by volume), also appear to be relatively early and to precede quartz cementation and possibly chlorite (Figure 3.11A). Pore-rimming chlorite followed the

dissolution of the early calcite cements and at some point were followed by authigenic illite (Figure 3.11D). Dissolution of these early cements resulted in at least two scenarios. In one scenario, which is based on analysis of RSWC R26 (from 5152.5ft), early dissolution of the majority of the spar resulted in a high degree of compaction and pressure/solution. Another scenario, which is based on analysis of RSWC R37 (from 5702.5ft [1.74km]), early cementation and dissolution of gypsum-anhydrite was followed by early precipitation of quartz overgrowths (within less than one kilometer of burial; Group 1 in Figure 3.4). The Group 1 quartz cement was formed in sufficient volumes to prevent compaction. Consequently, sufficient intergranular porosity was preserved to allow a second phase of quartz overgrowth cement (Group 2 in Figure 3.4). It is hypothesized that the strata was sufficiently permeable to allow pore waters in with sufficient silica to form the quartz cement. Subsequently, a late stage of calcite cementation and a prolonged period of increasing burial with accompanying pressure solution supplying additional silica for continued quartz cementation finally occluded the remaining pores (Group 3 in Figure 3.4). During early phases of inversion of the basin and uplift, localized metasomatism altered those sandstones in close proximity to igneous dikes and sills. For the most part, however, it is hypothesized that diagenetic processes were dormant since commencement of uplift in the Early Jurassic.

3.4.5 Prediction of Reservoir Properties within the SGRB

It can be reasonably assumed that the study interval and laterally equivalent sandstones within the same fault block are not suitable candidates for CO_2 sequestration. Regarding the likelihood of favorable reservoir properties for sandstones deeper in this fault block, the authors feel that unless these sandstones experienced early cementation and subsequent dissolution of the early cements to create secondary porosity or were overpressured early in their burial history and thus preventing compaction, it is unlikely they possess reservoir properties to be suitable candidates for CO_2 sequestration. Regarding the prospect of underlying sandstones being overpressured, since the numerous igneous dikes, which permeate the SGRB, are highly fractured and likely conduits for fluids and gases, it is unlikely any portion of the fault block that contains Rizer #1 is overpressured because these dikes are connected with the overlying, poorly lithified Cretaceous and younger coastal plain strata.

What cannot be predicted by the study results, however, are the reservoir properties of the estimated 9200.0ft (2.8km) of SGRB strata that was eroded off the top of the uplifted block which Rizer #1 penetrated. Presumably these strata are present within those portions of the SGRB that were not inverted. These strata are also overlain by the Early Jurassic basalt flow hypothesized to cover much of the SGRB (McBride et al., 1989). If any porous strata are present, however, there still would be a problem with these layers intersecting highly fractured dikes.

3.5 CONCLUSIONS

1. Reservoir quality of the study sandstone was substantially diminished by a complex series of diagenetic events, which include early cementation by calcite

and sphene, followed by evaporates and multiple stages of quartz overgrowth and calcite cements during the relatively rapid subsidence of the basin.

2. Based on modal analysis of compaction indices indicate a majority of the Rizer #1 sandstones appear to have been buried 2000ft to 6000ft (0.61km to 1.82km) deeper.
3. Based on results of SIMS analysis of δ^{18} O within quartz cements, the study sandstones were buried approximately 8200ft (2.50km) deeper than present burial depths at some point in their burial history.
4. Sandstones within Rizer #1 test borehole and those laterally equivalent sandstones within the same fault block are not suitable candidates for CO_2 sequestration.
5. Regarding reservoir properties for sandstones deeper within the Rizer #1 fault block, unless they experienced early cementation and subsequent dissolution of those cements to create secondary porosity or were over pressured early in their burial history, it is unlikely they possess reservoir properties to be suitable candidates for CO_2 sequestration.

3.6 CITATIONS

Blatt, H., Middleton, G., and Murray, G., 1987, Origin of Sedimentary Rocks, Second Edition: Prentice-Hall, Inc., Englewood Cliff, NJ, pp. 782 (p. 31).

Blatt, H., 1987, Oxygen isotopes and the origin of quartz: Journal of Sedimentary Petrology, v. 57, p. 373-377.

Bjørlykke, K. and Egeberg, P.K., 1993, Quartz cementation in sedimentary basins: American Association of Petroleum Geologists Bulletin, v. 77, p. 1538-1548.

Clayton, R.N., O'Niel, J.R., and Mayeda, T.K., 1972, oxygen isotope exchange between quartz and water: Journal of Geophysical Research, v. 77, p. 3057-3067.

Clendenin, C.W. Jr., Waddell, M.G., and Addison, A.D., 2011, Reactivation and Overprinting of South Georgia Rift Extension, Abstract Annual GSA Meeting, Minneapolis, MN

Colquhoun, D. J., Woollen, L. D., Van Nienwenhuise, D. S., Padgett, G. G., Oldham, R. W., Boylan, D. C., Bishop, J. W., and Howell, P. D., 1983, Surface and subsurface stratigraphy, structure and aquifers of the South Carolina Coastal Plain: Columbia, SC, State of South Carolina, Office of the Governor, 78 p

Ferry, J.M., Ushikubo, T., and Valley, J.W., 2011, Formation of forsterite by silicification of dolomite during contact metamorphism: Journal of Petrology Advance Access, v. 0, p. 1-22.

Folk, R. L., 1980, Petrology of Sedimentary Rocks: Austin, University of Texas Publication, 170 p.

Epstein, S., Graf, D.L., and Degens, E.T., 1964, Oxygen isotope studies on the origin of dolomites. In: Craig, H., Miller, S.L., Wasserburg, G.J. (eds.), Isotopic and Cosmic Chemistry, North Holland, Amsterdam, p. 169-180

Gretz M., Lathuilière, B., Martini, R., Bartolini, A., 2013, The Hettangian corals of the Isle of Skye (Scotland): An opportunity to better understand the palaeoenvironmental conditions during the aftermath of the Triassic–Jurassic

boundary crisis: Palaeogeography, Palaeoclimatology, Palaeoecology, v. 376, p. 132-148

Harwood, J., Aplin, A.C., Fialips, C.I., Iliffe, J.E., Kozdon, R., Ushikubo, T., and Valley, J.W., 2013, Quartz cementation history of sandstones revealed by high-resolution SIMS oxygen isotope analysis: Journal of Sedimentary Petrology, v. 83, p 522-530.

Hervig, R.L., Williams, L.B., Kirkland, I.K., and Longstaffe, F.J., 1995, Oxygen isotope microanalysis of diagenetic quartz: possible low temperature occlusion of pores: Geochimica et Cosmochimica Acta, v. 59, p. 2537-2543.

Hiatt, E.E., Kyser, T.K., Fayek, M., Polito, P., G.J., Holk, and Riciputi, L.R., 2007, Early quartz cements and evolution of paleohydraulic properties of basal sandstones in three paleoproterozoic continental basins: Evidence from *in situ* δ^{18} O analysis of quartz cements: Chemical Geology, v. 238, p. 19-37.

Katz, D.A., Eberli, G.P., Swart, P.K., and Smith, Jr., L.B., 2006, Tectonic-hydrothermal brecciation associated with calcite precipitation and permeability destruction in Mississippian carbonate reservoirs, Montana and Wyoming: American Association of Petroleum Geologists Bulletin, v. 90, p. 1803-1841.

McBride, E.F., 1989, Quartz cement in sandstones: a review: Earth-Science Reviews, v. 26, p. 69-112.

McBride, E.F., Diggs, T.N., and Wilson, J.C., 1991, Compaction of Wilcox and Carrizo Sandstones (Paleocene-Eocene) to 4420 M, Texas Gulf Coast: Journal of Sedimentary Petrology, v. 61, p 73-85.

McBride, J.H., Nelson, K.D., Brown, L.D., 1989, Evidence and implications of an extensive early Mesozoic rift basin and basalt/diabase sequence beneath the southeast Coastal Plain: Geological Society of America Bulletin, v. 101, p. 512-520.

Milliken, K.L., Land, L.S., and Loucks, R.G., 1981, History of burial diagenesis determined from isotopic geochemistry, Frio Formation, Brazoria County, Texas: American Association of Petroleum Geologists Bulletin, v. 65, p. 1397-1413.

O'Neil, J.R., Clayton, R.N., and Mayeda, T.K., 1969, Oxygen isotope fractionation in divalent metal carbonates, Journal of Chemical Physics, v. 51, p. 5547-5558

Parcerisa, D., Gomez-Graz, D., and Trave, A., 2005, A model of early calcite cementation in alluvial fans: Evidence from the Burdigalian sandstones and limestones of the Valles-Penedes half-graben (NE Spain): Sedimentary Geology, v.178, p. 197-217.

Pettijohn, F. J., Potter, P. E., and Siever, R., 1973, Sand and Sandstones: Springer- Verlag; New York, Heidelberg, Berlin, Heidelberg, London, Paris, Tokyo, pp. 618. Pittman, E.D. and Larese, R.E., 1991, Compaction of lithic sands: experimental results and applications, American Association of Petroleum Geologists Bulletin, v. 75, p. 1279-1299.

Temples, T.J. and Waddell, M.G., 1996, Application of petroleum geophysical well logging and sampling techniques for evaluating aquifer characteristics: Ground Water, V. 34, p. 523-531.

Tillman, J.E. and Barnes, H.L. 1983, Deciphering fracturing and fluid migration histories in northern Appalachian Basin, American Association of Petroleum Geologists Bulletin, v. 67, p. 692-705.

Tseng, Hsin-Yi, Onstott, T.C., Burruss, R.C., and Miller, D.S., 1996, Constraints on the thermal history of Taylorsville Basin, Virginia, U.S.A., from fluid-inclusion and

fission-track analyses: implications for subsurface geomicrobiology experiments: chemical Geology, v. 127, p. 297-311.

Waddell, M. G., Addison, A. D., Daniel Brantley, D., and Knapp, C., 2011, Using P- Wave Reflection data to Map Potential Caprock and Reservoir Rock for Possible CO2 Geologic Sequestration in the South Georgia Rift (SGR) in the Lower Coastal Plain of South Carolina, American Association of Petroleum Geologists 2011 Annual Convention, Houston, TX.

Wilson, J.C. and McBride, E.F., 1988, Compaction and Porosity evolution of Pliocene sandstones, Ventura Basin, California: American Association of Petroleum Geologists Bulletin, v. 72, p 664-681.

Withjack, M.O., Schlische, R.W., and Olsen, P.E., 1998, Diachronous rifting, drifting, and inversion on the passive margin of central eastern North America: An analog for other passive margins: AAPG Bulletin, v. 82, p. 817-835

Withjack, M. O., Schlische, R.W. and Olsen, P. E., 2012, Development of the passive margin of eastern North America: Mesozoic rifting, igneous activity, and breakup. In: Bally, A. W. & Roberts, D. G. (eds), Principles of Phanerozoic Regional Geology, v. 1, Elsevier, Amsterdam, p. 301–335

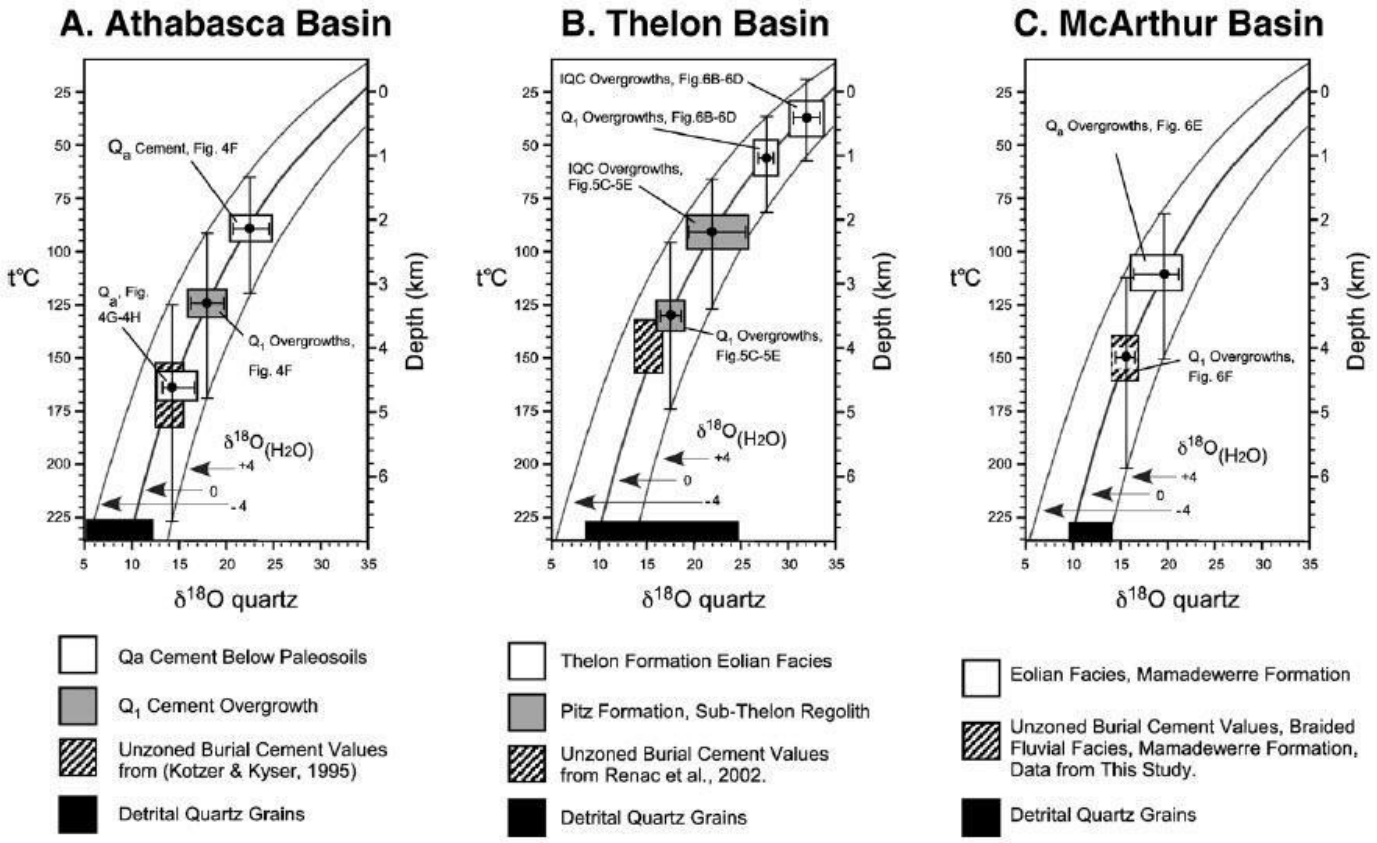

Figure 3.1 Diagrams from study by Hiatt et al. (2007) of three Proterozoic basins showing equilibrium δ^{18} O values of quartz (curves) calculated using isotopic composition of pore fluid (δ^{18} $O_{(H2O)}$= -4, 0, +4‰ VSMOW) and with δ^{18} O values based on SIMS analyses and temperatures calculated using the equation of Clayton et al. (1972). Depths are calculated based on the geothermal gradient of 30°C/km with a surface temperature of 25 °C. From Hiatt et al. (2007).

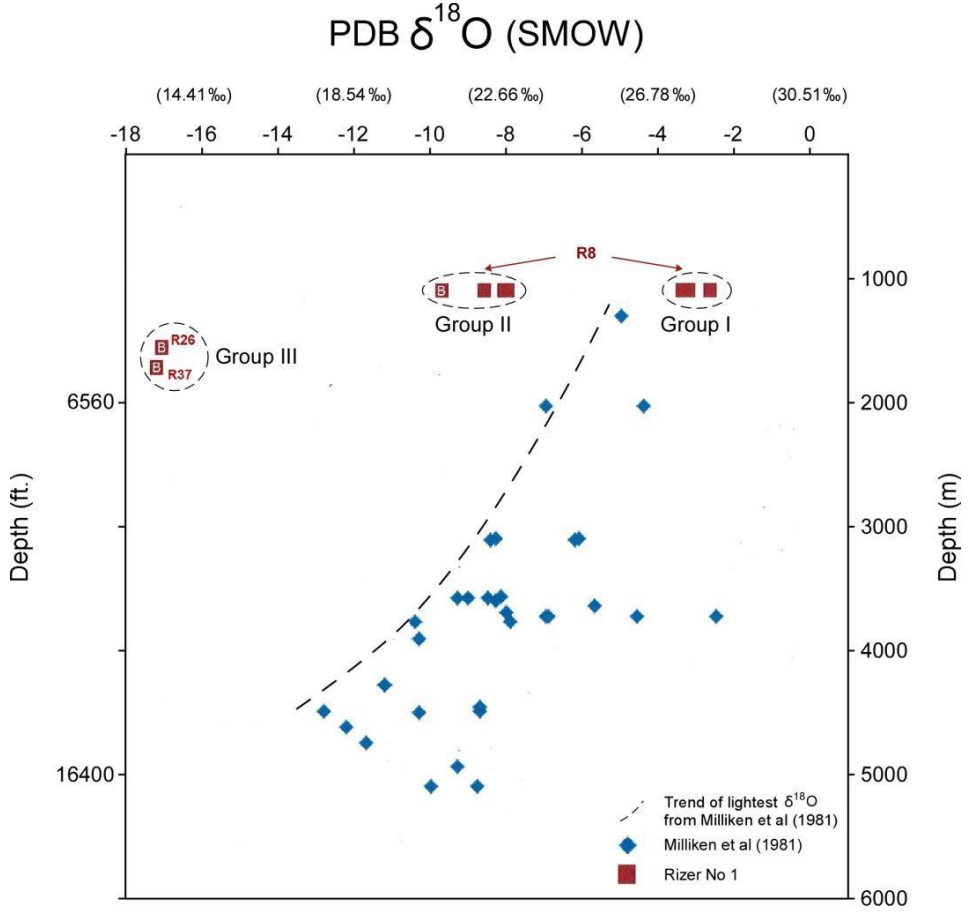

Figure 3.2 Plot of δ^{18} O values of primarily calcite cements versus depth from study by Milliken et al. (1981; blue diamonds) from well samples in Brazoria County, Texas. Dashed line indicates trend for lightest δ^{18} O values from Milliken et al. (1981) study. δ^{18} O values of primarily calcite cements from Rizer #1 samples are plotted with red squares with sample numbers denoted (Table 3.1). A majority of the Rizer #1 data are from SIMS analyses except for three (3) samples obtained from bulk samples (white "B" within square). Comparison of Rizer #1 data with Texas data indicates Rizer #1 calcite cements formed much deeper than their present-day burial depth. Modified from Milliken et al. (1981).

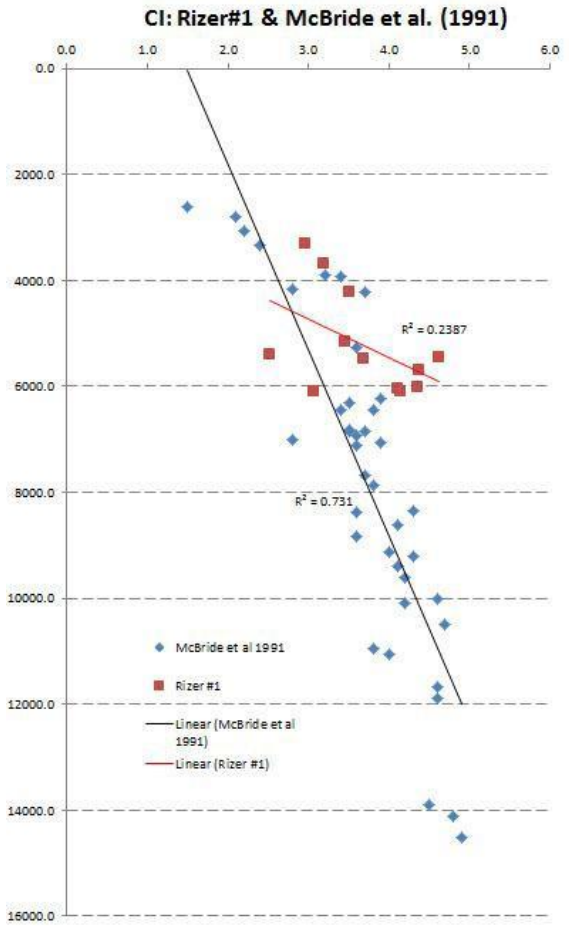

A

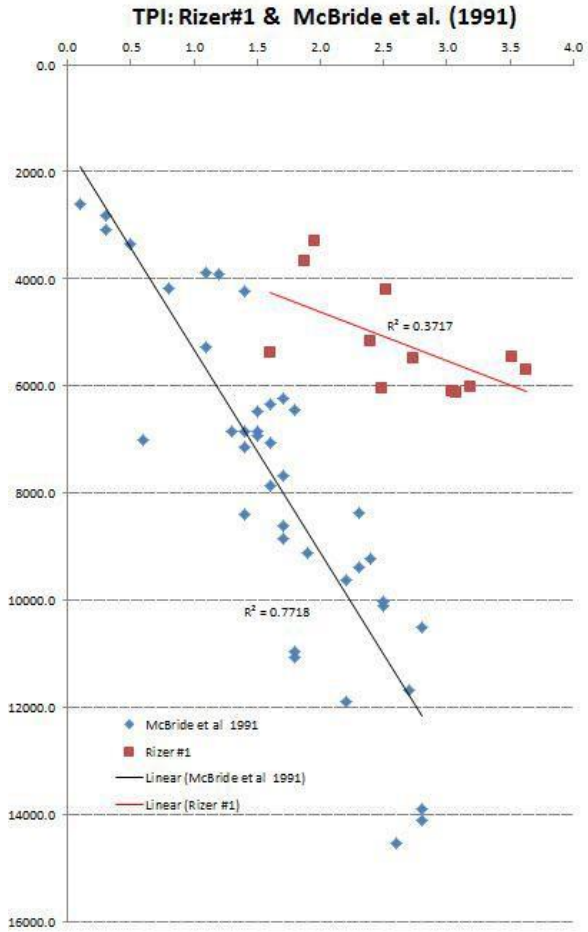

B

Figure 3.3 Cross-plots of contact index or CI (A) and tight packing index (TPI) values versus depth for forty (40) samples from McBride et al. (1991) study (blue diamonds) and twelve (12) samples from test borehole Rizer #1 (red squares). In both plots, the majority of Rizer #1 samples plot with higher values than McBride et al. (1991) samples from corresponding depths.

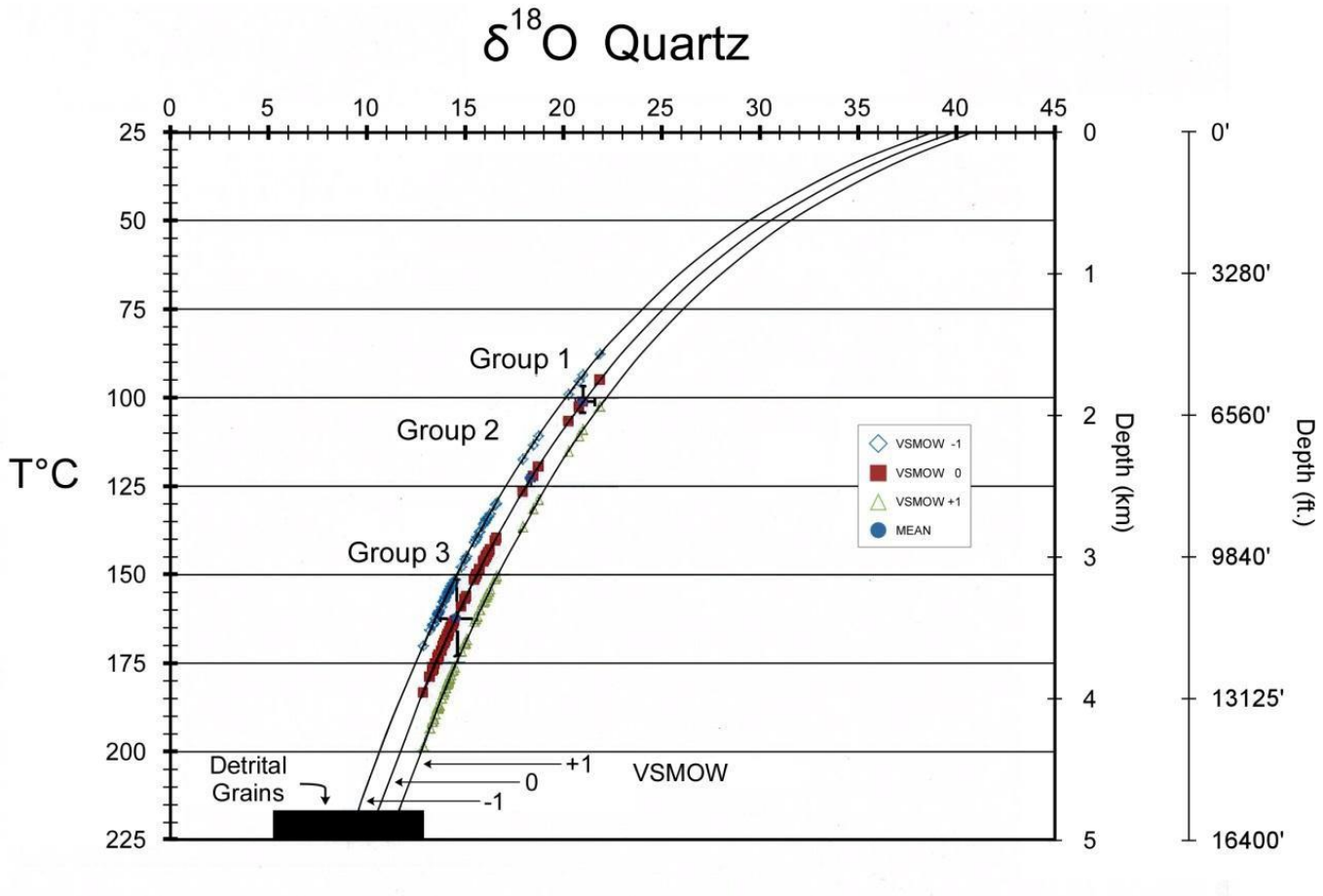

Figure 3.4 Diagrams showing equilibrium δ^{18} O values of quartz (curves) calculated using isotopic composition of pore fluid ($\delta^{18}O_{(H2O)}$= -1, 0, +1‰ VSMOW) and with δ^{18} O values based on SIMS analyses performed on two samples from Rizer #1 (R26 from 5152.5ft and R37 from 5702.5ft). Paleo pore water or precipitation temperatures are calculated using the equation of Clayton et al. (1972). Depths are calculated based on the geothermal gradient of 40°C/km with a surface temperature of 25 °C. Data are from Appendix O and summarized in Table 3.2.

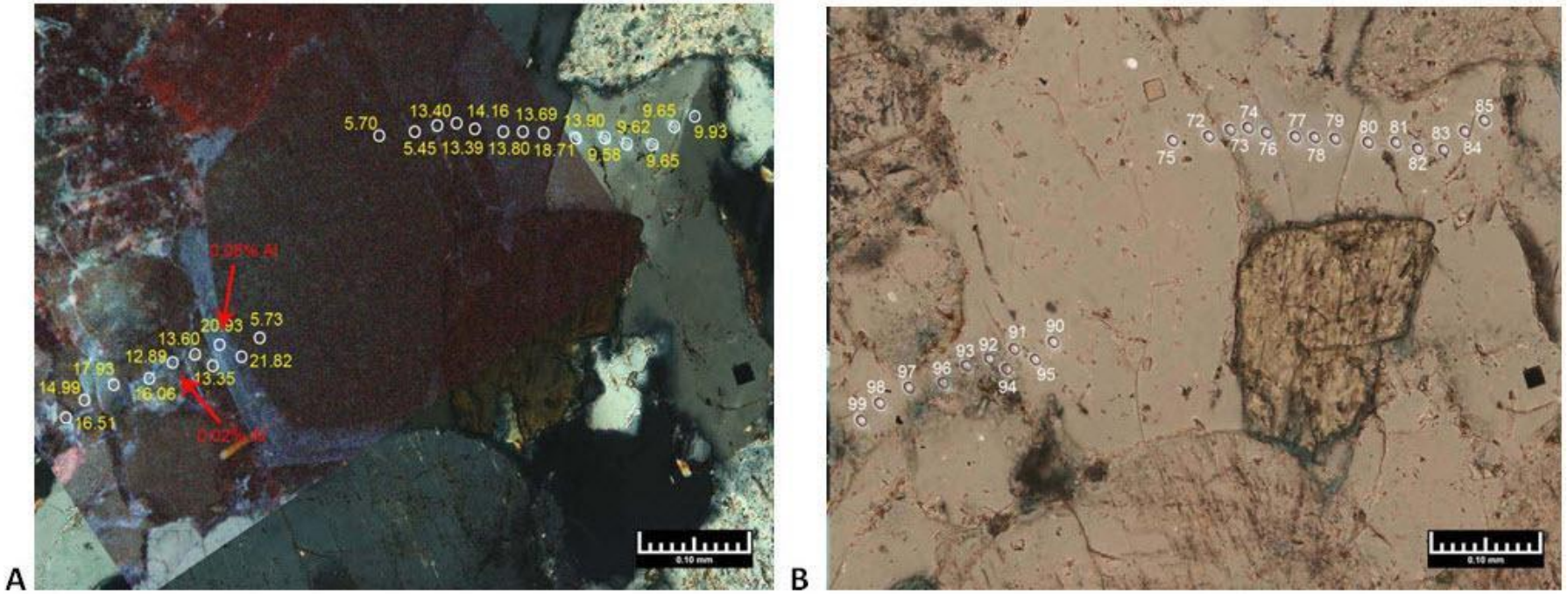

Figure 3.5 Photomicrographs of the sample from 5702.5ft (R37) show locations of spots analyzed by SIMS for δ^{18} O (white circles in A and sample pits shown in B). Figure 3.5A, which is a cross polarized light view with a portion of the view overlain with a CL SEM image, displays δ^{18} O values (yellow numbers in ppt [‰] relative to V SMOW) next to the circled SIMS sample pits. The sample location #96, which appears to be a quartz overgrowth, has the lowest δ^{18} O value (12.89‰) of any quartz cement encountered in this study. Values lower are considered detrital quartz grains. Quartz cement with δ^{18} O values greater than 20.00‰ are within luminescing bands within the overgrowth and are associated with slightly higher aluminum content (percent values in red) than quartz cement with lower δ^{18} O values (based on electron microprobe results). Figure 3.5B, which is a plain light view, shows sample numbers displayed in white next to their respective SIMS sample pits.

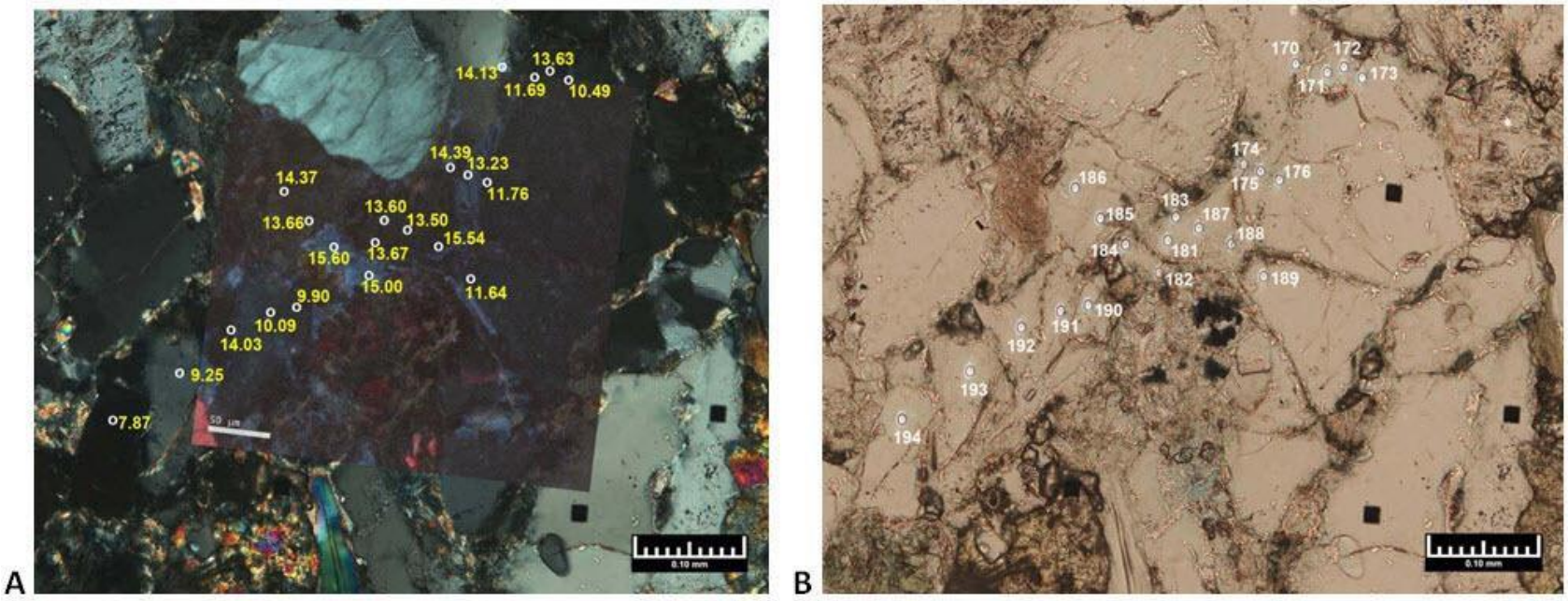

Figure 3.6 Photomicrographs of the sample from 5152.5ft (R26) show locations of spots analyzed by SIMS for δ^{18} O (white circles in A and sample pits shown in B). Figure 3.6A, which is a crossed polarized light view with a portion of the view overlain with a CL SEM image, displays δ^{18} O values (yellow numbers in ppt [‰] relative to V SMOW) next to the circled SIMS sample pits. δ^{18} O values greater than 12.00‰ are considered quartz cement and values that are lower are considered detrital quartz grains. Due to the high degree of compaction and accompanying pressure solution along grain-to-grain contacts, it is difficult to distinguish quartz cement from detrital grains. Figure 3.6B, which is a plain light view, shows sample numbers displayed in white next to their respective SIMS sample pits.

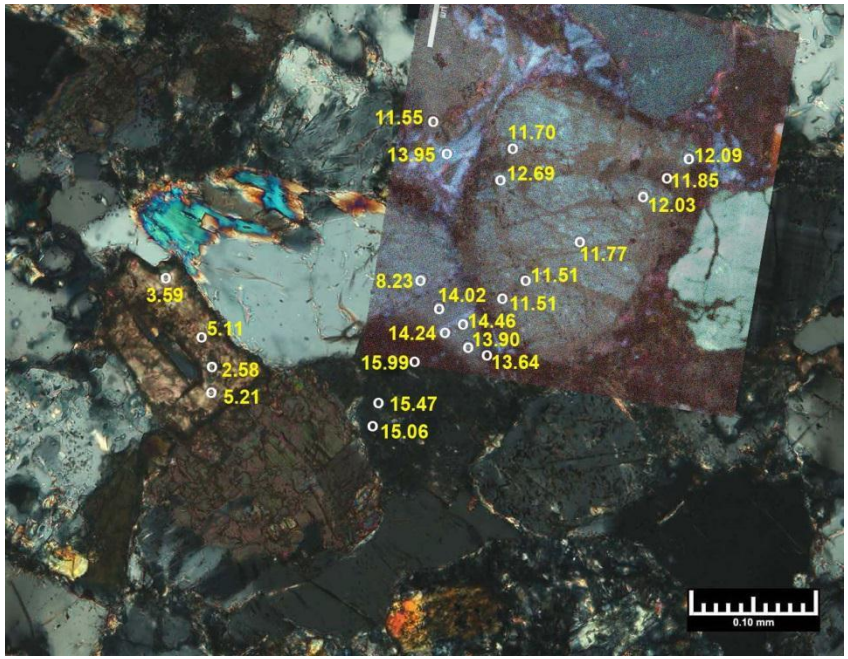

A

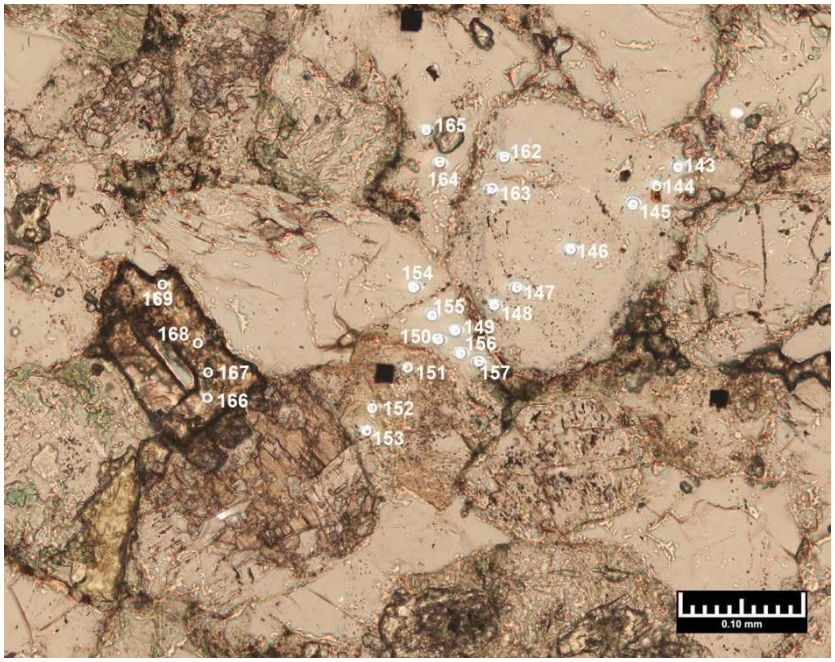

B

Figure 3.7 Photomicrographs of the sample from 5152.5ft (R26) show locations of spots analyzed by SIMS for δ^{18} O (white circles in A and sample pits shown in B). Figure 3.7A, which is a crossed polarized light view with a portion of the view overlain with a CL SEM image, displays δ^{18} O values (yellow numbers in ppt [‰] relative to VSMOW) next to the circled SIMS sample pits. Sample numbers 166 through 169 are within what apparently is a detrital sphene based on its low δ^{18} O values (2.58 to 5.21; yellow numbers in per mill relative to VSMOW). The dark, irregular border of the sphene grain may be sphene overgrowths but the surfaces are too rough to make a SIMS measurement. All other SIMS measurements in these photomicrographs are within quartz with δ^{18} O values greater than 12.88‰ considered to be from quartz cement and values that are lower are considered detrital quartz grains. The grain pictured in Figure 3.7 (sample numbers 143 through 148 and 162 and 163) is judged to have been fractured prior to deposition, since the quartz fracture-fill does not appear to possess similar fluorescence as the adjoining intergranular quartz cement.

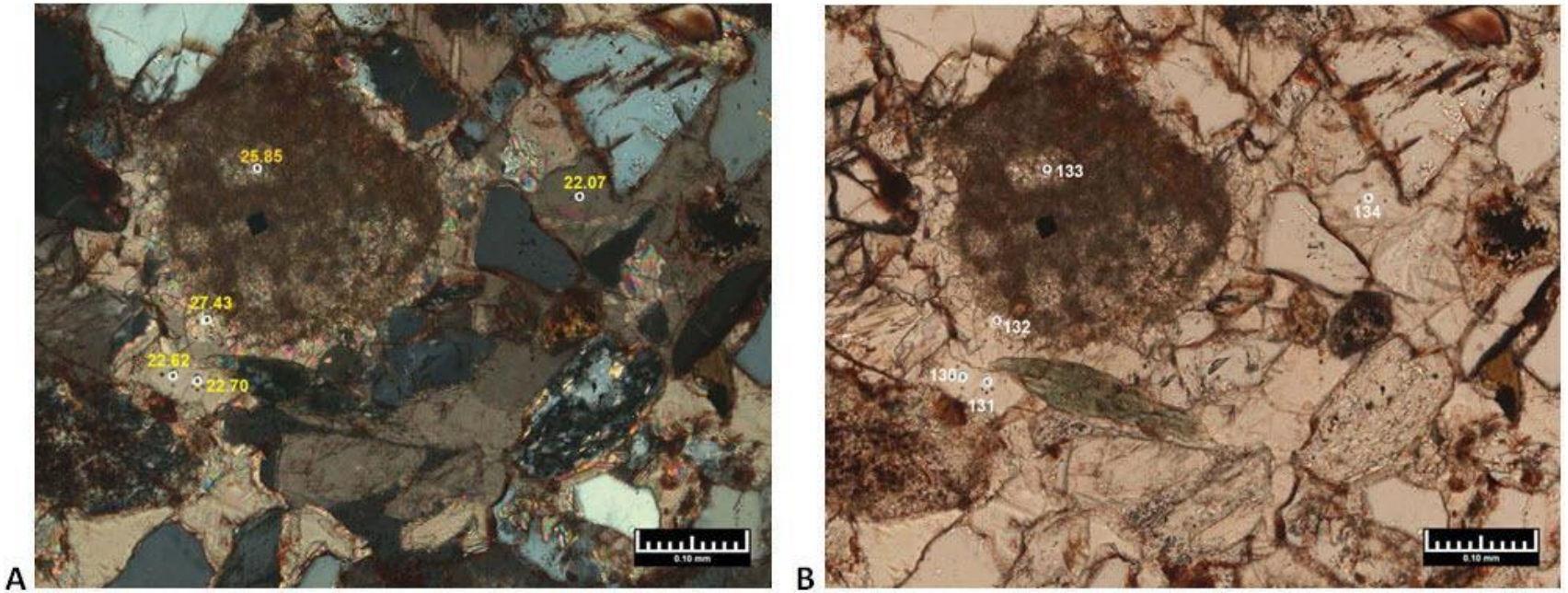

Figure 3.8 Photomicrographs of the sample from 3674.0ft (R8) show locations of spots analyzed by SIMS for δ^{18} O (white circles in A and B). Figure 3.8A, which is a cross polarized view, displays δ^{18} O values (yellow and gold numbers in ppt [‰] relative to VSMOW) next to the circled SIMS sample pits. δ^{18} O values from calcite spar (yellow) indicate there are two distinct groups of δ^{18} O values (22.07‰-22.70‰ and 27.43‰). The δ^{18} O value from a micritized grain (gold; sample site #133 in Figure 3.8B) may not be an accurate measurement due to the roughness of the sample surface. Figure 3.8B, which is a plain light view, shows sample numbers displayed in white next to their respective SIMS sample pits.

A

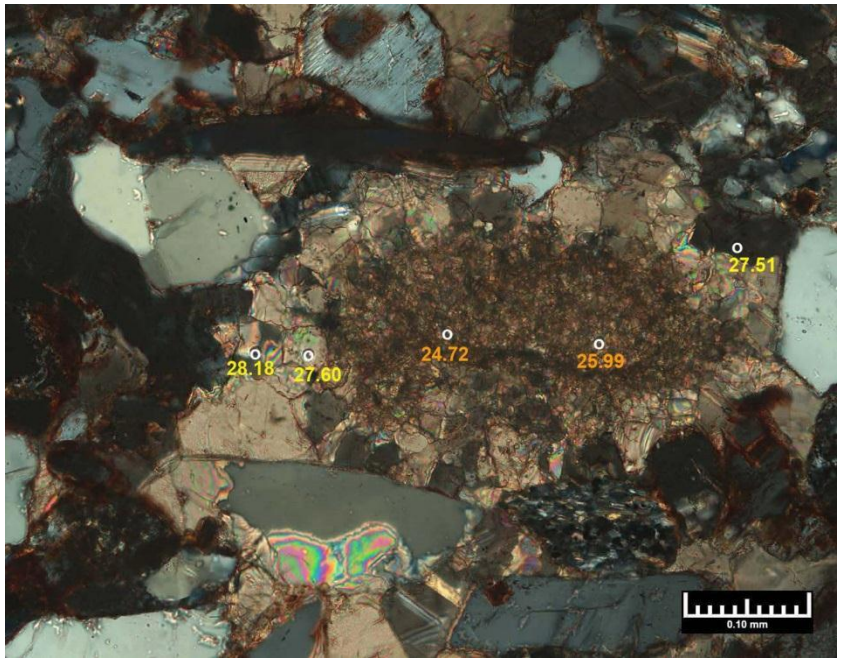

B

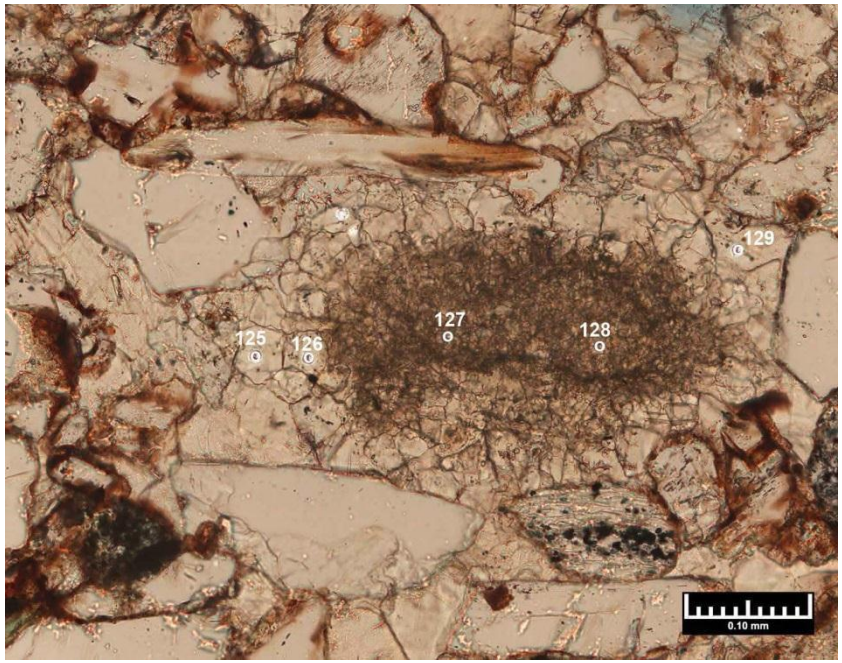

Figure 3.9 Photomicrographs of the sample from 3674.0ft (R8) show locations of spots analyzed by SIMS for δ^{18} O (white circles in A and B). Figure 3.9A, which is a XN view, displays δ^{18} O values (yellow and gold numbers in per mill relative to V- SMOW) next to the circled SIMS sample pits. δ^{18} O values from calcite spar (yellow) indicate there are two distinct groups of δ^{18} O values (22.07‰-22.70‰ and 27.43‰). δ^{18} O values from micritized grain (gold; sample sites #127 and #128 in Figure 3.9B) may not be an accurate measurement due to the roughness of the sample surface. Figure 3.9B, which is a plain light view, shows sample numbers displayed in white next to their respective SIMS sample pits.

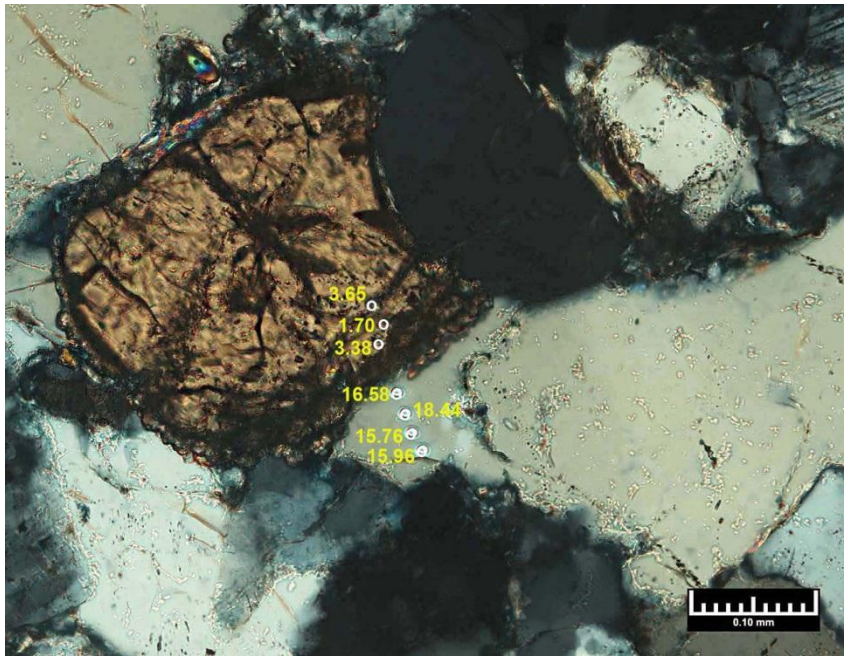

A

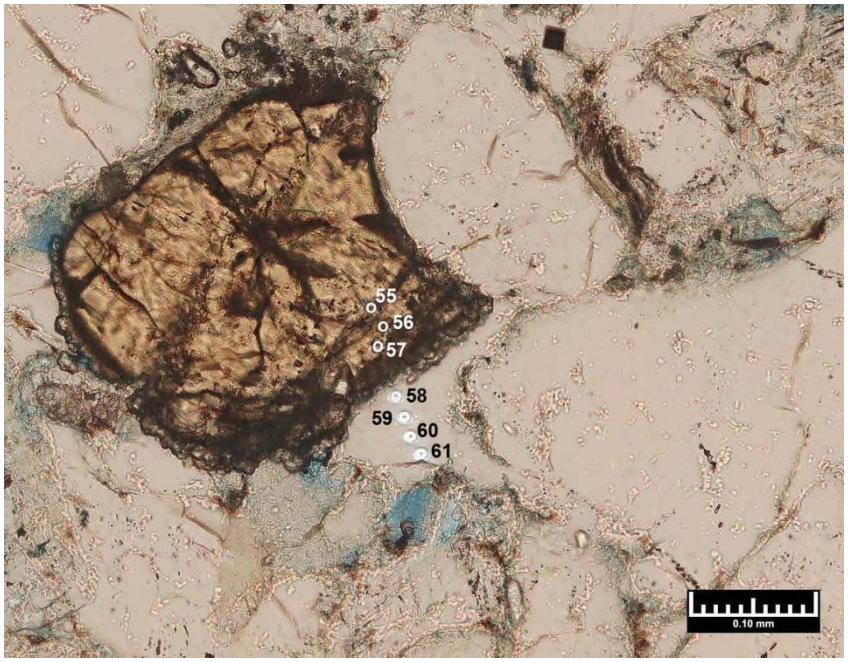

B

Figure 3.10 Photomicrographs of the sample from 5702.5ft (R37) show locations of spots analyzed by SIMS for δ^{18} O (white circles in A and sample pits shown in B). Figure 3.10A, which is a cross polarized view with a portion of Figure 3.10B, which is a plain light view, shows sample numbers displayed in black next to their respective SIMS sample pits. Sample numbers 55 through 57 are within what apparently is a detrital sphene based on its low δ^{18} O values (1.70 to 3.65; yellow numbers in per mill relative to VSMOW). The dark, irregular border of the sphene grain may be sphene overgrowths but the surface was too rough to make a SIMS measurement. The higher δ^{18} O values (15.76 to 18.44) are within quartz overgrowth cement (sample spots 58 to 61).

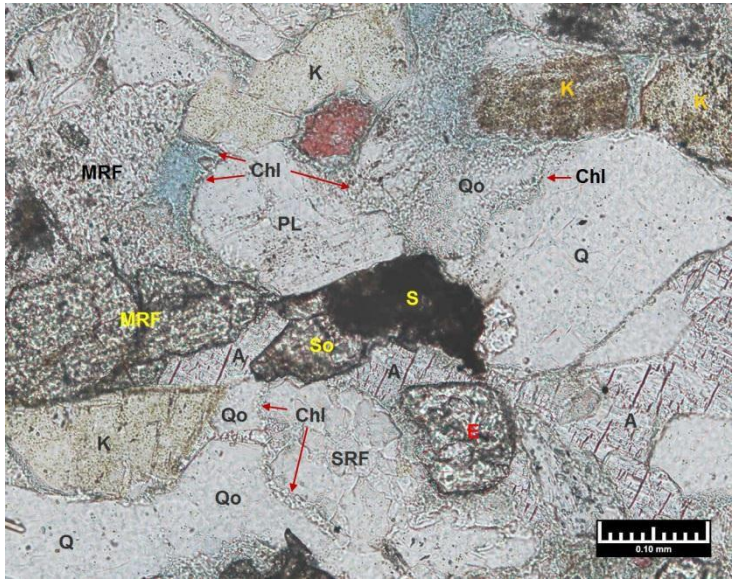

A

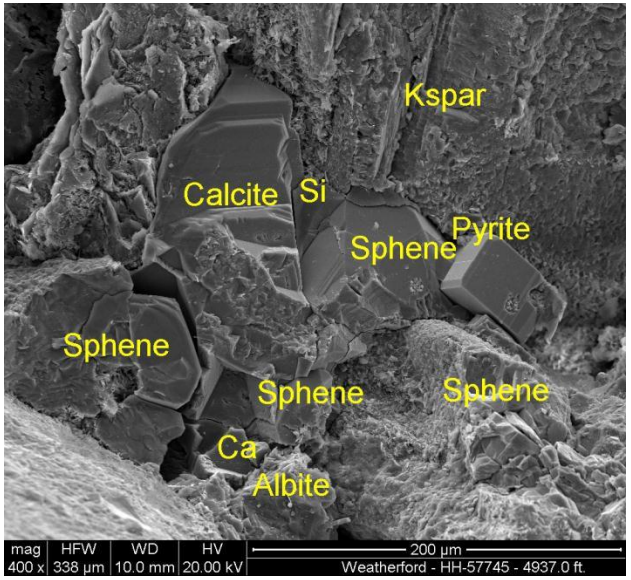

B

C

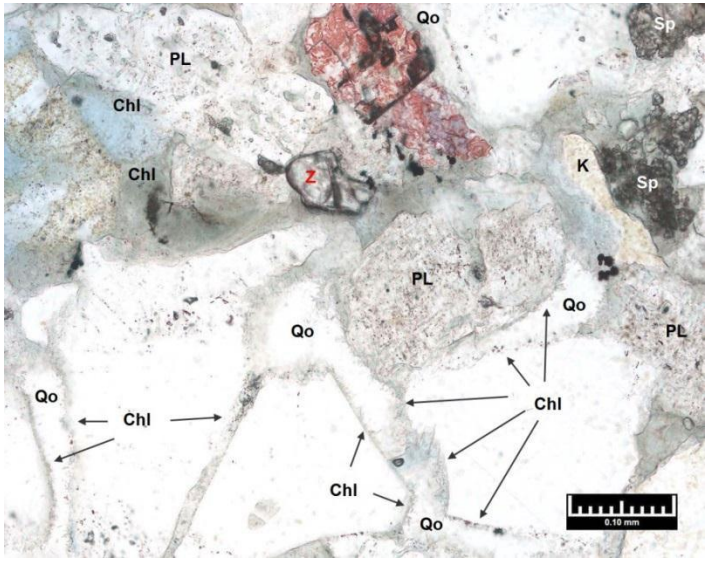

D

Figure 3.11

Figure 3.11 Photomicrographs from various RSWC samples illustrating stages of diagenesis. A. Plain light photomicrograph of sample from 5360.0ft (1-62R) shows relationship of anhydrite cement (A), sphene detrital grain (S) with extensive overgrowth (So), authigenic chlorite clay (Chl), and quartz overgrowth cement (Qo). Also present in the photomicrograph are detrital grains of quartz (Q), sedimentary rock fragments (SRF), metamorphic rock fragments (MRF), plagioclase (PL), epidote (E), and potassium feldspar (K). B. SEM image of RSWC from 4937.0ft shows the coincidence of authigenic sphene, calcite (Ca), and pyrite with framework grains of quartz (Si) and potassium feldspar (Kspar). C. SEM image showing quartz overgrowths partially engulfing pore-lining authigenic chlorite and illite clays. D. Photomicrograph (with transmitted white light) of fine-grained lithic arkose in RSWC from 5360.0ft showing abundance of grain coating chlorite clay (Chl) with some being engulfed by quartz overgrowth cement (Qo). Patches of sphene cement are present (Sp). Calcite appears to be replacing a grain (stained red). Framework grains consist of quartz (white), plagioclase (PL), potassium feldspar (K), and zircon (Z). Porosity (blue) consists of secondary intragranular and microporosity associated with clays.

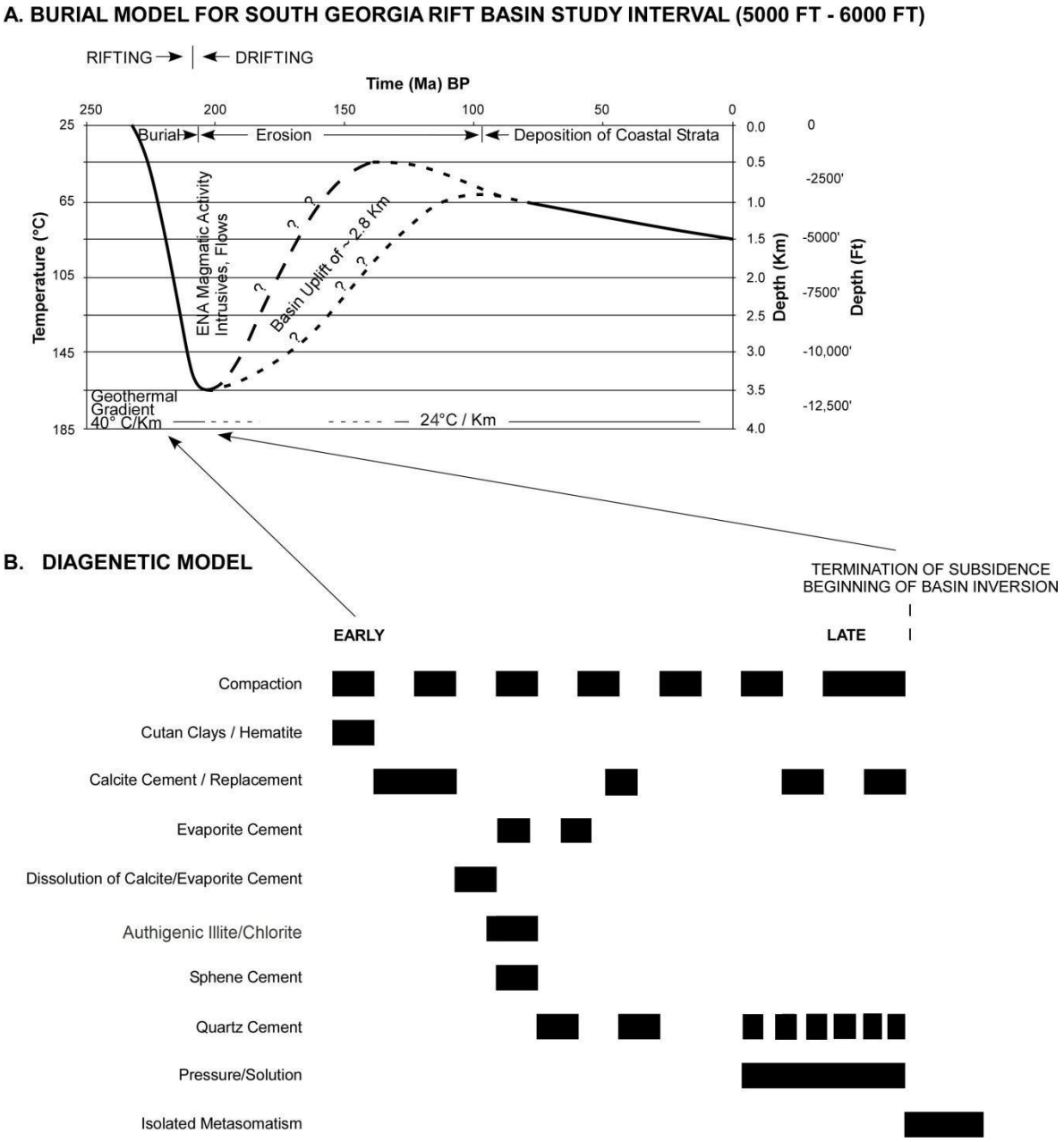

Figure 3.12 Burial (A) and diagenetic (B) models for South Georgia Rift Basin based on paleo-pore water temperatures inferred from δ^{18} O analyses of quartz cements in sandstones between present burial depths of 5000ft to 6000ft (1.5km to 1.8km). Calculations of paleo-pore water temperatures derived from the SIMS δ^{18} O values are based on the equation of Clayton et al. (1972) and use the VSMOW values of 0 (normal sea water). Timing of the rifting and drifting phases is based on Withjack et al. (1998, 2012). Age of end of uplift at 140 Ma BP is based on model of Tseng et al. (1996) for Taylorsville Basin in Virginia. The unconformity at the top of the Late Triassic/Early Jurassic is overlain by South Carolina coastal plain strata beginning with the Turonian/Coniacian-aged (94 Ma BP) Middendorf Formation (Colquhoun et al., 1983). Recent to Cretaceous geothermal gradient is based on Temples and Waddell (1996).

SECTION 4

4.0 Elemental Analysis of Rizer #1 Test Borehole, Colleton County, South Carolina

4.1 INTRODUCTION

4.1.1 Background

This section presents whole-rock elemental analysis data collected by energy- dispersive X-ray fluorescence (ED-XRF) in an effort to better characterize the stratigraphy at the Rizer#1 test borehole from the 2660ft to 6200ft interval. Chemostratigraphy is a geochemical technique designed to complement stratigraphy and petrology in basins where this information is lacking or poorly understood (Weibel et al., 2010; Ratcliffe et al., 2004), as in the case of the South Georgia Rift Basin (SGRB). For more detailed information concerning the geologic background, please refer to Section 1 of this report.

4.1.2 Goals

The primary objective in this chemostratigraphy study was to establish a chemostratigraphic zonation representing variations in the general lithology, particularly where no conventional core or rotary sidewall core (RSWC) samples had been obtained and only cutting samples were available. Additional objectives include making relevant inferences relating to source lithologies and weathering using the elemental data collected and extrapolating to existing information derived from core description, thin section modal analyses, scanning electron microscope (SEM) images, X-ray diffraction (XRD) data, and borehole imaging logs.

4.2 METHODS

4.2.1 ED-XRF Sample Resolution

A total of 342 whole-rock samples (10 conventional core samples, 33 RSWC samples, and 299 cuttings samples) were analyzed by ED-XRF for elemental composition. All cuttings for this project were collected at 10-foot intervals, which is a common spacing for most field-wide or basin-wide chemostratigraphic studies. Since cuttings comprise the majority of the samples analyzed and were nearly continuous from 2775 feet to
6200 feet, elemental data from the cuttings were used as the primary input for establishing the chemostratigraphic zonation.

High-resolution results from conventional core require an average spacing of 1-2 feet (0.3-0.6 meters). A medium-resolution zonation requires core samples to be taken at an average spacing of 2-6 feet (0.6-1.8 meters), while low resolution results from an average spacing of 6-10 feet (1.8-3.0 meters). Where average spacing exceeds 10 feet (3.0 meters) for core, elemental variations cannot be closely defined, and the data provides only a reconnaissance zonation. These same criteria for chemostratigraphic resolution apply to RSWC samples. Due to these resolution restrictions, data from

conventional core plugs and sidewall cores were used to augment the cuttings data. All sample types were plotted together when interpreting the elemental data.

4.2.2 Sample Preparation and Data Acquisition

All sample fragments were cleaned with tap water to remove superficial contamination from coring fluid or dust. They were then crushed to approximately pea-sized fragments, placed in tungsten-carbide (WC) jars with tungsten carbide grinding balls, and powdered using a high-speed mechanical mixing mill. The powdered material from each sample was then pressed under approximately 15,000 pounds of pressure into pellets 31 mm in diameter.

Pellets were analyzed on a table-top ED-XRF (energy-dispersive X-ray fluorescence) instrument to obtain elemental data. The ED-XRF uses a Pd-anode X-ray tube as an excitation source, with a maximum operating voltage of 50 kV and a maximum powder output of 50 W. Four separate secondary X-ray targets are used to optimize sample irradiation. The X-ray fluorescence detector is a large- area, Peltier-cooled, silicon-drift detector (SDD). Weatherford-proprietary calibration and correlation procedures for siliciclastic lithologies were applied for the Rizer #1 samples.

Quality control and corrections were achieved using well-established international geochemical reference materials (GRMs). For this study, the GRMs chosen were AGV-2 (andesite), BHVO-2 (basalt), JG-2 (granite), GBW-07106 (sandstone), and SDC-1 (schist). SDC-1 was used to perform drift corrections, as it was most comparable with the range of values encountered in the full set of samples.

The ED-XRF produced high precision data of good to very good for the 12 standard major elements and 20 trace elements. The major elements quantified are SiO_2, TiO_2, Al_2O_3, Fe_2O_3, MnO, MgO, CaO, Na_2O, K_2O, P_2O_5, SO_3, and Cl; all are reported in weight percent (%) of the whole rock. Except for Cl, the major elements are always given as oxides, per usual geochemical practice. The 20 trace elements measured for this study include V, Cr, Co, Ni, Cu, Zn, Ga, As, Br, Rb, Sr, Y, Zr, Nb, Mo, Ba, Hf, Pb, Th, and U; all are given in parts per million (ppm) by weight.

Sample contamination for this data set is minimal, and consists only of anomalously high values of cobalt (Co) in most samples with greater than 60% SiO_2. The Co was derived by slight abrasion of the interior of the WC grinding jars by the sand grains in the samples. Co values were therefore not used for chemostratigraphic interpretation. Barium (Ba) is a common contaminant in most cuttings samples due to the addition of powdered barite as a weighting agent in drilling fluids. It is therefore always necessary to assess if Ba is present as a contaminant. Values of Ba for all Rizer #1 samples range from < 2 ppm to 1908 ppm, with an average of 592 ppm. This is within the range expected for samples containing K-feldspar, biotite, some sedimentary rocks fragments, and minor amounts of clay. K-feldspar and biotite in particular have Ba as a substituting cation in their crystal structures, and this Ba is transferred to clays upon weathering in the sediment source area. The data for this study therefore indicate that Ba is not

present as a significant contaminant in the Rizer #1 samples.

4.2.3 Reference Lithologies

In several of the figures presented in this report, reference lithologies are included with the Rizer #1 sample data to provide compositional context. Reference lithologies are accepted data compilations, and their average values have been derived from large data sets from past studies. Averages for shale, cratonic sandstone, upper continental crust, basalt, andesite, and granite are employed in this study. They are used as reference points for understanding the compositional shifts within the siliciclastic sequence drilled in the Rizer #1 well. In particular, the following reference lithologies are shown on selected plots in this report:

- **Average Basalt.** Three compiled compositions for Late Proterozoic, Paleozoic, and Mesozoic–Cenozoic time intervals (all from Condie 1993).

- **Average Andesite.** Three compiled compositions for Late Proterozoic, Paleozoic, and Mesozoic–Cenozoic time intervals (all from Condie 1993).

- **Average Granite.** Two compiled compositions for Proterozoic and Phanerozoic time intervals (both form Condie 1993).

- **Average Upper Continental Crust (UCC).** Three compiled compositions from Taylor and McLennan (1985), McLennan (1995), Wedepohl (1995), and Rudnick and Gao (2004).

- **Average Cratonic Sandstone.** One compiled composition for the Phanerozoic (Condie 1993). This comprises data from clean sandstones, and does not included clay-bearing greywackes.

- **Average Shale.** Four compiled compositions from Taylor and McLennan (1985), McLennan (1995), Wedepohl (1971, 1991), and Condie (1993).

It should be noted that the elemental values for the reference lithologies, particularly the shales, cannot be considered strictly definitive. The current compilations for shale date to the early 1990s and are in need of revision. They are biased toward Paleozoic and Mesozoic outcrop samples, mostly from North America and Australia. In particular, there are thousands of kilometers of late Mesozoic and Cenozoic mudstones that have been drilled in the offshore continental shelves worldwide that are not represented in the compilations.

Despite this qualification, the average shale compiled by Taylor and McLennan (1985) and McLennan (1995) is considered to be the best current approximation to "normal grey shale" of Paleozoic–Mesozoic age. This compilation is known as PAAS for "Post- Archean Average Australian Shale", and is widely used by chemostratigraphers and petrologists.

4.3 RESULTS

4.3.1 Delineating Elemental Packages and Units

A clear chemostratigraphic zonation is recognized in the Rizer #1 Test Borehole, but is often subtle in character. Six elemental packages (P1 through P6 in ascending order) and 21 Elemental Units have been defined. A summary of the bases, tops, and thicknesses of the recognized elemental packages and units are given in Table 3 (Appendix P). Figures 4.1 and 4.2 show the zonation as depth plots of major elements and Al_2O_3-normalized major-element ratios. Figures 4.3 and 4.4 show the zonation as depth plots of trace elements and Al_2O_3-normalized trace elements. Figure 4.5 demonstrates the zonation as depth plots of relatively immobile element ratio affinities. Each package and unit is described in detail as follows. For more information regarding the elemental demarcation of various packages and units, please refer to Appendix P.

Package 1 (6070 feet to 6200 feet)

This deepest interval sampled in the Rizer #1 is defined as Package 1 (referred to as P1), which is further divided into two units (U1-1 and U1-2). Overall, P1 is characterized by relatively high values of bulk-rock TiO_2, Al_2O_3, Fe_2O_3, MnO, MgO and CaO (Figure 4.6a), and overall low Al_2O_3-normalized ratios of SiO_2 and Na_2O (Figure 4.6b). Relatively high values of V, Cr, Co, Y (slight), Zr (slight), and high bulk rock values of Zn, Ga, Rb, Th and U are present (Figure 4.6c). When normalized to Al_2O_3, overall high trace element ratios of V, Cr, Ni, Zn, and Cu are characteristic (Figure 4.6d). Relatively low but increasing bulk rock values of Zr, ratios of Zr (Zr/Ti, Zr/Cr, Zr/Y, Zr/Th, Zr/U), slightly high Th ratios (Th/Mn, Th/P, Th/ Co, Th/Y), and distinctly higher Th/Zr values are observed in P1 (Figure 4.5).

- **Unit 1-1.** This deepest sampled interval of Package 1 is defined as Unit 1-1 (U1-1) and is characterized by higher bulk rock concentrations of Fe_2O_3, MgO, K_2O and lower concentrations of the bulk rock Na_2O. Higher Al_2O_3-normalized ratios of Mg and Fe, and lower P/Al differentiate U1-1 from the overlying Unit 1-2 (U1-2). Bulk-rock trace elements V, Cr, Co, Ni, Cu, Zn, Ga, Sr, and normalized ratios V/Al, Ni/Al and Cu/Al are relatively high (Figure 6d). Other Al-normalized ratios like Th and U are lower in U1-1 compared to the overlying unit. Of the relatively immobile element ratios, lower ratios of Y/Ti, Zr/Cr and Zr/Ti stand out in U1-1.

- **Basalt I**. The two basal samples of U1-1 (6190 feet and 6200 feet) are inferred to be basalts, collectively termed Basalt I. The identification is based on very low SiO_2, Na_2O, K_2O, Y, Zr, Nb, and Ba, very high Fe_2O_3, MgO, Cr, Co, Ni, and moderately high V. TiO_2 is unusually low in these basalts (< 0.55 %), and in all basalts analyzed by XRF for this study.

- **Unit 1-2.** Higher bulk rock MnO, CaO, Al-normalized ratios like Na/Al, P/Al and lower Al-normalized ratios like Fe/Al and Mg/Al displays the subtle lithological variations between Unit 1-1 and Unit 1-2. Higher trace element concentrations of Y, Zr, Mo and U and lower V, Cr, Co, Ni and Cu, along with lower Al-normalized ratios like V/Al, Cr/Al, Ni/Al and Cu/Al and higher Ga/Al, Rb/Al, Y/Al, Zr/Al, Th/Al,

Mo/Al and U/Al differentiates Unit 1-2 from underlying Unit 1-1. Of the relatively immobile ratios, higher Y/Ti, Zr/Cr, Th ratios (Th/Al, Th/P, Th/Zr) and lower Zr/Nb and Ti/P can be observed in U1-2.

Package 2 (4860 feet to 6070 feet)

Major element composition shows that Package 2 (P2) can be recognized by higher bulk-rock SiO_2 , Na_2O, lower TiO_2, Fe_2O_3, MnO, MgO, CaO, and SO_3 (Figure 4.7a), along with overall high Al_2O_3 normalized major element ratios like Si/Al, Na/Al, K/Al, and low Fe/Al, and Mg/Al (Figure 4.7b). Overall, high concentrations of the relatively immobile element ratios like Ti/Fe, Zr/Ti, Zr/Cr, Nb/Ti, Th/P and low Ti/Si help delineate P2 (Figure 4.5).

- **Unit 2-1.** Unit 2-1 (U2-1) is recognized by the slightly higher SiO_2 and Na_2O, higher K_2O, and lower TiO_2, Al_2O_3, Fe_2O_3, MnO, MgO, CaO and P_2O_5. When major elements are normalized to Al_2O_3, higher Si/Al, Na/Al and K/Al and lower Fe/Al, Mg/Al and P/Al differentiates U2-1 from the underlying U1-2. Lower bulk- rock trace elements concentrations of V, Cr, Zn, Ga, Sr, and Mo, and higher Co, Nb, and U are observed in U2-1 (Figure 7c). When trace elements are normalized to Al_2O_3, lower ratios of V/Al, Cr/Al, Zn/Al, Ga/Al, Mo/Al and higher Nb/Al and U/Al differentiate U2-1 from underlying U1-2 (Figure 7d). Of the relatively immobile ratios, higher Zr/Ti, Zr/Cr, Zr/Y, Nb/Ti, Nb/P, Th/P, Th/Zr and Th/Y is observed in U2-1.

- **Unit 2-2.** Higher bulk-rock Al_2O_3, P_2O_5 and lower Fe_2O_3, MnO, MgO, and CaO clearly distinguish U2-2. When normalized to Al_2O_3, higher P/Al and lower Si/Al, Ti/Al, Ca/Al, Na/Al and K/Al also aids in differentiating U2-2 from the underlying U2-1. Higher bulk trace element concentration of Cr, Zn and lower bulk rock Co and Ga, in conjunction with lower ratios of Al_2O_3-normalized trace ratios Ga/Al, Rb/Al, Nb/Al, Th/Al and U/Al, are observed in U2-2. Lower ratios of the relatively immobile element ratios like Ti/Al, Ti/Fe, Ti/P, Y/Ti, Zr/Y, Zr/Hf, Nb/Ti, Nb/P, Nb/Y and Th/Co are also observed in U2-2.

- **Unit 2-3.** Unit 2-3 (U2-3) can be partitioned from the underlying U2-2 by lower bulk-rock TiO_2, Al_2O_3, Fe_2O_3 and higher CaO and SO_3, as well as higher Al_2O_3- normalized major element ratios Si/Al, Na/Al, K/Al, P/Al, and SO_3/Al. Also lower bulk trace element concentrations of Ga, Rb, Y, Zr, Nb, Mo, Th, and U is observed in U2-3. When trace elements are normalized to Al_2O_3, higher ratios of Ga/Al but lower ratios of Cr/Al, Nb/Al, Th/Al, and U/Al are observed. Of the relatively immobile element ratios higher Zr/Cr and lower Nb/Ti, Nb/P, Nb/Y, Th/Ti, Th/P, Th/Co, Th/Y and Th/Zr are observed.

- **Unit 2-4.** Of the major elements, higher bulk-rock concentrations of TiO_2, Fe_2O_3, MgO, K_2O and lower concentrations of bulk-rock MnO, CaO and SO_3 help delineate U2-4 from the underlying U2-3. When normalized to Al_2O_3, lower ratios of Ca/Al, Na/Al, P/Al, SO_3/Al is observed in the unit. Slightly higher trace element concentrations of Ga, Rb, Zr, Nb, Th and slightly lower Al-normalized trace element ratios like Y/Al, Th/Al, U/Al also help characterize this unit. Of the relatively immobile ratios higher Ti/Mn, Zr ratios (Zr/Y, Zr/Th, Zr/U, Zr/Hf) and

Th/Co is observed compared to the underlying U2-3.

- **Unit 2-5.** Major elemental composition show that the sampled zonation defined as Unit 2-5 (U2-5) chemically resembles U2-3, and is characterized by lower bulk-rock TiO_2, Al_2O_3, Fe_2O_3, K_2O, higher CaO, and higher Al_2O_3-normalized ratios like Si/Al (slight), Ca/Al, K/Al, and P/Al. Of the trace elements, higher bulk- rock Co and lower Rb (slight), Y, Zr, and Nb differentiate U2-5 from the underlying unit. Higher ratios of Rb/Al and Th/Al and lower ratios of the relatively immobile elements like Ti/P, Zr/Ti, Zr/Hf, Nb/Ti, Nb/P and Nb/Y provide additional data for characterizing U2-5.

- **Unit 2-6.** Higher bulk-rock concentrations of major elements SiO_2 (slight), K_2O and SO_3, and lower bulk-rock Fe_2O_3 and CaO characterize 2-6 (U2-6). Also higher bulk-rock trace element concentration of Rb, and lower Ga, Y, Zr and Hf can be observed in U2-6. Of the relatively immobile element ratios, higher Nb/Ti, Nb/Y, Th/P and Th/Zr and lower Ti/Al, Ti/Si, Y/Al and Zr/Cr can be observed.

Package 3 (4130 feet to 4860 feet)

Although very subtle, slightly higher bulk-rock and Al_2O_3-normalized ratios of major elements (Fe_2O_3, MnO, MgO, CaO) and distinctly higher P_2O_5 delineate Package 3 (P3; Figure 4.8a-b). Lower SiO_2 , K_2O, Si/Al, and K/Al also feature in P3 (Figure 4.8a- b). Overall, higher concentration of the trace elements V, Zn, Ga, Y, Zr are present (Figure 4.8c), and lower Rb/Al, Th/Al (Figure 4.8d). Additionally, higher values for the ratios of the relatively immobile elements, in particular Zr/Th and Zr/Hf, are useful in distinguishing the boundary between P3 and the underlying P2 (Figure 4.5).

- **Unit 3-1.** Unit 3-1 (U3-1) is characterized by high bulk rock TiO_2, Al_2O_3, Fe_2O_3, MnO, MgO, CaO and P_2O_5, and lower K_2O. Higher bulk-rock trace element concentration of Zn, Ga, Y and Zr and lower Cr and Co also help delineate U3-1 from the underlying unit. When normalized to Al_2O_3 lower ratios of Si/Al, Rb/Al, Th/Al, Mo/Al are observed in U3-1. Of the relatively immobile element ratios higher Zr/Th, Zr/Hf and Th/Co and lower Ti/P, Y/Ti, Zr/Cr, Nb/Ti, Nb/P, Nb/Y, Th/Ti, Th/Zr differentiate U3-1 from the underlying U2-6.

- **Unit 3-2.** Higher bulk-rock concentrations of the major elements TiO_2, Al_2O_3, Fe2O3, MgO, CaO and P2O5, along with lower bulk-rock SiO_2 and K_2O characterize Unit 3-2 (U3-2). When normalized to Al_2O_3, higher ratios of Mg/Al, Ca/Al, P/Al and lower Si/Al, K/Al and S/Al can also be observed in U3-2. Of the trace elements, higher Zn, Ga, Y, Zr, Y/Al, and Zr/Al are present. Relatively high ratios of the immobile element ratios Ti/Al (slight), Ti/Si, Zr/Th and Zr/Hf are present in U3-2, as are lower Nb ratios (Nb/Ti, Nb/P, Nb/Y) and Th ratios (Th/Ti, Th/P, Th/Zr).

- **Unit 3-3.** Higher bulk-rock TiO_2, Al_2O_3, Fe_2O_3, Na_2O and P_2O_5 and lower CaO, in conjunction with higher Mg/Al, Ca/Al and P/Al and lower Si/Al, K/Al and S/Al values differentiate Unit 3-3 (U3-3) from the underlying U3-2. Relatively higher trace element concentrations of Zn, Ga, Y and Zr and lower Th are observed in U3-3. When trace elements normalized to Al_2O_3, higher Y/Al and Zn/Al

differentiate U3-3 from the underlying U3-2. Of the relatively immobile element ratios higher Ti/Al (slight), Ti/Si, Zr/Th and Zr/Hf and lower Nb/Ti, Nb/P, Nb/Y, Th/Ti, Th/P and Th/Zr are observed in U3-3.

- **Unit 3-4.** The interval defined as Unit 3-4 (U3-4) is differentiated from the underlying unit by relatively higher bulk-rock Al_2O_3, Fe_2O_3, MgO, P_2O_5 and lower CaO and SO_3. When normalized to Al_2O_3, higher Mg/Al but lower Si/Al, Ti/Al, Na/Al, SO_3/Al can be observed in unit U3-4. Relatively higher trace element concentrations of Zn, Ga, Rb, Y and Zr and slightly lower Cr are present in U3-4. Of the relatively immobile ratios, higher Zr/Cr, Zr/Th, Nb/Ti, Th/Ti and lower Th/Co help differentiate U3-4 from the underlying U3-3.

- **Unit 3-5.** Relatively higher major element concentrations like Fe_2O_3, MnO, MgO and CaO and lower Al_2O_3, K_2O and P_2O_5 differentiate Unit 3-5 (U3-5) from the underlying U3-4. When normalized to Al_2O_3, higher ratios of Fe/Al, Mn/Al, Mg/Al and lower ratios of K/Al, and P/Al is observed in U3-5. Higher trace element concentrations of V, Cr, Co, Ni, Cu and lower Ga, Rb, Y, Zr, Nb and Th, along with higher Al_2O_3 normalized trace element ratios like V/Al, Cr/Al, Ni/Al, Cu/Al, Mo/Al and lower Rb/Al, Nb/Al and Th/Al are characteristic of U3-5. Of the relatively immobile element ratios, higher Zr/Th and lower Ti/Fe, Zr/Cu, Zr/U, Nb/Ti, Nb/P, Nb/Y, Th/Ti and Th/Co aid in differentiating U3-5 from the underlying U3-4.

Package 4 (3645 feet to 4130 feet)

The interval assigned to Package 4 (P4) characterized by overall high bulk-rock major elements like TiO_2, Al_2O_3, Fe_2O_3, MnO, MgO and CaO and overall high Al_2O_3 normalized major element ratios like Si/Al, Mg/Al, and Na/Al (Figs. 4.9a and 4.9b). High bulk rock trace elements like Zn, Ga, Rb, Th and U and lower V, Cr, Co, Y (slight), and Zr (slight) are observed in P4 (Figure 4.9c). When trace elements are normalized to Al_2O_3, higher ratios of Zn/Al, Ga/Al, Rb/Al, Th/Al, Mo/Al and lower V/Al and Cr/Al help delineate P4 (Figure 4.9d). Of the relatively immobile element ratios, slightly higher Ti/Mn, Th/P, Th/Co, Th/Y, distinctly higher Th/Zr and lower Zr/Ti, Zr/Cr, Zr/Y, Zr/Nb, Zr/Th and Zr/U are observed in P4 (Figure 4.5).

- **Unit 4-1.** Higher bulk-rock Na_2O and lower bulk-rock TiO_2, Al_2O_3, Fe_2O_3, MnO, MgO and K_2O differentiates Unit 4-1 (U4-1) from the underlying U3-5. Relatively lower bulk concentration of trace elements like V, Cr, Co, Ni, Ga, Rb, Y, Zr, and higher Al_2O_3 normalized ratios like Rb/Al, Nb/Al, Th/Al and Mo/Al is also observed in U4-1. Of the relatively immobile element ratios, higher Zr/Cr, Th/P and Th/Zr but lower Zr/Ti, Zr/Y, Zr/Nb, Zr/Th and Zr/U differentiates U4-1 from the underlying U3-5.

- **Basalts II and III.** In ascending stratigraphic order, Basalt II is present in U4-1 at 4113 feet, and Basalt III is present at 4091 feet. These basalts are variably altered to calcite, as indicated by high CaO (15.25% and 25.20% respectively); basalts will typically have 10% to 12% CaO in plagioclase when not altered. In addition SiO_2, Na_2O, and Total values (83.9% and 73.8% respectively) are very low. Basalt II appears less altered and still retains high values for the mafic trace

metals V, Cr, Co, Ni, and Cu. Basalt III has elevated Ni, but very low values for TiO_2, Al_2O_3, MnO, V, Cr, Co, and Cu, suggesting extensive alteration and likely mobilization of elements.

- **Unit 4-2.** Relatively higher bulk-rock concentrations of TiO_2, Al_2O_3, Fe_2O_3, MnO, MgO, K_2O and P_2O_5 and lower bulk-rock CaO and Na_2O along with higher Al_2O_3 normalized ratios like Mg/Al, Ga/Al, Rb/Al, Th/Al and lower Si/Al, and Na/Al lithologically differentiate U4-2 from the underlying U4-1. Higher bulk-rock trace elements like V, Co, Zn, Ga, Rb, Th, higher Al_2O_3 normalized trace element ratios like Ga/Al, Rb/Al, Th/Al and Zn/Al and lower Cr/Al, Y/Al, Nb/Al and Mo/Al is observed in U4-1. Of the relatively immobile element ratios, higher Ti/Al, Ti/Si, Th/Al, Th/P, Th/Y, Th/Zr and lower Y/Ti, Nb/Ti and Th/Co can be observed in U4-2.

Package 5 (3065 feet to 3645 feet)

Package 5 (P5) is characterized by relatively higher bulk-rock CaO (slight), Na_2O, lower Fe_2O_3, MnO, MgO and K_2O (Figure 4.10a), along with slightly lower Fe/Al, Mn/Al, Mg/Al and higher Na/Al, Ca/Al (slight) and P/Al (Figure 4.10b). Higher bulk-rock concentrations of trace elements like Y and Zr and lower Co, Ni, Cu, Zn, Ga, and Rb (Figure 4.10c). Of the relatively immobile-element ratios, higher ratios of Zr (Zr/Ti, Zr/Cr, Zr/Y, Zr/Th) as well as higher Th/Co are observed in P5, along with lower Th/Zr (Figure 4.5).

- **Unit 5-1.** Higher bulk-rock CaO, Na_2O, and lower TiO_2, Al_2O_3, Fe_2O_3, MnO, MgO, K_2O, P_2O_5 along with relatively higher Na/Al, P/Al, Y/Al, Zr/Al, Nb/Al and lower Ti/Al, Fe/Al, Ni/Al, Cu/Al, Rb/Al, Th/Al and Ga/Al define U5-1. Higher bulk- rock trace elements like Sr, Y, Zr, Nb, and Hf and lower Co, Zn, Ga, Rb and U, along with higher Al_2O_3 normalized ratios like Y/Al, Zr/Al and Nb/Al and lower Cu/Al, Zn/Al, Ga/Al, Rb/Al, Th/Al and U/Al is observed in U5-1 (Figure 4.10d). Of the relatively immobile element ratios, higher Ti/Mn, Y/Ti, Zr/Ti, Zr/Cr, Zr/Y, Zr/Th, Zr/U, Th/Co and lower Ti/Si, Th/Y and Th/Zr is observed in U5-1.

- **Basalt IV** is present in U5-1 at 3595 feet, and is clearly recognized by low SiO_2, K_2O, Zr, Nb, and Ba, moderate Na_2O, very high Fe_2O_3, MgO, V, Co, and Ni. Al_2O_3 and Sr are relatively high, suggesting presence in calcic plagioclase but CaO (4.13 %) and Na_2O are low. TiO_2 and Cr are low compared to Average Basalt, but this does not negate the identification of the sample as basalt.

- **Unit 5-2.** Relatively higher bulk-rock TiO_2, Al_2O_3, Fe_2O_3, MgO, K_2O and lower concentration of bulk-rock CaO and Na_2O differentiate Unit 5-2 (U5-2) from the underlying U5-1. Higher concentrations of trace elements like Co, Zn, Ga, Rb, Th, U, higher Al_2O_3 normalized ratios like Cu/Al, Zn/Al, Ga/Al, Th/Al, and lower Y/Al, Zr/Al, and Nb/Al are observed in U5-2. Of the relatively immobile-element ratios, higher Ti/Si, Zr/Hf, Th/P and Th/Zr and lower Y/Ti, Zr/Ti, Zr/Cr and Zr/Y can be observed in U5-2.

- **Unit 5-3.** Similar the U5-1, the sampled interval defined as Unit 5-3 (U5-3) can be characterized by higher bulk-rock CaO, Na_2O and lower Fe_2O_3, MgO, and K_2O. Higher Zr and lower V, Cr, Zn, Ga, Rb, V/Al, Zn/Al, Ga/Al, and Rb/Al are

also observed. Relatively higher ratios of the immobile elements Y/Ti, Zr/Ti, Zr/Cr, Zr/Y, Zr/Th and Zr/U are also present.

- **Unit 5-4.** Higher values of Fe_2O_3, MnO, and MgO, and Na/Al, along with lower CaO and Na_2O differentiate Unit 5-4 (U5-4) from the units above and below. Also higher trace elements concentrations of V, Zn Ga, Rb and lower Cr help differentiate U5-4 from the underlying U5-3. Of the relatively immobile elements ratios higher Th/Zr and lower Ti/Mn, Zr/Ti, Zr/Y, Zr/Th and Th/Co can be observed.

Package 6 (2775 feet to 3065 feet)

The uppermost part of the sampled interval is assigned to package P6 (P6). It can be differentiated from the underlying packages by higher bulk-rock TiO_2, CaO, and Na_2O, and by lower Fe_2O_3, MnO and K_2O (Figure 4.11a). Al_2O_3-normalized major element ratios such as Ti/Al, Na/Al, and P/Al are higher than P5, while Fe/Al, Mn/Al and Mg/Al are lower (Figure 4.11b). Higher bulk-rock values of the trace elements Y and Zr occur in P6, as do lower values of Cr, Cu, Zn, Ga, As, and Rb (Figure 4.11c). For trace elements normalized to Al_2O_3, slightly higher ratios of Cr/Al, Y/Al, Zr/Al, Nb/Al, and Th/Al are observed relative to P5 (Figure 4.11d). Ratios of the relatively immobile elements such as Ti (Ti/Al, Ti/Fe, Ti/Mn), Y (Y/Al, Y/Ti), and Zr (Zr/Ti, Zr/Co, Zr/Y, Zr/Th, Zr/Hf) are higher, while lower ratios of Th (Th/Ti, Th/P, Th/Y and Th/Zr) differentiate P6 from the underlying P5 (Figure 4.5).

- **Unit 6-1.** Higher bulk-rock SiO_2, CaO, Na_2O, P_2O_5 and lower Al_2O_3, Fe_2O_3, MgO and K_2O together with higher major element Al_2O_3 normalized ratios like Si/Al, Ti/Al, Na/Al, P/Al, Cr/Al, Y/Al, Th/Al, Zr/Al, Nb/Al and lower Mg/Al, Zn/Al, Ga/Al and Rb/Al lithologically characterize this interval defined as Unit 6-1 (U6-1). Higher trace element concentrations of V, Cr, Y, Zr, Nb, Hf and U and lower Co, Zn, Ga, and Rb is also observed in U6-1. Higher Al_2O_3 normalized trace element ratios like Cr/Al, Y/Al, Zr/Al, Nb/Al, Th/Al and U/Al and lower Cu/Al, Zn/Al, Ga/Al, Rb/Al differentiate U6-1 from the units above and below. Of the relatively immobile element ratios higher Ti/Al, Ti/Fe, Ti/Mn, Y/Al, Zr/Ti, Zr/Y, Zr/Th, Zr/Hf, and Th/Co and lower Th/Ti, Th/P, Th/Y, Th/Zr help delineate U6-1.

- **Unit 6-2.** Slightly higher bulk-rock Al_2O_3, Fe_2O_3, MgO, CaO, and K_2O, coupled with lower ratios of Ti/Al, Y/Al, Th/Al, Zr/Al, and Nb/Al differentiate Unit 6-2 (U6-2) from the underlying U6-1. Of the trace elements, higher Co, Zn, Ga and Rb and lower Y, Zr and Nb can be observed in U6-2. When trace elements are normalized to Al_2O_3, higher Zn/Al and slightly higher Rb/Al are noted, as are lower Cr/Al, Y/Al, Zr/Al, Nb/Al, and Th/Al. Of the relatively immobile-element ratios, lower Ti/Al, Ti/Si, Ti/Fe, Y/Al, Zr/Hf, Th/Al, and Th/Co, as well as higher Y/Ti and Zr/U help differentiate U6-2 from the underlying U6-1.

4.3.2a Source Lithologies

Major-element data can be used to constrain the lithologies present in the Rizer #1 sequence that have not been characterized by thin-section petrography and XRD mineralogy analysis. Various ternary plots of major elements are routinely employed to

assess the lithology of sedimentary rocks. In this subsection, the focus will be determining the prevalence of felsic-affinity elements (Figure 4.12a) versus mafic-affinity elements (Figure 4.12b) using the ternary diagram of (SiO_2 /10) – (MgO + Fe_2O_3) – (Na_2O + K_2O). For reference, depth plots of the major elements used to construct the ternary plots are displayed in Figures 4.1, 4.12a, and 4.12b. Additional ternary diagrams used to determine the relative contribution of siliciclastic, carbonate, and evaporite components may be found in Appendix P.

The "average" lithologies defined in Section 4.2.3 (basalt, andesite, granite, upper continental crust [UCC], shale, and sandstone) are included for reference in the ternary plots to illustrate large-scale compositional trends. The basalt-andesite-granite trajectories in each plot illustrate the mafic-to-felsic compositional spectrum that characterizes the great majority of the upper crust. The composition of UCC always plots between andesite and granite, and approximates granodiorite. Average cratonic sandstone equates to clean arenites deposited in relatively stable tectonic environments, as opposed to greywackes that may be deposited in evolving orogenic belts. Average shales are compiled from both cratonic and orogenic settings. The sandstone and shale compositions represent the conversion of crystalline rocks to coarse-grained and fine-grained sediment, respectively, by the processes of weathering, transport, deposition, diagenesis, and recycling.

The (SiO_2 /10) – (MgO + Fe_2O_3) – (Na_2O + K_2O) ternary plot is an effective discriminator of siliciclastic detritus that is relatively enriched in mafic versus felsic composition. Mafic-dominated sediments plots toward the (MgO + Fe) apex, while the felsic-dominated sediments plot toward the (SiO_2 /10) – (Na_2O + K_2O) join. Of the felsic- dominated sediments, the (SiO_2 /10) apex can be a proxy of a more quartzose-sourced lithology while the (Na_2O + K_2O) apex can be an indicator of more feldspathic sources.

Note that multipliers or divisors are sometimes applied to elements comprising the ternary plots. These have no petrologic significance, and are used only to allow data points to plot in a more central position on the diagrams.

- **P1** samples (green squares on Figure 4.13a) plot on a tight linear trend from average shale to average basalts, and is centered on the composition of average andesites. This shows an influence of more-mafic sediment enriched in MgO and Fe_2O_3. It should also be noted that cutting samples from this interval are possibly influenced by drilling problems associated with trying to penetrate the basal basalt unit before the test borehole was abandoned, thus the tendency towards the more mafic apex.

- Samples from **P2** (red squares on Figure 4.13b) show a shift in overall composition away from the (MgO + Fe_2O_3) apex. They form an array from average andesites through average shales and then to MgO + Fe_2O_3 compositions similar to average granites and cratonic sandstones. This demonstrates the influence of a more-felsic sediment source and a declining influence of a more-mafic sediment source.

- **P3** samples (blue squares in Figure 4.13c) show a slight shift back to the (MgO + Fe_2O_3) apex, with the linear trend centered on average andesites

and average shales. This is consistent with mixing of detritus from more-mafic and more-felsic sources.

- Samples from **P4** (purple squares in Figure 4.13d) show a tight cluster with a relatively mafic composition (between average andesites and average basalts) and a scattering of eight samples with relatively felsic composition (between average shales average granites). This corresponds to P4 having an overall composition more influenced by mafic input, but eight intervals with more felsic composition.

- **P5** samples (yellow squares in Figure 4.13e) show a well-defined linear trend that has shifted slightly away from the ($MgO + Fe_2O_3$) apex, indicating greater influence of detritus composed of more felsic-affinity elements.

- **P6** samples (orange squares in Figure 4.13f), like the P5 samples, show a well-defined linear trend. It has shifted slightly further away still from the ($MgO + Fe_2O_3$) apex, showing a continued, increased influence of the more- felsic source.

4.3.2b Inferred Sandstone Classifications by Geochemical Proxy

The geochemical sandstone classification after Pettijohn et al. (1972) is designed to illustrate the relative abundance of quartzose versus feldspathic sedimentary components. Inferred sandstone classifications by bulk-rock analysis indicate that a majority of samples are generally split between subarkosic to sublitharenite with a few quartz arenite outliers found wholly within Package 2 (Figure 4.14a). Notably, Package
3 (blue squares in Figure 4.14a) demonstrates little geochemical lithology variance, staying mostly clustered within the subarkose field. In comparison, point-counted analyses of rotary sidewall and core samples range from arkose to feldspathic litharenites, with a greater part of samples falling within the lithic arkose field (Figure
4.14b).

As a result of the majority of the samples used for XRF analyses were cuttings, classification of lithologies using geochemical methods (Figure 4.14a) are intended to be complementary to modal thin section analyses (Figure 4.14b) and thin section descriptions (Appendices G, H, I).

4.3.3 Weathering

In this subsection, the focus will be determining the degree of weathering using the ternary diagram of SiO_2 – (Al_2O_3 X 2) – (CaO X 5). SiO_2 is a proxy for rigid framework- silicate grains (dominated by quartz and feldspar) that comprise the great majority of sand and silt in sedimentary rocks. The greater the amount of SiO_2 present in a sample, the greater the amount of quartz present, along with less feldspar, mica, and clay. In some cases, SiO_2 may indicate the presence of biogenic silica, but this does not apply to the sandstone-dominated sequence analyzed from the Rizer #1 test borehole. Al_2O_3 can be used as a proxy for the weathering of sandstones, reflecting the presence of clays and potential authigenic clays from the alteration of feldspars. CaO is an effective proxy for carbonate minerals, as there is seldom more than 3% of CaO in carbonate-free or sulfate-free siliciclastic rocks. Each package is described as

follows.

- **P1** sedimentary samples (green squares on Figure 4.15a), deposited immediately above Basalt I at the base of the studied section, show a range in composition along the basalt-andesite-UCC-granite trend. Overall, however, they contain the greatest proportion of samples with an intermediate (clustered around andesite) to mafic bulk composition. The two **P1** sedimentary samples closest to the (CaO X 5) apex likely contain a moderate amount of carbonate (calcite) cement. Note that **Basalt I** plots at almost exactly the same position as the average basalt reference compositions, suggesting little or no alteration. This is not definitive, however, as multiple cutting samples were retrieved during this interval due to difficulties encountered drilling into the basal basalt unit.

- **P2**, the thickest of the packages, also shows the most scatter in sedimentary composition (red squares on Figure 4.15b). A central cluster of data points follows the basalt-andesite-UCC trend, but at least four samples show evidence of some carbonate (calcite) cementation. Another cluster is relatively enriched in Al_2O_3, plotting more toward the (Al_2O_3 X 2) apex than average shales. This suggests the presence of more aluminous minerals such as micas, or more-weathered fine-grained material, including detrital and/or authigenic kaolinite. Most notably, **P2** contains the greatest proportion of samples that plot toward the (SiO_2) apex, suggesting the greatest abundance of detrital quartz, quartzose lithic fragments, and authigenic quartz.

- **P3** samples (blue squares in Figure 4.15c) are the most tightly clustered of all the Packages, with nearly every sample contained within the basalt-andesite- UCC trend. This suggests a low degree of weathering prior to deposition and burial, with the sediments retaining their crustal geochemical signal.

- The main cluster of samples from **P4** (purple squares in Figure 4.15d) parallels the basalt-andesite-shale trend, but shows a significant shift toward the (Al_2O_3 X 2) apex. This trend projects to a more aluminous composition that average shales on the (SiO_2) – (Al_2O_3 X 2) join of the plot, reflecting a relatively high degree of weathering and/or greater abundance of aluminous mica and/or kaolinite. This also may imply some samples from **P4** are indicative of clay-rich lithologies like siltstones and claystones. A small open cluster of five samples plots near the composition of UCC, with relative SiO_2 higher than all other samples in **P4**. **Basalts II** and **III** at the base of **P4** show compositions significantly higher in CaO than average basalt, and have clearly suffered variable degrees of alteration to calcite. Three sedimentary samples from **P4** also plot closer to the (CaO X 5) apex, also indicating some degree of calcite cementation.

- **P5** samples (yellow squares in Figure 4.15e) parallel the basalt-andesite- shale trend, but show a clear continuation of the compositional shift to higher relative Al_2O_3, with some samples approaching the composition of average

shale. This may reflect a further increase in the degree of weathering of detrital sediment or an increase in aluminous mineral content. Three samples that plot closer to the (CaO X 5) apex likely contain significant carbonate (calcite cement). **Basalt IV** (3590 feet to 3600 feet) shows a composition that plots closer to the (SiO_2) – (Al_2O_3 X 2) join than both average basalt and average andesite. This indicates CaO has been removed from the rock by alteration, and the overall composition relatively enriched in Al_2O_3.

- Relative to **P5** the samples from **P6** (orange squares in Figure 4.15f) show an overall shift toward the (SiO_2) apex, suggesting a slightly higher quartz and feldspar content. The trend toward relative enrichment in Al_2O_3 seen in **P5** is reversed in **P6**. Only one sample plots further toward the (CaO X 5) apex than average basalts, and it is likely that minor calcite cement is present in this sample.

4.3.4 Paleoclimate Setting

The depositional setting for the Rizer #1 borehole based on core description has been interpreted as an alluvial to braided fluvial to lacustrine setting (Appendix D). Suttner and Dutta (1986) proposed a diagram for alluvium sandstones in relation to paleoclimate using SiO_2 versus Al_2O_3+K_2O+Na_2O. Increased SiO_2 versus Al_2O_3+K_2O+Na_2O is indicative of a humid to semi-humid climate, whereas increased Al_2O_3+K_2O+Na_2O versus SiO_2 denotes an arid to semi-arid climate.

Almost all samples plot within the general arid range, with only one sample plotting within the semi-humid range (Figure 4.16). **P2** (red squares) is the most scattered package, with some samples ranging in the semi-arid range due to relatively increased SiO_2.

4.4 DISCUSSION

4.4.1. Chemostratigraphic Zonation of the Rizer #1 and Implications of Lithology

The chemostratigraphic zonation appears to be driven by changes in the relative input of more-mafic versus more-felsic sediments responsible for package and some unit divisions. Petrologic descriptions and modal analyses report varying degrees of mafic mineral (epidote, garnet, staurolite) abundance versus felsic minerals (quartz, plagioclase, potassium feldspar), with felsic minerals dominating. The average compositions for the elemental packages (excluding basalts) show subtle but significant changes in overall sediment composition, and are summarized in Table 4 (Appendix P). Overall the Rizer #1 chemostratigraphic zonation represents sandstones dominated by feldspars and lithic fragments (Figs. 4.14a and 4.14b). This is confirmed by lithological interpretations from the cuttings litholog (Figure 2.1), core description (Appendix D), and thin sections of sandstone, siltstone, and claystone (Appendices H and I), where sandstones are the dominant lithology. In correlation with the litholog, **Package 4** likely contains a siltstone to claystone unit that is denoted by spikes in clay-affinity major elements like Al_2O_3, Fe_2O_3, TiO_2, and MgO (Figure 4.1) and trace elements like Rb, Ga, and Th (Figure 4.4).

Discrete alternations between Na_2O and K_2O are found occurring between **Package 4** (**Unit 4-2**) versus **Package 5** (**Unit 5-1**) and **Package 2** (**Unit 2-6**) versus **Package 3** (**Unit 3-1**) (Figure 4.1). Although this may be a general reflection of sodic plagioclase and potassium feldspars interchanging abundance, petrography of the rotary sidewall cores from these packages/units are not entirely consistent with this interpretation. Thin- section descriptions of 1-10R, 1-11R, and 1-16R (**Unit 4-2**) indicate plagioclase dominance in lithic arkoses and siltstones; there are no available thin sections from the overlying unit (**U5-1**). Thin-section descriptions of 1-34R (**Unit 3-1**) compared to thin- section descriptions of 1-37R, 1-38R, 1-40R, and 1-43R (**Unit 2-6**) also do not indicate a prevalence of potassium feldspar as opposed to plagioclase. Instead it may be an geochemical signal expression of muscovite and low-grade metamorphic lithics rich in micas (phyllite, schist) being exaggerated by diagenetic illite and high-birefringence kaolinite observed in thin-section. This may also be confirmed by relatively high Ga (Figure 4.3) and Ga/Al (Figure 4.4), elements particular to aluminous micas and kaolinite. This interpretation also relates to the likelihood of a siltstone to claystone unit within **Package 4**.

Additionally, thin-section decriptions and modal analyses from **Package 2** possibly explains the inconsistency of the lithological sandstone characterization based primarily on 299 cuttings (Figure 4.14a). The quartz arenite field is populated by ten thin sections that range from **U2-5** to **U2-1**, eight of them being point-counted (1-44, 1-15, 1-89R, 1-85R, 1-73R, 1-68R, 1-62R, 1-53R). These thin-sections have been classified arkose to feldspathic litharenites (Figs. 2.11-2.16; Appendices H and I). In each point-counted thin-section, authigenic quartz cement (5-14%), quartz-replaced grains (1-3%) and quartzose lithics (gneiss, chert, sandstone/siltstone, volcanic siliciclastics, and schist) range from minor to common rock components (Appendices G, J, K). Because the Pettijohn et al. (1972) plot relies on SiO_2 for determining the geochemical prevalence of quartz (i.e., the more SiO_2 in SiO_2/Al_2O_3, the more likely the rock is to be a quartz arenite), the frequency of authigenic quartz and quartzose lithics have skewed these samples into the realm of the quartz arenite field.

4.4.2 Weathering Interpretations

Excluding the likelihood that **P4** is siltstone to claystone dominated, **Package 2** and **Package 5** are the most weathered lithologies based on frequency of samples plotting towards the (Al_2O_3 X 2) in Figures 4.15a-f. This is confirmed petrographically by zeolite cement in thin-section (Appendices G and H) and laumontite in XRD in 1-6R (**Package 5**; Appendix F), each weathering products of volcanic glass. It should also be noted there is only one thin-section from the **Package 5** interval. **Package 2** thin-sections consistently contain the highest amount of authigenic chlorite and illite, both as cement and grain-replacements, with the exception of one sample (Appendices G-I). Dissolution of unstable chemical grains observed in **Package 2** may also be the result of weathering or contact with water at near-surface depths.

By contrast, **Package 3** is most likely the least weathered of all packages, indicated by its tight cluster between Average Andesite and Average Upper Continental Crust in the

(SiO_2) – (Al_2O_3 X 2) – (CaO X 5) ternary diagram (Figure 4.15c). This allows for the suggestion that **Package 3** was eroded and deposited very quickly, possibly from a marginally different source lithology relative to other packages (Figure 4.12a-b, Appendix P). This also implies that authigenic clays found within **Package 3** are likely the result of burial diagenesis rather than at-surface weathering. This is also partly supported by little to no kaolinite described in thin-section or modal analysis (1-22R, 1-23R, 1-24R, 1-33R, 1-34R, Appendices G and H).

For the Rizer #1 borehole, the Suttner and Dutta (1986) paleoclimate plot overall suggests that rapid erosion, deposition, and burial occurred within an arid environment (Figure 4.16). This is consistent with previous interpretations of other southeastern Triassic rift basins (Withjack et al., 1998; Withjack et al., 2012). In conjunction with petrographic analysis, the frequency of minerals and rock fragments associated with metamorphic to igneous lithologies suggests massive erosion and rapid deposition of crystalline rocks, either as crystalline basement faulted upward as a result of initial rifting (Figure 1.2) or the steady unroofing of a mountain belt.

Overall, the weathering observed within Rizer #1 is minimal, with no strong trends towards the aluminum apex (Figure 4.15a-f) and a majority of samples plotting with elemental associations associated with sediments derived from rapid erosion, deposition, and burial in an arid environment (Figure 4.16). This is consistent with very little clay authigenesis associated with weathering (e.g., kaolinite) observed in thin- section, SEM, and XRD (Appendices F-K). It should be noted, however, implications of weathering in sandstones are tenuous due to two problems: 1) dependency of weathering plots on the mobility of aluminum and 2) the sheer volume of aluminum-rich minerals (micas, feldspars, clays) commonly found in sandstones. In the Rizer #1 samples, there is some partial evidence of aluminum mobility manifested in higher aluminum concentrations present within some bands of quartz overgrowth cements (Figure 3.5A).

4.4.3 Provenance

The Carolina Zone is the eastern-most belt of metamorphic and igneous rocks that is exposed west of the Atlantic Coastal Plain (Figure 4.17; Hibbard et al., 2002). The Carolina Zone is overlain by Mesozoic rift basins which are concentrated along its exposed eastern margin and extends in the subsurface under the Atlantic Coastal Plain eastward to the East Coast magnetic anomaly (Horten et al., 1989; Hall, 1990). Two terranes associated with the Carolina Zone are likely sources for the igneous and metamorphic detritus within the SGRB. These are the Carolina terrane and Charlotte terrane. The Carolina terrane is the eastern most belt in the Carolina zone and consists of low-grade metamorphosed, sedimentary, and felsic intrusive and volcanic rocks. The Charlotte terrane is dominated by Neoproterozoic and late Paleozoic plutonic rocks that intrude metavolcanic rocks with minor quartzite, mica schist, phyllite and marble. This mixture of metamorphic and igneous rocks satisfies both petrologic and geochemical conditions set for a viable provenance.

4.4.4 Intrusive Basalts and Metasomatism Versus Diagenesis

Four igneous bodies identified through XRF methods were interpreted to be of overall mafic origins, all making slight but discernable impacts on overlying and underlying cutting samples. A fifth intrusive body was determined by thin-section analysis (3278.0 feet, 1-5R; Appendix H), but went undetected using XRF methods due to poor cuttings resolution. The Average Basalt standard used for interpretation is derived from the mean of basalts from Late Proterozoic, Paleozoic, and Meso-Cenozoic time periods and is meant to act as a geochemical reference point to compare samples against (Condie,
1993).

Basalt I (cuttings from 6180-6200 feet) is geochemically relatively unaltered, as indicated by its close proximity to the average basalt standard in the (SiO_2) – (Al_2O_3 X2) – (CaO X 5) ternary diagrams (Figure 4.15a). There is a notable increase in magnesium, nickel and chromium (Table 2, Appendix P), possibly representing the incorporation of partially melted ultramafics within the parental magma (Wilson, 1989; El-Hasan and Al-Malabeh, 2008).

Basalts II and III (RSWC from 4091.0 and 4113.0 feet, respectively) are highly altered alkali olivine basalts according to thin section descriptions (Figure 2.24a-c). Geochemistry performed confirms higher amounts of CaO relative to Average Basalt (Figure 4.15d), suggesting significant alteration to calcite. **Basalts II and III** plot near the apex of MgO + Fe_2O_3 (Figure 4.13d), far surpassing the average basalt reference standard, and may likely reflect the secondary formation of dolomite and polymorphic amphiboles observed in thin section.

Basalt IV (3590-3600 feet) is derived from cuttings, but a thin-section from 3593.0 feet (1-7R) decribes the unit as an altered alkali olivine basalt (Figure 2.23; Appendix H). The amount of CaO relative to Al_2O_3 indicates minor to rare calcite compared to an enrichment in Al_2O_3 (Figure 4.15e), which is likely related to the common amphibolite and chlorite replacement observed in 1-7R.

Basalts I-IV were plotted on the (Hf/3)-(Th)-(Nb/16) ternary diagram after Wood (1980) to determine approximate geochemical basaltic composition (Figure 4.18). This diagram is based on atomically heavy immobile elements conventionally resistant to diagenesis and was used as opposed to the more orthodox diagrams (e.g., AFM diagram or Na_2O + K_2O vs. SiO_2 basalt classification scheme) that utilize mobile elements likely to be affected in diagenesis. **Basalts I**, **II**, and **IV** plot within the calc-alkaline (CA) range with **Basalt III** barely outside the CA field. Alkali olivine basalts are more mafic than calc- alkaline basalts due to a deficiency in silica; however, this inconsistency may be explained by the intrusive basalt bodies assimilating some felsic-associated elements (i.e., moderately thorium-enriched) from the sandstone host rock (Aoki and Oji, 2012).

This raises the issue of what precisely is the influence of these basalts on the surrounding country rock. Metasomatism is a hydrothermal metamorphic processes associated with intrusions (Winter, 2001), usually at temperatures higher than diagenetic conditions are conventionally defined (50 °C to 300 °C; Milliken, 2003). Thin- sections and geochemistry of **Basalts II and III** indicate chemical weathering, likely by

deuteric processes, and data from Schlumberger FMI logs indicate multiple fractures, with some basalts exhibiting steep-angle faults (> 60°), around basalt units (Figure 2.22a-b to 2.24).

Highly altered sediments above **Basalt I** suggest a metasomatic influence based on petrologic investigation of thin-sections and scanning electron microscope (SEM) analysis (6140.0ft, 1-107R; Figure 2.21). No FMI log of Basalt I is available because the borehole terminated in the basalt. A marked increase of metasomatic elements (K_2O, MgO) and hydrous fluid-soluble elements (Rb, Ba, Sr, U) were detected in 1-107R (Figs. 4.6a-d; Tables 1 and 2, Appendix P). It is hypothesized that fractures and high- diagenetic to metasomatic temperatures associated with Basalt I combined with saline pore waters to create conditions conducive for the transfer of soluble elements (Brenan, 1991; Winter, 2001).

Basalts II and III, like all the basalts analyzed in Rizer #1, were unlikely ever at the surface (Appendix H). Therefore, the leached appearance of **Basalts II and III** observed in thin-sections are likely the result of a period of continuous groundwater flow. The intrusions appear heavily fractured, according to Schlumberger FMI logs (Figs. 2.24), providing conduits for enriched pore water mobility and plausibly conducted groundwater flow at one point in a similar fashion observed in the Triassic rift-basins in North Carolina (NCDENR, 2012). No thin-sections from the unit underlying **Basalt II** are present; however increases in major elements Fe_2O_3, MgO, and CaO (Figure 4.1) and trace elements (Figure 4.3) may indicate authigenic calcite (CaO, MgO, Fe_2O_3), and chloritic (MgO, Fe_2O_3, Ni, Cr) and illitic clay (Zn, V) diagenesis.

Basalt IV had little to no metasomatic or diagenetic effect on the surrounding rocks. Other than spikes in mafic elemental indicators (MgO, Fe_2O_3, MnO) isolating **Basalt IV** within the chemostratigraphic zonation, no other increases in metasomatic or diagenetically-linked major elements are observed above or below **Basalt IV** (Fig. 4.10a). Although an unusually sharp peak in Sr is indicated above the basalt (Fig. 4.10c), without further geochemical testing and a lack of a petrographic sample from the affected sediments, it is difficult to distinguish whether it represents a depositional signal versus a diagenetic signal.

4.4.5 Element Mobility Overprinting

Provenance usually exerts the primary control on the geochemical signal contained in a sequence of siliciclastic rocks. The Rizer #1 signal likely represents the lithological makeup of the sediment source area(s), the evolution of that composition as the source area is unroofed, and mixing of sediment from multiple sources. While the provenance signal may be variably overprinted by weathering, sorting during transport, physical and biological processes in the depositional environment, and diagenesis during burial, it can usually be recognized and exploited for stratigraphic purposes. Relatively short sediment transport (which is characteristic of many rift basins), as well as location in an arid and/or cold climatic regime, are usually optimal conditions for preserving the provenance signal. This is particularly true for sandstones, where labile components

such as rock fragments are not significantly reduced by mechanical abrasion or chemical weathering over a long transport path.

Central to the recognition and use of the provenance signal in chemostratigraphic studies is the issue of elemental mobility. Elements that are not readily dissolved and transported into or out of the sediment during deposition and burial are the most reliable provenance indicators. These are commonly called "immobile elements", and for XRF- generated data sets include TiO_2, V, Co, Y, Zr, Nb, Hf, and Th. In many depositional settings, Fe_2O_3, Cr, and Ni can be largely immobile also. Many of these elements are carried in resistant minerals (such as zircon, monazite, and rutile) or in micas and clays. A number of studies have demonstrated these elements show little or no tendency to be redistributed during fluid-rock interactions beyond the scale of a few millimeters or a few centimeters, even during high-temperature diagenesis (Hollings and Wyman, 2005).

Superimposed on the source rock signal may be source-area weathering, sorting during transport, paleoenvironmental conditions during deposition, and subsequent diagenesis. Mobile elements such as Na_2O, K_2O, CaO, Rb, and Sr may be removed from or added to the rock during interaction with pore fluids associated during these processes. K_2O in particular is widely accepted to be a common diagenetic addition during burial diagenesis, due to the conversion of mixed-layer clays to illite (Ratcliffe et al., 2004).

4.5 CONCLUSIONS

Mixing of sandstone and mudstone lithologies in cuttings samples, especially in intervals containing significant calcite cement, have slightly obscured the chemostratigraphic zonation. Nevertheless, a clear zonation is present, and is characterized by compositional shifts between more-mafic and more-felsic input over vertical intervals ranging from 200 feet to over 1000 feet. These shifts are interpreted to be controlled by the erosion of different source rocks, possibly terranes associated with the Carolina Zone, as the SGRB complex evolved. The elemental data are consistent with only limited weathering and chemical modification of detritus during most of sedimentation. This may be due to relatively rapid erosion and deposition, at a rate which did not allow time for significant modification to occur. The elemental data alone cannot unequivocally establish whether Basalts I-III are extrusive or intrusive, although FMI logs permit the likelihood of them being heavily fractured intrusions with some evidence of high-angle faulting associated with some of the intrusions. Basalt IV is best interpreted as an intrusion, with no elemental data supporting an extrusive origin. Only metasomatism is likely with Basalt I, constrained by petrology and geochemistry.

4.6 CITATIONS

Aoki, Ken-ichiro and Oji, Yoshio, Calc-alkaline volcanic rock series derived from alkali- olivine basalt magma, Journal of Geophysical Research, v. 71, p. 2156-2202

Brenan, J.M., 1991, Development and maintenance of metamorphic permeability: Implications for fluid transport. In D.M. Kerrick (ed.), *Contact Metamorphism. Rev. in Mineralogy*, 26, Mineral. Soc. Amer., p. 291-320.

Condie, K.C., 1993, Chemical composition and evolution of the upper continental crust:

Contrasting results from surface samples and shales: Chemical Geology, v. 104, p. 1-37.

Cox, R., Lowe, D.R., and Cullers, R.L., 1995, The influence of sediment recycling and basement composition on evolution of mudrock chemistry in the southwestern United States: Geochimica et Cosmochimica Acta, v. 59, p. 2919-2940.

El-Hasan, T. and Al-Malabeh, A., 2008, Geochemistry, Mineralogy, and Petrogenesis of El-Lajjoun Pleistocene Alkali Basalt of Central Jordan: Jordan Journal of Earth and Environmental Sciences, v. 1, p. 53-62.

Hall, D.J., 1990. Gulf Coast-East Coast magnetic anomaly I: Root of the main crustal decollement for the Appalachian-Ouachita orogen: Geology, v. 18, p. 862-865.

Hibbard, J.P., Stoddard, E.F., Secor, D.T., and Dennis, A.J. 2002. The Carolina Zone: overview of Neoproterozoic to early Paleozoic peri-Gondwanan terranes along the eastern flank of the southern Appalachians. Earth-Science Reviews, 57(3–4): 299–339.

Hollings, P., and Wyman, D., 2005, The geochemistry of trace elements in igneous systems: Principles and examples from basaltic systems, in Linnen, R.L., and Samson, I.M., eds., Rare-element geochemistry and mineral deposits: Saint John's, Newfoundland, Geological Association of Canada, Short Course Notes Volume 17, p. 1-16.

Horton, W., Drake, A., Rankin, D., 1989. Tectonostratigraphic terranes and their Paleozoic boundaries in the central and southern Appalachians. In: Dallmeyer, D. (Ed.), Terranes in the Circum-Atlantic Paleozoic Orogens. Geological Society of America Special Paper, vol. 230, pp. 213– 245.

Milliken, K.L., 2003, Late Diagenesis and Mass Transfer in Sandstone-Shale Sequences, In: Mackenzie, F.T. (ed), Sediments, Diagenesis, and Sedimentary Rocks, Elsevier, Amsterdam, p. 159-190.

McLennan, S.M., 1995, Sediments and soils: Chemistry and abundances, in Ahrens, T.J., ed., Rock physics and phase relations – A handbook of physical constants: Washington, D.C., American Geophysical Union, Reference Shelf 3, p. 8-19.

NCDENR, 2012, Final North Carolina Oil and Gas Study: North Carolina Department of Environment and Natural Resources, p. 327.

Nesbitt, H.W., and Young, G.M., 1982, Early Proterozoic climates and plate motions inferred from major element chemistry of lutites: Nature, v. 299, p. 715-777.

Pettijohn, F.J., Potter, P.E., Siever, R., 1972. Sand and Sandstones. Springer-Verlag, New York.

Rattcliffe, K.T., Wright, A.M., Hallsworth, C., Morton, A., Zaitlin, B.A., Potocki, D., and Wray, D.S., 2004, An example of alternative correlation techniques in a low- accomodation setting, nonmarine hydrocarbon system: The (Lower Cretaceous) Mannville Basal Quartz succession of southern Alberta: AAPG Bulletin, v. 88, p. 1419-1432.

Ratcliffe, K.T. and Zaitlin, B.A., eds., 2010, Application of modern stratigraphic techniques: Theory and case histories: Tulsa, Oklahoma, SEPM (Society for Sedimentary Geology), Special Publication 94, 241 p.

Rudnick, R.L., and Gao, S., 2003, The composition of the continental crust, in Rudnick, R.L., ed., The Crust: Oxford, United Kingdom, Pergamon, Treatise on Geochemistry, Volume 3, p. 1-64.

Suttner, L.J., Dutta, P.K., 1986. Alluvial sandstone composition and paleoclimate. Journal of Sedimentary Petrology, 56, p. 329–345.

Taylor, S.R., and McLennan, S.M., 1985, The continental crust: Its composition and evolution: Oxford, United Kingdom, Blackwell Scientific Publications, 312 p.

Wedepohl, K.H., 1971, Environmental influences on the chemical composition of shales and clays, in Ahrens, L.H., Press, F., Runcorn, S.K., and Urey, H.C., eds., Physics and chemistry of the Earth: Oxford, Pergamon, p. 307-331.

Wedepohl, K.H., 1991, The composition of the upper earth´s crust and the natural cycles of selected metals: Metals in natural raw materials; natural resources, in Merian, E., ed., Metals and their compounds in the natural environment: Weinheim, Germany, VCH-Verlagsges., p. 3-17.

Wedepohl, K.H., 1995, The composition of the continental crust: Geochimica et Cosmochimica Acta, v. 59, p. 1217-1239.

Weibel, R., Johannessen, P.N., Dybkjær, K., Rosenberg, P., and Knudsen, C., 2010, Chemostratigraphy of upper Jurassic reservoir sandstones, Danish Central Graben, North Sea: Marine and Petroleum Geology, v. 27, p. 1527-1594.

Wilson, M., 1989, Igneous petrogenesis, a global tectonic approach, London: Unwin Hyman.

Winter, J., 2001, An Introduction to Igneous and Metamorphic Petrology. New Jersey: Prentice Hall.

Withjack, M.O., Schlische, R.W., and Olsen, P.E., 1998, Diachronous rifting, drifting, and inversion on the passive margin of central eastern North America: An analog for other passive margins: AAPG Bulletin, v. 82, p. 817-835.

Withjack, M. O., Schlische, R.W., and Olsen, P. E., 2012, Development of the passive margin of eastern North America: Mesozoic rifting, igneous activity, and breakup. In: Bally, A. W. & Roberts, D. G. (eds), Principles of Phanerozoic Regional Geology, v. 1, Elsevier, Amsterdam, p. 301–335.

Wood, D.A., 1980, The application of a Th-Hf-Ta diagram to problems of tectonomagmatic classification and to establishing the nature of crustal contamination of basaltic lavas of the British Tertiary volcanic province, Earth and Planetary Science Letters, v. 50, p.11-30.

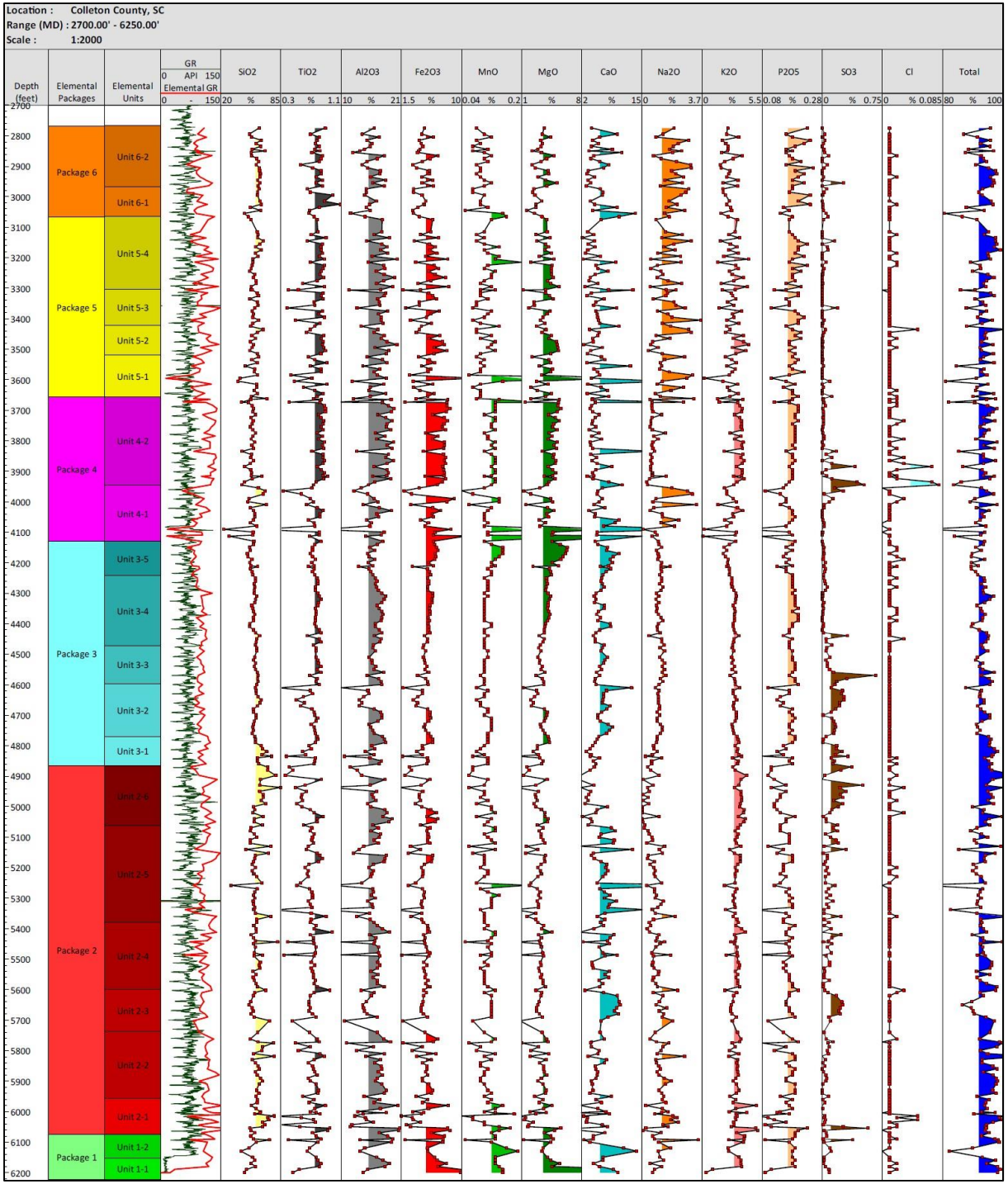

Figure 4.1. The Rizer #1 test borehole's chemostratigraphic zonation presented as depth plots of major elements. Six Elemental Packages are subdivided into 21 Elemental Units.

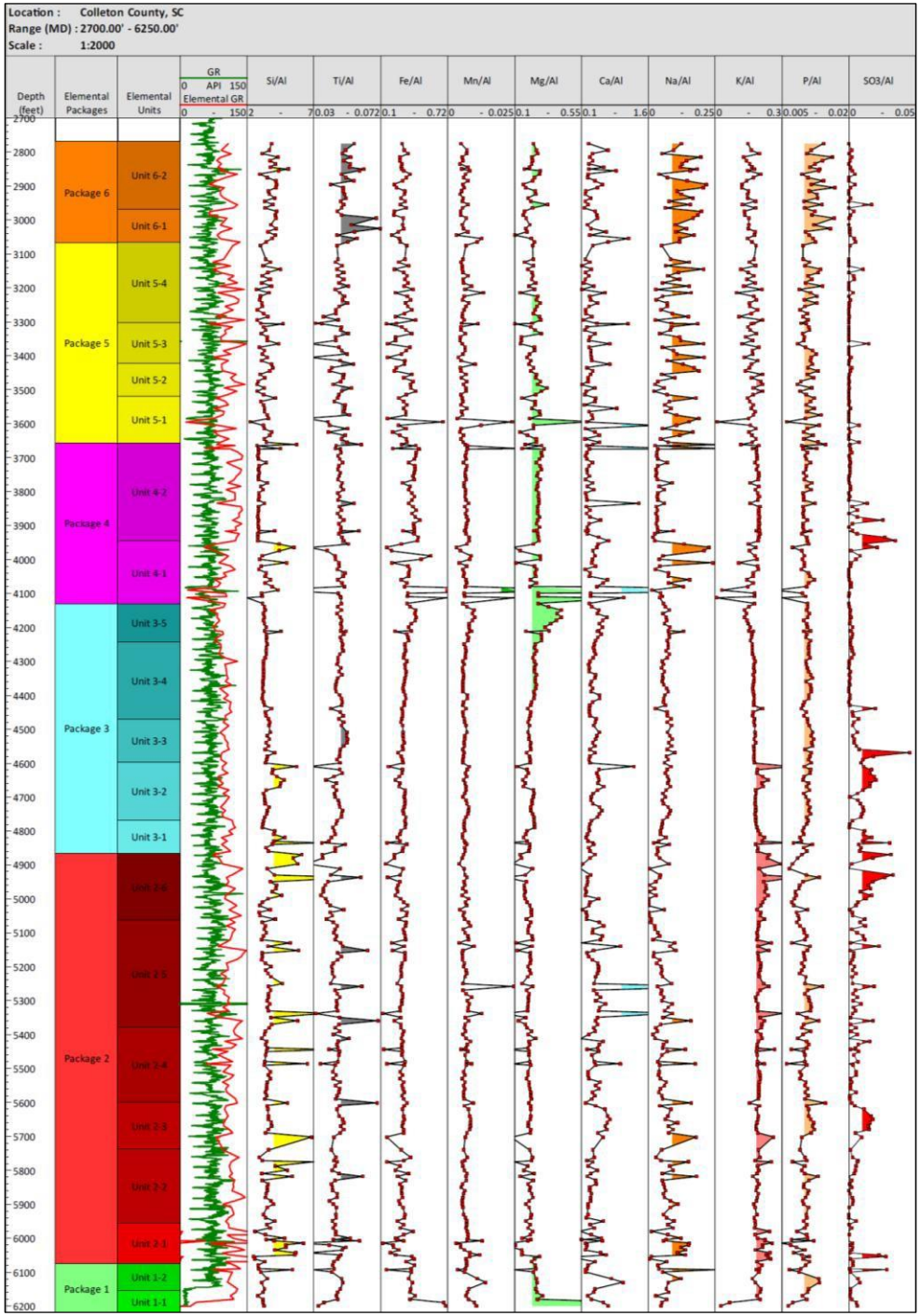

Figure 4.2. The Rizer #1 test borehole's chemostratigraphic zonation presented as depth plots of major elements normalized to aluminum. Six Elemental Packages are subdivided into 21 Elemental Units.

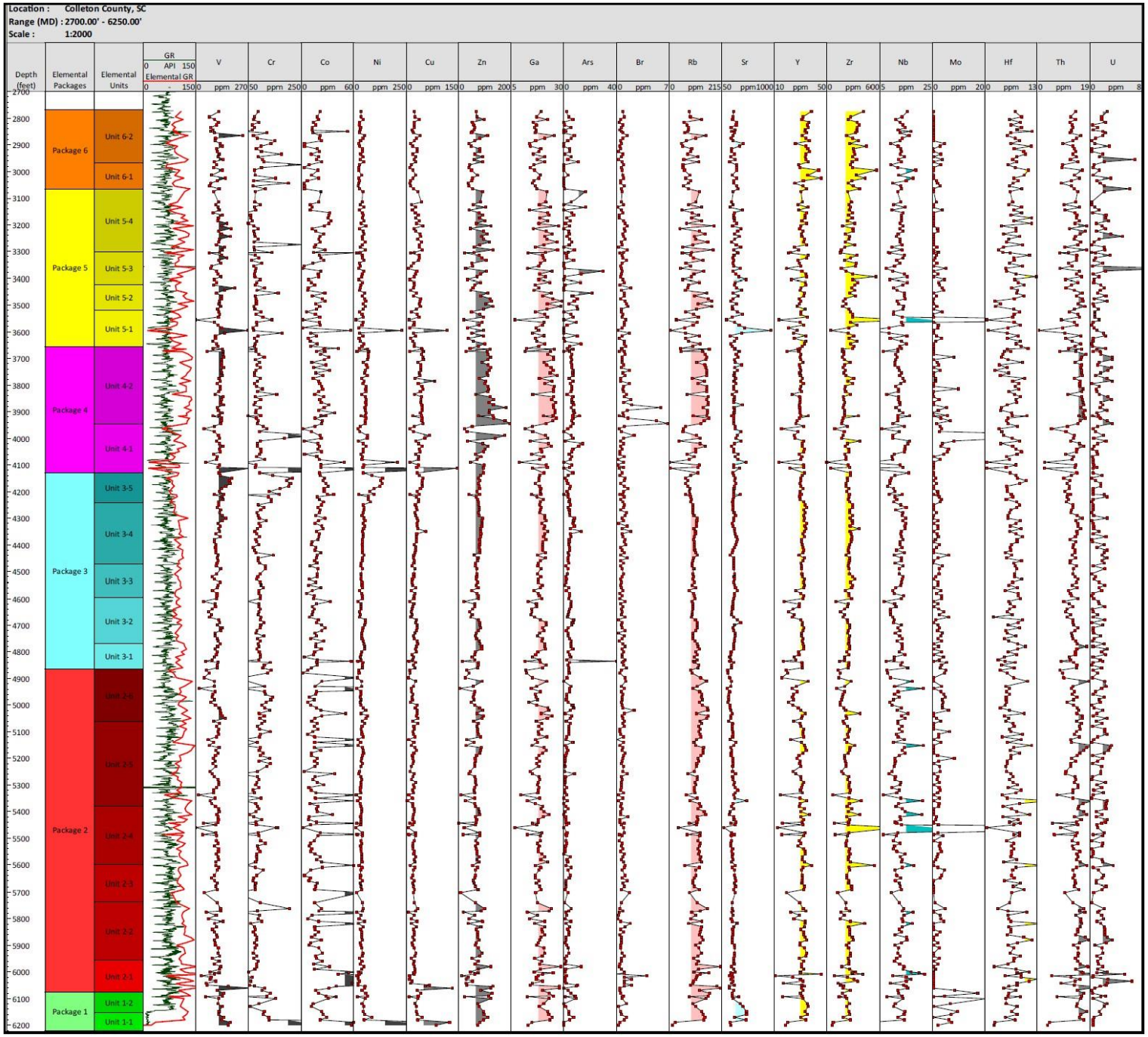

Figure 4.3. The Rizer #1 test borehole's chemostratigraphic zonation presented as depth plots of trace elements. Six Elemental Packages are subdivided into 21 Elemental Units.

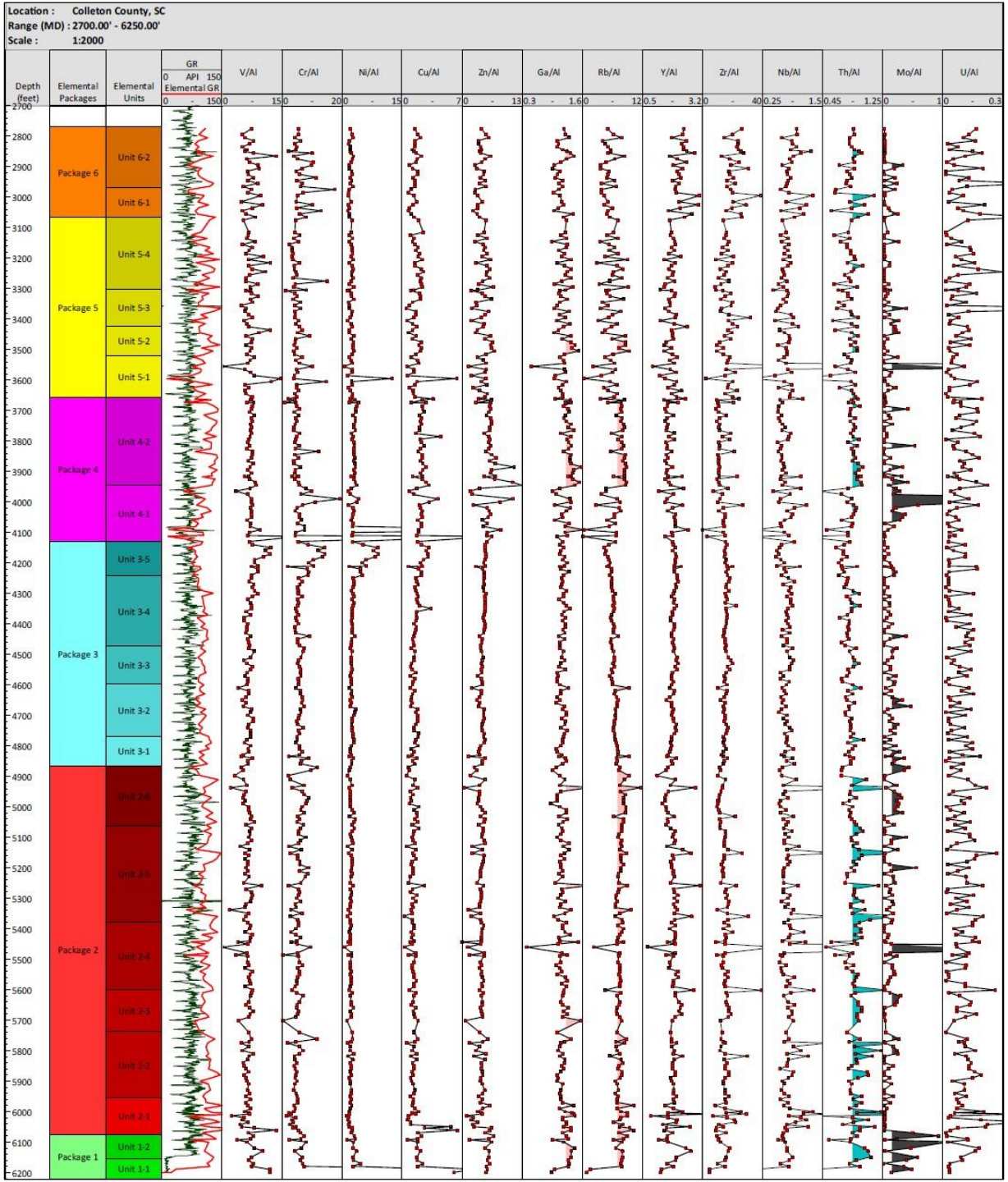

Figure 4.4. The Rizer #1 test borehole's chemostratigraphic zonation presented as depth plots of trace elements normalized to aluminum. Six Elemental Packages are subdivided into 21 Elemental Units.

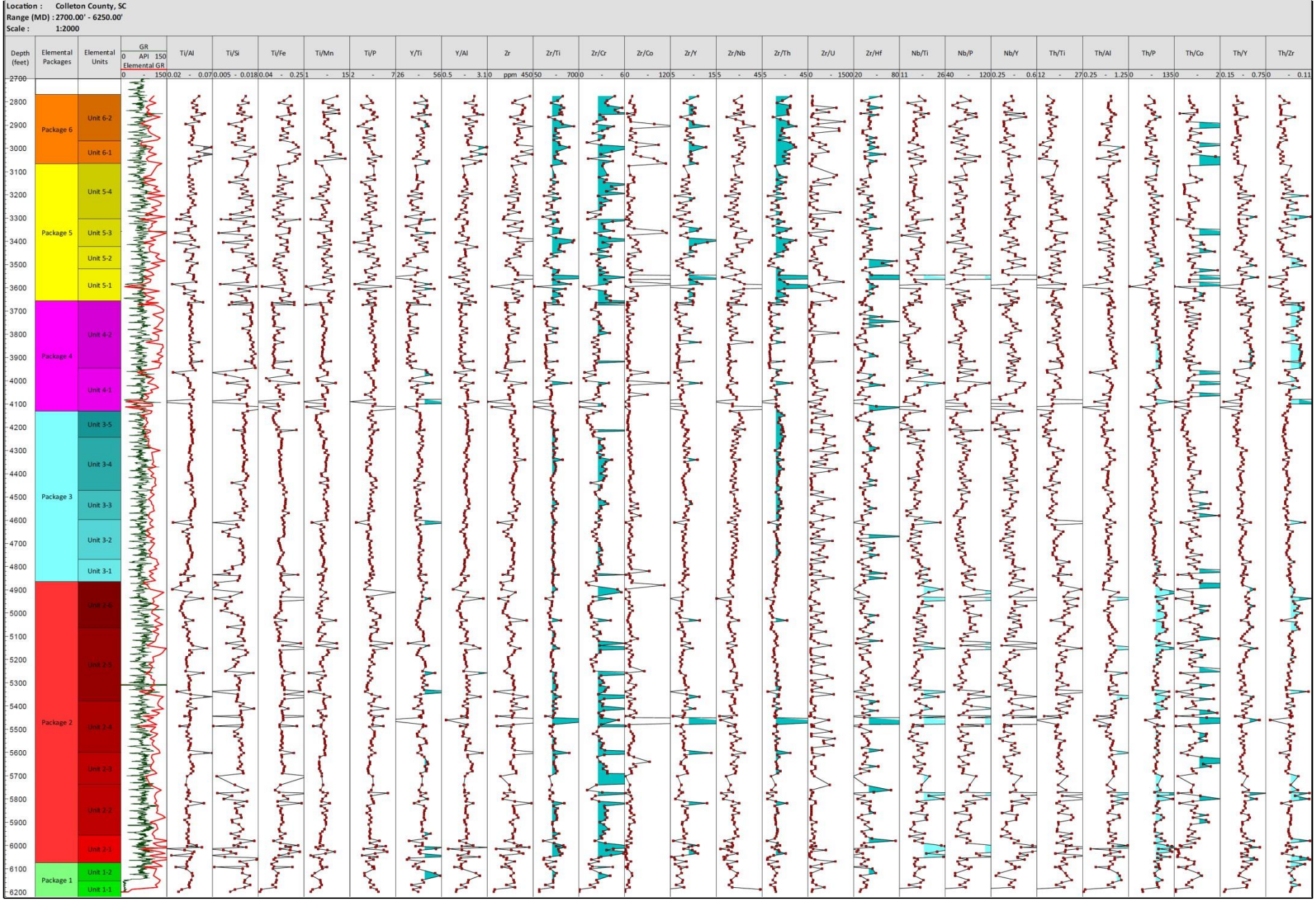

Figure 4.5. The Rizer #1 test borehole's chemostratigraphic zonation presented as depth plots of relatively immobile element ratio affinities. Six Elemental Packages are subdivided into 21 Elemental Units.

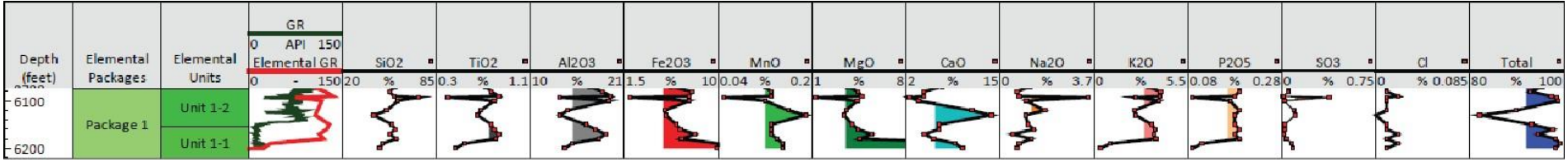

Figure 4.6a. Package 1 depth plots of bulk-rock major elements.

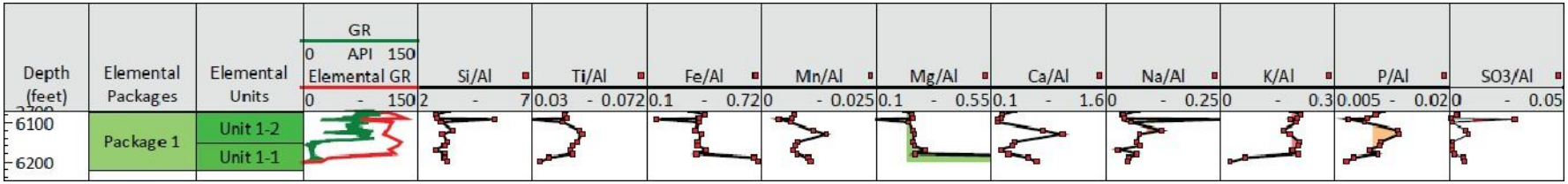

Figure 4.6b. Package 1 depth plots of major elements normalized to aluminum.

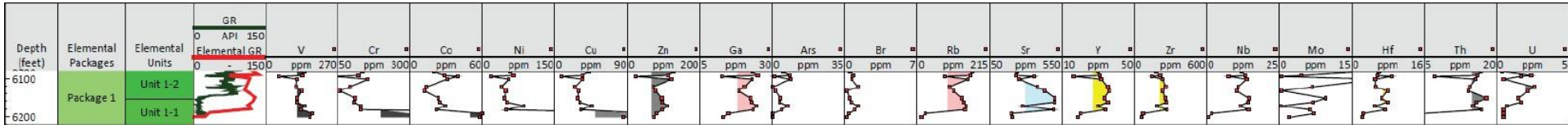

Figure 4.6c. Package 1 depth plots of bulk-rock trace elements.

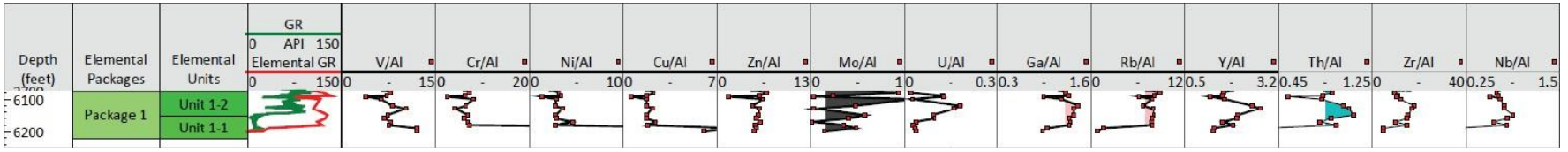

Figure 4.6d. Package 1 depth plots of trace elements normalized to aluminum.

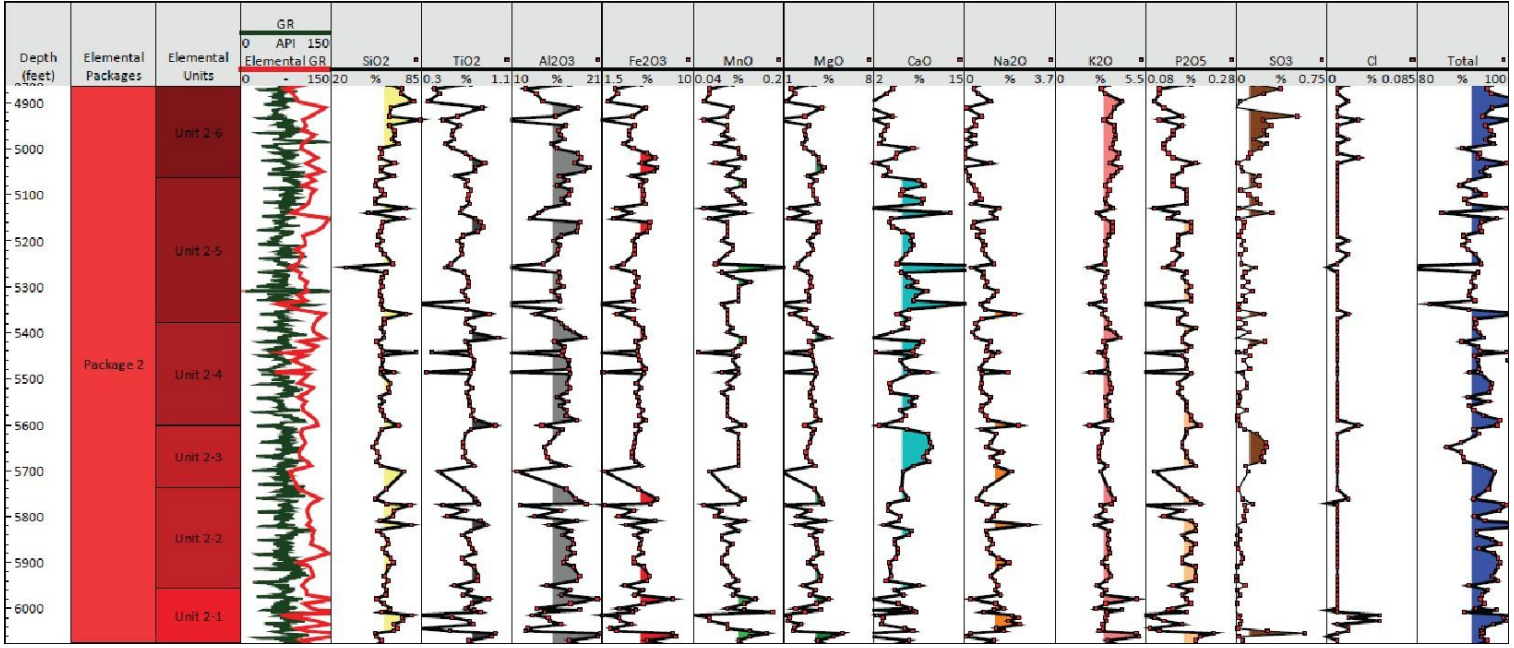

Figure 4.7a. Package 2 depth plots of bulk-rock major elements.

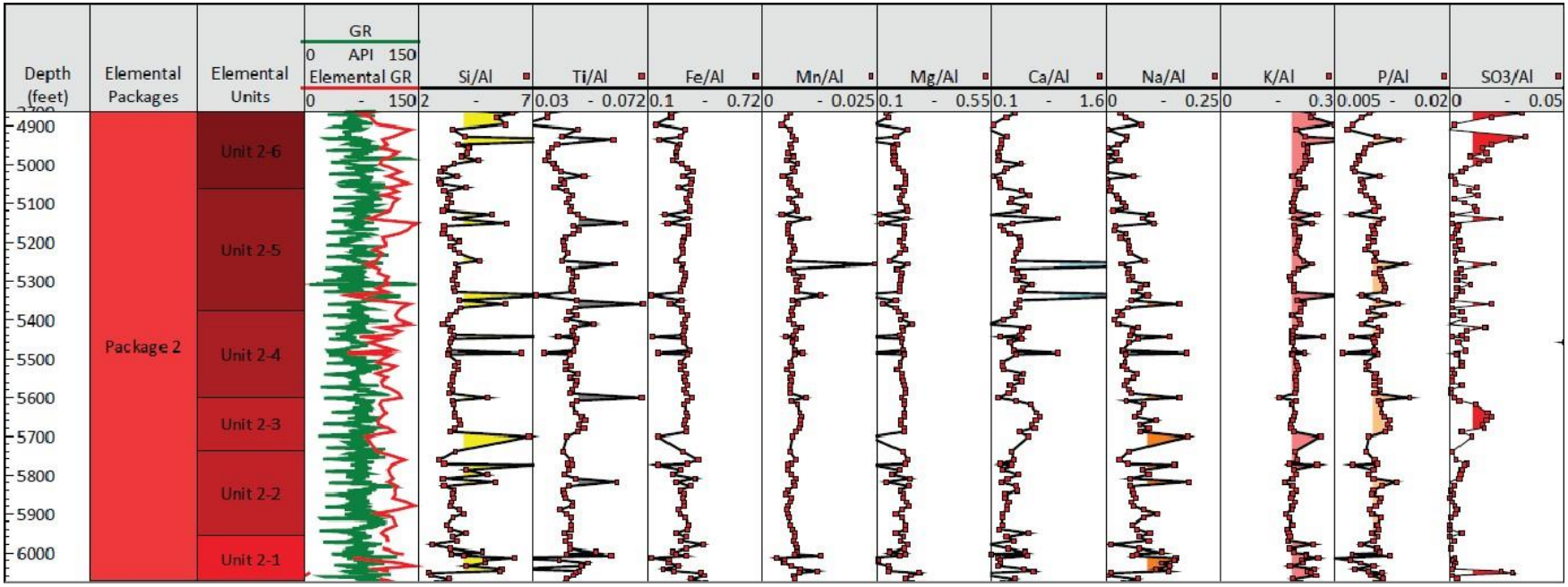

Figure 4.7b. Package 2 depth plots of major elements normalized to aluminum.

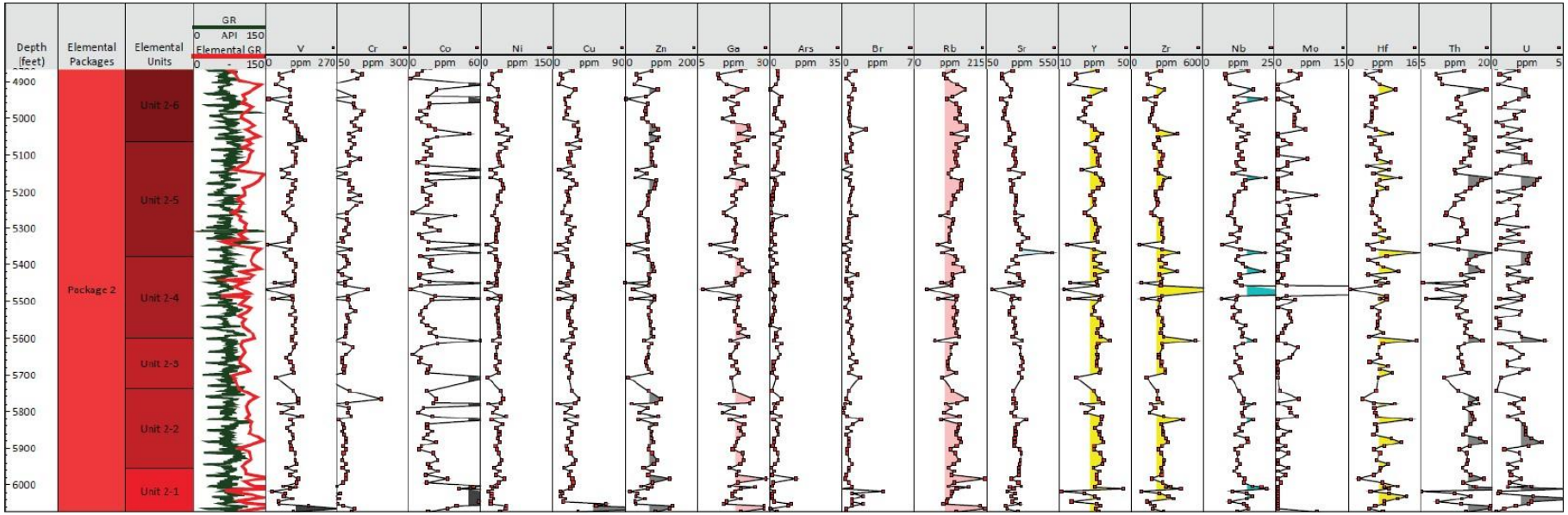

Figure 4.7c. Package 2 depth plots of bulk-rock trace elements.

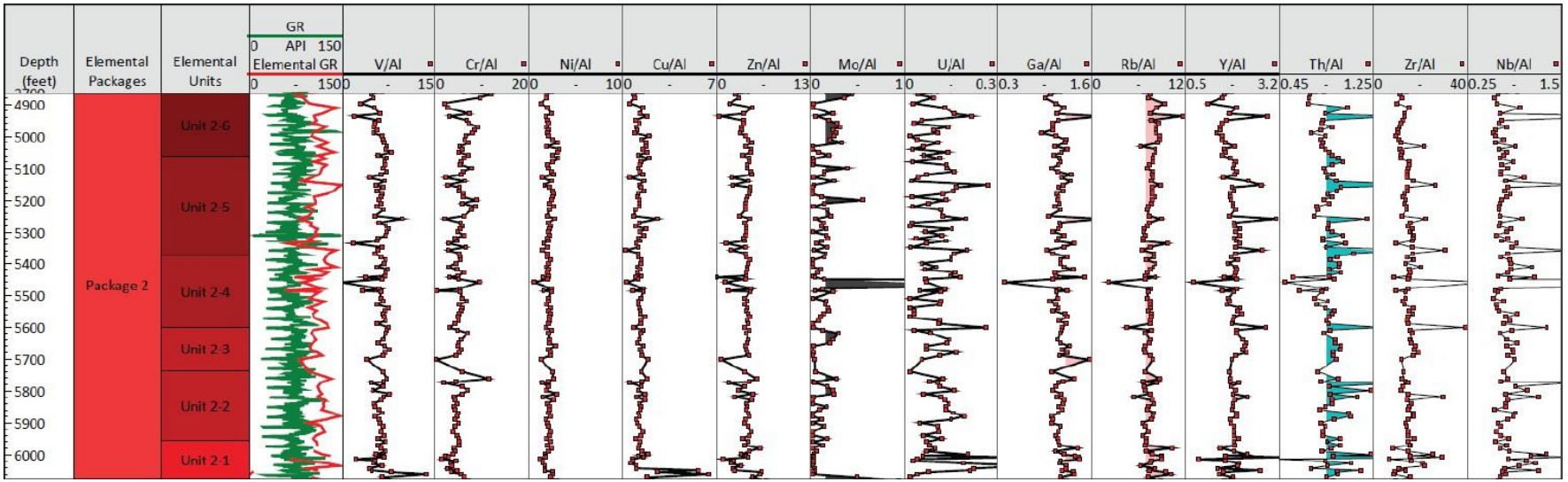

Figure 4.7d. Package 2 depth plots of trace elements normalized to aluminum.

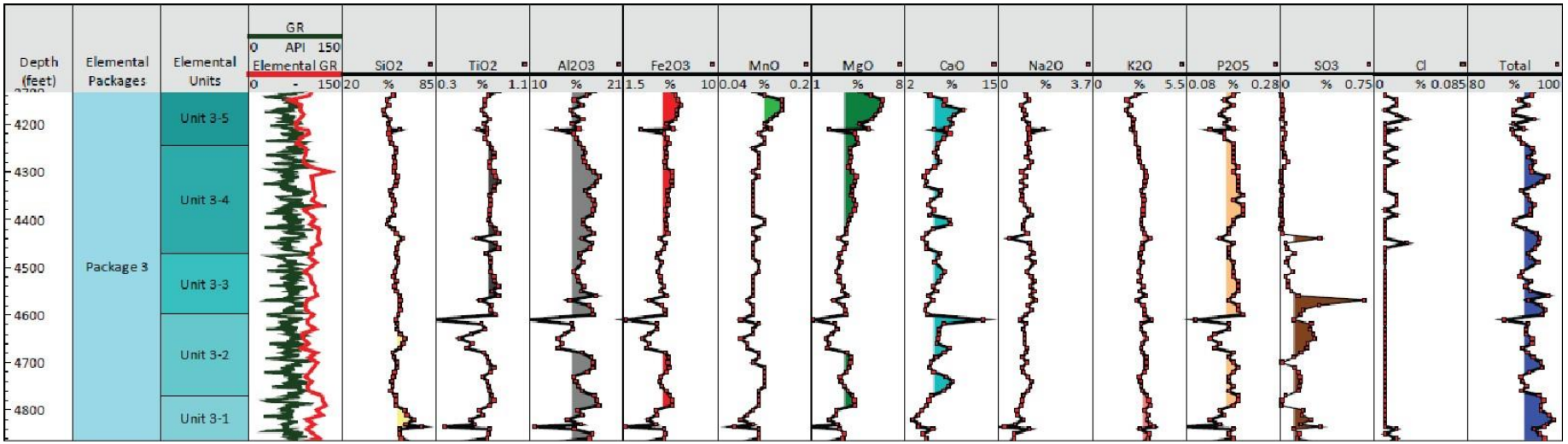

Figure 4.8a. Package 3 depth plots of bulk-rock major elements.

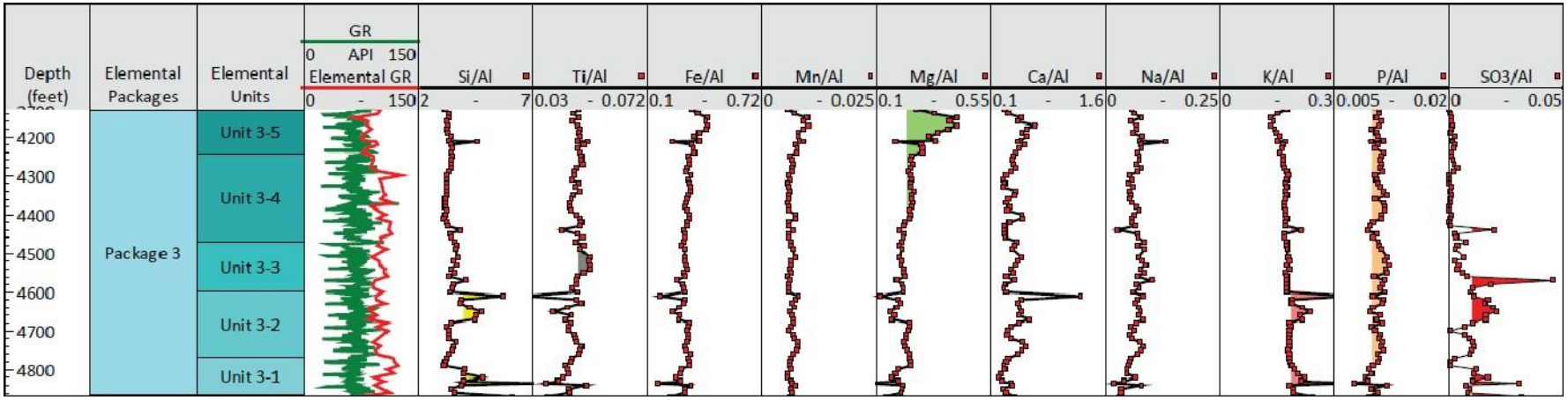

Figure 4.8b. Package 3 depth plots of major elements normalized to aluminum.

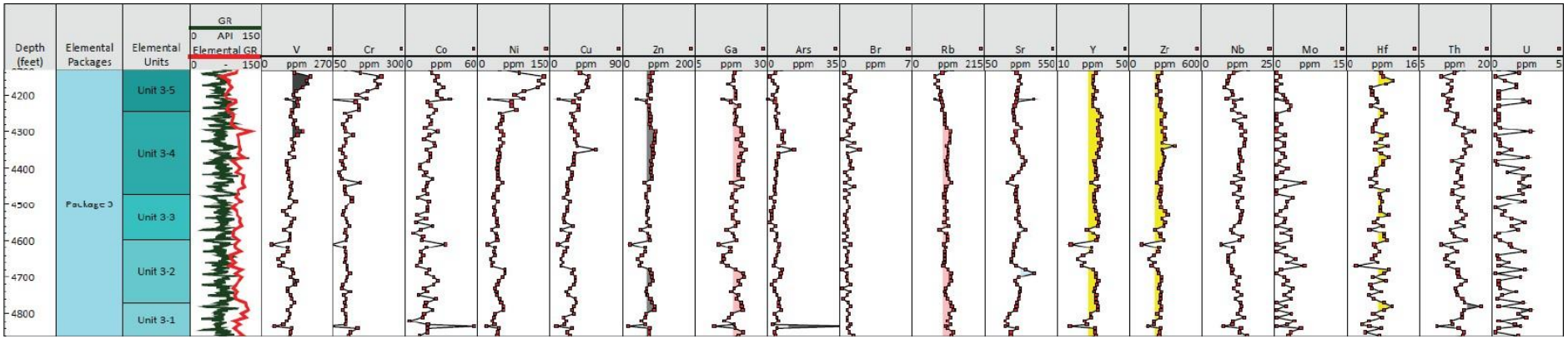

Figure 4.8c. Package 3 depth plots of bulk-rock trace elements.

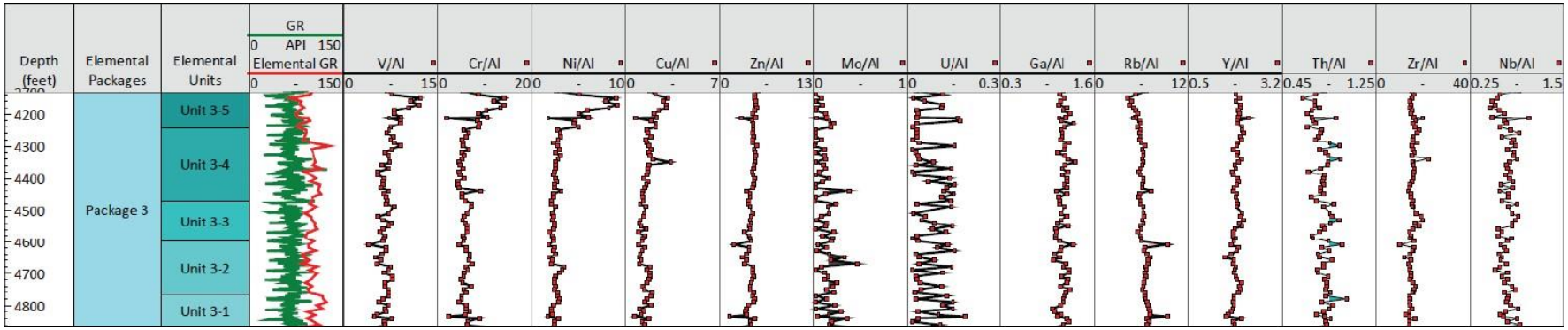

Figure 4.8d. Package 3 depth plots of trace elements normalized to aluminum.

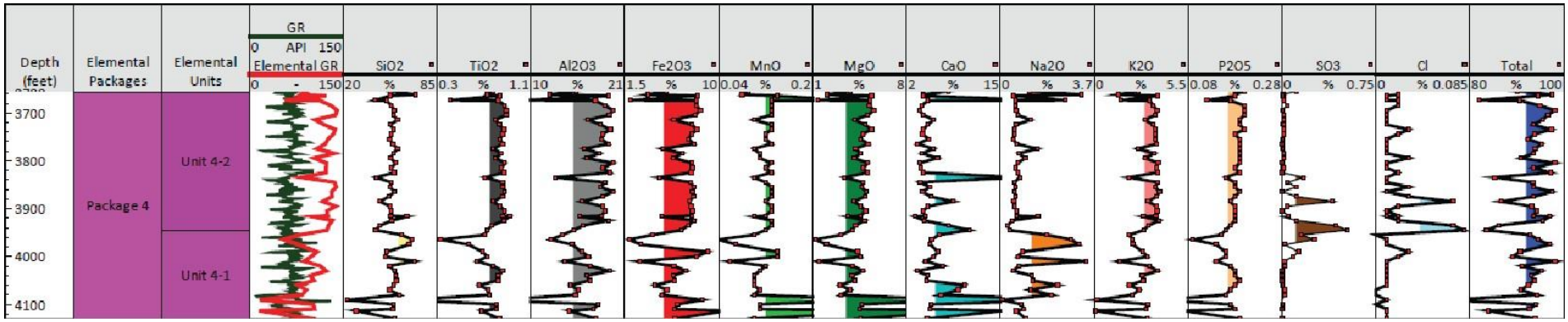

Figure 4.9a. Package 4 depth plots of bulk-rock major elements.

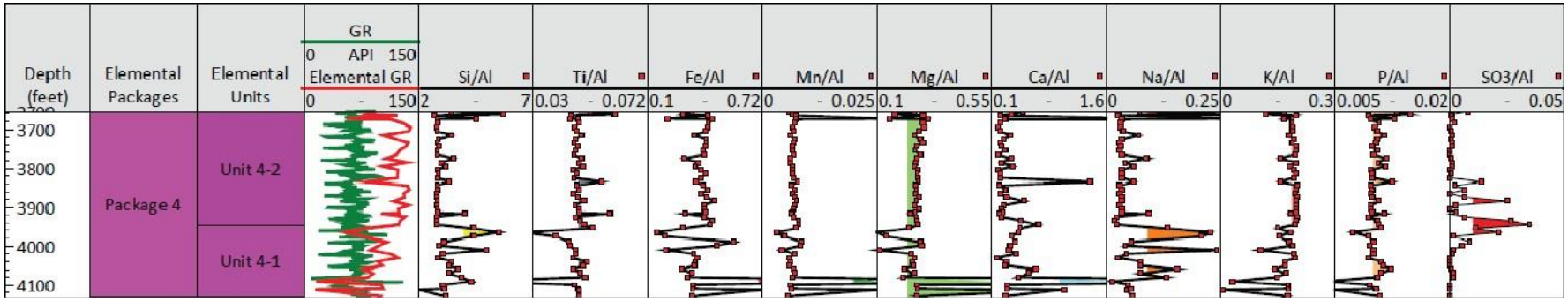

Figure 4.9b. Package 4 depth plots of major elements normalized to aluminum.

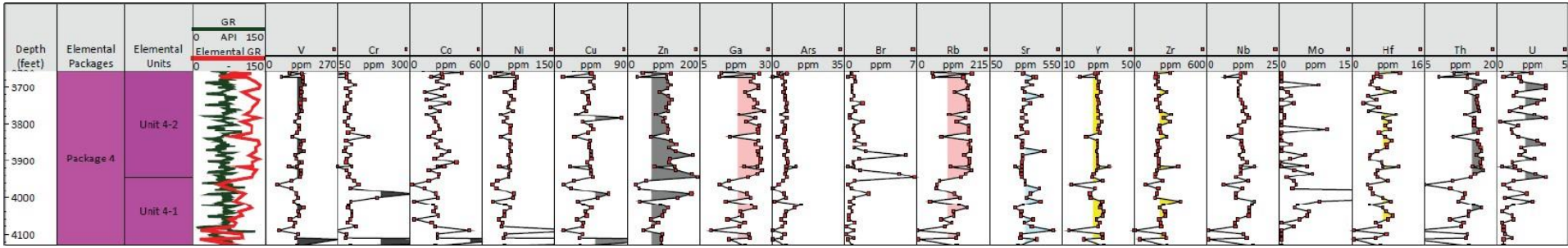

Figure 4.9c. Package 4 depth plots of bulk-rock trace elements.

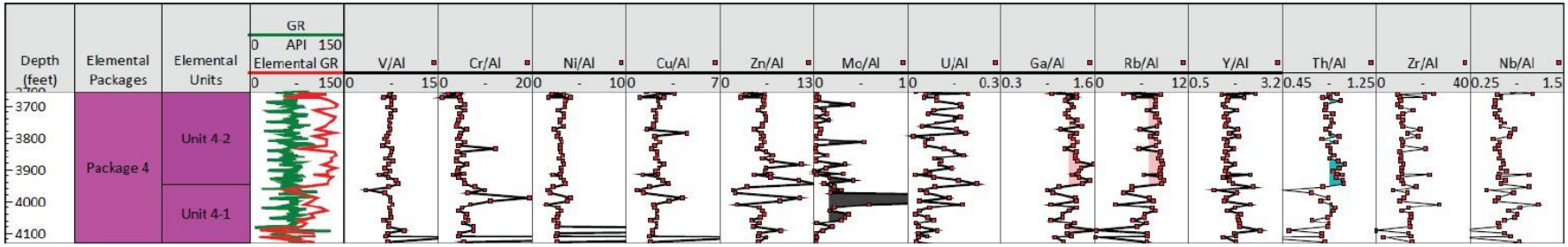

Figure 4.9d. Package 4 depth plots of trace elements normalized to aluminum.

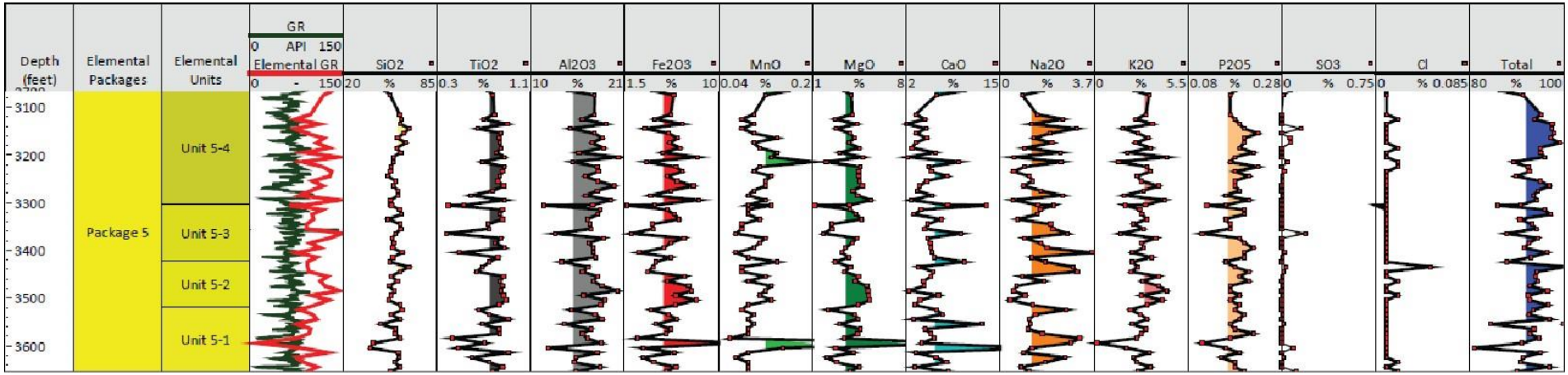

Figure 4.10a. Package 5 depth plots of bulk-rock major elements.

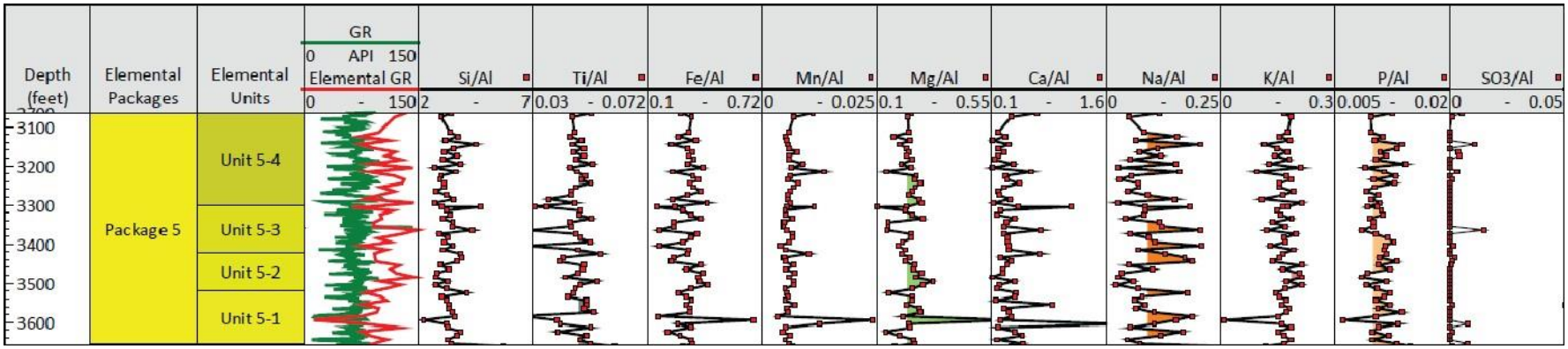

Figure 4.10b. Package 5 depth plots of major elements normalized to aluminum.

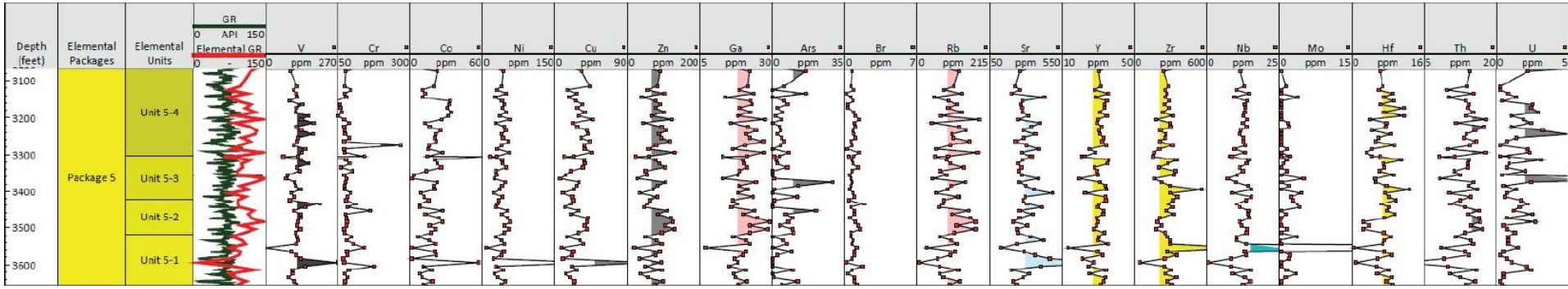

Figure 4.10c. Package 5 depth plots of bulk-rock trace elements.

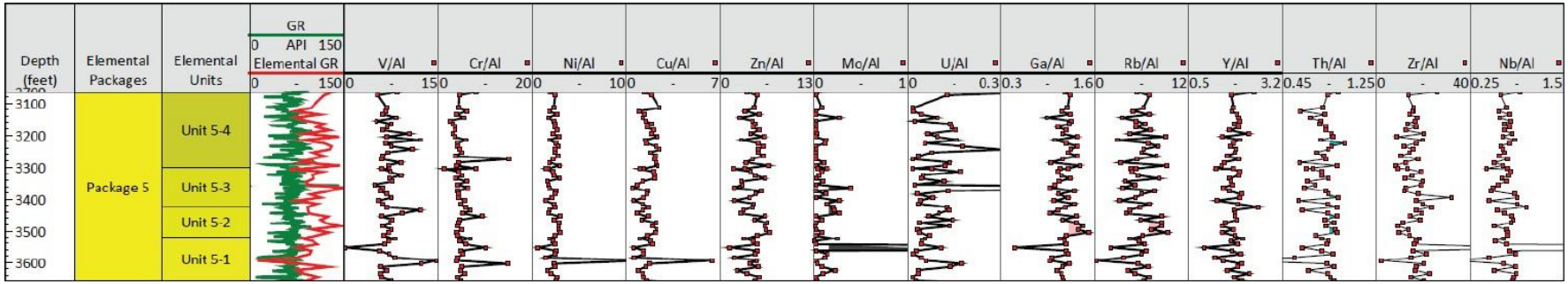

Figure 4.10d. Package 5 depth plots of trace elements normalized to aluminum.

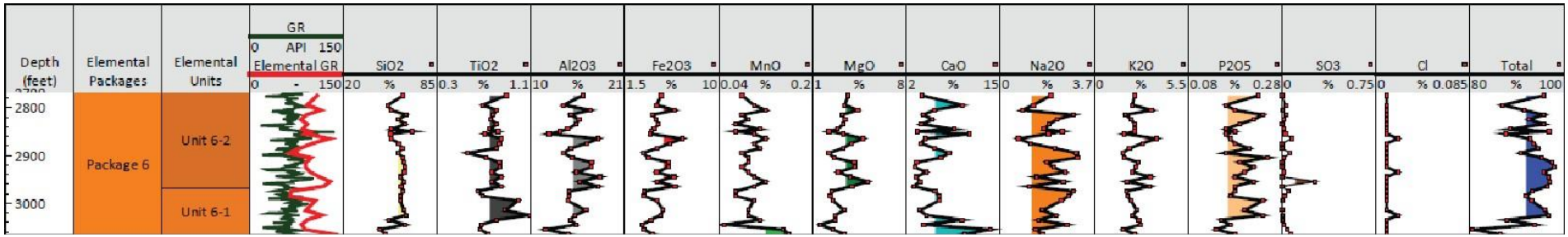

Figure 4.11a. Package 6 depth plots of bulk-rock major elements.

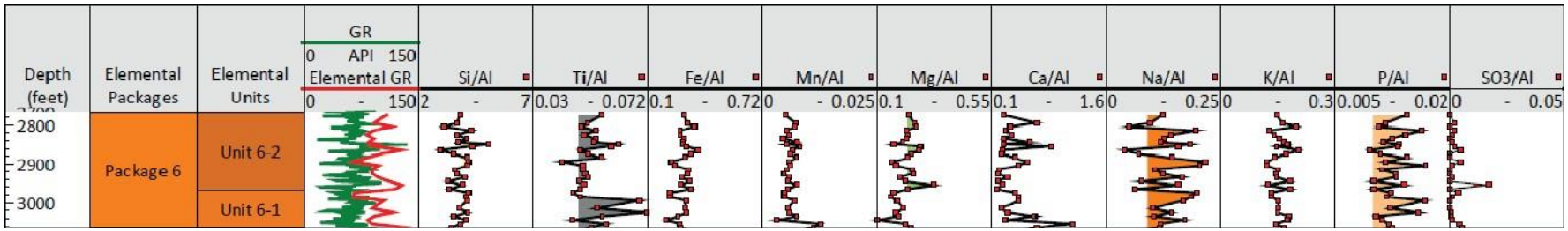

Figure 4.11b. Package 6 depth plots of major elements normalized to aluminum.

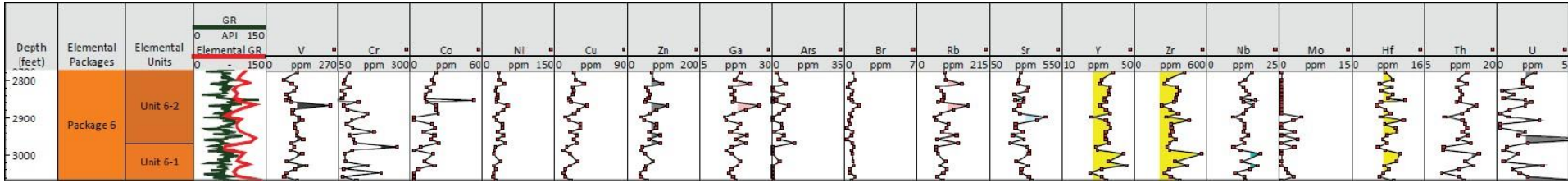

Figure 4.11c. Package 6 depth plots of bulk-rock trace elements.

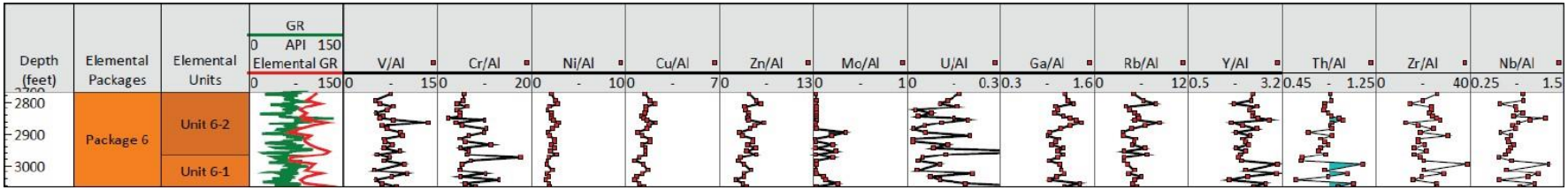

Figure 4.11d. Package 6 depth plots of trace elements normalized to aluminum.

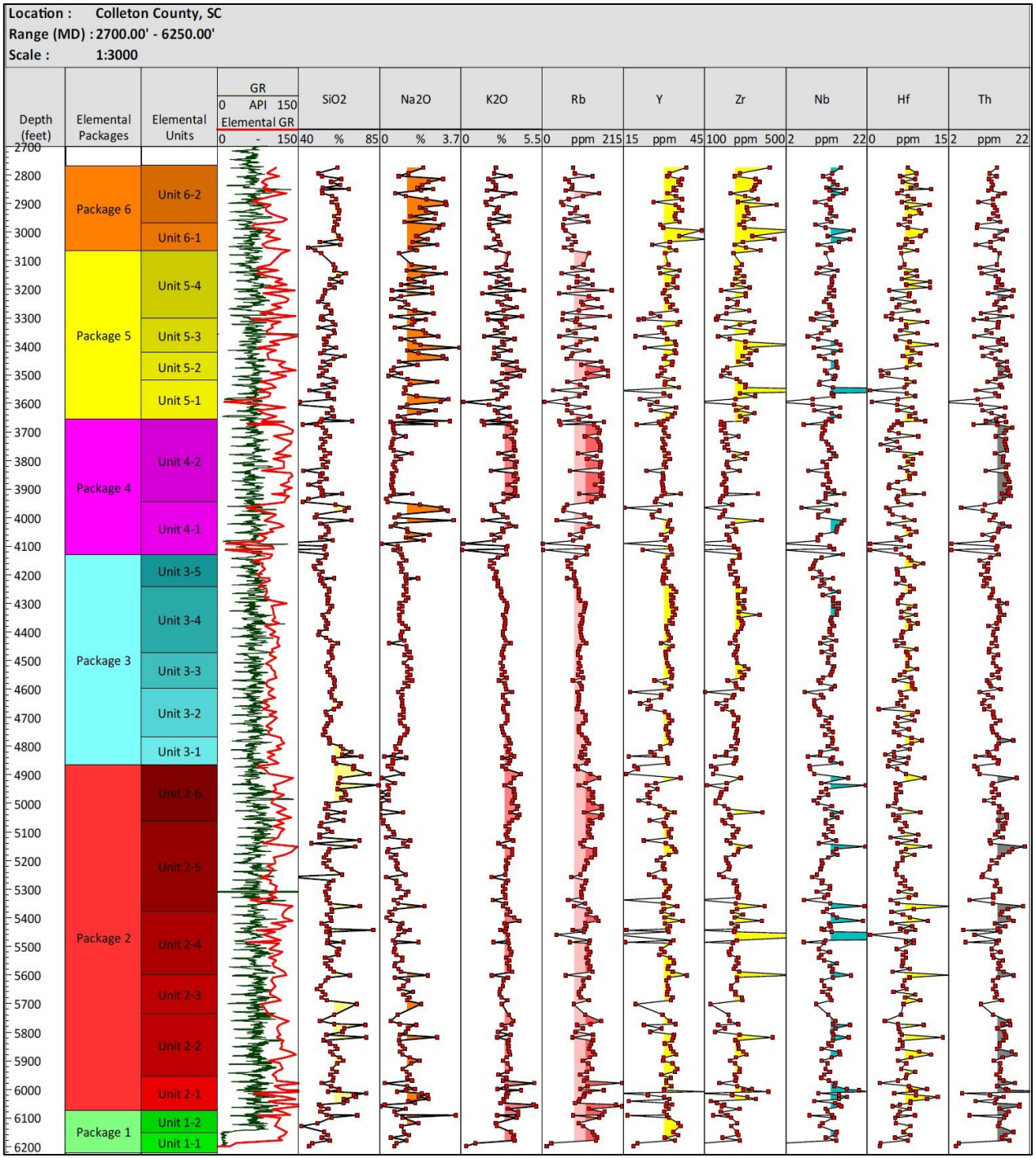

Figure 4.12a. The Rizer #1 test borehole's chemostratigraphic zonation presented as depth plots of elements associated with felsic minerals.

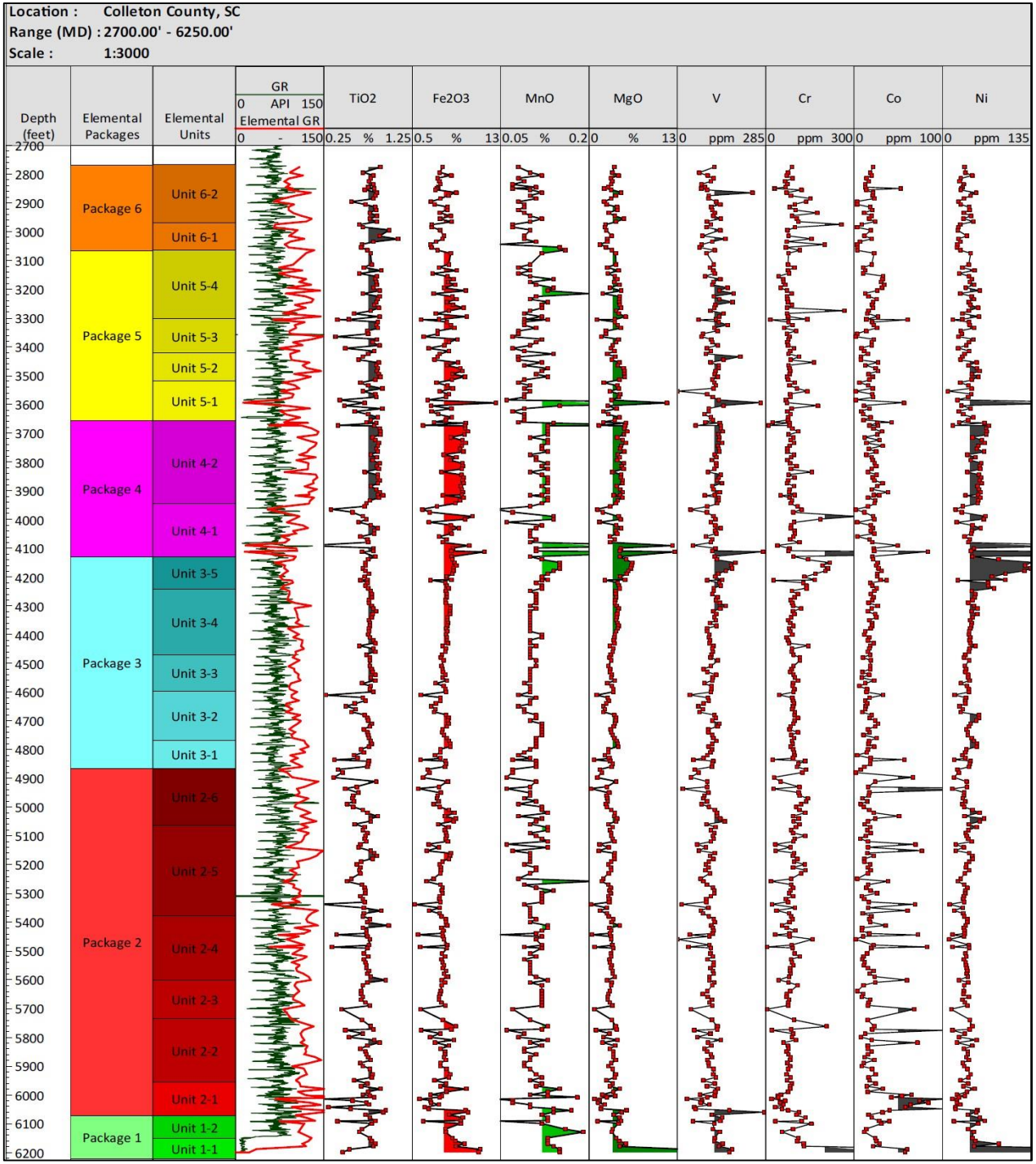

Figure 4.12b. The Rizer #1 test borehole's chemostratigraphic zonation presented as depth plots of elements associated with mafic minerals.

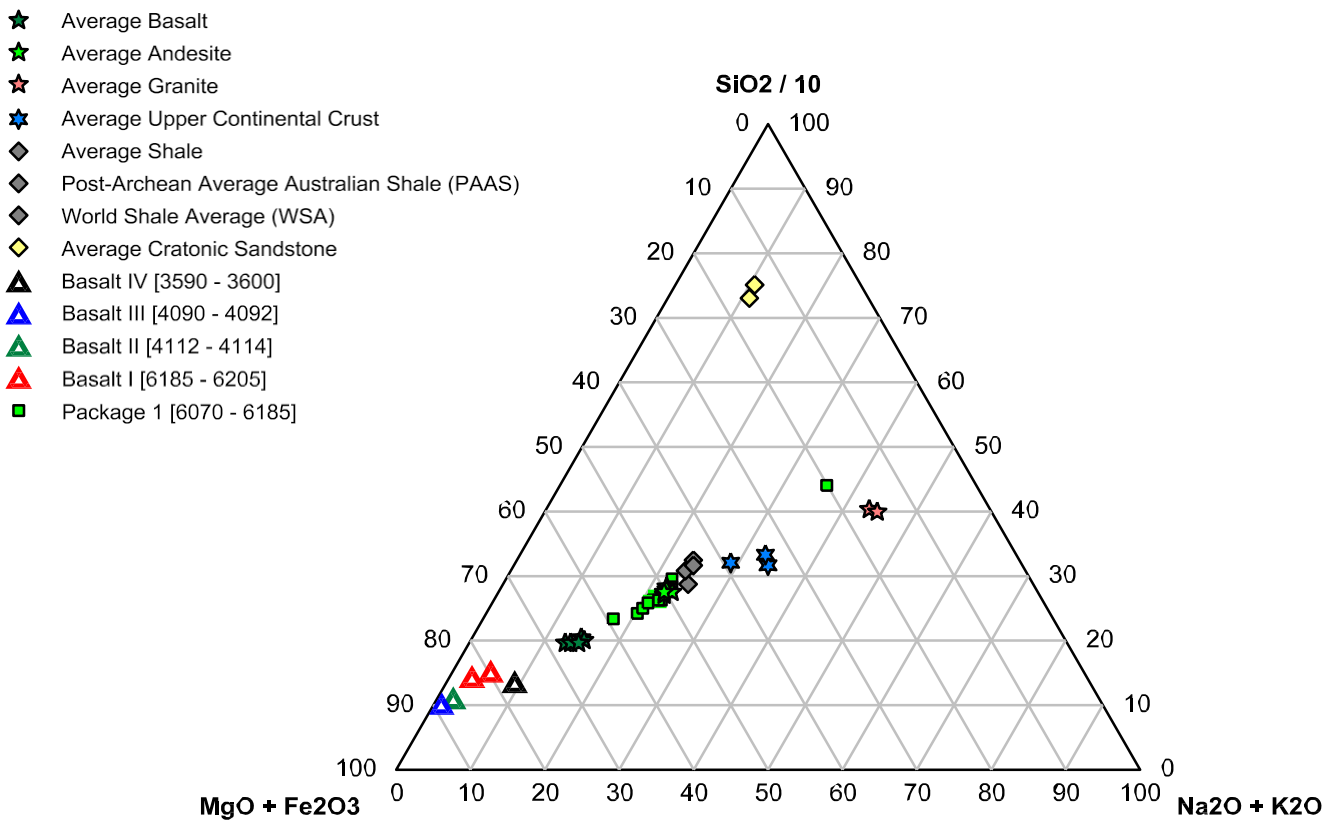

Figure 4.13a. Prevalence of felsic-affinity elements versus mafic-affinity elements using the ternary diagram of (SiO_2 /10) – (MgO + Fe_2O_3) – (Na_2O + K_2O) in Package 1. Although mafic mineral sediments may dominate this package, it is also possibly influenced by drilling problems encountered while trying to penetrate the basal basalt unit (Basalt I).

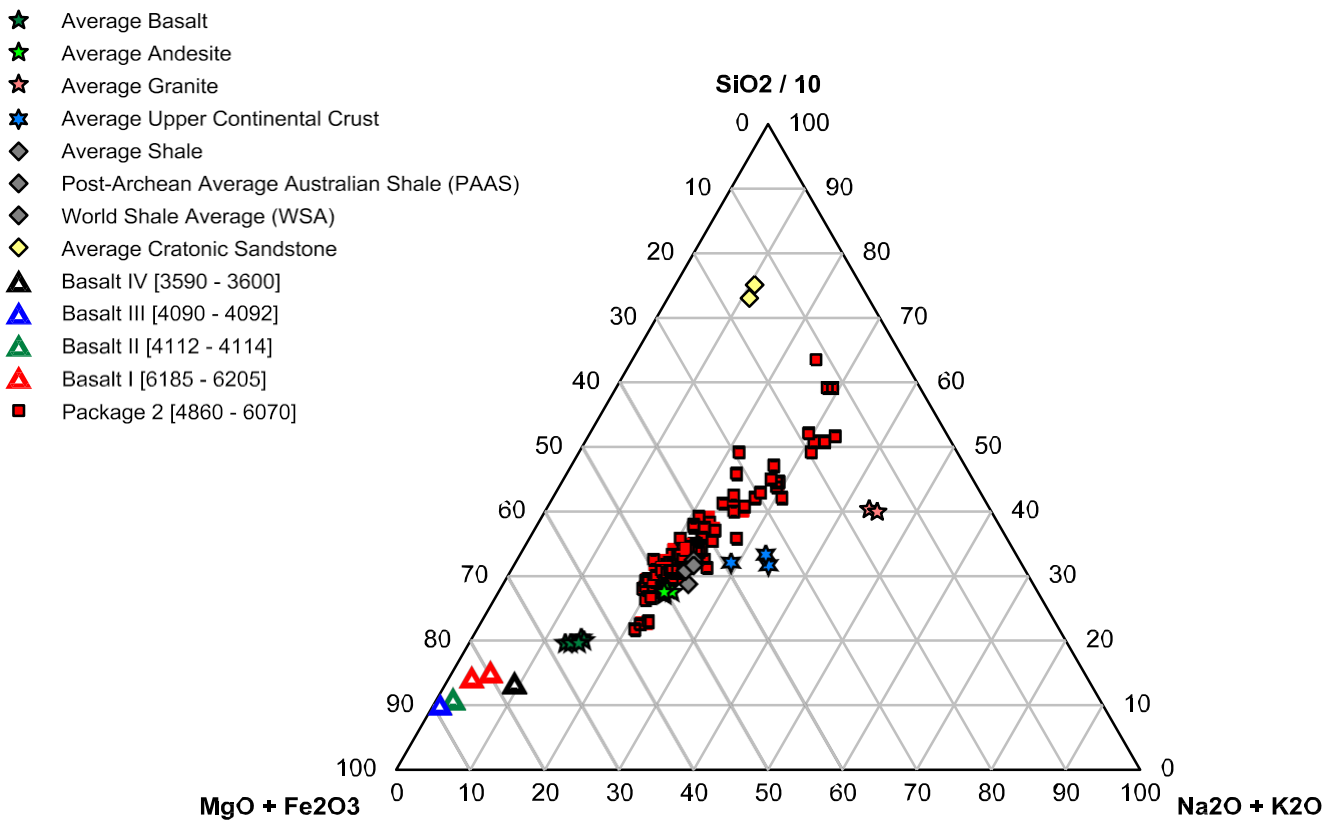

Figure 4.13b. Prevalence of felsic-affinity elements versus mafic-affinity elements using the ternary diagram of (SiO_2 /10) – (MgO + Fe_2O_3) – (Na_2O + K_2O) in Package 2. Sample compositions similar to average granites and cratonic sandstones demonstrates the influence of a more-felsic sediment source and the declining influence of a more-mafic sediment source.

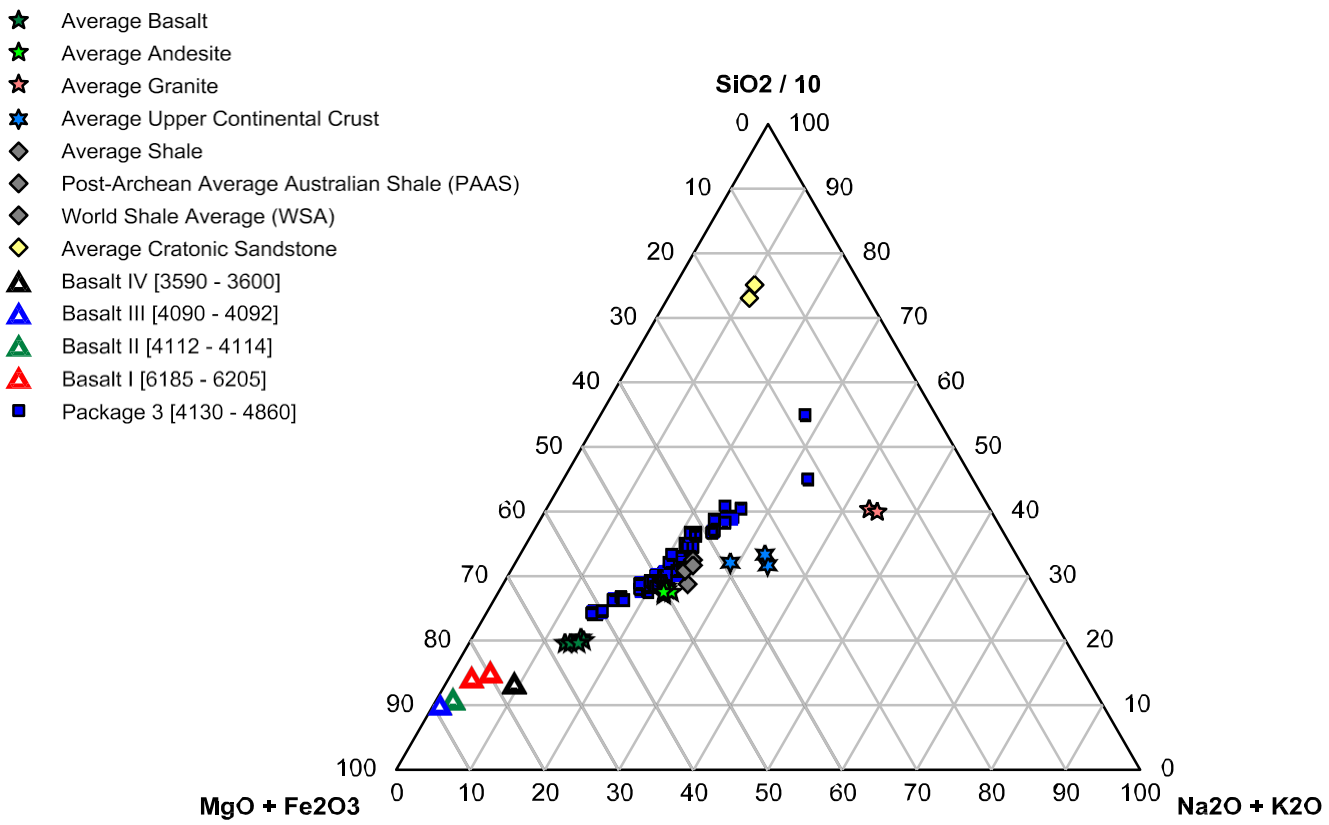

Figure 4.13c. Prevalence of felsic-affinity elements versus mafic-affinity elements using the ternary diagram of (SiO_2 /10) – ($MgO + Fe_2O_3$) – ($Na_2O + K_2O$) in Package 3. The linear trend centered on average andesites and average shales is consistent with mixing of detritus from more-mafic and more-felsic sources.

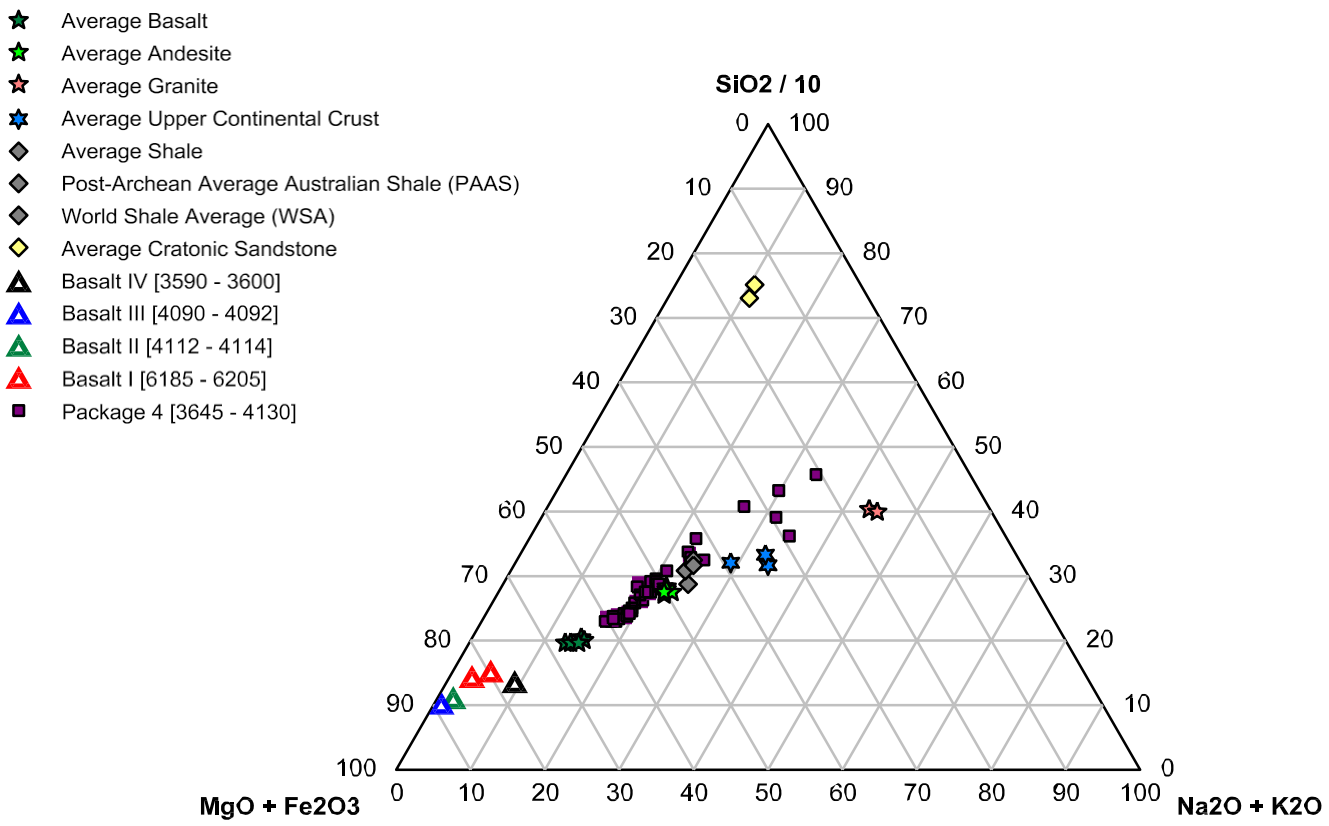

Figure 4.13d. Prevalence of felsic-affinity elements versus mafic-affinity elements using the ternary diagram of (SiO_2 /10) – (MgO + Fe_2O_3) – (Na_2O + K_2O) in Package 4 corresponds to P4 having an overall composition more influenced by mafic input, but eight intervals with more felsic composition.

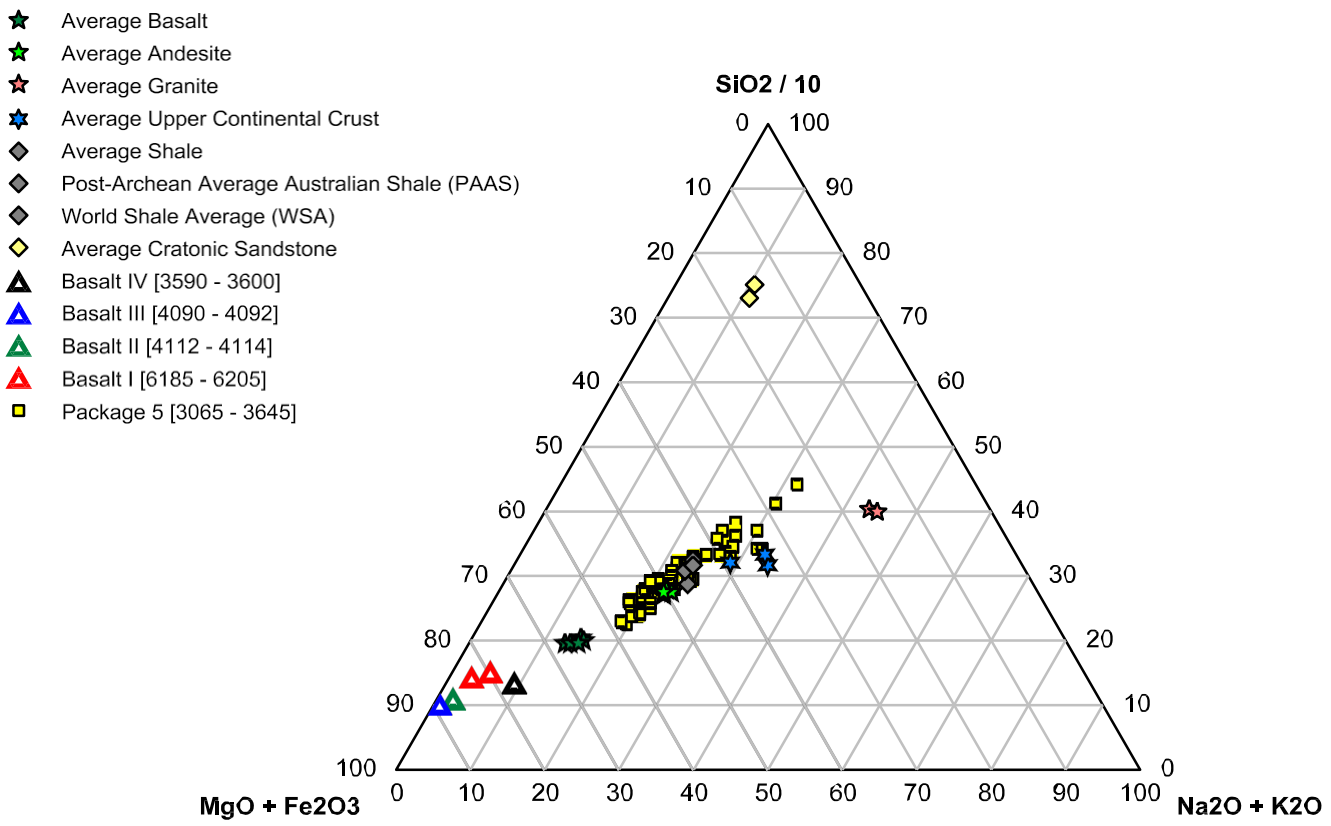

Figure 4.13e. Prevalence of felsic-affinity elements versus mafic-affinity elements using the ternary diagram of (SiO_2 /10) – (MgO + Fe_2O_3) – (Na_2O + K_2O) in Package 5 shows a well- defined linear trend that has shifted slightly away from the (MgO + Fe_2O_3) apex, indicating greater influence of detritus composed of more felsic-affinity elements.

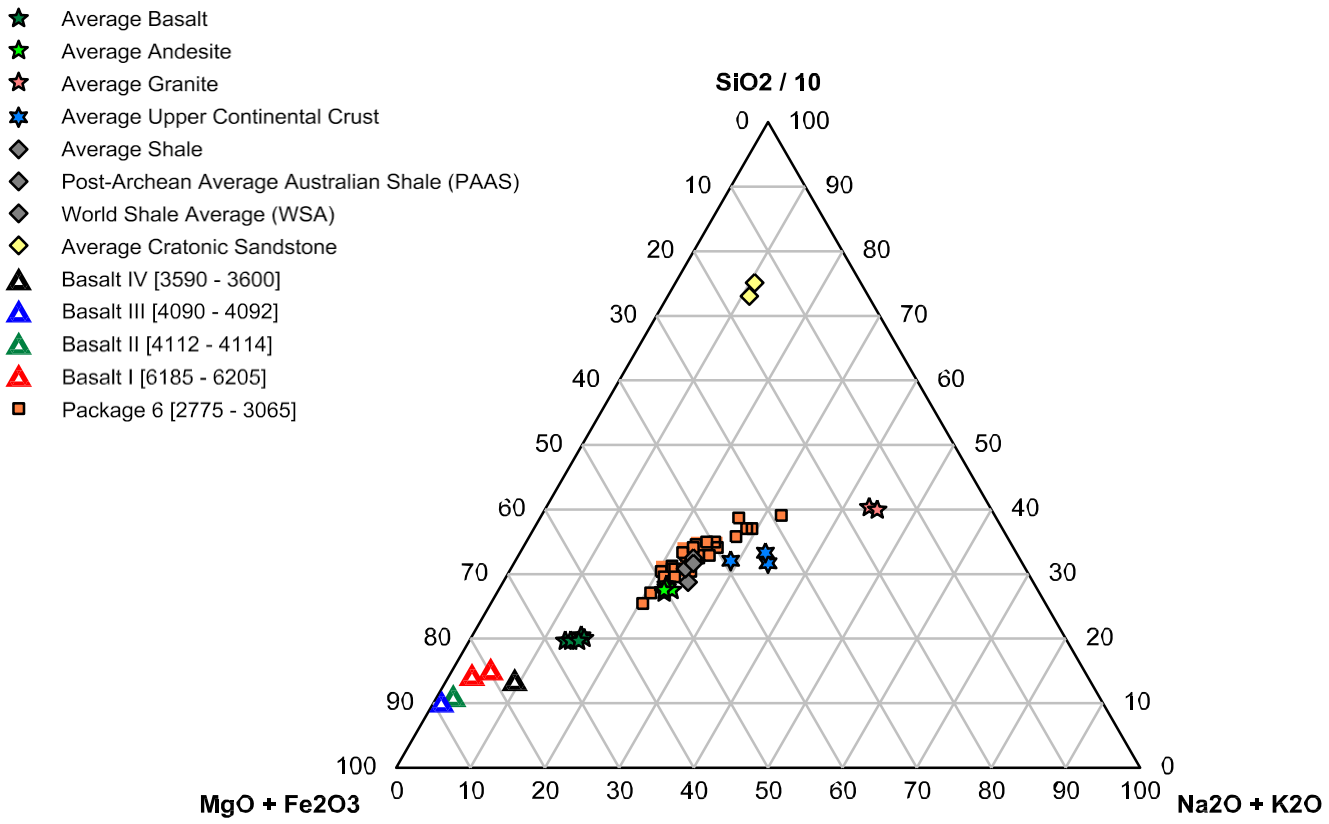

Figure 4.13f. Prevalence of felsic-affinity elements versus mafic-affinity elements using the ternary diagram of (SiO_2 /10) – (MgO + Fe_2O_3) – (Na_2O + K_2O) in Package 6 demonstrates a continued, increased influence of the more-felsic source.

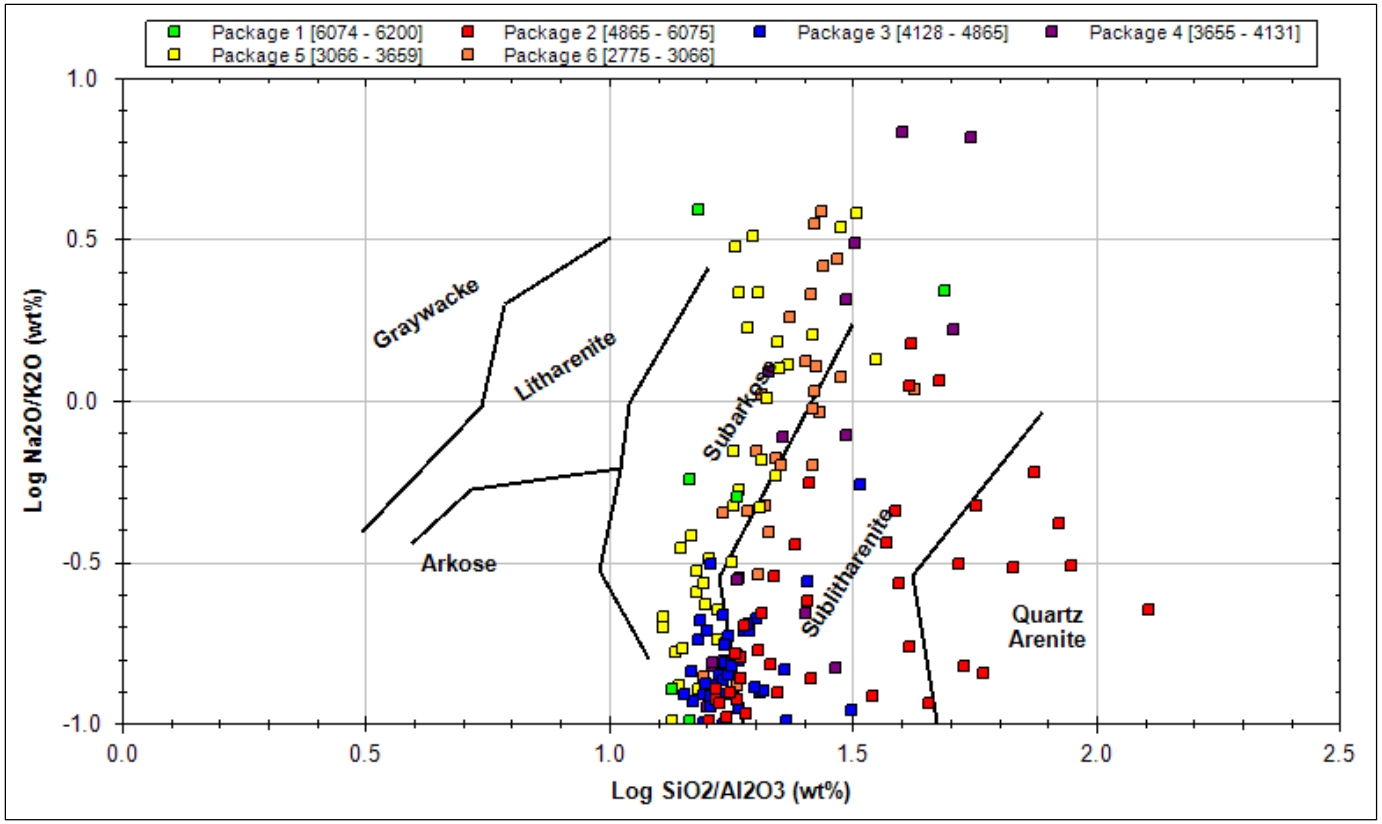

a

After Pettijohn et al. (1972)

b

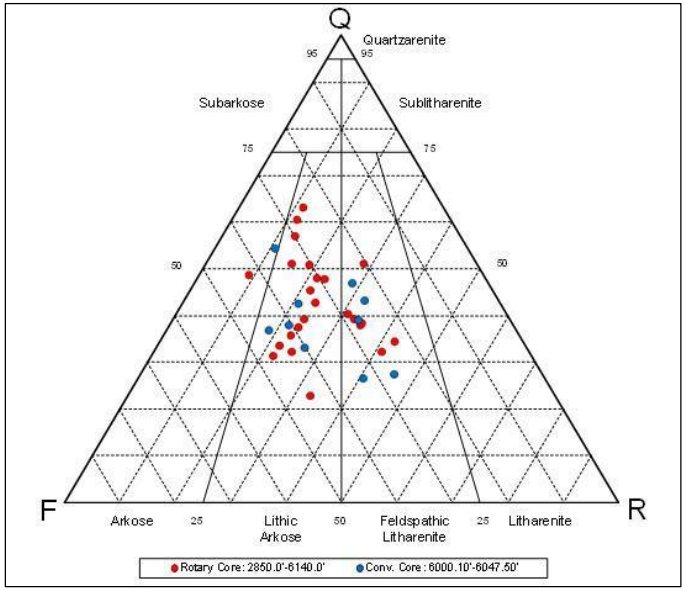

Figure 4.14. A majority of samples used for the geochemical approximation of sandstone lithology (**a**) are comprised of cuttings collected at 10-foot intervals. Rotary sidewall and core samples are also included. According to this plot, samples are weighted more favorably towards relative silica enrichment as compared to modal analyses performed on rotary and core thin-sections (**b**).

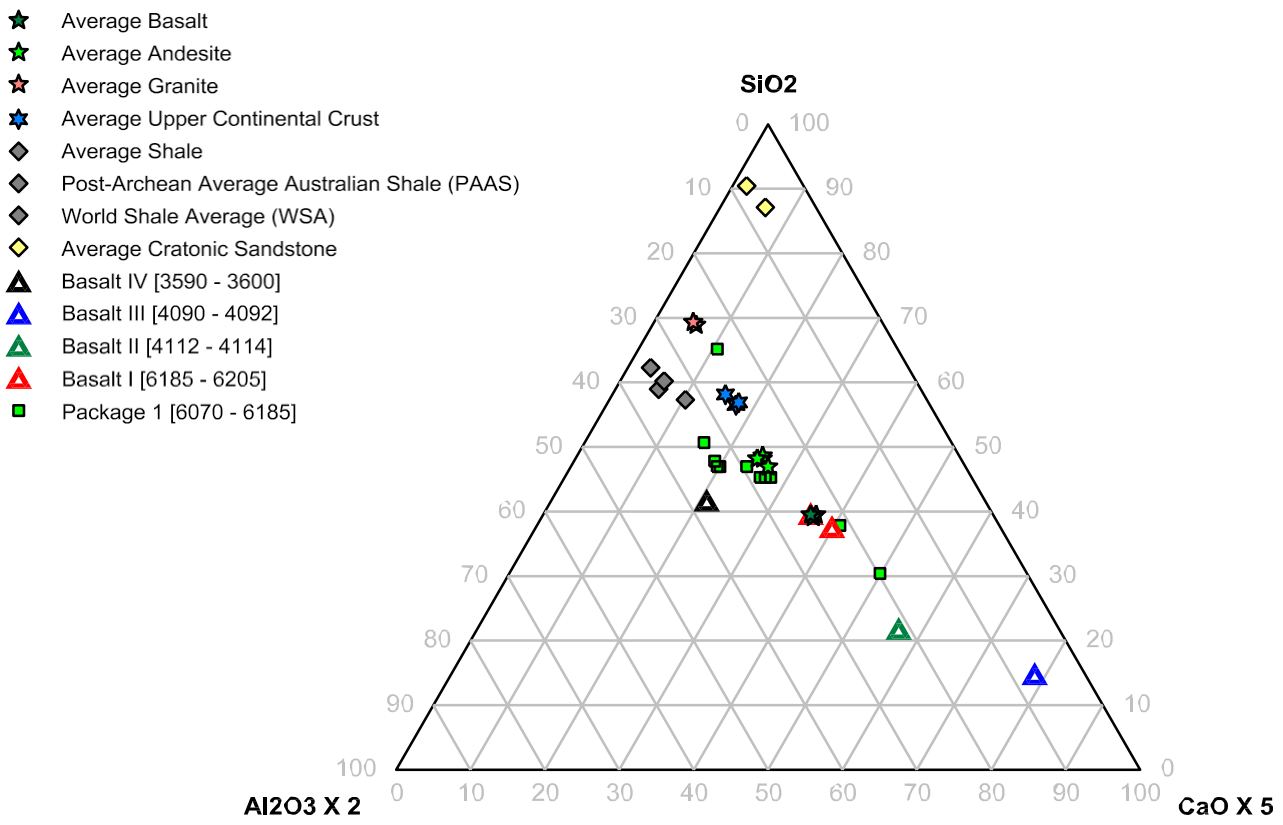

Figure 4.15a. The degree of weathering for Package 1 can be determined using the ternary diagram of (SiO_2) – (Al_2O_3 X 2) – (CaO X 5). They contain the greatest proportion of samples with an intermediate (clustered around andesite) to mafic bulk composition. Samples plotting towards the (CaO X 5) apex likely contain calcite cement.

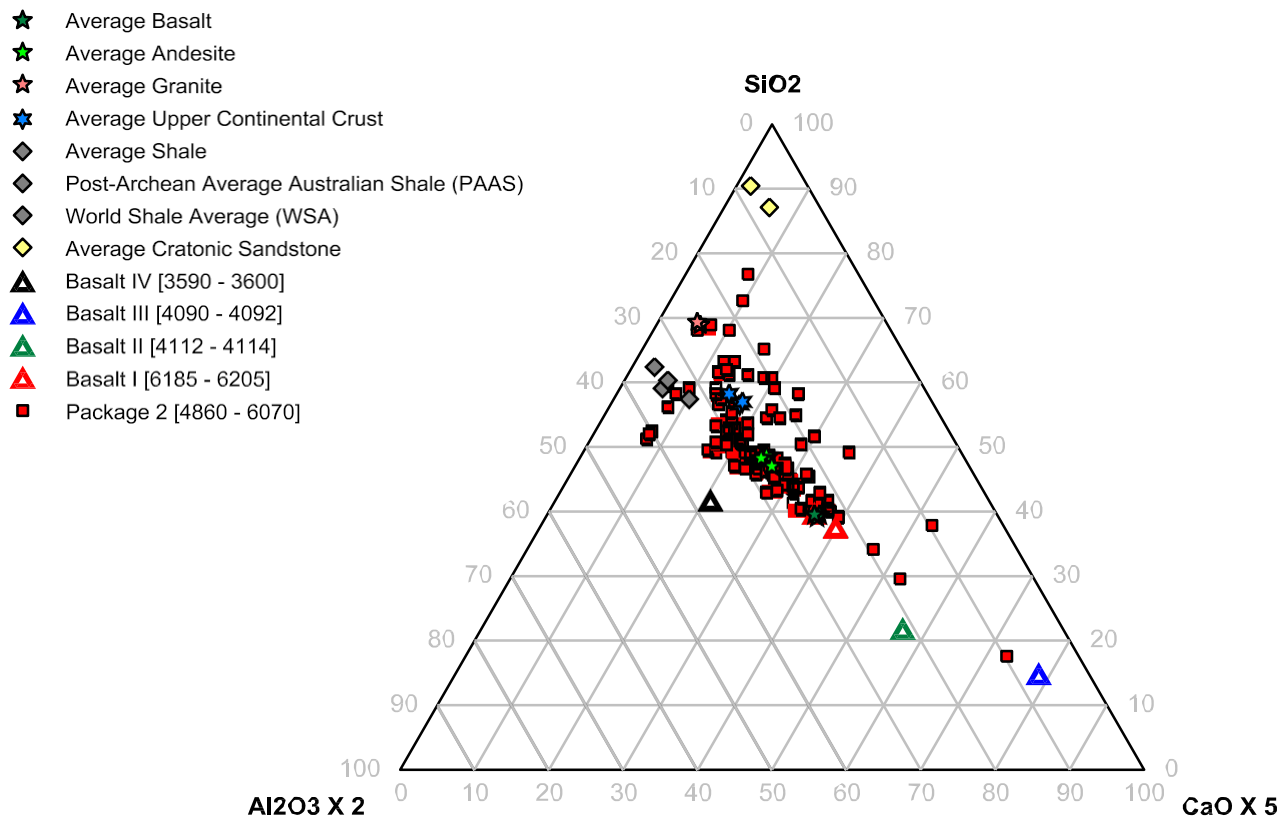

Figure 4.15b. The degree of weathering for Package 2 can be determined using the ternary diagram of (SiO_2) – (Al_2O_3 X 2) – (CaO X 5). This package contains the greatest proportion of samples that plot toward the (SiO_2) apex, suggesting the greatest abundance of detrital quartz, quartzose lithic fragments, and authigenic quartz. Sample clusters around the shale reference standards likely contain more
weathered samples. Samples plotting towards the (CaO X 5) apex likely contain calcite cement.

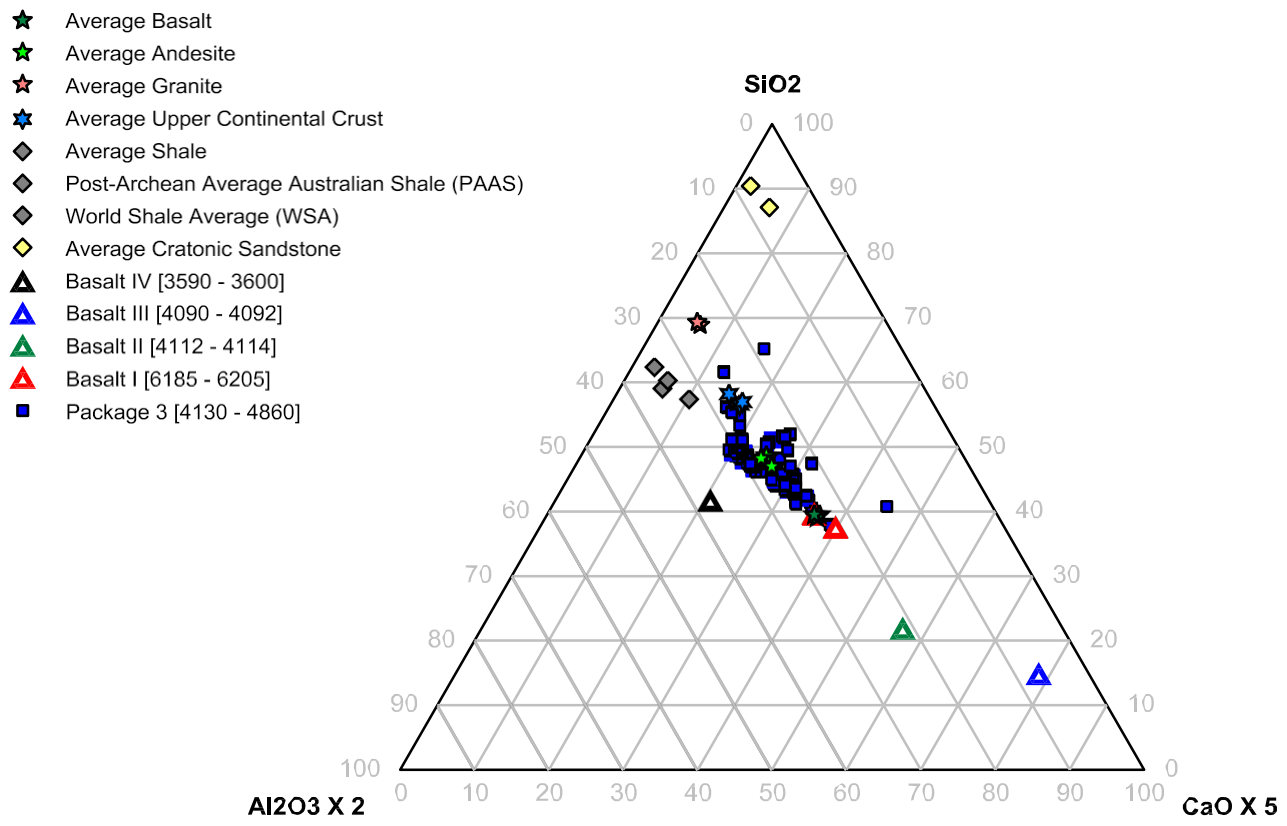

Figure 4.15c. The degree of weathering for Package 3 can be determined using the ternary diagram of (SiO_2) – (Al_2O_3 X 2) – (CaO X 5). These samples are the most tightly clustered of all Packages, likely indicating a low degree of weathering prior to deposition and burial.

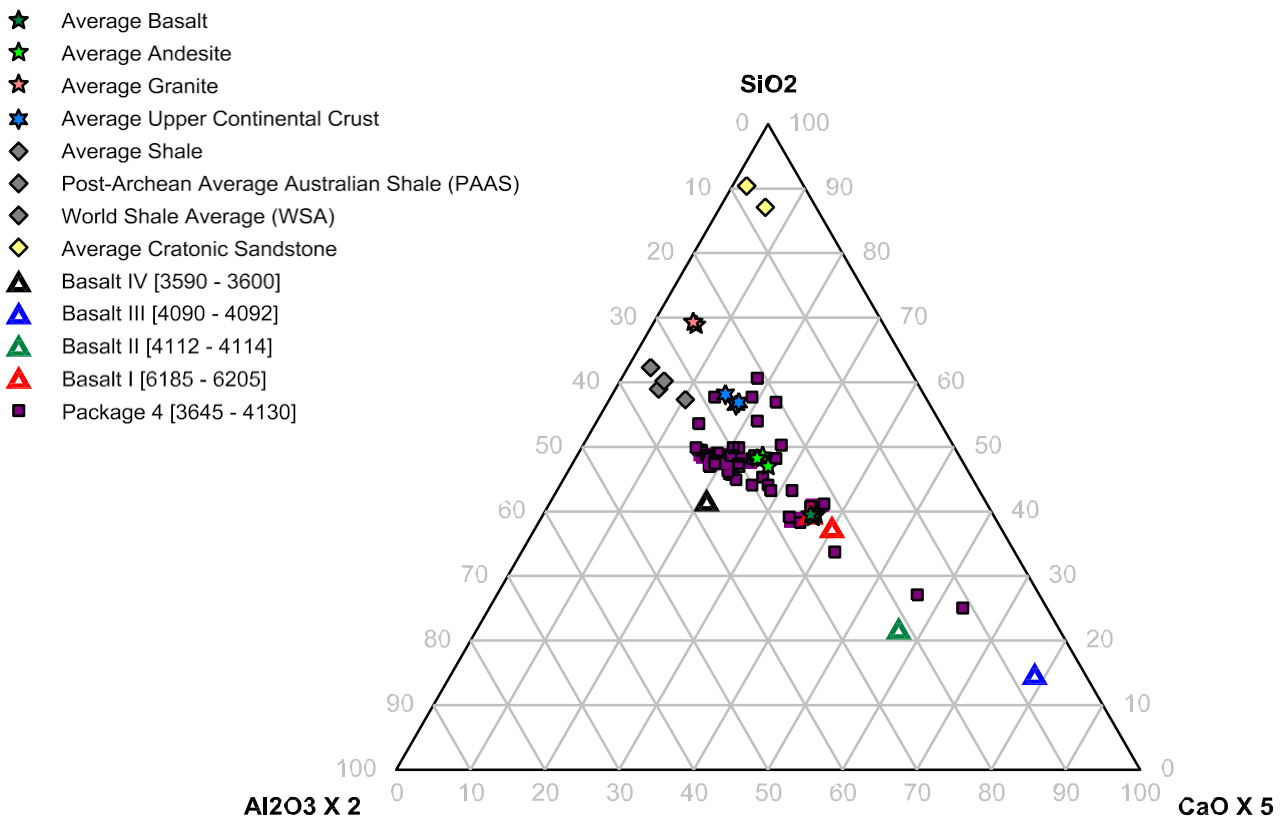

Figure 4.15d. The degree of weathering for Package 4 can be determined using the ternary diagram of (SiO_2) – (Al_2O_3 X 2) – (CaO X 5). This trend projects to a more aluminous composition that average shales on the (SiO_2) – (Al_2O_3 X 2) join of the plot, reflecting a relatively high degree of weathering and/or greater abundance of aluminous mica and/or
kaolinite. Samples plotting towards the (CaO X 5) apex likely contain calcite cement.

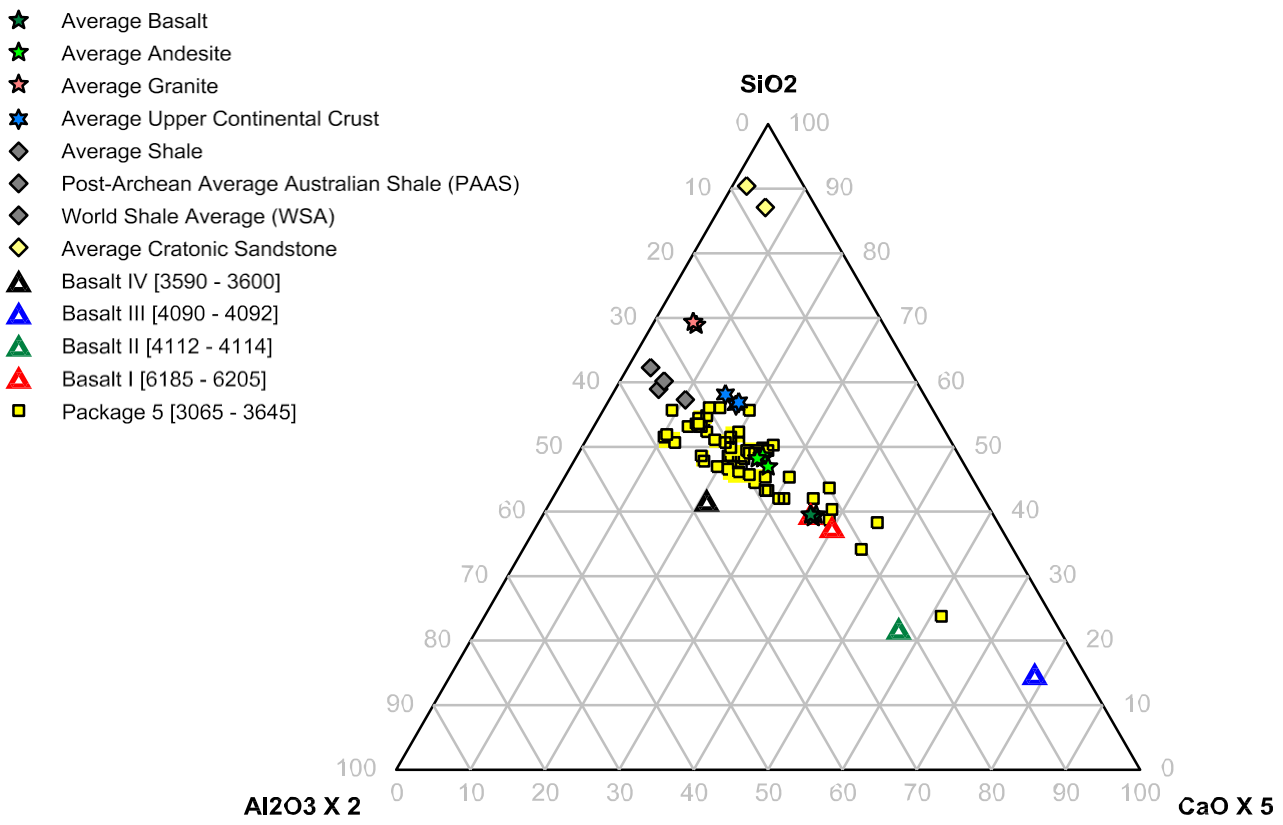

Figure 4.15e. The degree of weathering for Package 5 can be determined using the ternary diagram of (SiO_2) – (Al_2O_3 X 2) – (CaO X 5). A shift towards the (Al_2O_3 X 2) may reflect a further increase in the degree of weathering of detrital sediment or an increase in aluminous mineral content. Samples plotting towards the (CaO X 5) apex likely contain calcite cement.

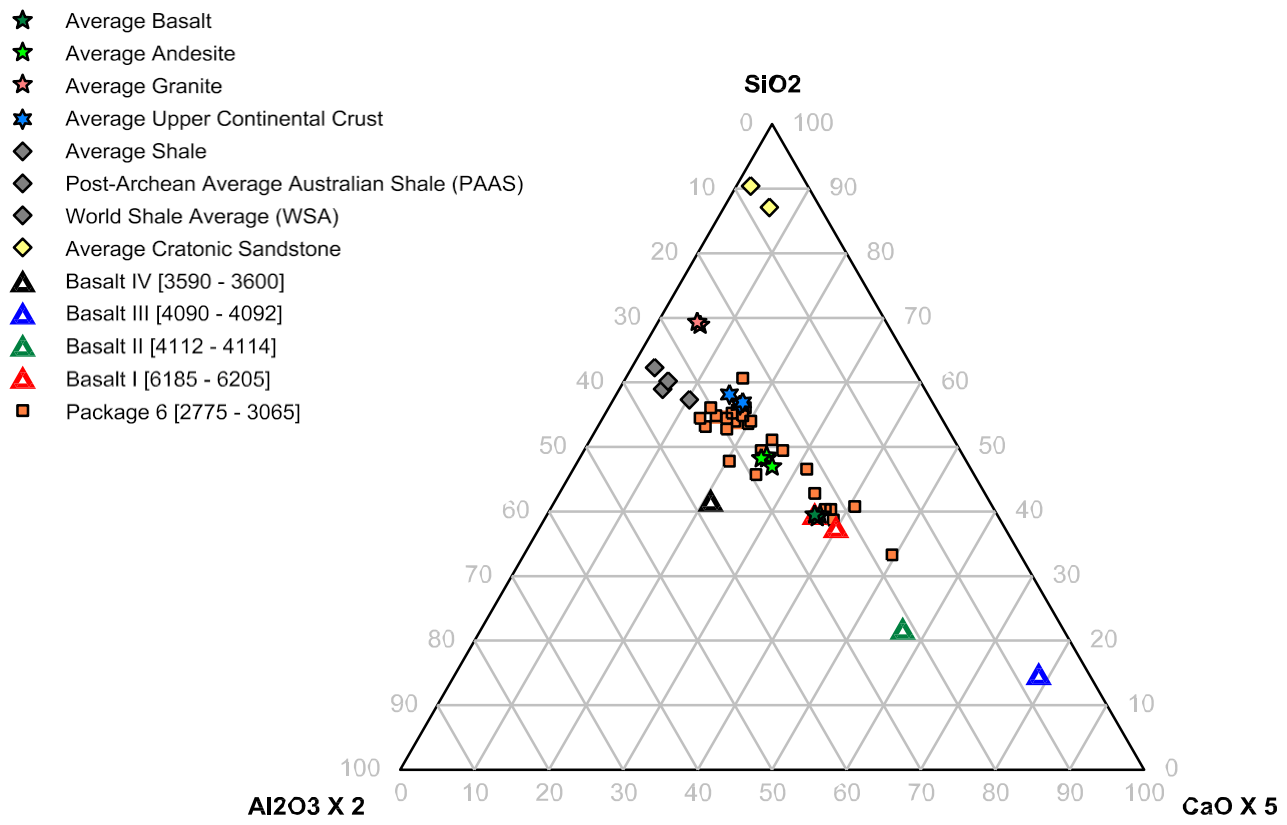

Figure 15f. The degree of weathering for Package 6 can be determined using the ternary diagram of (SiO_2) – (Al_2O_3 X 2) – (CaO X 5). A shift towards the (SiO_2) apex suggests a slightly higher quartz and feldspar content with little to no clay/mica content. Only one sample plots towards the (CaO X 5) apex, likely indicating minor calcite cement.

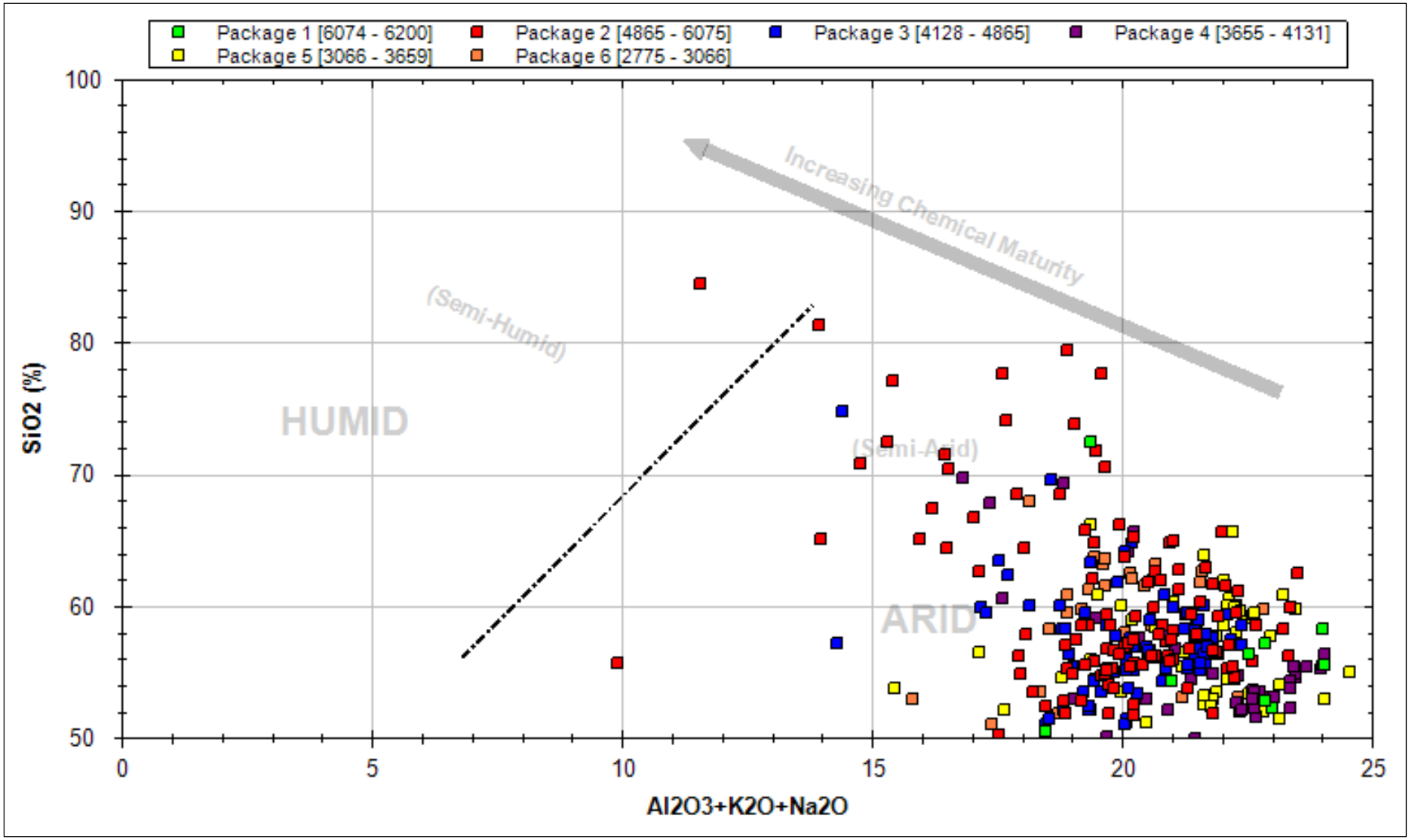

(After from Suttner and Dutta, 1986)

Figure 16. The Suttner and Dutta (1986) paleoclimate plot suggests that rapid erosion, deposition, and burial occurred due to an arid environment. This is consistent with previous interpretations of other southeastern Triassic rift basins (Withjack, 1998; Withjack et al., 2012).

(Modified from Hibbard et al, 2002)

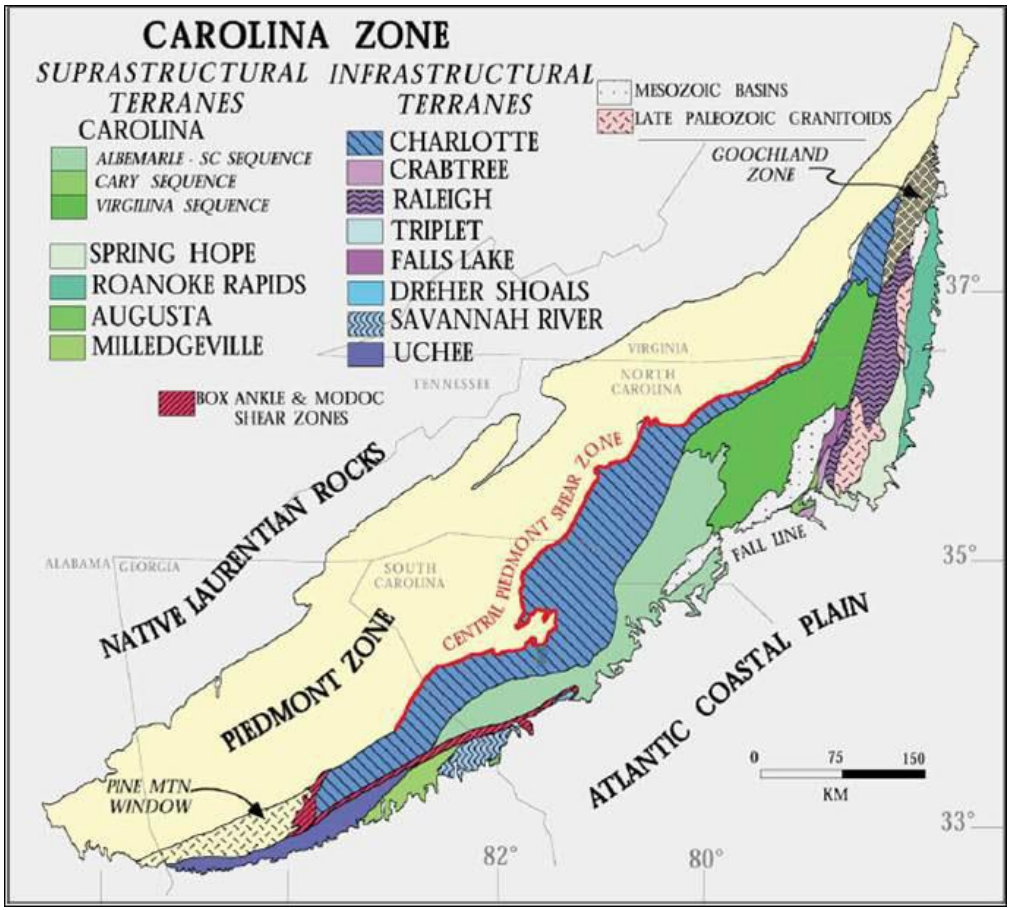

Figure 4.17. The mix of igneous and metamorphic rocks associated with the Carolina Terrane and Charlotte Terrane within the Carolina Zone represent likely source lithologies that match both the rock fragments and minerals observed in thin section and mafic-element and felsic-elements mirrored in the chemostratigraphic zonation.

(After Wood, 1980)

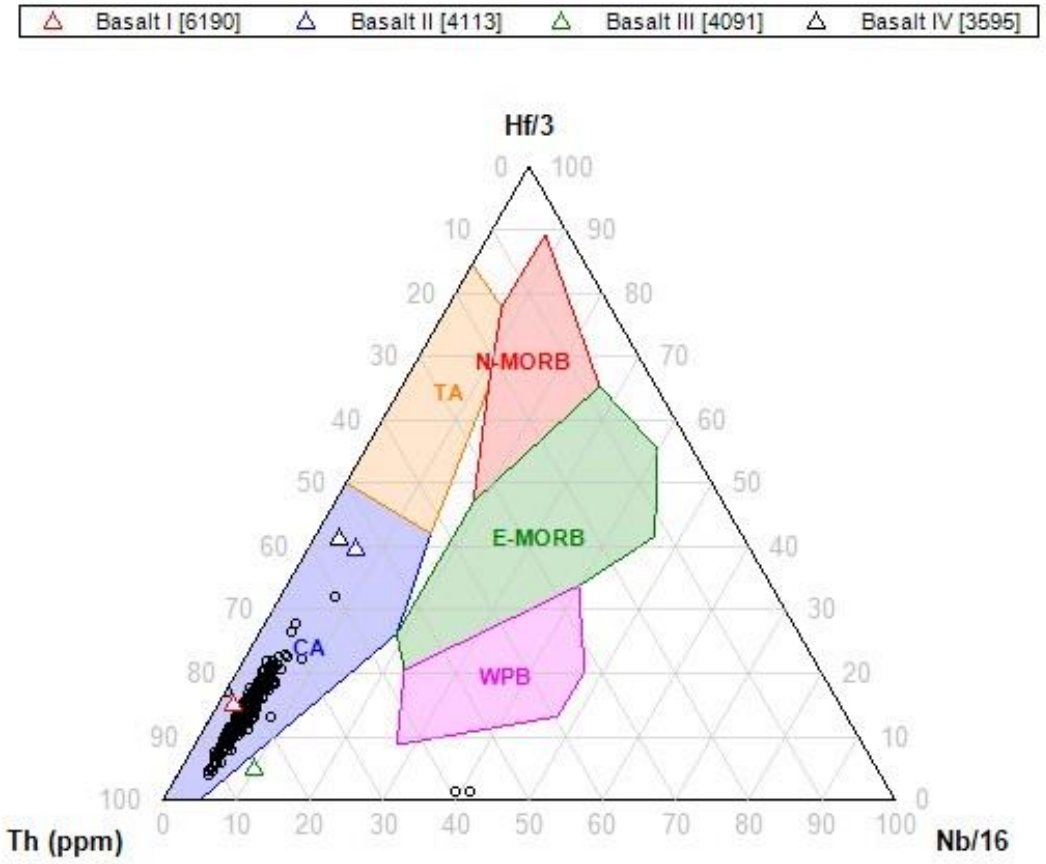

Figure 4.18. Due to the possibility of the intrusive basalts being chemically altered, the (Hf/3)-(Th)-(Nb/16) ternary diagram was selected for basalt geochemical classification because of its reliance on high field strength elements typically resistant to diagenesis. More common plots like Alkali-Ferro-Magneisian (AFM) diagrams consists of elements susceptible to diagenetic mobility (e.g., magnesium, sodium).

Black empty circles plotted represent all non-igenous Rizer #1 samples.

CA = Calc-alkali basalt; TA = Tholeiite (Island Arc); N-MORB = normal mid-ocean ridge basalt; E-MORB = enriched mid-ocean ridge basalt; WPA = within-plate alkali basalt

SECTION 5

5.0 Caprock and CO_2 Storage Assessment of a Portion of the South Georgia Rift Basin Based on Examination of Samples from Test Borehole Rizer #1, Colleton County, SC and USGS Clubhouse Crossroads Test Hole No. 3, Dorchester County, SC

5.1 INTRODUCTION

This section assesses the feasibility of CO_2 injection and storage within the Jurassic/Triassic strata of the South Georgia Rift Basin (SGRB) based on rock properties of and petrologic analyses performed on samples obtained from Rizer #1 test borehole drilled in Colleton County, SC. Only 57.20 linear feet of conventional core was recovered out of the originally proposed 720ft (660ft of reservoir and 60ft of caprock) because the borehole was abandoned at approximately 6200.0ft due to technical difficulties. Since sandstone from the interval originally hypothesized as most favorable for sequestration (well depth 6200.0ft [1.90km] and 9000.0ft [2.74km] was not recovered, the study objectives were revised to collect data to help extrapolate rock character at depths below where Rizer #1 terminated. Subsequently, 108 RSWC were obtained between the depths 2016.0ft (0.61km) and 6140.0ft (1.87km) for the purpose of adding to the petrologic data set and to determine if geologic characteristics significantly changed with depth. A listing of samples and the subsequent analyses performed on them is in Appendix A.

Since the Rizer #1 borehole did not conventionally core any potential caprock (basalt), samples of caprock were obtained from a nearby USGS Clubhouse Crossroads Test Hole No. 3, from Dorchester County, SC (approximately 38.5 miles [62.00km] from Rizer #1; Figure 1.1; Appendices A and B). The USGS Clubhouse Crossroads Test Hole No. 3 is one of three stratigraphic test wells completed in 1975 to study the Charleston, SC earthquake of 1886 (Rankin, 1977). These samples were obtained in July 2012 from the South Carolina Geological Survey and transported to WFT Labs. A listing of samples from USGS Clubhouse Crossroads Test Hole No. 3 and the subsequent analyses performed on them is in Appendix B. The basalt from the USGS Clubhouse Crossroads Test Hole No. 3 is part of an extensive 100's of meters thick subaerial basalt flow covering much of the SGRB (Gohn, 1983b; Figure 1.5). It is also interpreted to be time equivalent with igneous intrusions present within Rizer #1 (Oh et al., 1995; Withjack et al., 2012) but not part of the same igneous body.

The initial scope of work of this project was designed to answer the following questions regarding the efficacy of CO_2 storage within the SGRB.

1. Are there porous horizons with the potential to store at least 30 millions tons of CO_2?
2. Are the trapping reservoirs structurally competent enough to contain the injected CO_2 from migrating upward into the overlying Cretaceous-aged and younger coastal plain aquifers?
3. Are the physical and chemical properties of the potential storage horizons conducive for CO_2 injection and long-term storage?
4. Will the injection of CO_2 enhance continuing injectivity or reduce injectivity?

This section will explain why the answers to questions 1 through 3 are negative for the fault block within the SGRB penetrated by the test borehole Rizer #1 and probably negative for the South Carolina portion of the SGRB. Regarding the 4th question, since the quality of injectivity within the study units is already so low, it is assumed that the little CO_2 which might be injected will not enhance or reduce the degree of injectivity over time.

5.2 METHODS

Assessment of reservoir properties of the study interval is based on routine core analysis of 103 samples from 108 rotary sidewall cores (RSWC) within the depth interval 2850.0ft to 6140.0ft in test borehole Rizer #1 and from twenty-nine (29) horizontal plugs and twelve (12) vertical plugs from the conventional core (CC) between the depths 6000.10ft to 6055.75ft (Appendix E). Porosity measurements were obtained after solvent cleaning and vacuum oven drying at 180°F (82°C) and either ambient or under a net confining stress (NCS) of 1900 psi for the CC plugs or a variable NCS of
900 psi to 1900 psi (Appendix E). Shale rock properties (SRP) analyses were performed on as received conventional core samples from the USGS Clubhouse Crossroads Test Hole No. 3 as obtained from the South Carolina Geological Survey. Porosity, dry bulk, and dry grain density measurements were made on crushed material (Appendix R).

Rock mechanics analyses comprising triaxial compressive tests and acoustic velocities were performed on two (2) vertical plugs from the Rizer #1 CC and the same analyses plus a Mohr-Coulomb failure analysis were performed on three (3) vertical plugs from whole core samples from USGS Clubhouse Crossroads Test Hole No. 3. More detailed descriptions of the procedures are in Appendix Q.

Petrologic analysis of the Clubhouse Crossroads Test Hole No. 3 was done using standard transmitted light petrography and XRD analysis described in Appendix C.

5.3 RESULTS OF ROUTINE CORE ANALYSIS (RCA)

Average (ambient) porosity for the 103 RSWC analyzed is 3.4% with average permeability to air being 0.049 millidarcys (mD). For the 29 CC samples the average (ambient) porosity is 3.1% with average permeability to air being 0.0049 mD (Appendix E).

Special core analysis, such as mercury-injection capillary pressure, generally requires a minimum of 0.2mD permeability (Comisky et al., 2007). Consequently, the special core analysis portion of this study for this project was abandoned. Instead of completing these analyses, an investigation into what destroyed the reservoir properties of the study interval within Rizer #1 was launched with the goal of determining whether more favorable storage horizons might be present within the SGRB lateral to or deeper than the Rizer #1 study interval.

Crushed porosity results from the two (2) samples from USGS Clubhouse Crossroads Test Hole No. 3 averaged 2.6% (Appendix R). These analyses show the hypothetical cap rock is only slightly less porous than a possible storage horizon recovered from Rizer #1.

5.4 RESULTS OF ROCK MECHANICS TESTS

Tests were run on the both surrogate caprock basalts from USGS Clubhouse Crossroads Test Hole No. 3 and possible storage horizon recovered from Rizer #1. Looking at two parameters, compressive strength and compressional ultrasonic wave velocity, the basalts had over twice the compressional strength (74841-76236 psi versus 25894–32107 psi; Appendix Q) and a significantly higher compressional ultrasonic wave velocity (19467-20041 ft/sec versus 14016-14763 ft/sec; Appendix Q) than the sandstones tested from Rizer #1. Mohr-Coulomb analysis conducted on two intervals from USGS Clubhouse Crossroads Test Hole No. 3 shows average internal friction angle and unconfined compressive strength of 52 degrees and 58732 psi, respectively.

5.5 RESULTS OF PETROLOGIC EXAMINATION OF BASALT CAPROCK FROM USGS CLUBHOUSE CROSSROADS TEST HOLE NO. 3

Petrologic examinations in the form of XRD and thin section petrography was performed on the shallowest (999.04m) and deepest (1008.69m) whole core samples selected from the USGS Clubhouse Crossroads Test Hole No. 3. Based on petrographic examinations, both samples are tholeiitic basalts (extrusives) with only minor degrees of weathering (Appendix R; Plates 1 and 2). This contrasts with the prevalence of low- temperature secondary replacement by calcite, dolomite, and chlorite present within the intrusives encountered in test borehole Rizer #1 (Figures 2.22, 2.23, 2.24).

Without chemical analysis of the Clubhouse Crossroads Test Hole No. 3 extrusives it is not possible to determine if they are related to the intrusive basalts recovered by RSWC in the test borehole Rizer #1.

5.6 DISCUSSION

As noted in the introduction, this section will propose answers to the questions from the original scope of work regarding the efficacy of CO_2 storage within the SGRB. The answers are based on results presented in this section, as well as other sections in this report.

Are there porous horizons with the potential to store at least 30 millions tons of CO_2 present within the SGRB? – Based on RCA results presented within this section, the sandstone intervals present within the recovered study interval of test borehole Rizer #1 are not suitable for the storage of CO_2. It can also be assumed that laterally equivalent sandstones within the same fault block underwent the same degree of compaction and cementation and, consequently, are not suitable candidates for CO_2

sequestration. Regarding the likelihood of favorable reservoir properties for sandstones deeper in this fault block, the authors feel that unless these sandstones experienced early cementation and subsequent dissolution of the early cements to create secondary porosity or were over pressured early in their burial history, it is unlikely they possess reservoir properties to be suitable candidates for CO_2 sequestration. Regarding the prospect of underlying sandstones being overpressured, since the numerous igneous dikes that permeate the South Carolina portion of the SGRB (Figure 1.5) are highly fractured and likely conduits for fluids and gases, it is unlikely the South Carolina portion of the SGRB that contains dikes is overpressured. What cannot be predicted by the study results, however, are the reservoir properties of the estimated 9200ft (2.8km) of SGRB strata that was eroded off the top of the uplifted block which Rizer #1 penetrated. Presumably these strata are present within those portions of the SGRB that were not inverted. These strata are also overlain by the Early Jurassic basalt flow hypothesized to cover much of the SGRB (McBride et al., 1989) and present in USGS Clubhouse Crossroads Test Hole No. 3.

Are the trapping reservoirs structurally competent enough to contain the injected CO_2 from migrating upward into the overlying Coastal Plain aquifers? – None of the projected igneous caprock units were encountered within the study interval recovered in test borehole Rizer #1. Due to the high dip angles of igneous bodies encountered, they are interpreted to be all intrusive dikes. Furthermore, these features also coincide with intervals of high angle fractures (Figures 2.22, 2.23, 2.24). The prevalence of low-temperature secondary replacement by calcite, dolomite, and chlorite indicates groundwater alteration by flow through the numerous fractures associated with these dikes. Studies of dikes within Triassic basins of North Carolina indicate "… the presence of dikes increases the probability of differential weathering, which could enhance groundwater movement along contact of the dike with adjacent country rock" (NCDENR, 2012). In conclusion, the presence of numerous dikes within the Rizer #1 fault block combined with the lack of a basalt flow cap rock at the top of the Triassic sequence indicates that portion of the of the SGRB is not structurally competent enough to prevent injected CO_2 from migrating upward into the overlying Cretaceous-aged and younger coastal plain aquifers.

Are the physical and chemical properties of the potential storage horizons conducive for CO_2 injection and long-term storage? - No, based on RCA and petrologic examinations of the study interval, there is insufficient reservoir potential for it to be a suitable candidates for CO_2 sequestration. It can also be assumed that laterally equivalent sandstones within the same fault block underwent the same degree of compaction and cementation and, consequently, also are not suitable candidates.

Will the injection of CO_2 enhance continuing injectivity or reduce injectivity? – Since the quality of injectivity within the study units is already so low, it is assumed that the little CO_2 which might be injected will not enhance or reduce the degree of injectivity over time.

5.7 CONCLUSIONS

1. Sandstone intervals present within recovered study interval of test borehole Rizer #1 are not suitable for the storage of CO_2.
2. The presence of numerous dikes within the South Carolina portion of the SGRB indicates that portion of the basin is not structurally competent enough to prevent injected CO_2 from migrating upward into the overlying Cretaceous-aged and younger coastal plain aquifers.
3. It can be assumed that underlying and laterally equivalent sandstones within the same fault block as test borehole Rizer #1 underwent the same degree of compaction and cementation and, consequently, are not suitable candidates for the storage of CO_2.

5.8 CITATIONS

Comisky, J.T., K.E. Newsham, and J.A. Rushing, and T.A. Blasingame, 2007. A Comparative Study of Capillary-Pressure-Based Empirical Models for Estimating Absolute Permeability in Tight Gas Sands: SPE 110050; 2007 SPE Annual Technical Conference and Exhibition: SPE, Texas A&M University, p. 1-18.

McBride, J.H., Nelson, K.D., Brown, L.D., 1989, Evidence and implications of an extensive early Mesozoic rift basin and basalt/diabase sequence beneath the southeast Coastal Plain: Geological Society of America Bulletin, v. 101, p.512-520

NCDENR, 2012, Oil and Gas Study: North Carolina Department of Environment and Natural Resources http://portal.ncdenr.org/web/lr/studies

Oh, J., Austin, J.A., Phillips, J.D., Coffin, M.F., and Stoffa, P.L., 1995, Seaward-dipping reflectors offshore the southeastern United States: Seismic evidence for extensive volcanism accompanying sequential formation of the Carolina trough and Blake Plateau basin: Geology v. 23, p. 9–12

Rankin, D.W., 1977. ed., 1983, Studies related to the Charleston, South Carolina earthquake of 1886-A Preliminary Report: U.S. Geological Survey Professional Paper 1028, 276 p.

Withjack, M. O., Schlische, R.W. & Olsen, P. E., 2012, Development of the passive margin of eastern North America: Mesozoic rifting, igneous activity, and breakup. In: Bally, A. W. & Roberts, D. G. (eds), Principles of Phanerozoic Regional Geology, v. 1, Elsevier, Amsterdam, p. 301–335

Appendix 2. List of Articles, Presentations and Posters produced by DE-FE0009165

Akintunde, M. (presenter), C.C. Knapp, J.H. Knapp, M. Prasad, and P.E. Olsen, 2011, Porosity and permeability of Jurassic-Triassic formations of the South Georgia Rift Basin: Potential implications for CO2 storage, AGU Fall Mtg., San Francisco, CA.

Akintunde, M., Knapp, C., Knapp, J., Heffner, D.M., and J.M. Shafer, 2011, Reinterpretation of the "J" basalt reflector from seismic data: Reprocessing across the coastal plain of southeastern Georgia: Potential implications for long term CO_2 sequestration, AAPG Annual Meeting, Houston, TX.

Akintunde, O.M., Knapp, C.C., and J.H. Knapp, 2012, Experimental Evaluation of the Physical Properties of Basalt Flows and Diabase Sills of the South Georgia Rift Basin: Potential Implications for CO_2 Sequestration, AAPG Search and Discovery Article 90142 (2012 AAPG Annual Convention and Exhibition).

Akintunde, O.M., Knapp, C.C., and J.H. Knapp, 2012, Rock physics characterization of the South Georgia Rift basin for supercritical CO_2 storage, Research Experience in Carbon Sequestration (RECS), Birmingham, AL.

Akintunde, O.M., C. Knapp, and J. Knapp, 2013b, Petrophysical characterization of the South Georgia Rift basin for supercritical CO2 storage: a preliminary assessment. *Environmental Earth Sciences,* doi 10.1007/s12665-013-2355-6.

Brantley, D.T., Shafer, J.M, and V. Lakshmi, 2015, CO_2 Injection Simulation into the South Georgia Rift Basin for Geologic Storage: A Preliminary Assessment, *Environmental Geosciences* (in press).

Clendenin, C.W., Waddell, M.G., Addison, A.D., 2011, Reactivation and overprinting of the South Georgia rift Extension. Geol. Soc. Am. Abstra. Programs43 (5), p551.

Clendenin, C.W., Waddell, M.G., Addison, A.D., 2012, Triassic rifting in western Pangea. Geol. Soc. Am. Abstra. Programs44 (7), p286.

Clendenin, C.W., 2013, Insights into mode of the South Georgia rift extension in eastern Georgia, USA. Tectonophysics 608, p 613-621.

Heffner, D.M., and J. Knapp, 2011, New constraints on geometry and structure of the South Georgia Rift from well data and seismic reflection interpretation, Southeastern GSA meeting, Wilmington, DE.

Heffner, D.M., J.H. Knapp, O.M. Akintunde, and C.C. Knapp, 2011, Preserved extent of the Jurassic flood basalt in the South Georgia Rift: A new interpretation of the J horizon, *Geology*, on-line.

Heffner, D.M., Knapp, J., Akintunde, M., Knapp, C., and J.M. Shafer, 2011, Carbon sequestration in the South Georgia Rift: Is the ubiquitous "J" reflection synonymous with basalt, AAPG Annual Meeting, Houston, TX.

Heffner, D.M., J.H. Knapp, O.M. Akintunde, and C. Knapp, 2011, Preserved extent of Jurassic flood basalt in the South Georgia Rift: a new interpretation of the J-Horizon, *Geology*, 40, doi:10.1130/G32638.1.

Heffner, D.M., 2013, Tectonics of the South Georgia Rift, PhD Dissertation, University of South Carolina.

Heffner, D.M., and J.H. Knapp, 2011, Transfer faults of the South Georgia Rift, Fall GSA Mtg., Minneapolis, MN.

Hollon, B., Mainali, P., Dix, M., Fu, R., Hoghton, N., Waddell, M.G., 2014, Whole rock bulk geochemistry in evaluating a CO_2 injection well, 2014 AAPG Annual Conference and Exhibition. Abstra.

Rine, J.M., Hollon, B., Fu, R., Houghton, N., Waddell, M.G., 2014, Diagenetic and burial history of a portion of the late Triassic South Georgia Rift Basin based on petrologic and isotopic (§^{18}O) analyses of sandstones from test borehole Rizer #1, Colleton County, SC, 2014 AAPG Annual Conference and Exhibition. Abstra.

Rine, J.M., Hollon, B., Fu, R., Waddell, M.G., 2014, Reconstruction of diagenetic and burial history of South Georgia Rift Basin- and example of rifting, drifting, and inversion along the passive margin of Eastern North America based on analyses of sandstones from Rizer #1 test borehole, Colleton County, SC. Houston Geological Society meeting.

Shafer, J.M., and D.T. Brantley, 2011, Characterizing a geologic formation, *Chemical Engineering Process*, 107(8), pp. 50-52.

Waddell, M.G., Addison, A.D., Brantley, D., Knapp, C., 2011, Reservoir and caprock assessment using existing seismic and well data for CO_2 geologic sequestration in the South Georgia rift basins of the lower Coastal Plain of SC, AAPG Annual conference and Exhibition. Abstra. 90124

Appendix 3: Best Practices Learned (BPL) for Carbon Sequestration Site Characterization in Unexplored Basins

Introduction

With the increase number of geologic CO_2 sequestration (CCS) projects there is a need for best practices or lessons learned in unexplored, data deficient basins. An example of a data deficient basin is the South Georgia Rift Basin. In data deficient area, site characterization must rely on the acquisition, processing, and interpretation of geophysical data such as 2D and 3D seismic reflection data. Listed below are two tables addressing issues we encountered during the initial characterization and drilling of the characterization test boring in an extremely data deficient basin. The BPLs listed are to minimize potential impacts for future projects in similar environments.

The main characterization tool in an area where there is virtually no geologic or well data is the collecting, processing, and interpreting 2D and 3D seismic reflection data. The second part are issues and lessons learned concerned with the drilling operations. This document should be used as template to develop BPLs in other areas of the country. The BPLs presented in this document are the issues and the BPLs to address these issues and potential impacts we encountered while conducting seismic surveys in South Carolina and Georgia and drilling a characterization test boring.

Objectives

The objectives of these lessons learned are highlight issues and subsequent lessons learned this project team encountered during characterization study of the South Georgia Rift Basin in parts of South Carolina and Georgia and issues and impacts encountered during drilling operations. It is important to remember that site characterization and drilling is very dynamic process.

Seismic Acquisition

Issues and Potential Primary Impacts Seismic lines & grids	Best Practices Lessons Learned
• Permits	• If collecting seismic along state and county roads, obtain all state and county permits and keep DOT personnel informed on the survey location and any lane closures. • In areas of heavy traffic, hire local law enforcement personnel for assisting in traffic control.
• Public Concerns about seismic operations • Notify state and local authorities	• Before seismic operations begin, the public should be notified in the areas affected by seismic operations. • If conducting seismic operations within a municipality, notify city or town officials of when the operations will be conducted and what areas are going to be affected by the operation. • Consider conducting operations during the night to reduce traffic congestion. • If operations are going to audibly affect residential areas, seismic activities should occur during daylight to reduce the effect of the noise.
• Damage to roads and right-away	• If using vibroseis or weight drop sources, constantly check for road damage. • If damage is observed, add either wood pad or neoprene pad to the base plate to prevent farther damage to the roadway.
• Damage to vegetation and crops	• Schedule operations after crop harvest. • Establish a fixed price for damaged crops and trees.
• Disturbance to wildlife and human populations from vibroseis machine vibrations and shot-hole drilling	• Schedule operations during least sensitive periods, avoiding migration, nesting and mating seasons.

	• Attempt to schedule after hunting season.
• Erosion and changes in surface hydrology from unplugged or improperly plugged shot holes and seismic lines (cleared vegetation)	• Shot-hole methods should be considered (in the place of vibroseis machinery) where vegetation cover is required and where access challenging. Ensure that the dynamite charge is small enough and deep enough to avoid cratering. Consider aquifer protection and suitable plugging. Use offsets to avoid specific sensitivities. **Ensure that misfired charges are disabled and removed**. • Mobilize clean-up crews after operations • If using vibroseis machinery on soft ground, avoid excessive compaction from vehicles and baseplates • Ensure appropriate handling and storage of fuels and hazardous materials (e.g. explosives) • Cut seismic line pathways by hand to minimize vegetative disturbance • Minimize the width of corridors to ensure compatibility with operational, health and safety requirements • Do not cut trees greater than 20 centimeters (8 inches) in diameter • Minimize clearing of vegetation and leave in place smaller vegetation, topsoil, root stock, seeds and endangered or protected species and species used by local communities for commercial or subsistence use. • Always let the land owner know what your intentions are on clearing or disturbing the land.

Drilling Operations

Issues and Potential Primary Impacts Drilling Operations	Best Practices Lessons Learned
• Permits	• Make sure project team understands the drilling regulations for the state the operation is occurring in. • Make sure the regulators understand the project objectives and keep them informed on drilling operations. • Prior to drilling operations, establish and approve by the regulators a well abandonment plan.
• Contractor	• Make sure the drilling contractor or integrated services contractor understands the local geology thereby reducing rig downtime. • Have a drilling engineer available 24/7. • Have the contractor or integrated services contractor write a final well plan for drilling of the borehole.
• Well Plan	• At a minimal, the well plan should have a general drilling plan (depth of conductor casing, depth of surface casing, hole diameter, casing and cementing plan, fluid plan, mud-logging plan, frequency of morning reports, coring plan and list of wireline logs). • Health and safety plan • Drilling schedule (including drill time curve and well cost estimate) • The most important details of the drilling plan need to be approved by the contactor, project team, and regulators.
• Site selection and site preparation	• Base the site selection on the geologic data • Make sure the site meets all the criteria outline in the NEPA. • Secure the site with a lease from the land owner.

	• Inform the landowner about how the site is going to be modified for drilling operation. • Present to the landowner a post drilling closure plan on how the site will be restored and obtain his approval in writing before site preparation. • Always have the integrated services and drilling contractor inform the project team of any changes to the post closure plan. • Have a reliable water source to supply water for drilling operation.
Drilling	• Notify regulators that drilling operation is beginning. • Notify adjacent landowners and homeowners that drilling is beginning. • Follow the drilling plan, however, drilling is a dynamic process. Any changes in the drilling plan need to be addressed by the integrated services manager. The manager then needs to notify all parties involved in the drilling operations about the changes. • Insure the integrated service manager has scheduled all drilling supplies and services to be there in a timely manner so there is no rig down time. • When finished drilling, notify the landowner drilling operations have ceased. • Obtained landowner approval for the site restoration plan and completion.